



Université du Québec
à Rimouski

**PROPRIÉTÉS BIO-OPTIQUES ET APPLICATIONS DE
TÉLÉDETECTION POUR LA CARTOGRAPHIE DE LA
DISTRIBUTION DES PRODUCTEURS PRIMAIRES DANS
LES ZONES CÔTIÈRES DE L'ESTUAIRE ET
DU GOLFE DU SAINT-LAURENT**

Thèse présentée

dans le cadre du programme de doctorat en sciences de l'environnement

en vue de l'obtention du grade de Philosophiæ Doctor (Ph.D.)

PAR

© CARLOS ALBERTO SAMPAIO DE ARAÚJO

Novembre 2023

Composition du jury :

Michel Gosselin, président du jury, Université du Québec à Rimouski

Simon Bélanger, directeur de recherche, Université du Québec à Rimouski

Jean-Éric Tremblay, codirecteur de recherche, Université Laval

Cédric Fichot, examinateur externe, Boston University

Jean-Pierre Blanchet, autre examinateur, Université du Québec à Montreal

Dépôt initial le 16 juin 2023

Dépôt final le 01 novembre 2023

UNIVERSITÉ DU QUÉBEC À RIMOUSKI
Service de la bibliothèque

Avertissement

La diffusion de ce mémoire ou de cette thèse se fait dans le respect des droits de son auteur, qui a signé le formulaire « *Autorisation de reproduire et de diffuser un rapport, un mémoire ou une thèse* ». En signant ce formulaire, l'auteur concède à l'Université du Québec à Rimouski une licence non exclusive d'utilisation et de publication de la totalité ou d'une partie importante de son travail de recherche pour des fins pédagogiques et non commerciales. Plus précisément, l'auteur autorise l'Université du Québec à Rimouski à reproduire, diffuser, prêter, distribuer ou vendre des copies de son travail de recherche à des fins non commerciales sur quelque support que ce soit, y compris Internet. Cette licence et cette autorisation n'entraînent pas une renonciation de la part de l'auteur à ses droits moraux ni à ses droits de propriété intellectuelle. Sauf entente contraire, l'auteur conserve la liberté de diffuser et de commercialiser ou non ce travail dont il possède un exemplaire.

Ao meu pai, dedico

« Ogum veio da beira mar

Foi mamãe Iemanjá quem mandou

Saravá Ogum de Malê no Ilê

Foi mamãe Iemanjá quem mandou »

Ode to Ogum, from a fragment of **Ogum de Malê**, a song by **Jackson do Pandeiro**, and written by **Laesse Miranda** and **Antônio Nuñez**. Recorded at 78 RPM, Columbia 3107, **1960**, matrix number CBO-2295 (A-side).

In Afro-Brazilian religious cults, Iemanjá is the goddess of the seas. Ogum Beira-mar, also a god, guards the shores and tides, and makes the connection between land and the kingdom of Iemanjá.

ACKNOWLEDGEMENTS

The development of this thesis brings with it an immersion in a journey that goes beyond the academic goals, which is already a challenge. In this way, I express here my sincere acknowledgements to everyone who participated in one way or another of this journey.

First, I would like to express my gratitude to my thesis supervisor, Simon Bélanger, which provided me the opportunity to do a doctorate, trusted and supported in several ways, and always allowed me to work in an independently way. I'm also grateful for the professional opportunities I had as Assistant teacher and Lecturer, at UQAR, and as Earth Observation Scientist, at ARCTUS Inc.

I extend my acknowledgements to my co-supervisor, Jean-Éric Tremblay, for his experience and constructive comments along the development of this work, as well as the other committee members of this thesis project, Christian Nozais and Mathieu Cusson. I also thank the thesis committee, Michel Gosselin, Cédric Fichot and Jean-Pierre Blanchet, for the interest they showed to evaluate this work.

From the warm reception, passing through days in the field or doing laboratory analysis, discussing codes or papers, or just present in relaxation time, I salute all my colleagues of AQUATEL Lab of today and erstwhile: Alexandre Théberge, Zélie Schuhmacher, François-Pierre Danhiez, Lucas Freitas, Thomas Jaegler, Zoe Amorena, Claudia Carrascal-Leal, Geneviève Arboit, Rémi Constanzo, Yanqun Pan, Brigitte Légaré, Soham Mukherjee, Rakesh Singh, Raphaël Mabit, Loïc Dallaire, Véronique Thériault, Alycia Boismenu, Daniela Walch, and Josiane Lavoie-Bélanger.

Doing regular fieldworks in the Bay of Sept-Îles would not be possible without the expertise of captains Glenn Galichon and Serge Galienne, and the logistical support of Julie

Carrière (INREST) and Claudy Deschênes. I also thank the collaboration of Jean-Luc Shaw, Kim Demers, Aurélie Le Hénaff, Laurence Paquette, Manon Picard, and Jonathan Gagnon.

The access to laboratory facilities and materials, fieldwork equipment, and all university-related bureaucracy can be difficult to reach and an extremely time-consuming task. Fortunately, these were done smoothly along my doctorate thanks to the following persons: Jonathan Coudé, Steeven Ouellet, Bruno Cayouette, Pascal Rioux, Melanie Simard, Claude Belzile, Marie-José Naud, Sophie Banville, Danie Massé, Diane Proulx, Edith Plourde, and Thomas Buffin-Bélanger.

I'm grateful to my past scientific advisors, which greatly contributed to the development of my scientific curiosity and rigor, they are: Valdenir Furtado, Luis Conti, João Lorenzetti, José Stech, and Claudio Barbosa. I also thank my colleagues Marcelo Curtarelli, Joaquim Leão, Igor Ogashawara and Fernanda Sampaio, for sharing their experiences with me while collaborating to develop my scientific skills.

As part of this journey, I thank all support that I received from my parents, Eronides (*in memorian*) and Fátima, and all family and friends who contributed to this cause, Maju, Luiz, Gilda, Mara, Beto and Ricardo. Finally, this PhD is also a conquer of my family, my life partner Inês, and my two daughters, Iara and Flora.

FOREWORD

The development of this thesis was only possible thanks to research projects awarded to (or in collaboration with) the *Laboratoire d'optique aquatique et de télédétection* (AQUATEL), at the *Université du Québec à Rimouski* (UQAR), and scholarships grants awarded to the author, as detailed below.

The first research project was the Canadian Healthy Oceans Network (CHONe-2), funded by the Natural Sciences and Engineering Research Council of Canada (NSERC) in partnership with Fisheries and Ocean Canada and INREST (representing the Port of Sept-Îles and City of Sept-Îles). Specifically, this thesis is part of the CHONe Project 2.1.2, which major objective was “*to evaluate and model how natural and anthropogenic stressors interact to impact pelagic and benthic communities along a sub-arctic coastline and develop bay-scale condition indicators*”. Because of common objectives and the possibility to integrate the same methodology in other areas (although the same regional context), this thesis contributed to other two research projects: WISE-Man and RQM 1. The WISE-Man Project (WaterSat Imaging Spectrometer Experiment [WISE] for Optically Shallow Inland and Coastal Waters Assessment) was funded by the Canadian Space Agency through the FAST program, Fisheries and Oceans Canada through the Coastal Environmental Baseline Program, and Québec-Ocean. The RQM 1 (subproject “*Eelgrass meadows in Québec: Evolution and status*”) was funded by the *Réseau Québec Maritime*. The scholarships were provided by the *Fonds de Recherche du Québec – Nature et technologies* (FRQNT), through a grant of the Merit Scholarship Program for Foreign Students (PBEEE); the *Fondation de l’UQAR*, through a Research Merit Scholarship; CHONe-2; a NSERC Discovery Grant of Simon Bélanger; RQM 1; and Québec-Océan.

This thesis is divided in five sections: a general introduction, the main body of the text with three research articles, and a general conclusion. The general introduction situates this thesis in an environmental science perspective and provides major guidelines to concepts that are explored along all the sections. Major research questions and the thesis objectives are presented in the end of the introduction. The research articles are written in journal-specific formats and, while containing original data and analysis, they also provide future perspectives in each domain explored in the manuscripts. The general conclusion integrates the work developed in each research article into a broader perspective and provides ideas for future work and research priorities. Finally, a supplementary material for each research article (annex) and a complete list of references for all the thesis is provided after the general conclusion.

List of publications made during the doctorate:

- Araújo CAS**, Belzile C, Tremblay J-É, Bélanger S. 2022. Environmental niches and seasonal succession of phytoplankton assemblages in a subarctic coastal bay: Applications to remote sensing estimates. *Frontiers in Marine Science*, 9:1001098. doi: 10.3389/fmars.2022.1001098
- Ferrario F, **Araújo CAS**, Bélanger S, Bourgault D, Carrière J, Carrier-Belleau C, Dreujou E, Johnson LE, Juniper SK, Mabit R, McKindsey CW, Ogston L, Picard MMM, Saint-Louis R, Saulnier-Talbot E, Shaw J-L, Templeman N, Therriault TW, Tremblay J-É, Archambault P. 2022. Holistic environmental monitoring in ports as an opportunity to advance sustainable development, marine science and social inclusiveness. *Elementa: Science of the Anthropocene*, 10:1. doi: 10.1525/elementa.2021.00061
- Mabit R, **Araújo CAS**, Singh RK, Bélanger S. 2022. Empirical remote sensing algorithms to retrieve SPM and CDOM in Québec coastal waters. *Frontiers in Remote Sensing*, 3:834908. doi: 10.3389/frsen.2022.834908
- Araújo CAS**, Bélanger S. 2022. Variability of bio-optical properties in nearshore waters of the estuary and Gulf of St. Lawrence: Absorption and backscattering coefficients. *Estuarine, Coastal and Shelf Science*, 264: 107688. doi: 10.1016/j.ecss.2021.107688
- Sampaio FG, **Araújo CAS**, Dallago BSL, Stech JL, Lorenzetti JA, Alcântara E, Losekann ME, Marin DB, Leão JAD, Bueno, GW. 2021. Unveiling low-to-high-frequency data sampling caveats for aquaculture environmental monitoring and management. *Aquaculture Reports*, 20: 100764. doi: 10.1016/j.aqrep.2021.100764
- Murphy GEP, Dunic J, Adamczyk EM, Bittick SJ, Côté IM, Cristiani J, Geissinger EA, Gregory RS, Lotze HK, O'Connor MI, **Araújo CAS**, Rubidge EM, Templeman ND, Wong MC. 2021. From coast to coast to coast: Ecology and management of seagrass ecosystems across Canada. *FACETS*, 6: 139-179. doi: 10.1139/facets-2020-0020
- Araújo CAS**, Sampaio FG, Alcântara E, Curtarelli M, Ogashawara I, Stech J. 2017. Effect of cold fronts on stratification and water quality of a tropical reservoir: implications for aquaculture. *Aquaculture Environment Interactions*, 9: 385-403. doi: 10.3354/aei00240

List of scientific communications presented during the doctorate (1st author only):

- Araújo CAS.** 2023. *Suivi satellitaire à long terme des herbiers de zostère dans la zone intertidale du Saint-Laurent avec Landsat*. Oral presentation (presented by Simon Bélanger) given at the *Rencontre d'échanges sur la végétation aquatique du fleuve Saint-Laurent*, organized by the MELCCFP, 12 April, Québec (Canada).
- Araújo CAS.** 2021. Seasonal succession and optical characterization of phytoplankton assemblages within surface waters of a subarctic coastal bay. Oral presentation given at a webinar for the Network on Coastal, Oceans & Lake Optics Remote sensing (NetCOLOR), 29 September.
- Araújo CAS.** 2021. Light and dynamic of primary producers in coastal and nearshore environments: a bio-optical-based assessment in the Estuary and Gulf of St. Lawrence. Oral presentation given at the Québec-Océan Annual Scientific Meeting, 8-11 February. (*Online event*)
- Araújo CAS, Tremblay J-É, Bélanger S.** 2020. Relationships between phytoplankton assemblages and bio-optical variability in a coastal environment of the Gulf of St. Lawrence. Poster presented at the Ocean Sciences Meeting, 16-21 February, San Diego (USA), and at the Québec-Océan Annual Scientific Meeting, 9-11 March, Beaufort (Canada).
- Araújo CAS, Danhez F-P, Bélanger S.** 2019. CDOM absorption and DOC concentration relationships in the coastal area of Sept Îles Bay: Preliminary results. Poster presented at the *Forum Québécois en Sciences de la Mer*, 11-13 November, Rimouski (Canada).
- Araújo CAS, Bélanger S, Tremblay J-É, Cusson M.** 2019. Light and primary producers' dynamics in a subarctic coastal embayment: A satellite-based assessment: Preliminary results. Oral presentation given at the International Congress on Industrial Port Research (CIRSIP), 27-31 May, Sept-Îles (Canada). (*Invited speaker*)
- Araújo CAS, Bélanger S, Cusson M.** 2019. Eelgrass (*Zostera marina*, L.) distribution variability in the St Lawrence Estuary as detected by Landsat historical images (1985 – 2017). Oral presentation given at the Vecteur Conference, 15-17 April, Rimouski (Canada).
- Araújo CAS, Schuhmacher Z, Cusson M, Bélanger S.** 2018. Eelgrass (*Zostera marina*, L.) distribution variability in the Bay of Sept Îles as detected by Landsat historical images (1985 – 2017). Poster presented at the CHONe II 3rd Network Meeting, 29 November - 1 December, Ottawa (Canada). (*Best poster award*)

BIO-OPTICAL PROPERTIES AND REMOTE SENSING APPLICATIONS FOR
MAPPING THE DISTRIBUTION OF PRIMARY PRODUCERS IN NEARSHORE
AREAS OF THE ESTUARY AND GULF OF SAINT LAWRENCE

ABSTRACT

The relationship between nature and humanity is in the spotlight in the 21st century, while the proximity of coastal zones is one of the most attractive areas in the world for human settlements due to their unique offer of environmental (social, economical, and ecological) goods. Notwithstanding, nearshore areas host diverse ecologically relevant and sensitive habitats. In this context, while forming the basis of trophic chains, primary producers such as phytoplankton and foundation species of coastal vegetated habitats constitute key organisms of such ecosystems. Specifically in northern high latitudes, the rising temperatures and sea-ice loss due to global warming are about twice as fast as in mid-latitudes (Arctic amplification), with consequences for ocean, coastal and nearshore processes. Because of the natural wide spatial and temporal variability of oceanographic and watershed processes acting over nearshore areas, the ability to monitor and manage them often represent a challenge for stakeholders, scientists, and decision-makers. Earth observation satellites (EOS) present themselves as a singular tool to address spatial and temporal variabilities of primary producers in nearshore areas. However, the possibility to retrieve biogeochemical information of surface waters from EOS applications requires knowledge about their optical properties. The main objectives of this thesis were to establish a baseline of knowledge about the optical properties and develop remote sensing tools to better understand the variability of primary producers in nearshore waters of subarctic and cold temperate environments. This thesis is composed of three research papers using a combination of *in situ* (ship-based) and satellite-based approaches to achieve these goals. The studied areas included nearshore subregions of the estuary and Gulf of St. Lawrence (EGSL), Eastern Canada, being the coastal areas near the Bay of Sept-Îles (BSI), the Manicouagan (MAN) Peninsula, Forestville (FV), Rimouski bay (RIB), and L'Isle Verte bay (IVE). In the first article, BSI, MAN and FV subregions were investigated using (distinct) *in situ* sampling design strategies, and all field campaigns collected optical and biogeochemical quantities (molar and dry-mass concentrations) to investigate their major relationships. The bio-optical properties of nearshore waters of the north part of EGSL are under the influence of major (or local) organic matter-rich riverine discharges. Specifically, it was shown that the absorption coefficient of the chromophoric dissolved organic matter (CDOM) strongly dominates the absorption budget, and that these waters have very low mass-specific backscattering coefficient. These factors characterize a strongly light-absorbing and weakly light-scattering medium, resulting

in low reflectance values and with implications for the applications of optical remote sensing approaches. Despite the dominance of terrigenous absorbing components, the biomass of phytoplankton was not negligible (chlorophyll-*a* concentrations $\geq 1 \text{ mg m}^{-3}$). Overall, the sampling strategy revealed a complex interplay of spatial (between and within subregions) and temporal (seasonal, synoptic, and circadian) variabilities acting on nearshore EGSL and influencing its optical properties. In the second article, we hypothesized that the composition of major phytoplankton assemblages in BSI subregion will covary with temperature and the bulk optical properties of the environment. The *in situ* sampling revealed a strong seasonal (spring to autumn) pattern modulating the composition of phytoplankton assemblages, while statistically significant differences of temperature and bio-optical properties between the different groups were observed. Before the freshet, spring bloom was dominated by large (microphytoplankton) cells (diatoms), and the succession followed a shift towards nanophytoplankton and picophytoplankton cells throughout summer and fall. Whilst confirming the hypotheses, it was also demonstrated the capability to retrieve the major phytoplankton assemblages from EOS sensors, with possible applications to monitoring programs. The third article used a long-term time series (~40 years) from EOS (Landsat missions) to address the interannual and decennial variability of seagrass (eelgrass, *Zostera marina* L.) meadows coverage in intertidal areas of BSI, MAN, RIB, and IVE subregions of EGSL. From the methodological aspect, knowledge about the variabilities of optical properties and tides were essential to optimize EOS approaches. The area of the meadows presented a significantly increasing trend (10 to 20-fold greater than the initial surface area, considering the period from 1984 to 2022). Particularly, in MAN and BSI subregions the observed growing trend was towards land. Overall, this thesis focused on the retrieval of the spatial distribution of two important primary producers (i.e., phytoplankton assemblages and seagrass meadows) using EOS approaches in changing EGSL nearshore subregions. An avenue of possibilities remains to be explored through incorporating EOS approaches in nearshore EGSL zones in social-ecological systems, where the environment and its interaction with the anthroposphere can be modeled and predicted. Nonetheless, this thesis represents a first step towards a more representative sampling of these two important environmental variables.

Keywords: nearshore habitats, bio-optical properties, CDOM, backscattering coefficient, phytoplankton seasonal succession, remote sensing, eelgrass meadows, *Zostera marina*, Landsat, Saint Lawrence Estuary

RÉSUMÉ

La relation entre la nature et l'humanité est une préoccupation grandissante du 21^e siècle, alors que la proximité des zones côtières est l'une des zones les plus attractives au monde pour les établissements humains en raison de leur offre unique de biens environnementaux (sociaux, économiques et écologiques). En effet, les zones littorales abritent divers habitats écologiquement pertinents et sensibles. Dans ce contexte, tout en constituant la base des chaînes trophiques, les producteurs primaires tels que le phytoplancton et les espèces fondatrices des habitats végétalisés côtiers constituent des organismes clés de tels écosystèmes. Plus précisément dans les hautes latitudes septentrionales, la hausse des températures et la perte de glace de mer due au réchauffement climatique sont environ deux fois plus rapides qu'aux latitudes moyennes (amplification arctique), avec des conséquences sur les processus océaniques, côtiers et littoraux. En raison de la grande variabilité spatiale et temporelle naturelle des processus océanographiques et des bassins versants agissant sur les zones littorales, la capacité de les surveiller et de les gérer représente souvent un défi pour les parties prenantes, les scientifiques et les décideurs. Néanmoins, les satellites d'observation de la Terre (SOT) se présentent comme un outil de choix pour aborder les variabilités spatiales et temporelles des producteurs primaires dans les zones côtières. Cependant, la possibilité de récupérer des informations biogéochimiques sur les eaux de surface à partir d'applications SOT nécessite une connaissance de leurs propriétés optiques. Les principaux objectifs de cette thèse étaient d'établir une base de connaissances sur les propriétés optiques et de développer des outils de télédétection pour mieux comprendre la variabilité des producteurs primaires dans les eaux côtières des environnements subarctiques et tempérés froids. Cette thèse est composée de trois articles de recherche utilisant la combinaison d'approches *in situ* (basées sur des navires) et satellitaires a été utilisée pour atteindre ces objectifs. Les zones étudiées comprenaient des sous-régions littorales de l'estuaire et du Golfe du Saint-Laurent (EGSL), dans l'est du Canada, étant les zones côtières proches de la Baie des Sept-Îles (BSI), Forestville (FV), la baie de Rimouski (RIB), and la baie de L'Isle Verte (IVE). Dans le premier article, les sous-régions BSI, MAN et FV ont été étudiées en utilisant des stratégies de conception d'échantillonnage *in situ* (distinctes), et tous les échantillons incluent (1) les propriétés optiques et (2) les quantités biogéochimiques (concentrations molaires et de masse sèche) pour étudier leurs principales relations. Les propriétés bio-optiques des eaux littorales de la partie nord de l'EGSL sont sous l'influence de débits fluviaux majeures (ou locaux) riches en matière organique. Plus précisément, il a été montré que le coefficient d'absorption de la matière organique dissoute chromophore (MODC) domine fortement le bilan d'absorption, et que ces eaux ont un coefficient de rétrodiffusion spécifique très faible (par rapport à la concentration en matière particulaire en suspension). Ces facteurs caractérisent un milieu absorbant fortement la lumière et diffusant faiblement la lumière, ce qui entraîne de faibles valeurs de réflectance et

des implications pour les applications des approches de télédétection optique. Malgré la dominance des composantes optiques d'origine terrigène dans le bilan d'absorption, la biomasse de phytoplancton n'est pas négligeable (concentrations en chlorophylle-*a* $\geq 1 \text{ mg m}^{-3}$). Dans l'ensemble, la stratégie d'échantillonnage a révélé une interaction complexe des variabilités spatiales (entre et au sein des sous-régions) et temporelles (saisonniers, synoptiques et circadiennes) agissant sur l'EGSL près du rivage et influençant ses propriétés optiques. Dans le deuxième article, nous avons émis l'hypothèse que la composition des principaux assemblages de phytoplancton dans la sous-région de BSI covarie avec la température et les propriétés optiques globales de l'environnement. La stratégie d'échantillonnage *in situ* a révélé un fort cycle saisonnier (du printemps à l'automne) modulant la composition des assemblages de phytoplancton, tandis que des différences statistiquement significatives de température et de propriétés bio-optiques entre les différents groupes ont été observées. Avant la crue des rivières au printemps (mi-mai), l'efflorescence de phytoplancton était dominée par de grandes cellules microphytoplanctoniques (diatomées), et la succession suivait un déplacement vers des cellules de nanophytoplancton et de picophytoplancton tout au long de l'été et de l'automne. Tout en confirmant les hypothèses, il a également été démontré la capacité d'estimer les principaux assemblages de phytoplancton à partir des capteurs SOT, avec des applications possibles aux programmes de surveillance. Le troisième article a utilisé une série temporelle à long terme (~ 40 ans) de SOT (missions Landsat) pour aborder la variabilité interannuelle et décennale de la couverture des herbiers marins (zostère marine, *Zostera marina* L.) dans les zones intertidales de BSI, MAN, RIB and IVE sous-régions littorales de l'EGSL. D'un point de vue méthodologique, la connaissance des variabilités des propriétés optiques et des marées était essentielle pour une meilleure utilisation des approches SOT afin d'obtenir les meilleurs résultats. La superficie des herbiers a présenté une tendance à l'augmentation significative (10 à 20 fois supérieure à la superficie initiale, en considérant la période de 1984 à 2022). En particulier, dans les sous-régions MAN et BSI, la tendance croissante observée était vers la terre (continent). Dans l'ensemble, cette thèse s'est concentrée sur l'analyse de la distribution spatiale et temporelle de deux importants groupes de producteurs primaires (i.e., les assemblages phytoplanctoniques et les herbiers de zostère) grâce aux approches SOT dans les sous-régions côtières changeantes de l'EGSL. Une voie de possibilités reste à explorer en incorporant des approches SOT dans les zones EGSL côtières dans les systèmes socio-écologiques, où l'environnement et son interaction avec l'anthroposphère peuvent être modélisés et prédits. Néanmoins, cette thèse représente une première étape vers un échantillonnage plus représentatif de ces deux variables environnementales importantes.

Mots clés : habitats côtiers et littoral, propriétés bio-optiques, MODC, coefficient de rétrodiffusion, succession saisonnière du phytoplancton, télédétection, herbiers de zostère, *Zostera marina*, Landsat, Estuaire du Saint Laurent

TABLE OF CONTENTS

ACKNOWLEDGEMENTS.....	xi
FOREWORD.....	xiii
ABSTRACT.....	xvii
RÉSUMÉ.....	xix
TABLE OF CONTENTS.....	xxi
LIST OF TABLES.....	xxv
LIST OF FIGURES.....	xxvii
GENERAL INTRODUCTION.....	1
ENVIRONMENTAL SCIENCES AND SYSTEMS ECOLOGY.....	1
NEARSHORE ENVIRONMENTS AND PRIMARY PRODUCERS.....	3
OPTICAL REMOTE SENSING OF NATURAL WATERS.....	5
AREAS OF STUDY AND PROBLEMATICS.....	11
THESIS OBJECTIVES AND STRUCTURE.....	13
ARTICLE 1 : VARIABILITY OF BIO-OPTICAL PROPERTIES IN NEARSHORE WATERS OF THE ESTUARY AND GULF OF ST. LAWRENCE: ABSORPTION AND BACKSCATTERING PROPERTIES.....	15
1.1 ABSTRACT.....	16
1.2 RÉSUMÉ.....	18
1.3 INTRODUCTION.....	20
1.3.1 Inherent optical properties in the Estuary and Gulf of St. Lawrence: an overview.....	24
1.4 METHODS.....	26
1.4.1 Study area and sampling design.....	26

1.4.2	Bio-optical data.....	29
1.4.3	Spatial and temporal analysis, ancillary data, and statistics	35
1.5	RESULTS.....	36
1.5.1	Optical properties of dissolved organic matter	41
1.5.2	Optical properties of particulate matter: phytoplankton and non- algal particles	45
1.5.3	Absorption budget.....	49
1.5.4	Spatial (subregion) and seasonal variability	50
1.5.5	Tidal and meteorological effects.....	55
1.6	DISCUSSION.....	56
1.6.1	Bio-optical variability	57
1.6.2	Seasonal and short-term bio-optical variability	65
1.7	CONCLUSIONS	70
ARTICLE 2 : ENVIRONMENTAL NICHEs AND SEASONAL SUCCESSION OF PHYTOPLANKTON ASSEMBLAGES IN A SUBARCTIC COASTAL BAY: APPLICATIONS TO REMOTE SENSING ESTIMATES.....		75
2.1	ABSTRACT.....	76
2.2	RÉSUMÉ.....	77
2.3	INTRODUCTION	78
2.4	METHODS	80
2.4.1	Study area and sampling design.....	80
2.4.2	Phytoplankton assemblages	83
2.4.4	Major nutrients and physical parameters	85
2.4.5	Inherent and apparent optical properties.....	86
2.4.6	Statistical analysis.....	87
2.5	RESULTS.....	88
2.5.1	Clusters of phytoplankton assemblages	88
2.5.2	Seasonal and spatial variability.....	95
2.5.3	Major nutrients and physical environment	97
2.5.4	Optical characterization	101
2.5.5	Seasonal succession and framework for remote sensing estimations....	106
2.6	DISCUSSION.....	113
2.7	CONCLUSIONS	119

ARTICLE 3 : MASSIVE AREAL COVERAGE INCREASES OF THE FOUNDATION SPECIES <i>ZOSTERA MARINA</i> L. IN A LARGE ESTUARINE SYSTEM REVEALED BY LANDSAT TIME SERIES IMAGERY.....	123
3.1 ABSTRACT	124
3.2 RÉSUMÉ	125
3.3 INTRODUCTION	127
3.4 MATERIAL AND METHODS	129
3.4.1 Study areas.....	129
3.4.2 Image repository and selection criteria.....	135
3.4.3 Eelgrass cover classification.....	138
3.4.4 Eelgrass cover analysis and accuracy assessment.....	139
3.4.5 Environmental variables	140
3.5 RESULTS	141
3.5.1 Image selection and classification accuracy	141
3.5.2 Eelgrass coverage, area, trends, and decennial changes.....	145
3.5.3 Environmental variables.....	150
3.6 DISCUSSION AND CONCLUSIONS.....	152
GENERAL CONCLUSION	157
ANNEX I - ARTICLE 1: SUPPLEMENTARY MATERIAL.....	167
ANNEX II - ARTICLE 2: SUPPLEMENTARY MATERIAL.....	171
ANNEX III - ARTICLE 3: SUPPLEMENTARY MATERIAL	179
REFERENCES	183

LIST OF TABLES

Table 1 List of acronyms and symbols, their definition, and units (if applicable)	21
Table 2 Summary of the sampling strategy	29
Table 3 Summary of fitted regressions and associated errors for the power model $y = A \cdot x^B$, where y is the dependent variable, x is the independent variable, and A and B are the regression coefficients. The reported metrics are the mean absolute error, MAE (and the mean absolute percentage error, $MAPE$); <i>bias</i> (and the percentage bias, $P - bias$); coefficient of determination, R^2 ; and the root mean square error, $RMSE$. The considered subset of the data and the corresponding scatterplot figure are also indicated	39
Table 4 Mean (μ) and standard deviation (σ) for chlorophyll concentration (Chla), the chlorophyll-specific phytoplankton absorption at 676 nm ($a_{\text{phi}}^*(676)$), the $a_{\text{phi}}^*(443) : a_{\text{phi}}^*(676)$ ratio, the size parameter from the phytoplankton absorption coefficient (S_f), and the ratios of total accessory pigments (TAP) to Chla, and the photoprotective to photosynthetic carotenoids (PPC:PSC). Rows represent each field campaign (or a single location, as for the PMZA-RIKI subregion).....	53
Table 5 Summary of the sampling strategy: dates and number of water samples. AZMP is the acronym for the Atlantic Zone Monitoring Program buoy location, and BSI is for the Bay of Sept-Îles	82
Table 6 Mean and (plus or minus) standard deviation of nutrient concentrations and physical parameters for each of the seven clusters of phytoplankton (PraD, PryD, Cy, Dia, Cry, CryP, and Chlo), for the Bay of Sept-Îles (BSI) region	99
Table 7 Mean and (plus or minus) standard deviation of temperature, inherent optical properties (including ratios), and remote sensing reflectance, at selected wavelengths, for each of the seven clusters of phytoplankton (PraD, PryD, Cy, Dia, Cry, CryP, and Chlo)	104
Table 8 Percentage of years mapped in relation to the 39-year period (1984 to 2022) and number of images per subregion and per Landsat sensor.....	142

Table 9 Confusion matrix and accuracy assessment of eelgrass coverage. The values shown correspond to the sum of areas (in km ²) of all four subregions considered in this study	144
Table 10 Climatological comparisons of environmental variables (mean ± standard deviation) surrounding eelgrass meadows of the different subregions of the estuary and Gulf of St Lawrence	152
Table 11 Summary of fitted regressions and associated errors for the optical properties of dissolved organic matter. The reported metrics are the mean absolute error, <i>MAE</i> (and the mean absolute percentage error, <i>MAPE</i>); <i>bias</i> (and the percentage bias, <i>P – bias</i>); coefficient of determination, <i>R</i> ² ; and the root mean square error, <i>RMSE</i> . The considered subset of the data and the corresponding scatterplot figure are also indicated	168
Table 12 Mean and (plus or minus) standard deviation of phytoplankton pigments concentrations (normalized by Chla) and pico- and nano-cells (eukaryotic and cyanobacteria) abundances, for each of the seven clusters obtained by the Hierarchical Cluster Analysis (PraD, PryD, Cy, Dia, Cry, CryP, and Chlo)	172
Table 13 Pigment and nutrient concentrations from samples collected in the phytoplankton spring bloom (April-May), including surface and deep waters in selected stations of the Bay of Sept-Îles	175
Table 14 Confusion matrix and accuracy assessment of eelgrass coverage for the four subregions of the Estuary and Gulf of St. Lawrence. The values shown correspond to the sum of areas (in km ²)	180

LIST OF FIGURES

Figure 1. Conceptual model from general systems theory.	2
Figure 2. Example of a Stommel Diagram applied to a biological system, highlighting the role of the most common sources of data in oceanography: ships, moorings, and satellites. Source: Kaiser et al. (2020); Marine Ecology: Processes, Systems, and Impacts; p. 218. Reprinted with permission by Oxford University Press.	4
Figure 3. Schematic diagram illustrating the main components and relationships of bio-optical properties and remote sensing of a coastal environment.	10
Figure 4. The nearshore areas of the estuary and Gulf of St. Lawrence (EGSL) contemplated in the three research articles of this thesis. The inset shows EGSL (red box) in the world and North America context.	12
Figure 5. (a) Map of the Estuary and Gulf of St. Lawrence (EGSL) showing the sampling areas in the regional context; the inset shows EGSL’s general localization in the North America context. The spatial distributions of sampling stations are shown for subregions (b) Bay of Sept-Îles (BSI), (c) Manicouagan Peninsula (MAN), and (d) coastal Forestville (FV).....	27
Figure 6. Relationship between molar and dry mass concentrations of (a) dissolved organic carbon (DOC) and chlorophyll- <i>a</i> (Chl <i>a</i>); (b) DOC and suspended particulate matter (SPM); and (c) SPM and Chl <i>a</i> . The colored symbols distinguish the four subregions of this study: The Bay of Sept-Îles (BSI), the Manicouagan Peninsula (MAN), the coastal area of Forestville (FV), and the buoy station (PMZA-RIKI). Marine (or brackish) stations are represented by circles, while stations located in the main channels of local rivers are represented by squares	37
Figure 7. General characterization of the optical properties of the chromophoric dissolved organic matter (CDOM) pool showing their relationships with dissolved organic carbon concentration (DOC) and spectral slopes. The relevant fitting equations, coefficients, and performance metrics for (a), (b), and (c) are provided in Table 11 (Annex 1). (a) CDOM absorption coefficient at 350 nm ($a_{\text{cdom}}(350)$) vs DOC. The black dashed line shows the fitted linear model (Table 11). (b) DOC-specific $a_{\text{cdom}}(350)$, $a_{\text{cdom}}^*(350)$, vs the CDOM spectral slope between 275 and 295 nm	

($S_{275-295}$). The ellipse indicates samples of the riverine endmembers, which were expected to have lower influence in the BSI subregion (i.e., with lower discharge in comparison to others). The curve of Fichot and Benner (2011) is shown for comparative purposes. The inset graphic illustrates the same relationship but for the CDOM spectral slope between 320 and 412 nm ($S_{320-412}$). **(c)** Relationship between the estimated DOC, modelled from CDOM absorption coefficients at 275 and 295 nm (see text), and the measured DOC. **(d)** Frequency distribution of the CDOM spectral slope between 350 and 500 nm ($S_{350-500}$). The Gaussian curve illustrates a normal distribution among the marine samples. The color code is the same as in Fig. 6 42

Figure 8. Optical properties of the chromophoric dissolved organic matter (CDOM) and their relationships with salinity. **(a)** CDOM absorption coefficient at 350 nm ($a_{\text{cdom}}(350)$) vs salinity. The median value of the river endmembers (salinity = 0) is shown for the Bay of Sept-Îles (BSI) and Manicouagan peninsula (MAN) subregions. The reference lines of Xie et al. (2012) are for the Estuary and Gulf of St. Lawrence (EGSL) and for the Saguenay Fjord (SF). The inset shows the variability of $a_{\text{cdom}}(350)$ for the riverine endmembers in the BSI subregion. **(b)** Relationship between $S_{275-295}$ and salinity. The inset illustrates the same relationship but for the CDOM spectral slope ratio (S_R) with the same salinity range. The relevant fitting equations, coefficients, and performance metrics for (a) and (b), while considering the two most numerous datasets (BSI and MAN) separately, are provided in Table 11 (Annex 1). The color code is the same as in Fig. 6 44

Figure 9. General relationships of the optical properties of particulate matter and dry mass concentrations of chlorophyll-*a* (Chl_a) and suspended particulate matter (SPM). **(a)** Phytoplankton absorption coefficient at 676 nm ($a_{\text{phy}}(676)$) vs Chl_a; **(b)** absorption coefficient of non-algal particles at 443 nm ($a_{\text{nap}}(443)$) vs SPM; and **(c)** the particulate backscattering coefficient at 550 nm ($b_{\text{bp}}(550)$) vs SPM. The reference lines showed in (a), (b), and (c) are from the studies of Bricaud et al. (1995), Babin et al. (2003), and Reynolds et al. (2016), respectively. The color code is the same as in Fig. 6..... 45

Figure 10. Characteristics and relationships of the optical properties of particulate matter and dry mass concentrations of particulate organic matter (POM) and particulate inorganic matter (PIM). The relevant fitting coefficients (power model) and performance metrics for (b), (c), (d), and (f) are provided in Table 3 **(a)** Frequency distribution of the non-algal particles spectral slope (S_{nap}). The Gaussian curve displayed illustrates the normal distribution among the marine samples. **(b)** Particulate absorption (a_p) in the near-

infrared region (mean of a_p between 745 and 755 nm), a_{pNIR} vs PIM. **(c)** The result of the subtraction of $a_p(NIR)$ from the particulate absorption coefficient at 440 nm ($a_p(440)$) vs POM. The reference lines of **(b)** and **(c)** are from the study of Konovalov et al. (2014). **(d)** Relationship between the particulate backscattering at 550 nm ($b_{bp}(550)$) and POM divided by 2. The reference line is from the study of Reynolds et al. (2016). It is worth mentioning that the reference curves on **(c)** and **(d)** are originally provided in terms of particulate organic carbon concentration (POC), and here we made the rough estimation $POM = POC \times 2$. **(e)** Spectral slope of b_{bp} , γ , vs $b_{bp}(550)$ The inset shows the frequency distribution of γ . **(f)** Relationship between the SPM-specific $b_{bp}(555)$ and $a_{nap}(555)$, i.e., $b_{bp}^*(555)$ and $a_{nap}^*(555)$. The reference line is from the study of Blondeau-Patissier et al. (2017). The color code is the same as in Fig. 6.....48

Figure 11. Ternary plots illustrating the relative contribution of CDOM (a_{cdom}), non-algal particles (a_{nap}) and phytoplankton (a_{phy}) to total absorption coefficient (minus the contribution of water) for wavelengths **(a)** 443, **(b)** 550, and **(c)** 676 nm. The relative proportions were normalized from 0 to 1, in such way that $a_{cdom} + a_{nap} + a_{phy} = 1$. The readings for the three components, and for each sample, should consider its corresponding axis and tick orientation (and corresponding grid). The color code is the same as in Fig. 649

Figure 12. Variability (median, 25th and 75th percentiles, minimum, maximum and outliers) of **(a)** DOC, **(b)** Chla, **(c)** SPM, **(d)** $a_{cdom}(350)$, **(e)** $\frac{a_{phy}(443)}{a_p(443)}$, and **(f)** $b_{bp}(550)$. Data are shown as a function of different sampling strategies: type (marine or river), location (BSI, MAN, FV, PMZA-RIKI) and different legs of these same campaign (BSI only). The number of observations (n) is provided for each sampling strategy, and the vertical grey dashed lines delimit the 2017 seasonal period for BSI. No boxplots are shown when $n < 5$. The color code is the same as in Fig. 652

Figure 13. Meteorological (synoptic) and hydrodynamic forcing and variability in inherent optical properties of nearshore zones of the Estuary and Gulf of St. Lawrence. **(a)** Wind velocity and direction, air temperature, and precipitation. **(b)** Semi-diurnal tidal variability, chromophoric dissolved organic matter absorption coefficient at 350 nm, and particulate backscattering coefficient at 550 nm, for the same period. **(c)** Vertical stratification of the water column as shown by temperature and salinity profiles, with a photo **(d)** depicting water samples collected at different depths56

Figure 14. **(A)** The Estuary and Gulf of St. Lawrence in the North America context, and **(B)** study area sampling locations: the Bay of Sept-Îles and the AZMP buoy. **(C)** Spatial distribution and number of revisits of the sampling stations in the Bay of Sept-Îles 81

Figure 15. **(A)** Linkage distance as a function of the number of clusters obtained from the dendrogram (shown in **(B)**). The L-method (Salvador and Chan 2004) is first applied considering all dataset ($n = 108$), and then to a restricted range for the number of clusters (inset). The resulting “knee” corresponds to a linkage distance cutoff of 11.9, which divides the input dataset in seven clusters. **(B)** Dendrogram obtained from the Hierarchical Cluster Analysis. The dashed line corresponds to the linkage distance cutoff, and the number above each cluster shows the corresponding number of samples. The clusters are denoted by PraD (purple), PryD (red), Cy (blue), Dia (yellow), Cry (orange), CryP (teal) and Chlo (green) 89

Figure 16. Variability (median, 25th and 75th percentiles, minimum, maximum and outliers) of **(A)** four classes of phytoplankton cell abundances **(B and C)** and eight accessory pigments to Chla ratios concentrations. The autotrophic cells concentration is separated by eukaryotes and phycoerythrin-containing (PE-) cyanobacteria, and by pico- ($<2 \mu\text{m}$) and nano-size (>2 and $<20 \mu\text{m}$) classes. The color code, associated to each cluster group, is the same as in Figure 15 90

Figure 17. Relative (or fractional, f) contributions of phytoplankton size classes to Chla, for each phytoplankton cluster. **(A)** Two methods to obtain the picophytoplankton fractional contribution to chlorophyll- a (f_{pico}): $f_{\text{pico}}^{\text{FC}}$ and $f_{\text{pico}}^{\text{HPLC}}$ (see text for details). **(B)** Ternary plot of $f_{\text{pico}}^{\text{HPLC}}$, $f_{\text{nano}}^{\text{HPLC}}$, and $f_{\text{micro}}^{\text{HPLC}}$. This approach (pigment-based) considers a global relationship using seven diagnostic pigments as inputs (Uitz et al. 2006). The color code is the same as in Figure 15 94

Figure 18. Temporal and spatial variability of the phytoplankton clusters. **(A)** Boxplots showing the variability of Chla for each cluster, for the Bay of Sept-Îles (BSI). **(B)** Bars showing the temporal variability of Chla in the AZMP buoy station (DOY = Day of Year). The color of the bars corresponds to the class of phytoplankton clusters. **(C)** Relative distribution of phytoplankton clusters for AZMP and for the temporal series in BSI (BSI-1 to 8; Table 5). **(D-H)** Spatial distribution for each campaign that presented noticeable variability of phytoplankton clusters 96

Figure 19. Nutrient concentrations and physical parameters relationships associated with each phytoplankton cluster. **(A)** Silicate ($[\text{Si}(\text{OH})_4^{4-}]$) versus nitrate ($[\text{NO}_3^-]$); **(B)** phosphate ($[\text{PO}_4^{3-}]$) versus nitrate concentrations; and **(C)**

temperature versus salinity. Samples from the Lower St. Lawrence Estuary station (AZMP) are presented by squares, and outliers from the Bay of Sept-Îles (BSI) are presented by diamonds. The gray-shaded area corresponds to undetectable nitrate levels ($\sim 0 \mu\text{M}$).....98

Figure 20. Inherent optical properties spectra: absorption coefficients of **(A)** chromophoric dissolved organic matter ($a_{\text{cdom}}(\lambda)$); **(B)** non-algal particles ($a_{\text{nap}}(\lambda)$); and **(C)** phytoplankton ($a_{\text{phy}}(\lambda)$); **(D)** total absorption coefficient ($a(\lambda)$); **(E)** particulate backscattering ($b_{\text{bp}}(\lambda)$); and **(F)** total backscattering coefficient $b_b(\lambda)$. For each graph, the different lines represent the median spectra for each cluster of phytoplankton groups, and the color code is the same as in Figure 15..... 102

Figure 21. Spectra of **(A)** the ratio of total backscattering to total absorption coefficients ($b_b/a(\lambda)$), and **(B)** the measured remote sensing reflectance ($R_{\text{rs}}(\lambda)$). The vertical gray dashed lines on **(B)** indicates the original spectral bands of the C-OPS instrument used to derive R_{rs} . For each graph, the different lines represent the median spectra for each cluster of phytoplankton groups, and the color code is the same as in Figure 15..... 105

Figure 22. Seasonal succession of phytoplankton assemblages in the Bay of Sept-Îles. **(A)** Moisie River discharge for years 2017, 2019, and climatological median (1965-2021). Source: Ministère de l'Environnement et de la Lutte contre les changements climatiques (<https://www.cehq.gouv.qc.ca/>). **(B)** Phytoplankton assemblages distribution (see Table 13 in Annex 2 for details of samples collected in April 19); and **(C)** environmental conditions as showed by nutrient concentrations and physical parameters (Temperature and Salinity, T and S) along the year 2017. The durations of the events of both occurrence of phytoplankton assemblages and environmental conditions are extrapolated from punctual field campaigns (BSI-1 to BSI-7, refer to Table 5), represented by vertical transparent lines 107

Figure 23. Idealized framework to separate the different phytoplankton assemblages using satellite-derived sea surface temperature (SST) and remote sensing reflectance in the blue ($R_{\text{rs}}(465)$), green ($R_{\text{rs}}(566)$), and red ($R_{\text{rs}}(665)$) regions of the spectrum 110

Figure 24. Application of the exposed framework shown in Figure 23 in satellite images of the Operational Land Imager (OLI) and the Thermal Infrared Sensor (TIRS) of Landsat 8. The atmospherically corrected images of the blue, green, and red bands, the sea surface temperature, and the resulting classification of the groups of phytoplankton assemblages are shown for two dates: April 4 and May 15, 2017 112

Figure 25. (A) Study areas (subregions) locations in the Estuary and Gulf of St. Lawrence (EGSL). The inset shows EGSL in North America context. Primary delimitation of areas of interest (red dashed lines) for the (B) Bay of Sept-Îles (BSI), (C) L’Isle-Verte bay (IVE), (D) Manicouagan Peninsula (MAN), and Rimouski bay (RIB). The main local riverine outlets are indicated for each subregion and the background images are a true-color composition of a recent (2020s) Landsat 8 (or 9) OLI scenes (USGS L2SP).... 130

Figure 26. General characteristics of eelgrass meadows in the Estuary and Gulf of St. Lawrence and physical processes affecting their distribution. (A) Oblique aerial photograph taken in the L’Isle-Verte bay subregion at low-tide conditions (image courtesy from the *Laboratoire de dynamique et de gestion intégrée des zones côtières*, UQAR). (B) Tidal variability for a 20-day period in 2022 (tidal gauge in Baie-Sainte-Catherine, mouth of Saguenay Fjord - data available from the Canadian Hydrographic Service). (C) Some optical characteristics of the water column surrounding meadows: the spectral diffuse attenuation coefficient of downwelling irradiance ($K_d(\lambda)$) and the light penetration depth ($Z_{90}(\lambda)$). The solid and dashed lines indicate the mean values of K_d and Z_{90} , respectively, and the shaded areas indicate the (\pm) standard deviation. 133

Figure 27. Methodological flowchart of the processing and analysis chain to assess the yearly and decadal variability of intertidal eelgrass meadows coverage in four subregions of the Estuary and Gulf of St. Lawrence 137

Figure 28. Examples of Landsat images used in the classification process of eelgrass meadows (green patches) inside the polygons of the emerged areas (solid lines with varying colors for subregions: blue for BSI, yellow for MAN, red for RIB, and green for IVE). Images on the left (right) correspond to the approximately years of minimum (maximum) area of meadows..... 146

Figure 29. Temporal evolution of areal cover of eelgrass meadows in the four subregions. The values in parenthesis in y-axis are the percentage of the eelgrass areal cover in relation to the total emerged area. The color codes for the subregions are the same as in Fig. 28..... 148

Figure 30. Eelgrass meadows areal trends in the Estuary and Gulf of St. Lawrence in the last four decades, and comparison with other seagrass areal trends in the North Atlantic West (East Europe) and East (West North America) coasts. 149

Figure 31. Decadal spatial changes of eelgrass patches in the four subregions of the Estuary and Gulf of St. Lawrence..... 151

Figure 32. Bar plots showing the percentage distribution of phytoplankton classes as assigned by the light microscopy technique. The names in the x-axis refer to

the phytoplankton groups and respective field campaigns (refer to **Table 5**). The number above each bar is the total phytoplankton cell count (in cells L⁻¹). Other flagellates include chlorophytes, chrysophytes, dictyophytes, euglenophytes, prasinophytes, prymnesiophytes and raphidophytes 176

Figure 33. (A) Cells concentration comparison of nanophytoplankton counts from flow cytometry (FC) versus light microscopy (LM) methods. Unidentified cells with sizes lower than 20 μm were included in the LM nanophytoplankton abundances. (B) Ternary plot showing the relative contribution (or fraction) of phytoplankton size classes to total cell concentration and for each phytoplankton cluster. Concentration of cells was derived from flow cytometry measurements for the pico- and nano-size classes, while micro-size classes concentration was obtained by counts using LM technique (*n* = 16). The phytoplankton clusters are denoted by PraD (purple), PryD (red), Cy (blue), Dia (yellow), Cry (orange), CryP (teal), and Chlo (green) 177

Figure 34. Vertical profiles of density of sea water ($\rho = \rho(S, T, p)$) and chlorophyll-*a* fluorescence (f_{Chla} , in Relative Fluorescence Units, RFU, as measured by the HS6 instrument). Captions (A) and (B) refer to two stations from 4 May 2017 (BSI-1 campaign), where the presence of a subsurface chlorophyll maximum (SCM) can be noticed. From these two stations, the concentrations of Chla, major nutrients, and the Fucoxanthin to Chla ratio are found in **Table 12**, for water samples collected at two different depths..... 178

GENERAL INTRODUCTION

ENVIRONMENTAL SCIENCES AND SYSTEMS ECOLOGY

Humanity is living in the Anthropocene era (Ellis et al., 2010; Folke et al., 2021; Lewis and Maslin, 2015) and facing challenges such as world climate change (IPCC, 2022). Consequently, the relationships between society and nature are in the spotlight in the twenty-first century. Social-ecological systems (SES), which can be defined as a set of critical resources (natural, socio-economic, and cultural) whose flow and use is regulated by a combination of ecological and social systems (Redman et al., 2004), is an useful concept in this context (see Folke et al., 2005; Ostrom, 2009). In turn, the so-called ecosystem-based approach guide to best management practices and protection of the environment through the scientific reasoning, while also considering the humans' interaction with the natural ecosystem with sustainability (Browman and Stergiou, 2004; Christensen et al., 1996; Leslie and McLeod, 2007).

In the discipline of environmental sciences, the ecologist Pierre Dansereau, author of the pioneering work "*Biogeography: An ecological perspective*" (Dansereau, 1957), also attempted that the theoretical framework of systems approach developed in ecology, with the seminal works of Arthur Tansley, Raymond Lindeman and G. Evelyn Hutchinson, among others, should also be incorporated in the study of the interaction of human and the environment (Audet, 2012). In fact, the ecosystem-based management is tightly related with and has advantages when analyzed through the lens of systems ecology (Kay et al., 1999; Van Assche et al., 2019).

Therefore, one may expect in social-ecological systems the perspectives of complexity, evolution, self-organization, and adaptation, constant in the general system theory (for reference, see Meadows, 2008; von Bertalanffy, 1950). Perhaps the most fundamental

concept of general systems theory is the interaction of the different elements of a simple conceptual model (Figure 1), where the dynamic of a system can be inferred by stocks (input and outputs) and processes. In this example, if the input is provided, and knowing the mechanisms of the process involved in the transformation of it, it is possible to predict the output. The idea of predictability through modeling approaches are central in general systems theory.

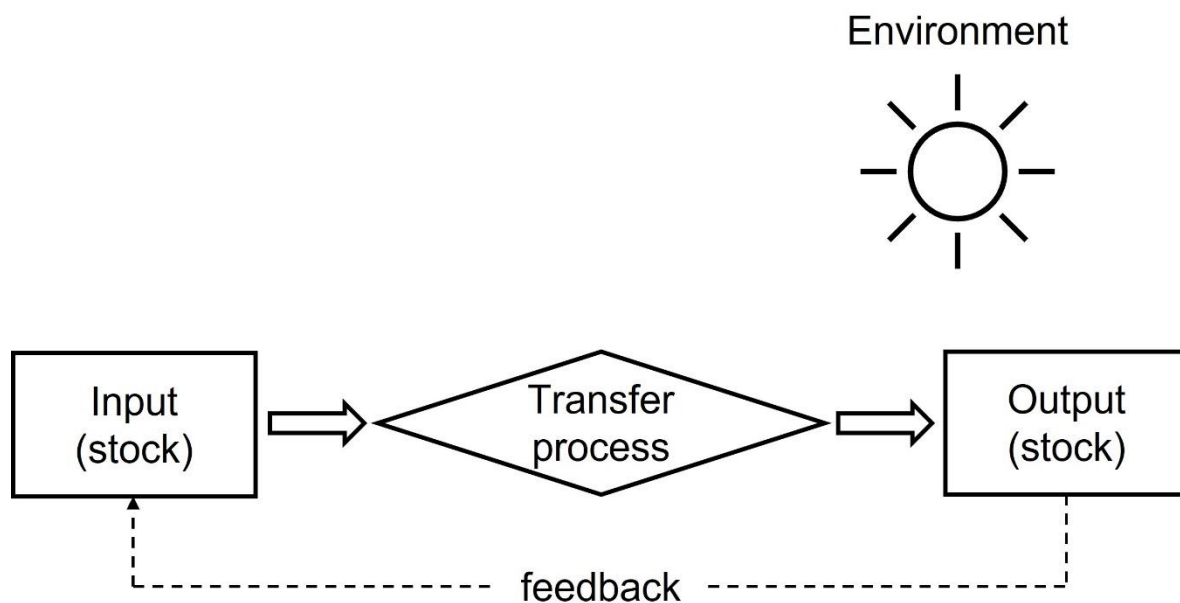


Figure 1. Conceptual model from general systems theory.

Particularly in environmental systems, a critical step in developing models is the adequate sampling for inputs and outputs (this last also for verification purposes, see Nordstrom, 2012). Ecosystems exhibit wide variability of spatial, temporal, and organizational scales, while it is important to note that the observer imposes his perceptual bias when investigating such systems (Levin, 1992). In summary, it is very important to address this problematic in SES and, consequently, in ecosystem-based management approaches.

NEARSHORE ENVIRONMENTS AND PRIMARY PRODUCERS

This thesis focuses on nearshore environments, which is an integral part of a coastal SES. Coastal zones are one of the most attractive areas in the world for human settlements (Small and Nicholls, 2003). This phenomenon occurs mainly due to its socioeconomic benefits, which includes access to ocean navigation, coastal fisheries, tourism, and recreation. Notwithstanding, anthropogenic modification of coastal and nearshore environments is substantive and presents an increasing trend, which can have deleterious effects to human itself (Doney, 2010; Turner et al., 1996).

Nearshore environments are naturally dynamical systems because of the simultaneous interaction of hydrosphere, lithosphere, cryosphere (in high latitudes), and atmosphere processes. Examples of processes acting in nearshore environments are the freshwater and groundwater discharge (watershed processes), ocean (-or estuarine) waters exchange, tidal and wave regime, material input (organic and inorganic), and climatic events. Thus, it is important to consider de various spatial and temporal scales of processes in coastal SES management (de Jonge, 2000).

A formal investigation of spatial and temporal scales acting in ocean was introduced in the so-called Stommel Diagram (Stommel, 1963), firstly used to describe the distribution of variabilities of the sea level. Later, the disciplines of ecology and biological oceanography used the same graphical concept to explain other phenomena, such as the scales of variability of phytoplankton, zooplankton, and fish populations (Vance and Doel, 2010). Figure 2 shows an example of a biological version of the Stommel Diagram applied to the ocean, where the variabilities of biomass (z-axis; e.g., zooplankton) are superimposed by the main sources of oceanographic data (ships, moorings, and satellites; from Kaiser et al., 2020). It is important to note the diversity of scales and processes (legend in Fig. 2) acting in this example, but also the complementarity of the three different sources of data to address oceanographic phenomena, and the singularity of the satellite approach. However, one may expect even more complexity in nearshore environments.

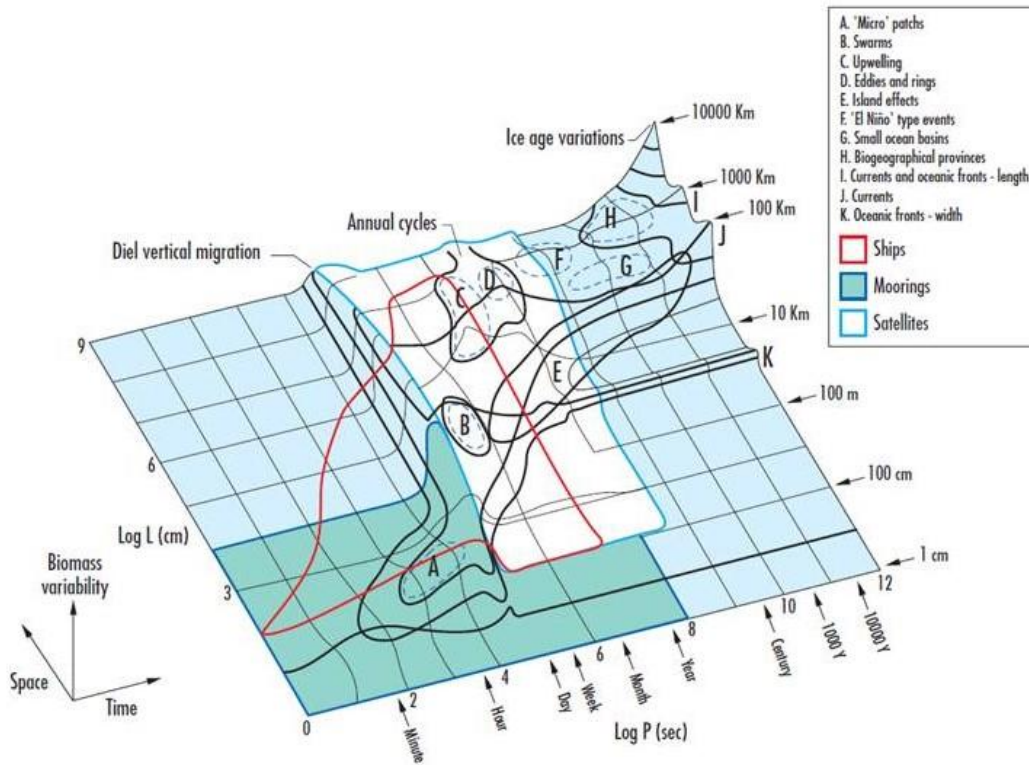


Figure 2. Example of a Stommel Diagram applied to a biological system, highlighting the role of the most common sources of data in oceanography: ships, moorings, and satellites. Source: Kaiser et al. (2020); Marine Ecology: Processes, Systems, and Impacts; p. 218. Reprinted with permission by Oxford University Press.

Salt marshes, mangroves, seagrass meadows, macroalgal beds and microphytobenthic films, besides the pelagic habitat itself, are examples of ecologically relevant habitats that are found in nearshore environments. The ecological and economic importance of these habitats is vast, including nursery of diverse species, primary production, nutrients cycling, carbon storage, and coastline protection as representative examples. Notwithstanding, a high economic value of ecosystem services is attributed to these biomes (Costanza et al., 2014). For practical purposes, ecosystem services can be simply defined as the benefits people obtain from ecosystems.

The synthesis of organic matter from inorganic matter by autotrophs organisms (i.e., primary production) constitutes the basis of trophic chains in food webs, and the most important process is the photosynthesis. In an ecosystem, the energy sources and associated trophic linkages that supports food webs are key to understand its structure and function (Lindeman, 1942). In nearshore environments of high latitudes, for example, stable isotopes analysis revealed the complex contribution of the different primary producers, but also the relative importance of allochthonous organic matter from terrestrial sources (Corbisier et al., 2004; McMahon et al., 2021; St. Pierre et al., 2020). In these high latitude regions, the primary producers can include phytoplankton, macroalgae, seagrass, sea ice algae, and microphytobenthos.

Specifically in the pelagic environment, the knowledge about the composition of phytoplankton assemblages is of particular interest for biogeochemical models, as they are intrinsically related to ecological processes (Le Quéré et al., 2005), and it can also be used to access the ecosystem health (Tett et al., 2008).

Because of their characteristic of foundation species (i.e., species that play a major role in creating and maintaining a habitat) and to constitute the base of trophic chains, the characterization of primary producers is primarily important in nearshore environments. Next, we examine how remote sensing, particularly in the optical domain, can address the problem of spatial and temporal sampling in coastal and nearshore areas.

OPTICAL REMOTE SENSING OF NATURAL WATERS

Remote sensing, through Earth Observation satellites, has advantages when compared to other approaches to sample the coastal environment, such as its acquisition repeatability (temporal resolution), spatial coverage, and synoptic view. In particular, the retrieval of biogeochemical information of surface waters has been developed (and are in constant development) since the launch of the first space-based experimental sensor dedicated to

ocean color remote sensing, the Coastal Zone Color Scanner experiment (CZCS), which operated from 1978 to 1986 (McClain, 2009). A decade after CZCS, the Sea-viewing Wide Field-of-view Sensor (SeaWiFS) was an ocean color remote sensing mission that operated from 1997 to 2010 and initiated the long term systematic and uninterrupted Ocean Colour Radiometry (OCR) era. Among others, the Moderate Resolution Imaging Spectroradiometer (MODIS), aboard Terra and Aqua satellites, are sensors still in operation (since 1999). An emblematic modeling approach that uses ocean color remote sensing products (namely the chlorophyll-*a* concentration, Chl_a) is the estimation of global net primary production (NPP) by phytoplankton (e.g., Antoine et al., 1996; Behrenfeld and Falkowski, 1997; Longhurst et al., 1995). Phytoplankton was found to account for approximate 50% of Earth NPP (Field et al., 1998). OCR provided biogeochemical proxies of the surface ocean that has transformed our understanding of the ocean response to climate variability (e.g., Behrenfeld et al., 2006).

Due to their coarse spatial resolutions, OCR sensors that are adequate for the global ocean are not suitable for application in coastal and nearshore areas (see Bissett et al., 2004; Moses et al., 2016). The ability of remote sensing products in addressing the spatial and temporal scales of variability will be determined by their spatial and temporal specifications. Additionally, the capability of discrimination of targets will strongly vary in function of the spectral and radiometric resolutions of the sensor, besides the spatial resolution as well. Targeting the Essential Biodiversity Variables (EBV; Pereira et al., 2013) monitoring across coastal zones, Muller-Karger et al. (2018) defined what they called the H4 imaging, where sensors characteristics of spatial, spectral, and temporal resolutions, as well as radiometric quality, were described to better achieve this purpose. Apropos, an EBV is defined as a measurement required for study, reporting, and management of biodiversity change, and could be used as the basis for monitoring programs worldwide (Pereira et al., 2013). Notwithstanding, since the beginning of the twenty-first century several ocean color sensors onboard satellite missions have been launched and others are scheduled (IOCCG, 2023a, 2023b), with technical characteristics that goes towards an ideal H4 imaging for nearshore environments.

According to Muller-Karger et al. (2018), H4 imaging should combine the following characteristics: (1) spatial resolution on the order of 30 to 100-m pixels or smaller; (2) spectral resolution on the order of 5 nm in the visible and 10 nm in the short-wave infrared spectrum (or at least two or more bands at 1,030, 1,240, 1,630, 2,125, and/or 2,260 nm) for atmospheric correction and aquatic vegetation assessments; (3) radiometric quality with high signal to noise ratios (SNR > 800; relative to signal levels typical of the open ocean), 14-bit digitization, absolute radiometric calibration <2%, relative calibration of 0.2%, polarization sensitivity <1%, high radiometric stability and linearity, and operations designed to minimize sunglint; and (4) temporal resolution of hours to days. It is important to note that there are no current or planned sensor that combine all these characteristics. Instead, there are sensors that combine some of them, and the choice of using one or another will depend specifically on the objectives of the application.

The discipline of aquatic optics (Jerlov, 1968; Kirk, 2011) establishes a formal link between OCR and aquatic biogeochemistry. The propagation of light energy through a medium which absorbs, scatters and contains internal sources can be fully described by the radiative transfer equation (RTE; forward problem) [Mobley, 1994; Preisendorfer, 1976]. Two basic physical (radiometric) quantities of the light field are the radiance (L , in units of $\text{W m}^{-2} \text{nm}^{-1} \text{sr}^{-1}$) and the irradiance (E , in units of $\text{W m}^{-2} \text{nm}^{-1}$), and the spectral dependence of light is represented by the wavelength (λ , in nm). The most common (and desired) physical quantity that can be obtained from (optical) remotely sensed images is the remote-sensing reflectance (R_{rs} , in units of sr^{-1}), an apparent optical property (AOP), given by:

$$R_{rs}(\lambda) = \frac{L_w(\lambda)}{E_d(0^+, \lambda)}, \quad (1)$$

where $L_w(\lambda)$ is the water-leaving radiance and $E_d(0^+, \lambda)$ is the downwelling irradiance (0^+ indicates that it is referred to just above the water surface).

The optical characteristics of a light-transmitting medium can be specified in terms of its inherent optical properties (IOPs), being the absorption coefficient (a , in units of m^{-1}) and the volume scattering function ($\beta(\psi, \lambda)$, in $\text{m}^{-1} \text{sr}^{-1}$, where ψ is the scattering angle) the main quantities. The so-called optical closure states that, ideally, it should be possible to build a light field model from measured values of IOPs and given boundary conditions (e.g., bottom reflectance and sea surface state), which would precisely replicate radiometric measurements made at the same time (e.g., Gallegos et al., 2008). Nevertheless, estimating IOPs through satellite approaches (using $R_{\text{rs}}(\lambda)$, for example) constitute an inverse problem (from the RTE perspective), and the possibility of multiple solutions from the same input characterize a typical ill-posed problem (Defoin-Platel and Chami, 2007).

The spectral and spatial characteristics of the underwater light field are determined through the numerical integration of the RTE over all depths and angles, using as inputs the quality and geometry of the illumination conditions and IOPs. Notwithstanding, simplifications of the RTE, or semi-analytical approaches, were proposed by several studies, such as the ones presented by Morel and Prieur (1977), or the quasi-single scattering approximation (QSSA, Gordon et al., 1988, 1975). For practical purposes, a simple approximation relating IOPs and R_{rs} can be understood as (Lo Prejato et al., 2020):

$$R_{\text{rs}}(\lambda) \propto \frac{b_{\text{b}}(\lambda)}{a(\lambda)}, \quad (2)$$

where $b_{\text{b}}(\lambda)$ is the backscattering coefficient, obtained by integrating $\beta(\psi, \lambda)$ in the backward direction (2π). The total $a(\lambda)$ and $b_{\text{b}}(\lambda)$ can be considered as a sum of partial contributions of the water itself, suspended particles (including phytoplankton) and the coloured dissolved organic matter (CDOM), and these are commonly referred to as the optically active constituents (OACs) of the aquatic medium. The partial contribution from OACs to the IOPs can be related in a quantitative way, while it varies in optically different waters (more details in the section dedicated to **Article 1**).

The equation 2 exhibits a general relationship between $R_{rs}(\lambda)$ and IOPs in optically deep waters, i.e., without the influence of the bottom. However, coastal and nearshore environments where the contribution of the bottom (or benthos) affects $R_{rs}(\lambda)$ signals are known as optically shallow waters (see Albert and Mobley, 2003), and should be considered in remote sensing approaches. Although this work acknowledges the existence of optically shallow areas in the studied areas, its influence in $R_{rs}(\lambda)$ is restricted only to very shallow depths (maximum of ~3 m of water column, as will be shown later), and is out of the scope of this thesis. Figure 3 shows a schematic diagram illustrating the bio-optical properties and its link with the remote sensing approach of a nearshore environment.

Therefore, the estimation of biogeochemical-relevant information of surface waters by optical remote sensing is possible because the OACs shapes the IOPs which, in turn, will strongly influence the $R_{rs}(\lambda)$ signals. Furthermore, the amount and quality of light that reaches the bottom of coastal waters (benthic habitat) will also depend on IOPs, with consequences to the photosynthesis processes of benthic primary producers. Since $R_{rs}(\lambda)$ are more tightly related to IOPs than directly to OACs (see Werdell et al., 2018), the characterization and understanding of the drivers of its variability is a primary requirement when using remote sensing optical approaches to investigate nearshore environments.

In summary, integrating both aquatic optics and remote sensing tools to understand light dynamics in natural waters and the distribution of benthic primary producers' in nearshore environments can provide valuable data that can be used to access the ecosystem state.

Bio-optical properties

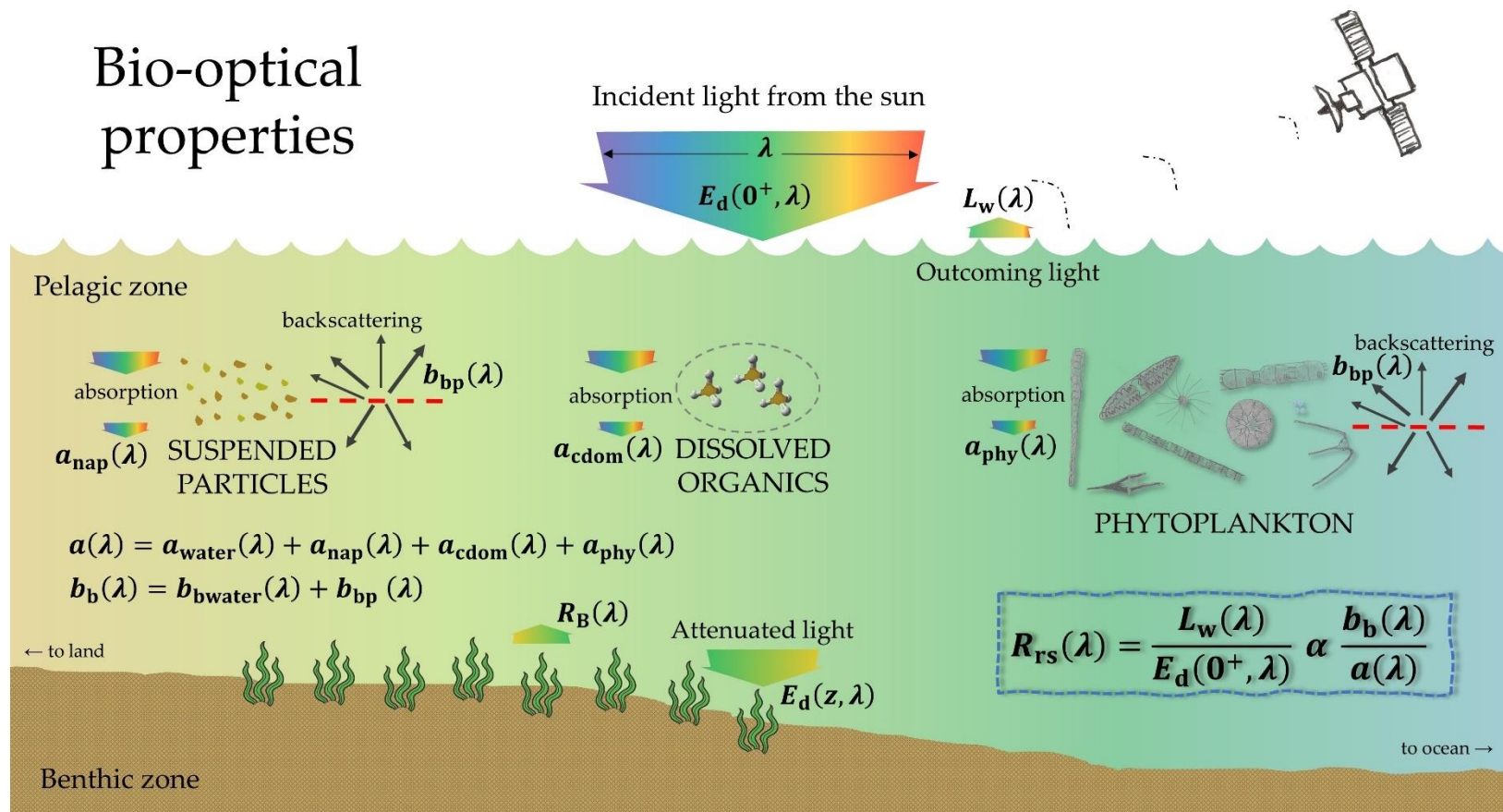


Figure 3. Schematic diagram illustrating the main components and relationships of bio-optical properties and remote sensing of a coastal environment.

AREAS OF STUDY AND PROBLEMATICS

The study areas of this thesis contemplate coastal and nearshore zones of the Estuary and Gulf of the St. Lawrence (EGSL; Fig. 4), East Canada. The EGSL connects the Great Lakes with the North Atlantic Ocean and encompasses one of the largest estuaries in the world (El-Sabh and Silverberg, 1990). Propitious conditions to phytoplankton growth occurs because of the upwelling of deep waters near the outlet of the Saguenay Fjord and because of other physical controls such as stratification (see Therriault et al., 1990). This gives the pelagic system of EGSL a very productive character and sustains a rich ecosystem that includes big marine mammals (e.g., beluga, blue, fin, humpback, and minke whales). In turn, common habitats found in nearshore zones of EGSL are seagrass meadows, macroalgal beds, and microphytobenthic films. Seagrass meadows are particularly dominant in some intertidal areas of EGSL (Jobin et al., 2021).

However, besides of being one of the coastal systems most studied in the world (from the oceanographic viewpoint), there is a lack of knowledge about the variability of bio-optical properties in nearshore areas of EGSL. This might hinder and/or add uncertainties in satellite estimations of water quality parameters, but also information about the distribution of submerged aquatic vegetation. Nearshore EGSL areas is expected to be influenced by river discharges bringing large amounts of (dissolved and particulate) terrigenous matter, which, in turn, will shape the optical properties of these environments. Consequently, common techniques applied to retrieve information about phytoplankton assemblages in the open ocean, where the bulk optical properties of the water generally covaries with phytoplankton, may not be valid for such dynamical optical environments of nearshore EGSL.

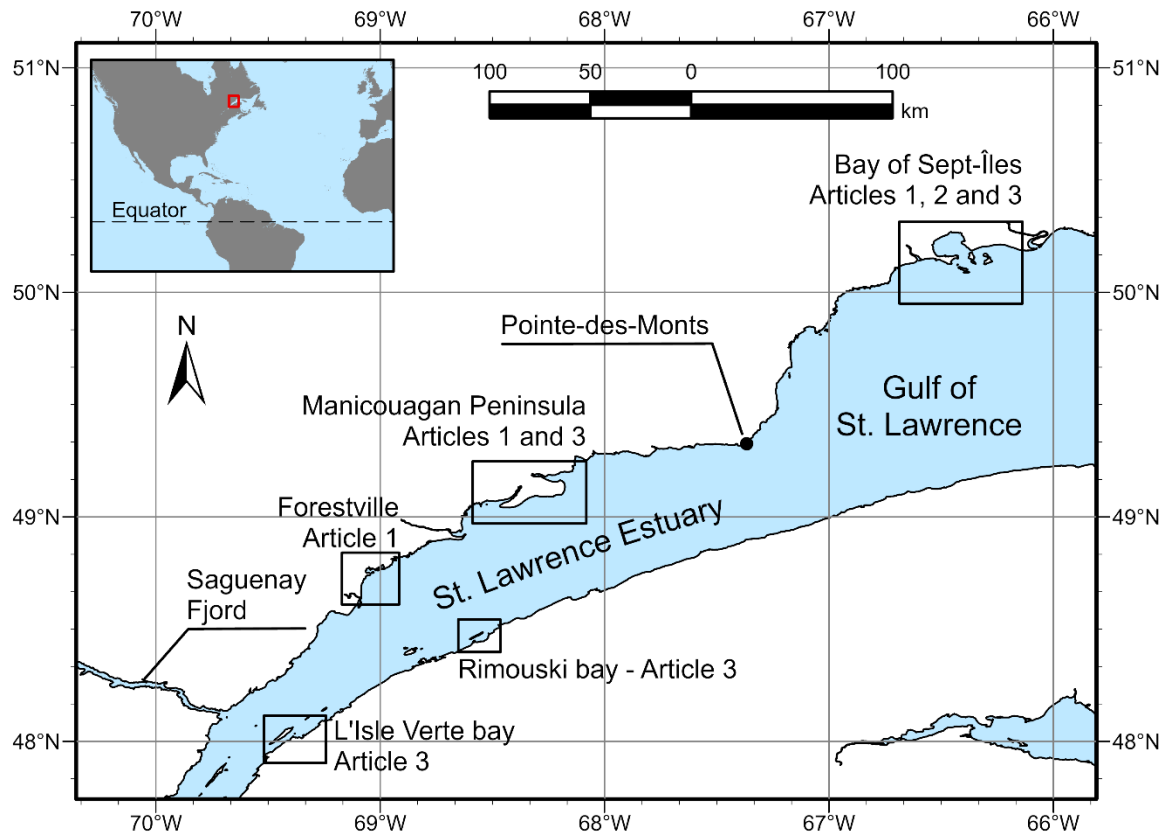


Figure 4. The nearshore areas of the estuary and Gulf of St. Lawrence (EGSL) contemplated in the three research articles of this thesis. The inset shows EGSL (red box) in the world and North America context.

In such scenario, and addressing only the overlooked nearshore zones of EGSL, the following research questions can be posed: How bio-optical properties of nearshore areas are compared to central parts of EGSL? What temporal scales are important in governing the variability of bio-optical properties and the composition of phytoplankton? Is it possible to retrieve information about different groups of phytoplankton from optical remote sensing? How is the actual spatial distribution of the benthic primary producers in EGSL? How is the temporal evolution of seagrass meadows?

By developing tools to answer these research questions, the same framework (with adaptations) could be used to address complex spatial and temporal patterns of nearshore environments worldwide.

THESIS OBJECTIVES AND STRUCTURE

The main objectives of this thesis were to establish a baseline of knowledge about the variability of optical properties and develop remote sensing tools to better understand the variability of primary producers in nearshore waters of subarctic and cold temperate environments. The thesis is composed by three research articles and a general conclusion. The study sites (or subregions of EGSL) and its links with the different articles are shown in Figure 4.

To achieve the goal of this thesis, a comprehensive *in situ* dataset (ship-based approach) of bio-optical properties was built in the context of different research projects. The objective of the first article was to contribute to the knowledge on bio-optical variability in nearshore environments of the EGSL, where local river input is likely to dominate optical variability. A secondary objective was to investigate domain scales (spatial and temporal) that are known to be driven by regional climatic, geomorphological, and hydrodynamical processes.

The objective of article 2 was to identify the major phytoplankton assemblages and their respective environmental niches, in respect to nutrient concentrations, physical parameters (temperature and salinity), and bio-optical properties. Through the hypotheses that the composition of major phytoplankton assemblages in a nearshore coastal area will covary with temperature and the bulk optical properties of the environment, the potential of using sea surface temperature (*SST*) and $R_{rs}(\lambda)$ [at selected wavelengths], retrieved from remote sensing, was demonstrated.

Finally, the objective of article 3 was to build a long-term dataset of seagrass distribution in ecologically significant areas of EGSL (Fig. 4) using satellite imagery. The

analysis of the dataset allowed to access yearly and decadal (1984-2022) changes of spatial variability in areal cover of the seagrass meadows.

The general conclusion revisits the main findings and limitations of the research articles of the present study, but also shed light to some gaps of knowledge and provide new insights for future work.

From the perspective of environmental sciences and systems ecology presented in the beginning of this chapter, this thesis aims to contribute to the knowledge of some important “stocks” of nearshore zones of the EGSL, with potential to use them in modelling frameworks (as in Fig. 1). The stocks include the distribution of major phytoplankton assemblages (Article 2) and the seagrass meadows coverage (Article 3). Also, in this case, both stocks could act either as input or output of a model. Because the two stocks explore the advantages of spatial and temporal information that can be obtained by Earth Observation satellites, the knowledge about aquatic optics was primarily important (Article 1).

ARTICLE 1:

**VARIABILITY OF BIO-OPTICAL PROPERTIES IN NEARSHORE WATERS
OF THE ESTUARY AND GULF OF ST. LAWRENCE: ABSORPTION AND
BACKSCATTERING PROPERTIES**

Published in Estuarine, Coastal and Shelf Science (2022), 264: 107688.

<https://doi.org/10.1016/j.ecss.2021.107688>

Authors:

Carlos A.S. Araújo^{a,b}, Simon Bélanger^{a,b}

^a Département de biologie, chimie et géographie et groupe BORÉAS, Université du Québec à Rimouski, Rimouski, QC G5L 3A1, Canada

^b Québec-Océan, groupe interinstitutionnel de recherches océanographiques du Québec, Québec, QC G1V 0A6, Canada

The following sections correspond to the published article, with small modifications to suit the structure of the thesis.

1.1 ABSTRACT

The inherent optical properties and the optically significant constituents in nearshore zones of the Estuary and Gulf of St. Lawrence (EGSL), eastern Canada, were systematically investigated. Molar and dry-mass concentrations of dissolved organic carbon (DOC), phytoplankton pigments, and suspended particulate matter (SPM) were determined together with the absorption coefficients of chromophoric dissolved organic matter, a_{cdom} ; non-algal particles, a_{nap} ; phytoplankton, a_{phy} ; and particulate backscattering coefficient, b_{bp} . The sampling design allowed analysis at different spatial scales and considered some intra-regional differences in distinctive zones (subregions) of the EGSL's north shore (separated by $\sim 10^2$ km), as well as within subregions (samples separated by $\sim 10^0$ to 10^1 km). Temporal analysis focused on seasonal variability (sampling time separated by $\sim 10^1$ to 10^2 days). Optical indices, such as the spectral slopes of a_{cdom} and a_{nap} , pigment ratios, mass-specific absorption and backscattering coefficients, and particulate matter fractioning (inorganic and organic) allowed a detailed characterization of the dissolved organic matter pool and provided useful information about particulate matter assemblages. The a_{cdom} was highly correlated with DOC and was found to have a conservative mixing behavior as the dominant process controlling its distribution, although differences among and within subregions were noted and related to differences in local river endmembers and seasonality. The a_{cdom} also dominated the absorption budget, even in long wavelengths of the visible range (e.g., 550 nm). Despite the highly light-absorptive characteristic of the waters, phytoplankton biomass was not negligible, as shown by mean chlorophyll-*a* (Chl*a*) concentrations generally above 1 mg m^{-3} . Analysis of the spectral shape of a_{phy} and pigment ratios revealed a seasonal modulation in the composition of phytoplankton assemblages and photoacclimation. The optical properties of particulate matter showed a very dispersed relationship when compared to dry-mass concentration proxies in the study area, but the extremely low SPM-specific b_{bp} values encountered were explained by the organic-rich characteristic of the nearshore zones of the EGSL. Short-term variability (atmospheric events) and the hydrodynamical regime also resulted in substantial variability in the optical

properties of these areas. Overall, we provide a general parametrization for the relationships among the investigated inherent optical properties and dry-mass concentrations, which, in turn, will provide a baseline for tuning and developing regional remote sensing algorithms for the retrieval of biogeochemically relevant constituents of the water.

Keywords: aquatic optics, nearshore environments, CDOM, phytoplankton, suspended particulate matter, remote sensing

1.2 RÉSUMÉ

Les propriétés optiques intrinsèques et les constituants optiquement significatifs dans les zones littorales de l'estuaire et du Golfe du Saint-Laurent (EGSL), dans l'est du Canada, ont été systématiquement étudiés. Les concentrations en carbone organique dissous (COD), pigments phytoplanctoniques et matières particulaires en suspension (MPS) ont été déterminées ainsi que les coefficients d'absorption de la matière organique dissoute chromophorique (a_{cdom}), particules non algales (a_{nap}), phytoplancton (a_{phy}), et le coefficient de rétrodiffusion de particules (b_{bp}). Le plan d'échantillonnage a permis une analyse à différentes échelles spatiales et a pris en compte certaines différences intra-régionales dans des zones distinctives (sous-régions) de la rive nord de l'EGSL (séparées par $\sim 10^2$ km), ainsi qu'au sein des sous-régions (échantillons séparés par $\sim 10^0$ à 10^1 km). L'analyse temporelle s'est concentrée sur la variabilité saisonnière (temps d'échantillonnage séparés par $\sim 10^1$ à 10^2 jours). Les indices optiques, tels que les pentes spectrales de a_{cdom} et a_{nap} , les ratios de pigments, les coefficients d'absorption et de rétrodiffusion spécifiques à la masse et le fractionnement des particules (inorganiques et organiques) ont permis une caractérisation détaillée de la matière organique dissous et fourni des informations utiles sur les assemblages de particules. Le a_{cdom} était fortement corrélé avec le COD et s'est avéré avoir un comportement de mélange conservatif le long d'un gradient de salinité en tant que processus dominant contrôlant sa distribution, bien que des différences entre et au sein des sous-régions aient été notées et liées aux différences dans les rivières locales et la saisonnalité. Le a_{cdom} a également dominé le budget d'absorption, même dans les longues longueurs d'onde de la gamme du visible (par exemple, le vert à 550 nm). Malgré le caractère très absorbant de la lumière des eaux, la biomasse phytoplanctonique n'est pas négligeable, comme le montrent les concentrations moyennes de chlorophylle-*a* (Chl_a) qui sont presque toujours supérieures à 1 mg m^{-3} . L'analyse de la forme spectrale de a_{phy} et des ratios pigmentaires a révélé une modulation saisonnière dans la composition des assemblages phytoplanctoniques et la photoacclimatation. Les propriétés optiques de la matière particulaire ont montré une relation très dispersée par rapport aux proxys de MPS dans la

zone d'étude, mais les valeurs extrêmement faibles de b_{bp} spécifiques à MPS rencontrées ont été expliquées par la caractéristique riche en matière organique des zones littorales de l'EGSL. La variabilité à court terme (événements atmosphériques) et le régime hydrodynamique ont également entraîné une variabilité importante des propriétés optiques de ces zones. Dans l'ensemble, nous fournissons une paramétrisation générale des relations entre les propriétés optiques inhérentes étudiées et les concentrations de masse molaire et sèche, qui, à leur tour, fourniront une base pour le réglage et le développement d'algorithmes de télédétection régionaux pour la récupération des constituants biogéochimiques pertinents de l'eau.

Mots-clés : optique aquatique, milieux côtiers, CDOM, phytoplancton, particules en suspension, télédétection

1.3 INTRODUCTION

Coastal zones are highly productive ecosystems that provide habitat for a wide variety of life. Because they are among the most attractive areas in the world for human settlements (Small and Nicholls, 2003), they are subject to extensive anthropogenic modification (Brown et al., 2017; Doney, 2010; Turner et al., 1996). Given the intrinsic dynamics of processes acting on coastal zones, their natural variability will occur over a wide range of spatial and temporal dimensions (de Jonge, 2000; Stommel, 1963). As is true for all ecosystems, the scientific study of coastal and nearshore environments is biased by the scale of the investigation, and this will have consequences on the patterns of variability observed (Levin, 1992). In this context, Earth Observation Satellite Missions (EOSM; a list of notations used is provided in Table 1) is another way to sample coastal regions, complementing and improving traditional monitoring strategies based on field campaigns (Dekker et al., 2018; Klemas, 2010).

Satellite remote sensing, particularly sensors with ocean color capabilities, has contributed substantially to our understanding of offshore marine biogeochemical cycles since the late 1970s (IOCCG, 2020, 2008; McClain, 2009). Recent advances by EOSM have shown that it is also promising tool for monitoring coastal zones at unprecedented spatial and temporal scales (Moses et al., 2016; Muller-Karger et al., 2018; Werdell et al., 2018).

In addition to the optical sensor design characteristics (see Muller-Karger et al., 2018, for a thorough discussion on this matter), the quality of the satellite-derived biogeochemical information will depend on the success of the method (or algorithms) used to retrieve the optically significant constituents of seawater. The theoretical basis of these algorithms relies on the relationships between these constituents and the inherent optical properties (IOPs) and, subsequently, the apparent optical properties (AOPs).

Table 1

List of acronyms and symbols, their definition, and units (if applicable)

Notation	Definition	Unit
AOPs	Apparent Optical Properties	-
BSI, MAN, FV, and PMZA-RIKI	Subregions investigated in this study: Bay of Sept-Îles, Manicouagan Peninsula, Forestville, and a moored buoy station in the St. Lawrence Estuary, respectively	-
CDOM	Chromophoric Dissolved Organic Matter	-
DFO	Fisheries and Oceans Canada	
DOM	Dissolved Organic Matter	-
EGSL	Estuary and Gulf of St. Lawrence	-
EOSM	Earth Observation Satellite Missions	-
IOPs	Inherent Optical Properties	-
<i>Bio-optical parameter</i>		
$a(\lambda)$	Total absorption coefficient	m^{-1}
$a_{\text{cdom}}(\lambda)$, $a_{\text{cdom}}^*(\lambda)$	CDOM absorption coefficient and DOC-specific CDOM absorption coefficient	m^{-1} , $\text{m}^{-1} \mu\text{M}^{-1}$
$a_{\text{nap}}(\lambda)$, $a_{\text{nap}}^*(\lambda)$	Non-algal particles absorption coefficient and SPM-specific non-algal particles absorption coefficient	m^{-1} , $\text{m}^2 \text{g}^{-1}$
$a_{\text{p}}(\lambda)$	Particulate absorption coefficient ($a_{\text{p}}(\lambda) = a_{\text{nap}}(\lambda) + a_{\text{phy}}(\lambda)$)	m^{-1}
$a_{\text{phy}}(\lambda)$, $a_{\text{phy}}^*(\lambda)$	Phytoplankton absorption coefficient and Chla-specific phytoplankton absorption coefficient	m^{-1} , $\text{m}^2 \text{mg}^{-1}$
$a_{\text{w}}(\lambda)$	Pure water absorption coefficient	m^{-1}
$b_{\text{b}}(\lambda)$	Backscattering coefficient	m^{-1}
$b_{\text{bp}}(\lambda)$, $b_{\text{bp}}^*(\lambda)$	Particulate backscattering coefficient, SPM-specific particulate backscattering coefficient	m^{-1} , $\text{m}^2 \text{g}^{-1}$
$b_{\text{bw}}(\lambda)$	Backscattering coefficient of pure seawater	m^{-1}

Table 1 (cont.)

Notation	Definition	Unit
Chla	Chlorophyll- <i>a</i> concentration	mg m ⁻³
DOC	Dissolved Organic Carbon concentration	μM
PIM	Particulate Inorganic Matter concentration	g m ⁻³
POM	Particulate Organic Matter concentration	g m ⁻³
PPC	Photoprotective Carotenoids (see text for details)	mg m ⁻³
PSC	Photosynthetic Carotenoids (see text for details)	mg m ⁻³
$R_{rs}(\lambda)$	Remote sensing reflectance	sr ⁻¹
S_f	“Size factor” parameter for phytoplankton packaging effect (dimensionless)	-
S_{nap}	Spectral slope of non-algal particles absorption coefficient	nm ⁻¹
$S_{\lambda_1-\lambda_2}$	CDOM spectral slope. λ_1 and λ_2 refer to the wavelength range (see text for details)	nm ⁻¹
S_R	CDOM slope ratio (dimensionless)	-
SPM	Suspended Particulate Matter concentration	g m ⁻³
TAP	Total Accessory Pigments (see text for details)	mg m ⁻³
$\beta(\lambda, \psi)$	Volume scattering function, with ψ being the scattering angle	m ⁻¹ sr ⁻¹
γ	Spectral slope of particulate backscattering (dimensionless)	-
λ	Wavelength of light in vacuo	nm

From the perspective of ocean color capabilities, the final desired parameters are derived from remote sensing reflectance ($R_{rs}(\lambda)$), an AOP retrieved after removing the atmospheric contribution from the top-of-atmosphere signal (Werdell et al., 2018). $R_{rs}(\lambda)$ is tightly related to IOPs namely the spectral absorption coefficient ($a(\lambda)$) and the volume scattering function ($\beta(\psi, \lambda)$), than directly to the optically significant constituents of

seawater because of the physical nature of the inversion problem (see the review of Werdell et al., 2018). This relationship can be approximated as $R_{rs}(\lambda) \propto b_b(\lambda) \cdot a(\lambda)^{-1}$ (Lo Prejato et al., 2020; Morel and Prieur, 1977), where the spectral backscattering coefficient ($b_b(\lambda)$) is the integration of $\beta(\psi, \lambda)$ in the backward direction ($\psi = 90$ to 180°).

The total absorption, $a(\lambda)$, can be decomposed by the additive contributions of the coefficients of absorption (eq. 3) of chromophoric dissolved organic matter ($a_{cdom}(\lambda)$), non-algal particles ($a_{nap}(\lambda)$), phytoplankton ($a_{phy}(\lambda)$), and pure water itself ($a_w(\lambda)$). Similarly, $b_b(\lambda)$ can be decomposed by the additive contributions of the coefficients of backscattering (eq. 4) of particulate matter ($b_{bp}(\lambda)$) and water ($b_{bw}(\lambda)$).

$$a(\lambda) = a_w(\lambda) + a_{cdom}(\lambda) + a_{nap}(\lambda) + a_{phy}(\lambda) \quad , \quad (3)$$

$$b_b(\lambda) = b_{bw}(\lambda) + b_{bp}(\lambda) \quad , \quad (4)$$

Understanding the relationships between IOPs and the optically significant constituents of seawater remains a central field of research in satellite ocean color remote sensing. The chemical composition of the chromophoric dissolved organic matter (CDOM) (Carder et al., 1989), the characteristics of particles (composition, size distribution, and geometric shape) (Stramski et al., 2004), and the nature of phytoplankton assemblages (Bricaud et al., 1995) will result in substantial variability in IOPs compared to the molar and dry-mass concentrations proxies of the optically significant constituents. Given the complex interaction of biological activity, terrestrial runoff, and resuspension events that modulate characteristics of the IOPs in coastal and nearshore zones, an assessment of these relationships at regional and local scales is a prerequisite because of the considerable variability that exists worldwide (e.g., Babin et al., 2003; Tzortziou et al., 2006).

The Estuary and Gulf of Saint Lawrence (EGSL) system is a prominent coastal feature in eastern Canada and one of the world's largest estuarine systems (El-Sabh and Silverberg, 1990a), connecting the Great Lakes to the Atlantic Ocean. Even though several studies examined IOP variability in the EGSL (see subsection 1.1), most focused on some aspects of

the bio-optical state, and the methods used to retrieve the IOPs varied widely among studies. Still, to the best of our knowledge, none of these studies focused on or sufficiently sampled nearshore environments of the EGSL (depths shallower than 30 m), even though these shallow regions are more susceptible to direct anthropic disturbances (Murphy et al., 2019).

The north shore of the EGSL is heavily influenced by numerous rivers that drain relatively large boreal watersheds and carry massive amounts of terrigenous optically significant constituents into the nearshore waters (Jaegler, 2014). Furthermore, the IOPs in these areas will strongly impact the amount of light that reaches the benthic surface, with consequences for the vegetated coastal habitats that are commonly found in the region (e.g., Murphy et al., 2021).

The objective of our study was to contribute to the knowledge on bio-optical variability in nearshore environments of the EGSL, where local river input is likely to dominate optical variability. Relationships between IOPs and biogeochemical parameters were studied to further develop algorithms to EOSM for monitoring purposes. We concentrated particularly on comparing our results with known relationships available worldwide. A secondary objective was to investigate domain scales (spatial and temporal) that are known to be driven by regional climatic, geomorphological, and hydrodynamical processes.

1.3.1 Inherent optical properties in the Estuary and Gulf of St. Lawrence: an overview

The characterization of IOPs in the EGSL was first performed in representative areas (transects) of the main body of the EGSL during the summers of 1989 and 1990, when the variabilities of $a_{\text{phy}}(\lambda)$ and $a_{\text{cdom}}(\lambda)$ were investigated (Babin et al., 1995, 1993; Nieke et al., 1997). Between 1997 and 2001, a series of field campaigns was conducted by the Fisheries and Oceans Canada (DFO), in distinct seasonal periods for each year (covering from spring to fall). During these campaigns, samples were collected to measure several optical and biogeochemical parameters across the EGSL (Çizmeli, 2008). This dataset

allowed the evaluation and development of regional remote sensing algorithms for suspended particulate matter concentration (SPM, particularly its inorganic fraction, PIM) and Chla, and provided information on the spatial and temporal variability of these parameters (Larouche and Boyer-Villemare, 2010; Yayla, 2009). The campaigns conducted in 2000 and 2001 provided a more complete set of IOPs, i.e., $a_{\text{cdom}}(\lambda)$, $a_{\text{nap}}(\lambda)$, $a_{\text{phy}}(\lambda)$, and $b_{\text{bp}}(\lambda)$ (Çizmeli, 2008). From this dataset, Roy et al. (2008) investigated the effect of pigment packaging on $a_{\text{phy}}(\lambda)$, and Montes-Hugo and Mohammadpour (2012) developed a model to estimate SPM from $R_{\text{rs}}(\lambda)$, while accounting for $a_{\text{cdom}}(\lambda)$ effects.

From a field campaign conducted in May 2007, which followed a transect in the main channel of the EGSL, Xie et al. (2012) investigated the absorption budget with special attention to $a_{\text{cdom}}(\lambda)$ and its relationship with salinity. The effects of different fractions of particulate matter on their respective absorption coefficients ($a_p(\lambda) = a_{\text{nap}}(\lambda) + a_{\text{phy}}(\lambda)$), and on the total scattering coefficient were investigated by Mohammadpour et al. (2017). By combining some of the previously mentioned datasets, Montes-Hugo and Xie (2015) developed a model to estimate $a_{\text{phy}}(\lambda)$ from $R_{\text{rs}}(\lambda)$ for the Lower St. Lawrence Estuary. For a specific region of the upper estuary, Mohammadpour et al. (2015) verified that a model to retrieve SPM from R_{rs} (near-infrared to red ratio model) achieved better results when partitioning the model for different classes of PIM / SPM. Finally, Bélanger et al. (2017) presented a seasonal characterization (from late spring to fall) of $a_{\text{cdom}}(\lambda)$, $a_{\text{nap}}(\lambda)$, $a_{\text{phy}}(\lambda)$, and $b_{\text{bp}}(\lambda)$ in a central portion of the St. Lawrence Estuary, although their study focused on the radiometric quality collected by an autonomous system (moored buoy).

Although these studies contributed to a better understanding of the general bio-optical variability in the EGSL and over an even wider context (see, for example, Bricaud et al., 1998, 1995), they were often limited in time to few field campaigns (e.g., Mohammadpour et al., 2017; Xie et al., 2012) or did not cover a wide spatial domain (e.g., Bélanger et al., 2017).

1.4 METHODS

1.4.1 Study area and sampling design

The present study used a comprehensive dataset of IOPs and molar and dry-mass concentrations proxies of optically significant constituents. The dataset includes samples collected in four geographically distinct areas of the EGSL (hereafter referred to as subregions; Fig. 5) within the Lower St. Lawrence Estuary (from the Saguenay River to Pointe-des-Monts) and on the north shore of the Gulf of St. Lawrence, near Sept-Îles. The first subregion is a relatively deep station (330 m) in the middle of the Lower St. Lawrence Estuary, where optical profiles and water samples were collected near a moored platform (the PMZA-RIKI buoy) maintained by DFO (see Bélanger et al., 2017, for more details). The other three subregions are nearshore environments on the north shore of the EGSL, where the spatial sampling strategy occurred in relatively shallow waters (Fig.5).

The Bay of Sept-Îles (BSI; Fig. 5b) is a relatively protected coastal embayment that hosts diverse human activities, including an important harbor mainly dedicated to heavy industrial activities (i.e., mining). The BSI subregion is subject to water exchange with the Gulf of St. Lawrence, and is also influenced by small rivers and streams that flow into the bay (Shaw, 2019). It is important to note that this subregion is also influenced by a major river, i.e., the pristine Moisie River (average discharge of $490 \text{ m}^3 \text{ s}^{-1}$), which is located just east of the bay.

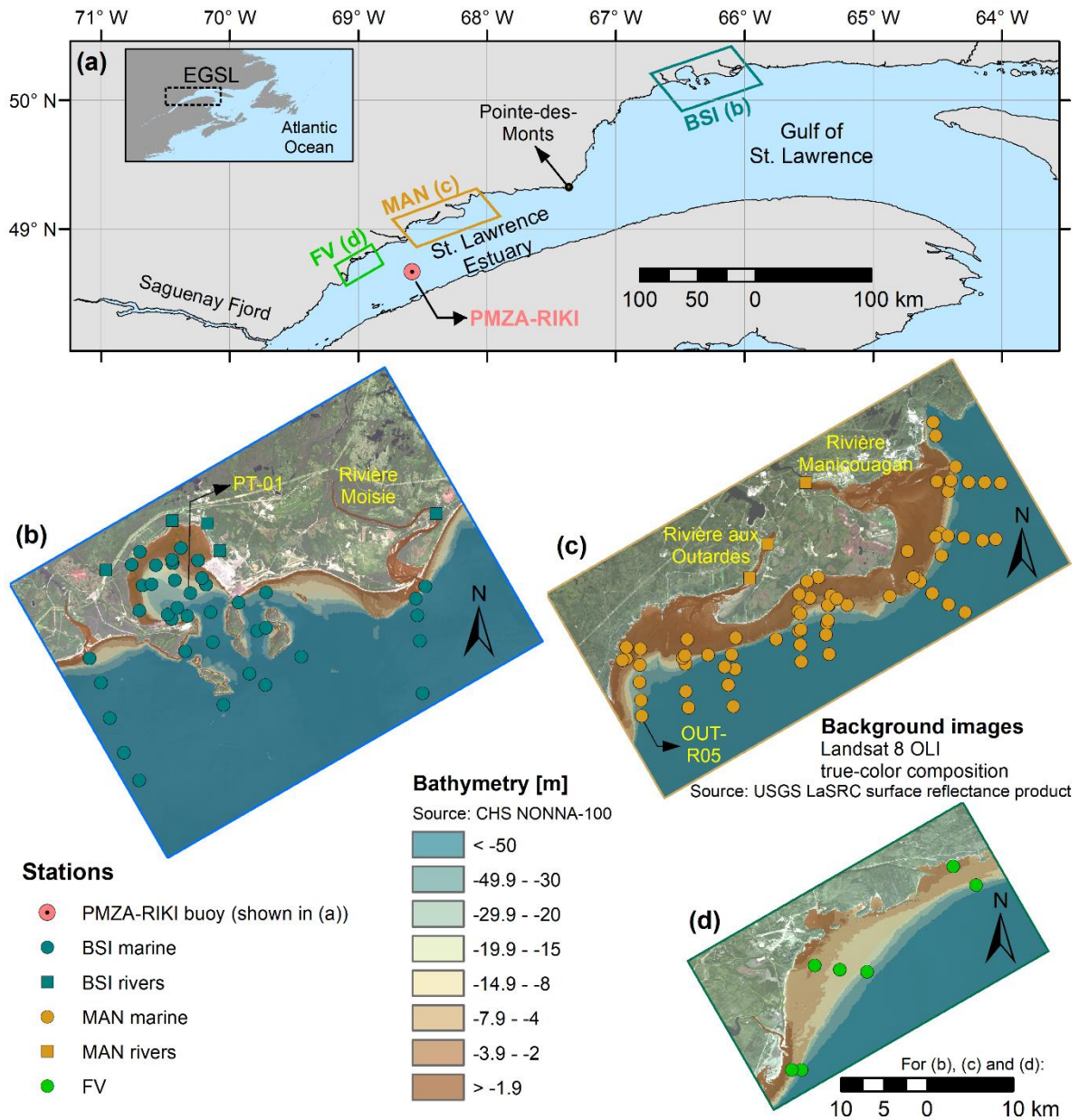


Figure 5. (a) Map of the Estuary and Gulf of St. Lawrence (EGSL) showing the sampling areas in the regional context; the inset shows EGSL's general localization in the North America context. The spatial distributions of sampling stations are shown for subregions (b) Bay of Sept-Îles (BSI), (c) Manicouagan Peninsula (MAN), and (d) coastal Forestville (FV)

The second nearshore subregion is a prominent geomorphological feature (delta), the Manicouagan Peninsula (MAN; Fig. 5c), which is influenced by the discharge of three major rivers: Betsiamites (discharge $\sim 340 \text{ m}^3 \text{ s}^{-1}$), Aux-Outardes (discharge $\sim 390 \text{ m}^3 \text{ s}^{-1}$), and Manicouagan (discharge $\sim 1000 \text{ m}^3 \text{ s}^{-1}$). These three rivers have their flow regulated by hydroelectric dams, with peak discharges in winter (Jaegler, 2014), and are known to form distinct river plumes in the Lower St Lawrence Estuary (Fauchot et al., 2008). Most of the above-mentioned rivers from BSI and MAN subregions were included in the sampling strategy to assess the local endmembers (see Figs. 5b and 5c). Finally, the third subregion corresponds to the coastal area near the city of Forestville (FV; Fig 5d). The FV subregion is relatively more exposed to the main body of the estuary and has a more gradual bathymetry characteristic compared to the other subregions.

The dataset consists of in situ profiles and discrete surface, subsurface, and riverine water samples, collected within the scope of different research projects. This exceptional dataset provided a unique opportunity to investigate different spatial and temporal variabilities in the bio-optical conditions of the nearshore environment in the northern part of the EGSL (Table 2).

The PMZA-RIKI station was sampled 19 times, between June and October 2015. The largest number of samples was from the BSI subregion, where 11 field campaigns were carried out between August 2016 and June 2019, but most samples covered the 2017 seasonal cycle (nine field campaigns from April to October). The BSI campaigns varied from 1 to 5 days, and the number of discrete samplings ranged from 2 to 42 (average ~ 15) per campaign at 44 stations, for a total of 170 water samples. In the MAN subregion, a single eight-day campaign took place in August 2019, with 85 discrete samples collected over 68 stations. Finally, the FV subregion was sampled on a one-day campaign in September 2017, and seven discrete samples were taken from different stations along the coast.

Table 2
Summary of the sampling strategy

Sampling area	Number of campaigns	Period	Number of stations	Number of samples		
				Surface	Subsurface	River
PMZA-RIKI	19	June - October 2015	1	19	0	Not applied
BSI	11	August 2016, April - October 2017, June 2019	44	121	9	40
MAN	1	August 2019	68	67	15	3
FV	1	September 2017	7	7	0	0
Total	32	June 2015 - August 2019	120	214	24	43

1.4.2 Bio-optical data

The optical and biogeochemical data used in this study were mainly collected from discrete samples. Data were obtained either by in situ instrumentation or by laboratory analyses of water samples. Optical parameters from in situ vertical profiles (e.g., $b_{bp}(\lambda)$) were matched with discrete samples for biogeochemical or other optical parameters (e.g., $a_{cdom}(\lambda)$, $a_p(\lambda)$) from the closest measured depth. The physical and biogeochemical parameters were temperature ($^{\circ}\text{C}$), salinity, Secchi disk depth, dissolved organic carbon concentration (DOC), SPM, and phytoplankton pigment concentrations, including Chla. The IOPs include $a_{cdom}(\lambda)$, $a_{nap}(\lambda)$, $a_{phy}(\lambda)$, and $b_{bp}(\lambda)$. Water samples were mainly collected with a Niskin bottle (or bucket) and were kept cool in a sun-protected container until further laboratory procedures, which were done each day immediately after the field work and consisted mainly of filtration operations. A total of 281 discrete samples were considered in this study (Table 2), although not all parameters were available all the time for each sample,

mainly due to logistical constraints. When appropriate, the total number of samples (n) considered in the analysis is presented.

1.4.2.1 Temperature, salinity, and molar and dry-mass concentrations

High-precision salinity (± 0.0003 , in practical salinity units, PSU) was measured on discrete water samples using a calibrated Portasal salinometer (model 8410A, Guildline Instruments, Smiths Falls, ON). In addition, in situ vertical profiles of temperature and conductivity were made with a CTD probe (SBE19, Sea-Bird Scientific, Bellevue, WA). Total and dissolved organic carbon (TOC and DOC) were determined on a high-temperature combustion Shimadzu TOC-Vcpn carbon analyzer, following the procedures described in Zhang and Xie (2015). DOC samples were filtered on precombusted Whatman GF/F filters and were quality-controlled using TOC samples (non-filtered). SPM was determined with the gravimetric method (Van der Linde, 1998), and the organic and inorganic fractions concentrations (POM and PIM, respectively) were determined by obtaining the organic matter lost on ignition (LOI) after combustion of the filters (Whatman GF/F) for 3 h at 500 °C.

Phytoplankton pigment concentrations were determined from filtered (Whatman GF/F) water samples through high-performance liquid chromatography (HPLC) analysis, following the method described in Zapata et al. (2000). Chla is the sum of monovinyl chlorophyll-*a*, chlorophyllids and the allomeric and epimeric forms of chlorophyll-*a*. Finally, Chla was also determined by fluorometric methods (in triplicate) following Parsons et al. (1984), and these values were used in the absence of HPLC measurements once the two methods showed good correlation.

1.4.2.2 Inherent optical properties

We determined the absorption coefficients from measurements made using a benchtop PerkinElmer Lambda-850 spectrophotometer equipped with an integrating sphere (used for particles only). Briefly, CDOM absorbance ($A(\lambda)$) was measured with filtered water samples (0.2 μm pore size) placed in a quartz cuvette (with a length [L] of 1 or 10 cm, depending on sample absorbance). A cuvette containing nanopure water, at the same temperature as the samples, was used as a reference. A baseline correction was applied by considering the average values over a 5-nm interval, centered at 685 nm (Babin et al., 2003; Matsuoka et al., 2012). Finally, the $a_{\text{cdom}}(\lambda)$ was obtained by the relation $a_{\text{cdom}}(\lambda) = 2.303A(\lambda)/L$.

For a_{p} , a known volume of water was filtered through Whatman GF/F glass-fiber filters, which retain particles larger than 0.7 μm (i.e., nominal filter pore size). The filters were placed inside the integrating sphere following the quantitative filter technique (Röttgers and Gehnke, 2012, and references therein), and the absorbance values were subtracted from those of the reference (blank) filters. Similarly, the $a_{\text{nap}}(\lambda)$ was obtained by placing the filters into the integrating sphere after phytoplankton pigment extraction using methanol (Kishino et al., 1985). Absorbance measurements were also corrected for the pathlength amplification (Stramski et al., 2015) and converted into absorption using the equation $a_{\text{p- nap}}(\lambda) = 2.303A(\lambda)(F_{\text{area}}/Vol)$, where F_{area} (m^2) is the clearance area of the filter occupied by the particles (in the filtration process) and Vol (m^3) is the volume of water filtered. A baseline (null-point) correction was performed for a_{nap} measurements, assuming that its values were equal to a_{p} in the near-infrared region, averaged between 745 and 755 nm (i.e., $a_{\text{phy}}(\text{NIR}) = 0$, or $a_{\text{p}}(\text{NIR}) = a_{\text{nap}}(\text{NIR})$). The wavelength (λ) varied from 230 to 800 nm for $a_{\text{cdom}}(\lambda)$ and 290 to 800 nm for $a_{\text{p}}(\lambda)$ and $a_{\text{nap}}(\lambda)$. Finally, $a_{\text{phy}}(\lambda)$ was determined by subtracting $a_{\text{nap}}(\lambda)$ from $a_{\text{p}}(\lambda)$.

The in situ b_{bp} was determined using a HydroScat-6P (HS6) backscattering meter (HOBI Labs Inc., Bellevue, WA). The HS6 measures the volume scattering function at a

scattering angle of 140° , $\beta_{(140)}$, and it was set to measure at six wavelengths (394, 420, 470, 532, 620 and 700 nm). The b_{bp} is derived from $\beta_{(140)}$ after correction for attenuation along the detector's viewing pathlength, using the total absorption coefficient measurements from another in situ instrument, the a-Sphere (HOBI Labs Inc.), and for the effects of temperature and salinity on the pure seawater scattering, following Doxaran et al. (2016) and Maffione and Dana (1997), as implemented in the *Riops* R package (<https://github.com/belasi01/Riops>).

1.4.2.3 Bio-optical indices

Given the approximately exponential decrease in $a_{cdom}(\lambda)$ with increasing wavelength, an exponential model (eq. 5) was used to derive information about the optical properties of CDOM (Bricaud et al., 1981; Jerlov, 1968):

$$a_{cdom}(\lambda) = a_{cdom}(\lambda_0)e^{-S(\lambda-\lambda_0)} \quad , \quad (5)$$

where λ_0 is a reference wavelength (nm). The spectral slope (S , nm^{-1}) describes the approximate exponential rate of decrease in absorption with increasing wavelengths. S can be a proxy for the chemical and structural nature of the dissolved organic matter pool (e.g., molecular weight, aromaticity), providing information about its sources and transformation (Fichot and Benner, 2012, 2011). Several wavelength ranges are described in the literature for the determination of S ($S_{(\lambda_1-\lambda_2)}$). In this study, S was calculated within fixed ranges for comparison with the literature: 275 to 295 and 350 to 400 nm (Helms et al., 2008), 320 to 412 nm (Danhiez et al., 2017), and 350 to 500 nm (Babin et al., 2003). The CDOM slope ratio (S_R) was obtained by the ratio $S_{(275-295)}:S_{(350-400)}$ (Helms et al., 2008). Fittings were performed either using a nonlinear least-squares Levenberg-Marquardt (NLS L-M) algorithm ($S_{(350-500)}$), or by loglinear functions (all other S). All slopes were calculated following the procedures according to the original work in which they were published.

Similarly, $a_{\text{nap}}(\lambda)$ was fitted to an exponential decay function (eq. 5), and the slope of non-algal particles S_{nap} was obtained by taking the wavelength range from 380 to 730 nm but excluding the 400-480 and 620-710 nm ranges to avoid potential contamination of residual pigment absorption from a_{p} (Babin et al., 2003).

Besides chlorophyll-*a* concentration, $a_{\text{phy}}(\lambda)$ is also influenced by community size structure and pigment composition (Lohrenz et al., 2003). We have evaluated the package effect from phytoplankton on $a_{\text{phy}}(\lambda)$ using the approach of Ciotti et al. (2002). Briefly, the $a_{\text{phy}}(\lambda)$ shape is reconstructed using a linear combination of two endmember's spectra (Ciotti et al., 2002, their equation 3) representing the contributions of the smallest (picophytoplankton) and largest (microphytoplankton) cell sizes. The picophytoplankton spectrum endmember used here was provided by Ciotti and Bricaud (2006). The retrieved parameter, S_{f} ("size factor"; dimensionless), is restricted to a variation from 0 to 1, with values tending toward 0 when large-celled phytoplankton are dominant and values tending toward 1 when small-celled phytoplankton dominates. Nonetheless, S_{f} can be a proxy for either the phytoplankton cell size or changes in accessory pigment concentrations that do not co-vary with Chl*a* and algal size, since the blue-to-red ratio in $a_{\text{phy}}(\lambda)$ tends to flatten the spectra due to increased concentrations of the latter (Ferreira et al., 2017).

The photoacclimation state of phytoplankton, i.e., the adjustments to the structure and function of the photosynthetic apparatus in response to changes in growth irradiance (Graff et al., 2016), was also evaluated using pigment concentrations grouped into three classes: photoprotective carotenoids (PPC), photosynthetic carotenoids (PSC), and total accessory pigments (TAP). TAP was considered as the sum of all chlorophylls *b* and *c*, Mg 2,4 divinyl pheoporphyrin *a*5 monomethyl ester, and all carotenoids (peridinin, fucoxanthin, 19'-butanoyloxyfucoxanthin, 19'-hexanoyloxyfucoxanthin, neoxanthin, prasinoxanthin, crocoxanthin, diadinoxanthin, diatoxanthin, violaxanthin, zeaxanthin, alloxanthin, lutein, β , ϵ -carotene, and β , β -carotene).

Since the allocation of certain pigments in one of the classes (PPC or PSC) is subject to variations due to specific functions according to the phytoplankton group, we used the approach proposed by Kauko et al. (2019). In short, different pigment allocations in each class were compared, and the authors concluded that a strict approach using only pigments involved in the xanthophyll cycle in the PPC class yielded better results when compared to its relationship with $a_{\text{phy}}(\lambda)$. Thus, PPC includes the pigments diadinoxanthin, diatoxanthin, violaxanthin, and zeaxanthin, while PSC includes peridinin, fucoxanthin, 19'-butanoyloxyfucoxanthin, 19'-hexanoyloxyfucoxanthin, neoxanthin, prasinoxanthin, and alloxanthin.

The spectral dependency of b_{bp} was modelled as a power-law function (Reynolds et al., 2016):

$$b_{\text{bp}}(\lambda) = b_{\text{bp}}(\lambda_0) \times \left(\frac{\lambda}{\lambda_0}\right)^\gamma, \quad (6)$$

where γ is a dimensionless parameter describing the spectral dependency of b_{bp} relative to a reference wavelength (λ_0). In our study, we used mostly $\lambda_0 = 550$ nm (as in Reynolds et al., 2016), but also $\lambda_0 = 555$ nm (as in Blondeau-Patissier et al., 2017).

To assure the validity of equation 6, the retrieved γ and $b_{\text{bp}}(550)$ were used to compute the fitted (*fit*) $b_{\text{bp}}(\lambda)$, and its residual differences (in percent values), were calculated as $100 \times [b_{\text{bp}}^{\text{fit}}(\lambda) - b_{\text{bp}}^{\text{obs}}(\lambda)]/b_{\text{bp}}^{\text{obs}}(\lambda)$, as in Reynolds et al. (2016). The means and standard deviations of the residual difference were always less than 5 and 7%, respectively, independently of the wavelength. These relatively low values indicate that the coefficients obtained in equation 6 - γ and $b_{\text{bp}}(\lambda_0)$ - can be used as good predictors of the spectral shape of $b_{\text{bp}}(\lambda)$ in our study area.

Finally, the mass-specific IOPs for the absorption and backscattering coefficients were calculated to establish a basis for comparison with other studies worldwide, since they have become a necessary step in the parametrization of (semi) analytical bio-optical models at

regional scales (Blondeau-Patissier et al., 2017; Brando et al., 2012; Le et al., 2015). The DOC-specific CDOM absorption coefficient ($a_{\text{cdom}}^*(\lambda)$) was obtained by the ratio $a_{\text{cdom}}(\lambda): \text{DOC}$; the Chla-specific phytoplankton absorption coefficient ($a_{\text{phy}}^*(\lambda)$) was obtained by the ratio $a_{\text{phy}}(\lambda): \text{Chla}$; the SPM-specific non-algal particles absorption coefficient ($a_{\text{nap}}^*(\lambda)$) was obtained by the ratio $a_{\text{nap}}(\lambda): \text{SPM}$; and the SPM-specific particulate backscattering coefficient ($b_{\text{bp}}^*(\lambda)$) was obtained by the ratio $b_{\text{bp}}(\lambda): \text{SPM}$.

1.4.3 Spatial and temporal analysis, ancillary data, and statistics

The first spatial analysis considered the four main subregions (Fig. 5) as different subsets of data, to check whether they were subject to distinct oceanographic and watershed processes (the average distance for a mean latitude/longitude for each subregion was $\sim 10^2$ km). The second spatial analysis explored the variability found in a single field campaign for the same subregion (the average distance between stations was $\sim 10^0 - 10^1$ km). In this case, the 11 field campaigns of BSI and 1 field campaign for both MAN and FV were considered.

The temporal analysis focused on seasonal variability ($\sim 10^1 - 10^2$ days) in each subregion where data were available, so only data from the BSI and the PMZA-RIKI subregions were considered. Daily and tidally induced variations were also investigated for illustrative purposes. The bio-optical properties of a single station located in the middle of the Bay of Sept-Îles (PT-01; Fig. 5b), which was visited several times during the first week of June 2019, were examined in comparison with tidal fluctuations and meteorological forcing. For this analysis, local ancillary data were used to access tidal height, air temperature, wind velocity and direction, and precipitation. While precipitation was available through the Environment and natural resources Canada website (www.climat.meteo.gc.ca), all the others were obtained from the St. Lawrence Global Observatory (SLGO) website (www.ogsl.ca/en).

Descriptive statistics (minimum, maximum, mean, standard deviation) and one-way ANOVA (analysis of variance) were used to quantitatively compare the populations identified by spatial and temporal variability. Data were confirmed to exhibit normal distributions using the Lilliefors test prior to all ANOVAs. When a significant difference was revealed between tested groups (p -value < 0.05), differences between pairs of means were assessed using the Tukey honest significant difference criterion.

Finally, regression analysis consisted of fitted equations; for example, in the power form $A \cdot x^B$, where x is the independent variable and A and B are regression coefficients, generally obtained by the NLS L-M algorithm (unless explicitly mentioned). We determined the performance metrics of regressions using mean absolute error, MAE (and its correspondent, the Mean Absolute Percentage Error, $MAPE$), as well as the *bias* (together with the percentage bias, $P - bias$), as suggested by Seegers et al. (2018). Furthermore, we report the coefficient of determination (R^2) and the root mean square error ($RMSE$). All data manipulations, statistics, and plots were done using Matlab (MathWorks) software.

1.5 RESULTS

The results are first presented considering the general bio-optical relationships, separating the analysis into i) the optical properties of CDOM, ii) the optical properties of the particulate matter (including phytoplankton), and finally iii) the absorption budget. The spatial (within each subregion) and seasonal variability are presented in subsection 3.4; subsection 3.5 provides an exploratory analysis with a mechanistic interpretation of how the combined effects of tidal and meteorological forcing can drive some optical properties at the scale of a subregion.

The sampling design covered a wide range of environmental conditions. If we consider only marine (or brackish) stations, samples were collected from depths as shallow as 0.5 m to as deep as 176 m (excluding the single station of the PMZA-RIKI subregion); temperature

and salinity ranged from ~ 0.3 to 18.1°C and from 3 to 31, respectively; and Secchi depths varied from 0.5 to 9 m. The general relationship between molar and dry-mass concentrations of DOC, Chla and SPM are provided in Figure 6, which highlights the differences between subregions as well as marine versus riverine samples.

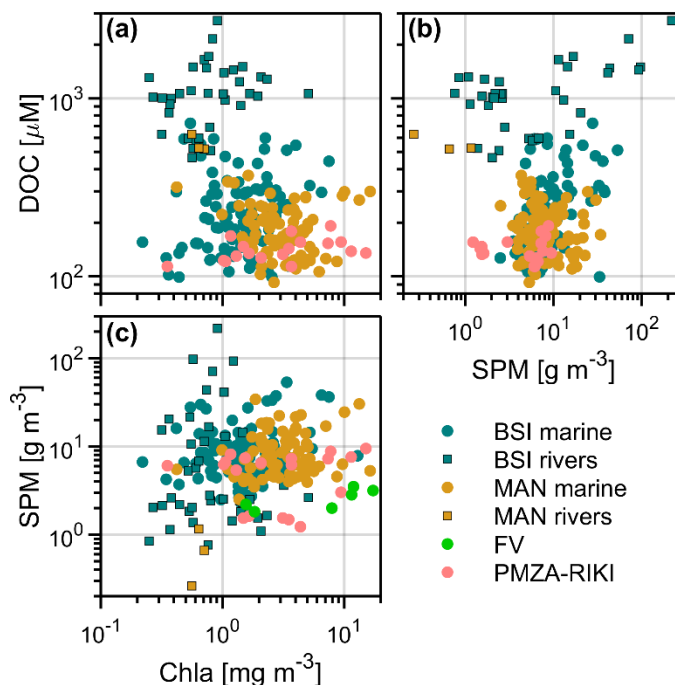


Figure 6. Relationship between molar and dry mass concentrations of (a) dissolved organic carbon (DOC) and chlorophyll-*a* (Chla); (b) DOC and suspended particulate matter (SPM); and (c) SPM and Chla. The colored symbols distinguish the four subregions of this study:

The Bay of Sept-Îles (BSI), the Manicouagan Peninsula (MAN), the coastal area of Forestville (FV), and the buoy station (PMZA-RIKI). Marine (or brackish) stations are represented by circles, while stations located in the main channels of local rivers are represented by squares

The DOC values (Fig. 6a, 6b) of the compared groups (river samples from different subregions were grouped, for practical purposes) had significant differences (one-way ANOVA, $p < 0.05$). The range of DOC for marine stations varied from 92 to 724 μM , corresponding to samples with a more brackish or saltier character, respectively. DOC mean and standard deviation for the PMZA-RIKI subregion were lower ($\mu \pm \sigma = 142 \pm 22 \mu\text{M}$)

compared to the BSI or MAN subregions (248 ± 132 and $190 \pm 63 \mu\text{M}$, respectively). The mean DOC values from riverine stations ($1081 \pm 483 \mu\text{M}$) were significantly higher than all other groups.

The range of Chla (Fig. 6a, 6c) varied by about two orders of magnitude (from 0.22 to 17.3 mg m^{-3}) and grouped samples were significantly different from each other ($p < 0.05$). This was especially true for samples from the FV subregion, which had higher concentrations ($8.7 \pm 6.2 \text{ mg m}^{-3}$). The BSI ($1.9 \pm 1.7 \text{ mg m}^{-3}$) and MAN ($3.6 \pm 2.5 \text{ mg m}^{-3}$) subregions also significantly differed from each other.

No significant difference was found for SPM (Fig. 6b, 6c), which varied from 1.3 to 53.5 g m^{-3} (marine samples only). The lowest values of SPM ($< 1 \text{ g m}^{-3}$) were found in riverine samples, mainly dammed rivers from the MAN subregion. Moreover, SPM concentrations from the PMZA-RIKI samples showed a distinctive bimodal distribution. The BSI and MAN subregions had similar means and standard deviations (9.9 ± 8.4 and $9.5 \pm 6.3 \text{ g m}^{-3}$, respectively).

The percentage of organic matter in the suspended particulate matter ($[\text{POM} : \text{SPM}] \cdot 100$, in %), i.e., the POM fraction, varied from 13 to 69% , with a mean value of 25% (marine samples only). Riverine samples were significantly higher than most of the marine subregions, with a mean value of 50% . No relevant correlations were found among DOC, Chla, and SPM for marine samples. However, DOC and SPM in river samples (squares in Fig. 6b) showed a moderate R^2 and a relatively low error (Table 3). Next, we further examine the variability of each molar and dry-mass concentrations presented above in relation to IOPs.

Table 3

Summary of fitted regressions and associated errors for the power model $y = A \cdot x^B$, where y is the dependent variable, x is the independent variable, and A and B are the regression coefficients. The reported metrics are the mean absolute error, MAE (and the mean absolute percentage error, $MAPE$); $bias$ (and the percentage bias, $P - bias$); coefficient of determination, R^2 ; and the root mean square error, $RMSE$. The considered subset of the data and the corresponding scatterplot figure are also indicated

Dependent variable	Independent variable	Locale or subset type	Ref. Fig.	Coefficients		MAE ($MAPE$)	$bias$ ($P - bias$)	R^2	$RMSE$
				A	B				
DOC	SPM	Rivers	6b	$7.8 \cdot 10^2$	0.18	$2.9 \cdot 10^2$ (33%)	$-8.0 \cdot 10^0$ (11%)	0.47	$3.5 \cdot 10^2$
$a_{phy}(676)$	Chla	BSI	9a	$2.1 \cdot 10^{-2}$	0.76	$5.6 \cdot 10^{-3}$ (16%)	$-9.0 \cdot 10^{-4}$ (3%)	0.67	$1.2 \cdot 10^{-2}$
$a_{phy}(676)$	Chla	MAN	9a	$2.7 \cdot 10^{-2}$	0.82	$8.2 \cdot 10^{-3}$ (10%)	$4.1 \cdot 10^{-3}$ (5%)	0.52	$2.1 \cdot 10^{-2}$
$a_{phy}(676)$	Chla	FV	9a	$9.5 \cdot 10^{-3}$	0.91	$8.4 \cdot 10^{-3}$ (18%)	$-2.1 \cdot 10^{-3}$ (10%)	0.95	$9.3 \cdot 10^{-3}$
$a_{phy}(676)$	Chla	PMZA-RIKI	9a	$1.8 \cdot 10^{-2}$	1.07	$8.3 \cdot 10^{-3}$ (16%)	$2.3 \cdot 10^{-3}$ (3%)	0.98	$1.2 \cdot 10^{-2}$

Table 3 (cont.)

Dependent variable	Independent variable	Locale or subset type	Ref. Fig.	Coefficients		<i>MAE</i> (<i>MAPE</i>)	<i>bias</i> (<i>P - bias</i>)	<i>R</i> ²	<i>RMSE</i>
				<i>A</i>	<i>B</i>				
$a_{\text{nap}}(443)$	SPM	Rivers	9b	$1.5 \cdot 10^{-1}$	0.64	$2.1 \cdot 10^{-1}$ (34%)	$-1.1 \cdot 10^{-1}$ (3%)	0.88	$3.7 \cdot 10^{-1}$
$b_{\text{bp}}(550)$	SPM	Marine	9c	$8.1 \cdot 10^{-3}$	0.31	$7.9 \cdot 10^{-3}$ (50%)	$-2.7 \cdot 10^{-3}$ (20%)	0.17	$1.3 \cdot 10^{-2}$
$a_{\text{p}}(\text{NIR})$	PIM	Rivers	10b	$2.7 \cdot 10^{-2}$	0.80	$4.2 \cdot 10^{-2}$ (37%)	$-1.0 \cdot 10^{-2}$ (21%)	0.91	$1.0 \cdot 10^{-1}$
$a_{\text{p}}(440)$ $- a_{\text{p}}(\text{NIR})$	POM	Rivers	10c	$2.4 \cdot 10^{-1}$	1.10	$2.0 \cdot 10^{-1}$ (35%)	$-6.0 \cdot 10^{-2}$ (6%)	0.82	$3.4 \cdot 10^{-1}$
$b_{\text{bp}}(550)$	POM \div 2	Marine	10d	$1.5 \cdot 10^{-2}$	0.39	$8.2 \cdot 10^{-3}$ (49%)	$-2.8 \cdot 10^{-3}$ (19%)	0.16	$1.3 \cdot 10^{-2}$
$b_{\text{bp}}^*(555)$	$a_{\text{nap}}^*(555)$	Marine	10f	$4.0 \cdot 10^{-2}$	0.61	$6.1 \cdot 10^{-4}$ (35%)	$-1.0 \cdot 10^{-4}$ (12%)	0.66	$7.1 \cdot 10^{-4}$

1.5.1 Optical properties of dissolved organic matter

The optical properties and environmental characteristics associated with the DOM pool are presented in Figure 7, and the associated relevant regressions (equations, coefficients, and performance metrics) are shown in Table 11 (Annex 1). We chose 350 nm as a reference wavelength, as reported in a number of studies (e.g., Fichot and Benner, 2012; Massicotte et al., 2017; Xie et al., 2012), and used both for comparisons and later in the discussion.

A strong relationship between $a_{\text{cdom}}(350)$ and DOC was observed (Fig. 7a) for all samples (riverine and marine), although PMZA-RIKI samples had slightly lower absorptions for a given DOC value compared to other subregions. The linear model presented in Table 11 (and shown in Fig. 7a) had a high R^2 , and relatively low errors considering the whole dataset. However, if the lower range of the $a_{\text{cdom}}(350)$ values were considered, as for PMZA-RIKI, the *MAE* and *RMSE* were high.

The potential linkages between DOC and a_{cdom} in different spectral ranges were investigated through the relationships between $a_{\text{cdom}}^*(350)$ and various spectral slopes (S). The strongest relationship was found with the slope between 275 and 295 nm, $S_{275-295}$ (Fig. 7b), as revealed by the moderate to high R^2 and low errors from the regressions for marine samples from the BSI and MAN subregions (Table 11, Annex 1), using the same equation form presented by Fichot and Benner (2012). The inset in Figure 7b depicts the same relationship, but for $S_{320-412}$, revealing it as a poor predictor of $a_{\text{cdom}}^*(350)$ for this dataset. The $a_{\text{cdom}}^*(350)$ range found in the EGSL (and local rivers) ranges from $6.6 \cdot 10^{-3}$ to $4.8 \cdot 10^{-2} \text{ m}^{-1} \mu\text{M}^{-1}$. We also notice a regional difference in the $a_{\text{cdom}}^*(350)$ versus $S_{275-295}$ relationship, with more absorbing DOM for a given spectral slope in the MAN subregion. Some river samples from the BSI subregion also showed this behavior, particularly those with characteristically and significantly lower discharges (Rivière aux Foins and Rivière Poste). Nevertheless, there is also a noticeable slight decrease in $S_{275-295}$ from the river-to-marine continuum for some samples.

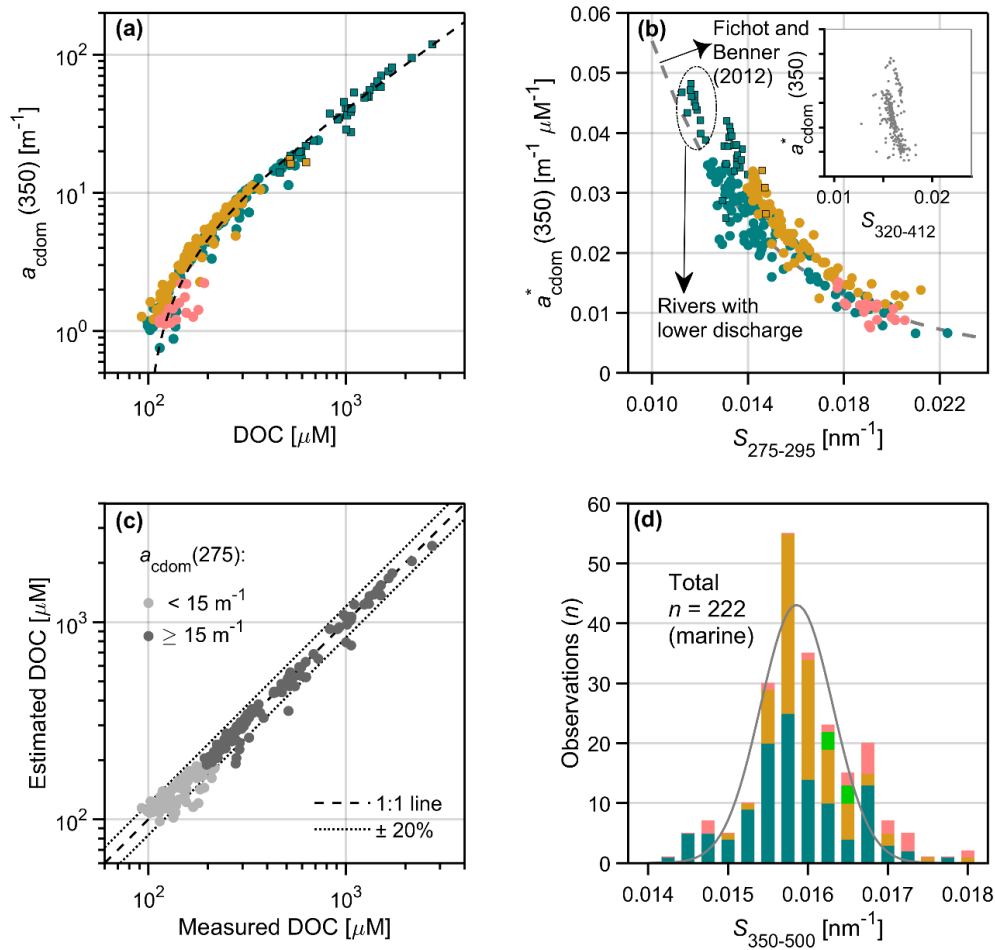


Figure 7. General characterization of the optical properties of the chromophoric dissolved organic matter (CDOM) pool showing their relationships with dissolved organic carbon concentration (DOC) and spectral slopes. The relevant fitting equations, coefficients, and performance metrics for (a), (b), and (c) are provided in Table 11 (Annex 1). **(a)** CDOM absorption coefficient at 350 nm ($a_{\text{cdom}}(350)$) vs DOC. The black dashed line shows the fitted linear model (Table 11). **(b)** DOC-specific $a_{\text{cdom}}(350)$, $a_{\text{cdom}}^*(350)$, vs the CDOM spectral slope between 275 and 295 nm ($S_{275-295}$). The ellipse indicates samples of the riverine endmembers, which were expected to have lower influence in the BSI subregion (i.e., with lower discharge in comparison to others). The curve of Fichot and Benner (2011) is shown for comparative purposes. The inset graphic illustrates the same relationship but for the CDOM spectral slope between 320 and 412 nm ($S_{320-412}$). **(c)** Relationship between the estimated DOC, modelled from CDOM absorption coefficients at 275 and 295 nm (see text), and the measured DOC. **(d)** Frequency distribution of the CDOM spectral slope between 350 and 500 nm ($S_{350-500}$). The Gaussian curve illustrates a normal distribution among the marine samples. The color code is the same as in Fig. 6

Taking this relationship into consideration, Fichot and Benner (2011) developed a model to predict DOC from a_{cdom} measured at two wavelengths (275 and 295 nm; see Table 11). We have reparametrized this model for our EGSL samples, by splitting the dataset into two groups, $a_{\text{cdom}}(275) < 15$ and $a_{\text{cdom}}(275) \geq 15 \text{ m}^{-1}$, since a single model for the whole dataset provided unsatisfactory results for the lower ranges of DOC. The results obtained yielded moderate and very high coefficients of determination (0.69 and 0.98, for the lower and upper range of $a_{\text{cdom}}(275)$, respectively), and very low associated errors for both groups (Fig. 7c).

Since $S_{350-500}$ is a widely used metric for describing a_{cdom} spectral behavior in coastal and estuarine systems (e.g., Babin et al., 2003; Noernberg et al., 2020; Para et al., 2010), we presented its distribution for the EGSL (marine samples only; Fig. 7d). It was found to be close to normal, with a mean of 0.0159 nm^{-1} and a standard deviation of $\pm 0.0009 \text{ nm}^{-1}$.

The $a_{\text{cdom}}(350)$ versus salinity relationships are presented in Figure 8a and compared to those reported for the central parts of the EGSL by Xie et al. (2012). The equations provided in Table 11 (Annex 1) for BSI and MAN subregions consider the median river $a_{\text{cdom}}(350)$ as freshwater endmembers (salinity = 0). From the presented linear models, a conservative mixing behavior can be observed, particularly for the MAN and to a lesser degree for BSI subregion. However, it is important to note that the $a_{\text{cdom}}(350)$ values in five endmembers from BSI varied widely and, the sampling strategy in this subregion also examined seasonal variability in 2017 (see Fig. 8a inset). Moreover, the median freshwater BSI endmember is more than twice that of MAN in terms of $a_{\text{cdom}}(350)$. Data from the PMZA-RIKI and FV subregions are close to the reference EGSL line from Xie et al. (2012), suggesting that the endmember is the same in that part of the Lower St. Lawrence Estuary. The adjusted linear model for the MAN subregion (Table 11) is also very similar to that for the Saguenay Fjord, reported in (Xie et al., 2012).

The relationship between $S_{(275-295)}$ and salinity (Fig. 8b) for BSI was notably different from the others, with lower spectral slope values for a given salinity. We see a similar trend

with salinity for S_R (Fig. 8b, inset). Overall, the spectral indices (Fig. 7b, Fig. 8b) indicate that CDOM in the BSI tends to have a flatter spectral slope compared to CDOM from the Lower St. Lawrence Estuary.

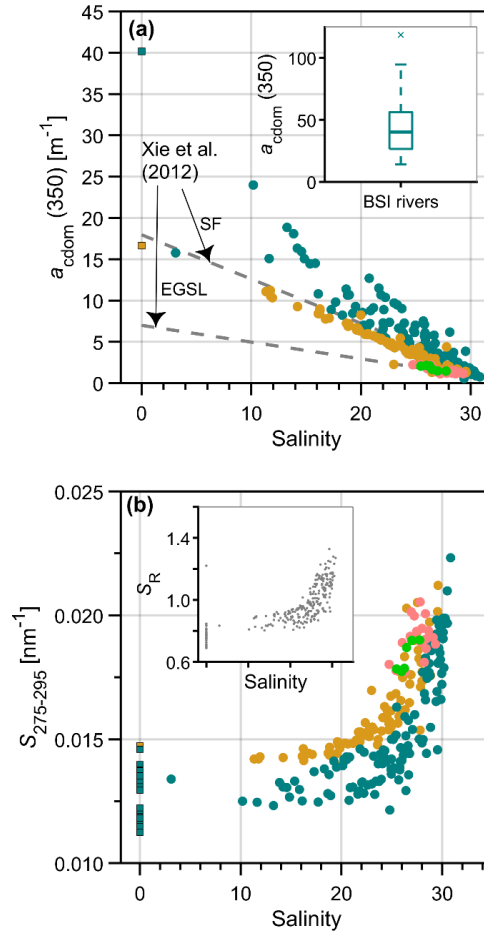


Figure 8. Optical properties of the chromophoric dissolved organic matter (CDOM) and their relationships with salinity. **(a)** CDOM absorption coefficient at 350 nm ($a_{\text{cdom}}(350)$) vs salinity. The median value of the river endmembers (salinity = 0) is shown for the Bay of Sept-Îles (BSI) and Manicouagan peninsula (MAN) subregions. The reference lines of Xie et al. (2012) are for the Estuary and Gulf of St. Lawrence (EGSL) and for the Saguenay Fjord (SF). The inset shows the variability of $a_{\text{cdom}}(350)$ for the riverine endmembers in the BSI subregion. **(b)** Relationship between $S_{275-295}$ and salinity. The inset illustrates the same relationship but for the CDOM spectral slope ratio (S_R) with the same salinity range. The relevant fitting equations, coefficients, and performance metrics for (a) and (b), while considering the two most numerous datasets (BSI and MAN) separately, are provided in Table 11 (Annex 1). The color code is the same as in Fig. 6

1.5.2 Optical properties of particulate matter: phytoplankton and non-algal particles

Relationships between optical properties of particulate matter and dry-mass concentrations at selected wavelengths are shown in Figure 9. The relationship between the red peak of the absorption coefficient of phytoplankton, $a_{\text{phy}}(676)$, and Chla (Fig. 9a) had moderate to high R^2 among all samples in general (Table 3). In contrast to BSI and MAN, stronger R^2 (and lower errors) were found for the PMZA-RIKI and FV subregions. The $a_{\text{phy}}(676)$ varied from as low as 0.0065 m^{-1} , from a subsurface sample collected offshore in the BSI subregion, to 0.3394 m^{-1} in PMZA-RIKI.

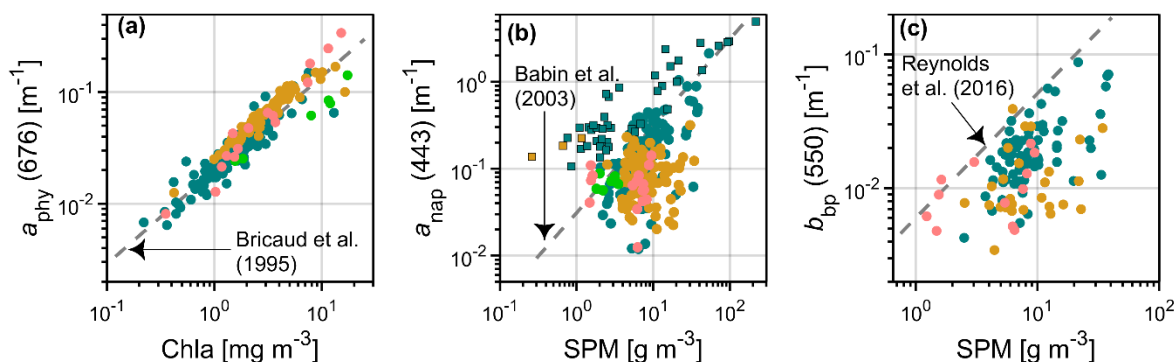


Figure 9. General relationships of the optical properties of particulate matter and dry mass concentrations of chlorophyll-*a* (Chla) and suspended particulate matter (SPM). (a) Phytoplankton absorption coefficient at 676 nm ($a_{\text{phy}}(676)$) vs Chla; (b) absorption coefficient of non-algal particles at 443 nm ($a_{\text{nap}}(443)$) vs SPM; and (c) the particulate backscattering coefficient at 550 nm ($b_{\text{bp}}(550)$) vs SPM. The reference lines showed in (a), (b), and (c) are from the studies of Bricaud et al. (1995), Babin et al. (2003), and Reynolds et al. (2016), respectively. The color code is the same as in Fig. 6

The $a_{\text{nap}}(443)$ and SPM relationship (Fig. 9b) showed a relatively high dispersion among the marine samples, especially those of the MAN subregion, where the standard deviation for $a_{\text{nap}}(443)$ was high ($\sigma = \pm 0.0546 \text{ m}^{-1}$). However, this relationship is comparable (same order of variability) with those obtained by Babin et al. (2003) for coastal

waters around Europe. Considering only marine samples, $a_{\text{nap}}(443)$ varied from around 0.0119 m^{-1} to 2.1223 m^{-1} (the high value was from a shallow [1.1 m] sample in the BSI subregion). We can also observe a strong relationship between $a_{\text{nap}}(443)$ and SPM for the river samples ($R^2 = 0.88$, Table 3), with $a_{\text{nap}}(443)$ lying well above the marine samples, suggesting more absorbing particles per unit SPM in the freshwater realm.

The relationship between $b_{\text{bp}}(550)$ and SPM is depicted in Figure 9c. As for $a_{\text{nap}}(443)$, $b_{\text{bp}}(550)$ versus SPM also showed relatively high dispersion, but the power-law fitting revealed a very low R^2 (Table 3) with higher errors than other regressions ($MAPE = 50\%$). Considering the whole dataset ($n = 120$), the mean $b_{\text{bp}}(550)$ value was 0.0178 with a standard deviation of 0.0140 m^{-1} . It is important to note that the reference line of Reynolds et al. (2016) in Figure 8c corresponds to their so-called “organic-dominant particles.”

To obtain more insights on the nature of particle assemblages in our study area, more relationships between particulate matter optical properties were explored and compared to those reported in the literature (Fig. 10). First, the spectral slope of non-algal particles (S_{nap} ; Fig. 10a) showed a normal distribution. The BSI subregion showed relatively lower values than other subregions ($0.0076 \pm 0.0008 \text{ nm}^{-1}$), reflecting the distinct particle assemblages among the nearshore EGSL zones, but similarities with river endmembers (not shown). The highest values of S_{nap} were found for the MAN subregion ($0.0090 \pm 0.0007 \text{ nm}^{-1}$).

The absorption characteristics of particulate matter were investigated following Konovalov et al. (2014), considering the different contributions of mineral (PIM) and organic (POM) particles to the absorption coefficients. We found a strong relationship ($R^2 = 0.91$; Table 3) between a_{p} in the near infrared region, $a_{\text{p}}(\text{NIR})$ (mean a_{p} between 745 and 755 nm), and PIM for the river samples (squares on Fig. 10b). Figure 10b also shows the occurrence of marine particles in the BSI subregion that tend to absorb more in the NIR region for a given concentration of PIM, while the relationship’s dispersion is lower than for the MAN subregion. As in Konovalov et al. (2014), we plotted POM versus $a_{\text{p}}(440) - a_{\text{p}}(\text{NIR})$, assuming that the subtraction of $a_{\text{nap}}(\text{NIR})$ from total particulate absorption in the

blue (440 nm) would yield a good approximation of the POM-related absorption. Again, we found a strong relationship when considering the river samples (Table 3, Fig. 10c). In contrast, the relationship for the marine environment was comparatively more dispersed, but still significant.

The relationship between $b_{bp}(550)$ and POM had a scattered distribution (Fig. 10d), but of the same order as the curve of Reynolds et al. (2016) for their organic-dominant particles subset (as previously mentioned for the $b_{bp}(550)$ vs SPM relationship). One may note that our proxy for organic matter (POM), as obtained by the LOI method, can be considered inaccurate compared with traditional CHN analyzers used to measure POC directly from filters (as for the studies of Konovalov et al., 2014, and Reynolds et al., 2016). However, simply dividing our POM by a factor of 2 (as suggested by Konovalov et al., 2014), gave us a useful indicator to compare with studies that report POC. Therefore, the POM used in this study was a useful proxy showing the interplay among organic and inorganic fractions of the particulate matter.

The spectral dependency of b_{bp} , as expressed by the fitted parameters γ and $b_{bp}(550)$, is presented in Figure 10e. We found no significant differences between subregions in γ , which had a global mean of $-0.46 (\pm 0.30)$. The lowest value of γ (-1.44) was from a BSI subregion station located far offshore, while the highest value (0.66) the station closest to the mouth of the Moisie River, under the plume influence (also for BSI subregion). A weak relationship was also found between γ and $b_{bp}(550)$ (not shown), suggesting that b_{bp} spectra become flatter as water turbidity increases.

Finally, the $b_{bp}^*(555)$ vs $a_{nap}^*(555)$ showed a strong relationship (Fig. 10f), with a moderate R^2 and relatively low errors (Table 3). One may note that the calculation of these two parameters uses three variables that were obtained using different methods: $b_{bp}(\lambda)$, $a_{nap}(\lambda)$, and SPM.

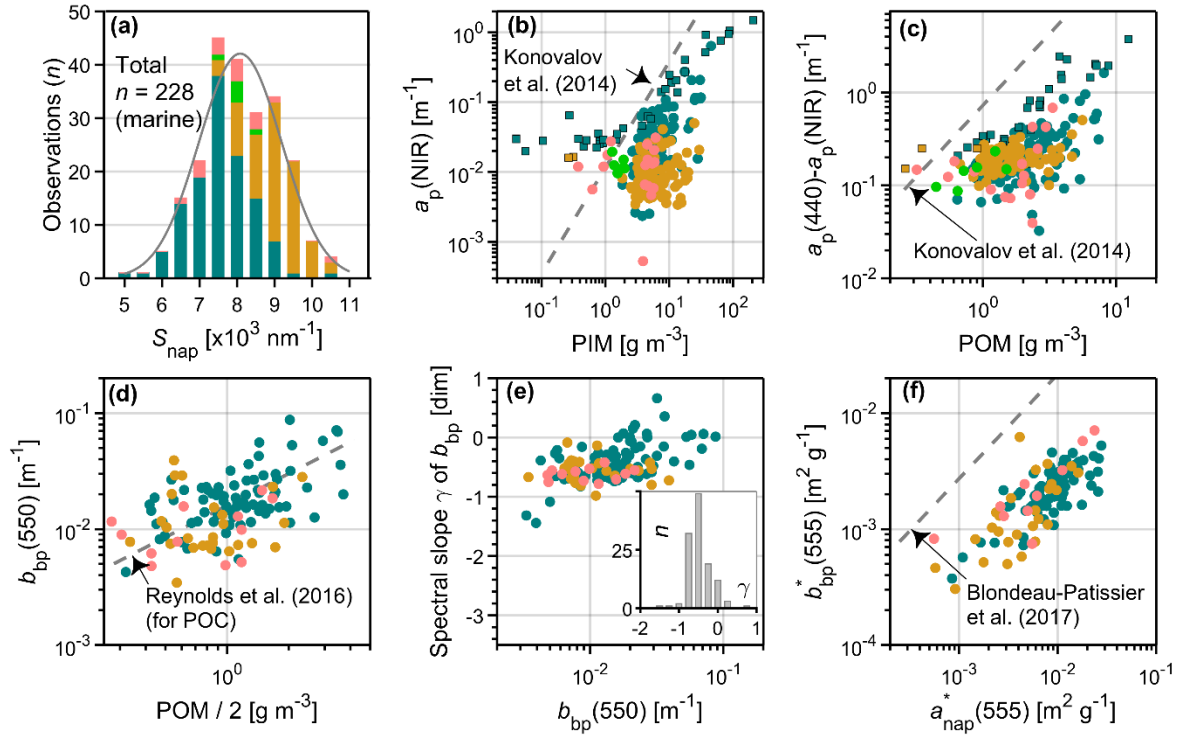


Figure 10. Characteristics and relationships of the optical properties of particulate matter and dry mass concentrations of particulate organic matter (POM) and particulate inorganic matter (PIM). The relevant fitting coefficients (power model) and performance metrics for (b), (c), (d), and (f) are provided in Table 3 (a) Frequency distribution of the non-algal particles spectral slope (S_{nap}). The Gaussian curve displayed illustrates the normal distribution among the marine samples. (b) Particulate absorption (a_p) in the near-infrared region (mean of a_p between 745 and 755 nm), $a_p(\text{NIR})$ vs PIM. (c) The result of the subtraction of $a_p(\text{NIR})$ from the particulate absorption coefficient at 440 nm ($a_p(440)$) vs POM. The reference lines of (b) and (c) are from the study of Konovalov et al. (2014). (d) Relationship between the particulate backscattering at 550 nm ($b_{\text{bp}}(550)$) and POM divided by 2. The reference line is from the study of Reynolds et al. (2016). It is worth mentioning that the reference curves on (c) and (d) are originally provided in terms of particulate organic carbon concentration (POC), and here we made the rough estimation $\text{POM} = \text{POC} \times 2$. (e) Spectral slope of b_{bp} , γ , vs $b_{\text{bp}}(550)$ The inset shows the frequency distribution of γ . (f) Relationship between the SPM-specific $b_{\text{bp}}(555)$ and $a_{\text{nap}}(555)$, i.e., $b_{\text{bp}}^*(555)$ and $a_{\text{nap}}^*(555)$. The reference line is from the study of Blondeau-Patissier et al. (2017). The color code is the same as in Fig. 6

1.5.3 Absorption budget

The relative contribution of the three (non-water) components of the absorption coefficient (CDOM, non-algal particles, and phytoplankton) are presented by ternary diagrams for selected wavelengths in the blue, green, and red regions (443, 550, and 676 nm; Fig. 11a-c, respectively). As expected, a_{cdom} dominates the absorption budget in the shorter wavelengths, but it is also important in longer wavelengths. For example, at 443 nm, 89% of the observations had more than 70% of the absorption budget related to a_{cdom} ; at 550 nm, 89% of the observations of a_{cdom} contributed to more than half of the absorption budget. The a_{cdom} is not negligible even at 676 nm: these accounted for 14% of the observations, contributing more than 40% of the total absorption.

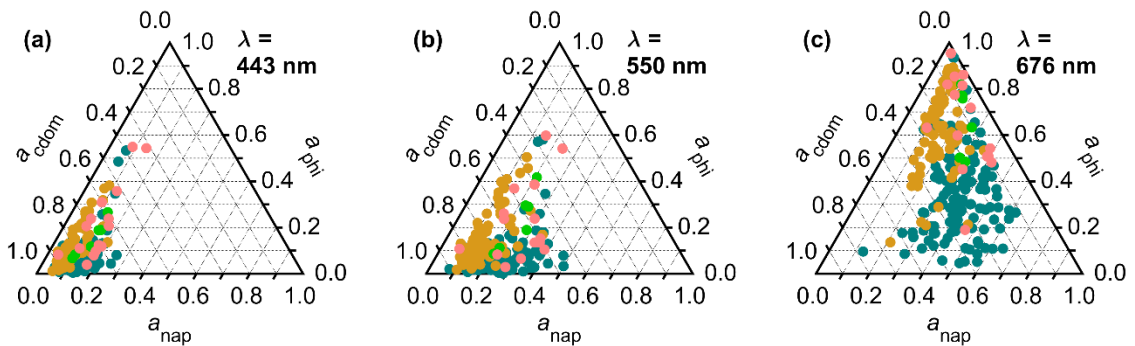


Figure 11. Ternary plots illustrating the relative contribution of CDOM (a_{cdom}), non-algal particles (a_{nap}) and phytoplankton (a_{phy}) to total absorption coefficient (minus the contribution of water) for wavelengths (a) 443, (b) 550, and (c) 676 nm. The relative proportions were normalized from 0 to 1, in such way that $a_{\text{cdom}} + a_{\text{nap}} + a_{\text{phy}} = 1$. The readings for the three components, and for each sample, should consider its corresponding axis and tick orientation (and corresponding grid). The color code is the same as in Fig. 6

Some samples had relatively low contributions of a_{cdom} , even at 443 nm ($< 50\%$; Fig. 11a), notably that were collected in the middle of the estuary in summer (PMZA-RIKI subregion) and those collected in April 2017 in BSI subregion, just before the freshet. In the red portion of the visible spectrum (676 nm), some samples maintained a very high

contribution of a_{cdom} to the absorption budget (>50%; Fig. 11c), with the majority from shallow waters influenced by river plumes that were sampled during early June (2017 and 2019) campaigns in the BSI subregion. Other than CDOM, it is also important to note that BSI samples had a distinct behavior in relation to particulate matter contributions when compared to other subregions. In longer wavelengths, the non-algal particle contribution was larger in the BSI, while the phytoplankton contribution to total particulate matter was greater in all other subregions (Fig. 11b, 11c).

1.5.4 Spatial (subregion) and seasonal variability

The seasonal variability and the variability within each subregion domain is presented for selected variables in Figure 12. A seasonal DOC modulation can be observed for the BSI subregion (Fig. 12a): samples collected in early June 2017 ($\mu \pm \sigma = 307 \pm 110 \mu\text{M}$) and 2019 ($324 \pm 161 \mu\text{M}$) were significantly higher than most samples collected at other times of the year. Chla (Fig. 12b) showed no significant seasonal variability, although relatively higher values were observed in both April and early May 2017. SPM values from the June 2019 field campaign in the BSI subregion had the highest values ($15.7 \pm 12.1 \text{ mg m}^{-3}$), and these were significantly higher than some of the other campaigns (notably from the September to October period) (Fig. 12c).

The seasonal and subregional variabilities of $a_{\text{cdom}}(350)$ are shown in Figure 12d. A marked seasonal pattern can be seen for the BSI subregion in 2017, as revealed by the median and the interquartile intervals. In BSI, CDOM increased from April to early June, followed by a decrease until July (but see also August 2016), a slight increase in September, and a decline in October. Although the sampling strategy can spatially bias this type of analysis, we consider our results to be representative of the variability found in the BSI area because the same stations were revisited, revealing distinct oceanographic characteristics in each field campaign. The range (minimum and maximum values) spans approximately one order of magnitude during some campaigns, such as those conducted during June 2019, in the BSI

subregion as well as the August 2019 field campaign in the MAN subregion. In contrast, despite the seasonal coverage of the PMZA-RIKI subregion (June to November 2015), the values of $a_{\text{cdom}}(350)$ remained low compared to the nearshore waters along the EGSL's north shore, with values ranging from 1.13 to 2.22 m^{-1} only.

The relative contribution of phytoplankton to total particulate absorption ($a_{\text{phy}}(443):a_{\text{p}}(443)$) is presented in Figure 12e. All groups were significantly different from each other ($p < 0.05$). Unlike other subregions, all field campaigns in the BSI subregion (except that of mid-April 2017) presented mean values lower than 0.5 (50%). A seasonal modulation in the BSI subregion was also observed, with the highest contribution of $a_{\text{phy}}(443):a_{\text{p}}(443)$ observed in mid-April 2017 (88%), and the lowest values ($\mu < 20\%$) found in June 2019.

Significant differences ($p < 0.05$) were found for seasonal and subregional values of $b_{\text{bp}}(550)$ (Fig. 12f), notably the higher values measured during the June 2019 field campaign (BSI subregion).

The mean and standard deviation of the bio-optical indices describing some properties of the $a_{\text{phy}}(\lambda)$ and phytoplankton pigment ratios are presented in Table 4, in which each subregion and field campaign were considered separately. Overall, it is possible to infer that the BSI subregion had a markedly seasonal pattern of phytoplankton assemblages, as revealed either by proxies related more to size distribution ($a_{\text{phy}}^*(676)$; the $a_{\text{phy}}^*(443):a_{\text{phy}}^*(676)$ ratio; and the S_f parameter) or by the photoacclimation state (the TAP:Chla and PPC:PSC indices).

The FV subregion was significantly different from others in relation to $a_{\text{phy}}^*(676)$ and the blue-to-red ratio ($a_{\text{phy}}^*(443):a_{\text{phy}}^*(676)$). The mean values of S_f were always below 0.4, with the minimum values observed in the FV subregion, followed by the samples collected in April and mid-September 2017 in the BSI subregion.

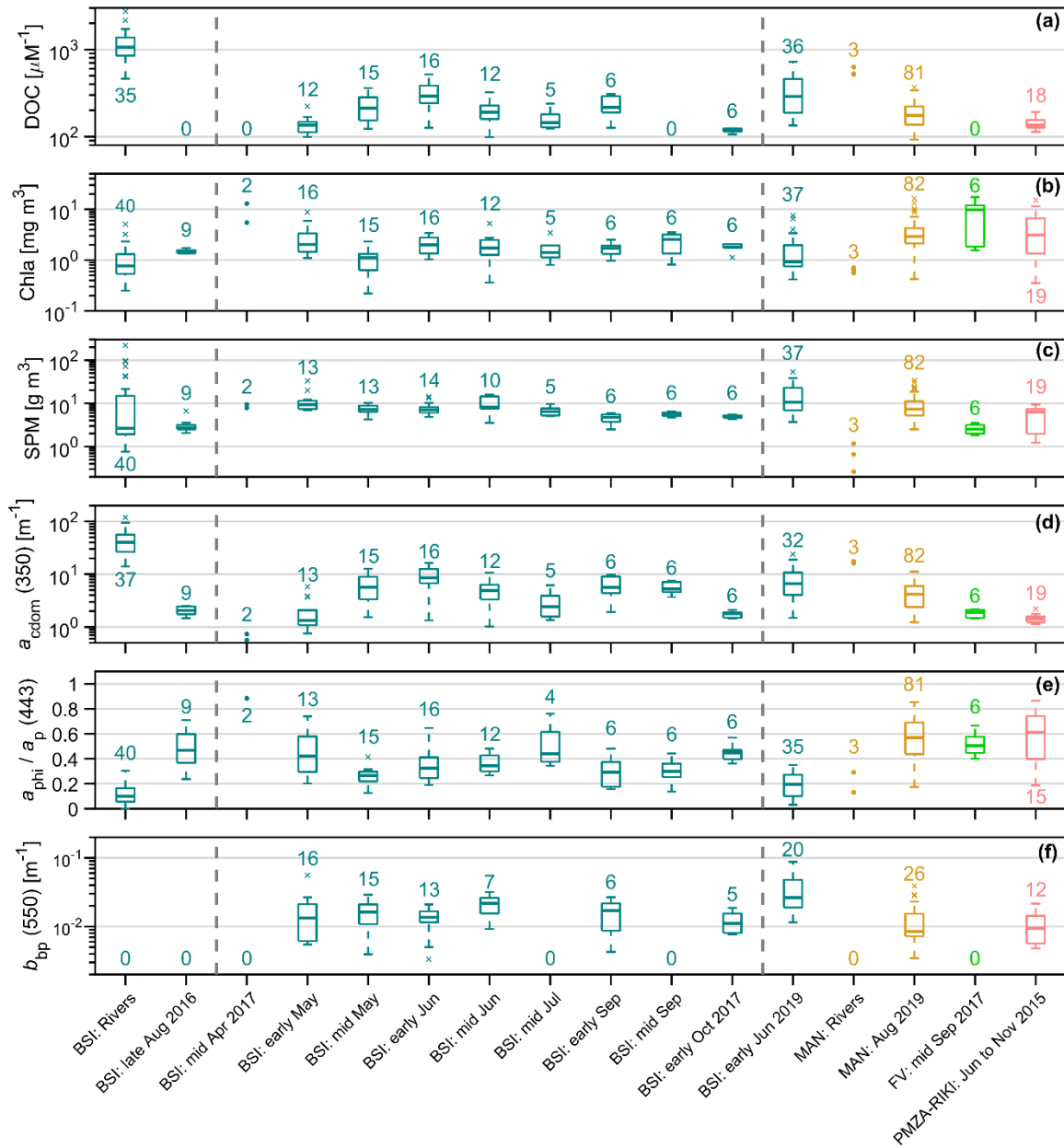


Figure 12. Variability (median, 25th and 75th percentiles, minimum, maximum and outliers) of (a) DOC, (b) Chla, (c) SPM, (d) $a_{\text{cdom}}(350)$, (e) $\frac{a_{\text{phy}}(443)}{a_{\text{p}}(443)}$, and (f) $b_{\text{bp}}(550)$.

Data are shown as a function of different sampling strategies: type (marine or river), location (BSI, MAN, FV, PMZA-RIKI) and different legs of these same campaign (BSI only). The number of observations (n) is provided for each sampling strategy, and the vertical grey dashed lines delimit the 2017 seasonal period for BSI. No boxplots are shown when $n < 5$. The color code is the same as in Fig. 6

Table 4

Mean (μ) and standard deviation (σ) for chlorophyll concentration (Chla), the chlorophyll-specific phytoplankton absorption at 676 nm ($a_{\text{phi}}^*(676)$), the $a_{\text{phi}}^*(443) : a_{\text{phi}}^*(676)$ ratio, the size parameter from the phytoplankton absorption coefficient (S_f), and the ratios of total accessory pigments (TAP) to Chla, and the photoprotective to photosynthetic carotenoids (PPC:PSC). Rows represent each field campaign (or a single location, as for the PMZA-RIKI subregion)

Spatial / temporal partition	Chla [mg m ⁻³]		$a_{\text{phy}}^*(676)$ [10 ² m ² mg ⁻¹]		$a_{\text{phy}}^*(443) : a_{\text{phy}}^*(676)$ [dim.]		S_f [dim.]		TAP: Chla [w w ⁻¹]		PPC:PSC [w w ⁻¹]	
	μ	σ	μ	σ	μ	σ	μ	σ	μ	σ	μ	σ
BSI: late Aug 2016	1.47	0.13	2.22	0.26	1.96	0.12	0.31	0.03	—	—	—	—
mid Apr	9.19	5.28	1.29	1.11	1.57	0.02	0.17	0.01	0.81	0.02	0.19	0.03
early May	2.89	2.15	1.73	0.21	1.87	0.16	0.27	0.04	0.78	0.04	0.24	0.09
mid May	1.08	0.58	1.94	0.46	3.08	1.13	0.30	0.05	0.69	0.12	0.26	0.15
BSI 2017: early Jun	2.02	0.79	1.89	0.36	2.49	0.45	0.35	0.02	0.94	0.09	0.38	0.10
mid Jun	1.95	1.28	1.99	0.38	2.21	0.41	0.31	0.06	0.92	0.07	0.34	0.10
mid Jul	1.67	1.03	1.91	0.10	2.09	0.42	0.38	0.11	1.04	0.13	0.32	0.08
early Sep	1.69	0.54	1.53	0.26	1.92	0.17	0.25	0.04	0.89	0.04	0.42	0.07
mid Sep	2.32	1.08	1.66	0.53	1.55	0.15	0.17	0.02	—	—	—	—
early Oct	1.76	0.34	1.75	0.13	2.04	0.30	0.30	0.02	0.91	0.04	0.24	0.03

Table 4 (cont.)

Spatial / temporal partition	Chla [mg m ⁻³]		$a_{\text{phy}}^*(676)$ [10 ² m ² mg ⁻¹]		$a_{\text{phy}}^*(443):$ $a_{\text{phy}}^*(676)$ [dim.]		S_f [dim.]		TAP: Chla [w w ⁻¹]		PPC:PSC [w w ⁻¹]	
	μ	σ	μ	σ	μ	σ	μ	σ	μ	σ	μ	σ
BSI: early Jun 2019	1.63	1.57	2.10	0.66	2.27	1.85	0.25	0.08	0.68	0.11	0.28	0.14
MAN: Aug 2019	3.63	2.54	2.15	0.35	1.65	0.20	0.19	0.06	0.92	0.10	0.23	0.17
FV: mid Sep 2017	8.68	6.18	0.99	0.38	1.33	0.32	0.06	0.09	—	—	—	—
PMZA-RIKI: Jun to Nov 2015	4.27	4.09	1.99	0.41	1.73	0.28	0.27	0.10	0.82	0.09	0.21	0.07

Bold values indicate groups that were significantly different from at least three or more other groups, as revealed by the Tukey honest significant criterion, that followed the one-way analysis-of-variance (ANOVA).

1.5.5 Tidal and meteorological effects

The short-term temporal variability of selected inherent optical properties ($a_{\text{cdom}}(350)$ and $b_{\text{bp}}(550)$) was investigated at a single station (PT-01; Fig. 5) of the BSI subregion, which was sampled eight times over the course of five days in June 2019 (Fig. 13a, 13b). This station was in the middle of the bay. Interestingly, the northerly and easterly winds changed direction to southerly on 2 June, and increased in velocity, reaching (and remaining) over 10 m s^{-1} on 3 June (Fig. 13a). Concurrently, the air temperature dropped to $\sim 6^\circ\text{C}$ (from an air mass coming from the EGSL), and a substantial amount of precipitation ($> 20 \text{ mm}$) fell between 2 and 3 June.

The impact of this meteorological event on the optical properties can be clearly noticed, with much higher values of both $a_{\text{cdom}}(350)$ ($\sim 19 \text{ m}^{-1}$) and $b_{\text{bp}}(550)$ ($\sim 0.09 \text{ m}^{-1}$) being observed on 4 June compared to earlier samples (Fig. 13b). We noted strong changes in these variables even during a single day, reflecting changes in the hydrodynamical regime due to tidal oscillations.

Figure 13c illustrates the effect of vertical thermohaline stratification in a relatively deep station (OUT-R05; Fig. 5) of the MAN subregion. A strong vertical thermal and saline gradient was observable, which is typical in nearshore zones of the EGSL. At this station, we collected water samples at the surface ($\sim 0.5 \text{ m}$) and at 5 m (approximately the base of the pycnocline). The temperature and salinity differences of these two samples were $\sim 6.5^\circ\text{C}$ and 7, respectively. The surface value of $a_{\text{cdom}}(350)$ was four times higher at the surface, while the $b_{\text{bp}}(550)$ was two times higher. These changes in water column IOPs resulted in visually different water colors (Fig. 13d).

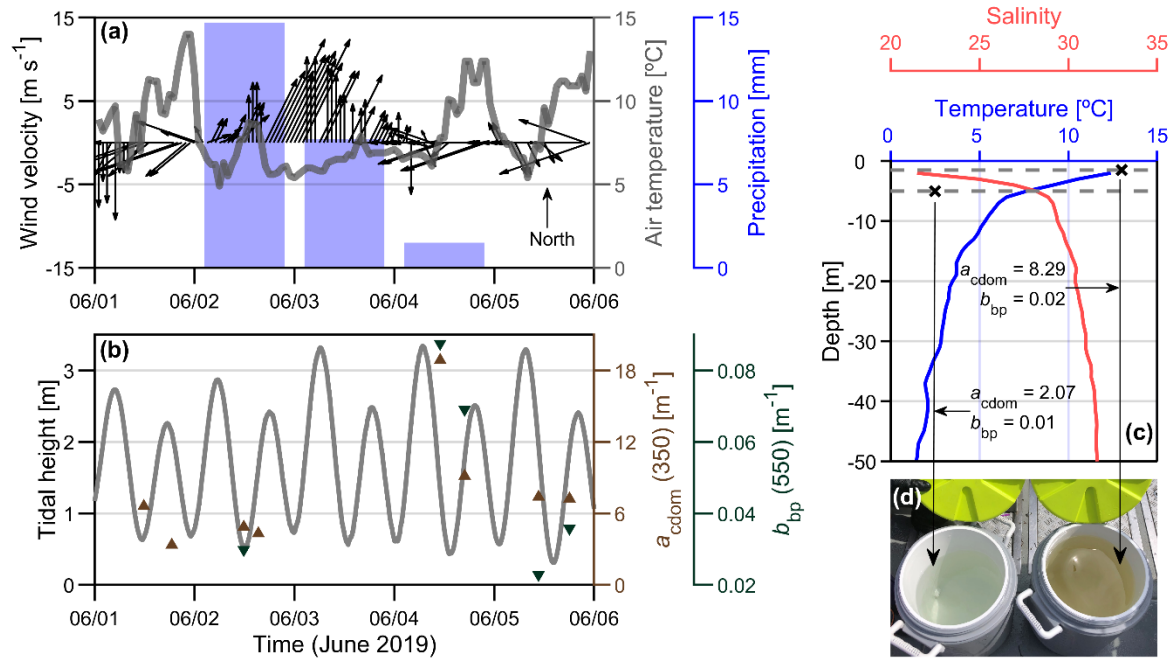


Figure 13. Meteorological (synoptic) and hydrodynamic forcing and variability in inherent optical properties of nearshore zones of the Estuary and Gulf of St. Lawrence. **(a)** Wind velocity and direction, air temperature, and precipitation. **(b)** Semi-diurnal tidal variability, chromophoric dissolved organic matter absorption coefficient at 350 nm, and particulate backscattering coefficient at 550 nm, for the same period. **(c)** Vertical stratification of the water column as shown by temperature and salinity profiles, with a photo **(d)** depicting water samples collected at different depths

1.6 DISCUSSION

The variabilities of absorption and backscattering coefficients (both magnitudes and spectral shapes) were systematically examined in nearshore waters of the Estuary and Gulf of St. Lawrence (EGSL). Although the sampling strategy was far from exhaustive in respect to covering all spatial and temporal variability, we consider the dataset used in this study to be representative of the optical variability of nearshore EGSL waters, especially those influenced by rivers draining boreal watersheds, which is the case for most of the north shore, from Tadoussac to Natashquan and beyond.

We first discuss the general bio-optical relationships and compare them to existing literature worldwide, considering the dissolved organic matter, the particulate matter pool, and the absorption budget separately. Next, we examine the seasonal and intra-regional variabilities of optically significant constituents between nearshore zones and central parts of the EGSL, focusing on differences of molar and dry-mass concentrations. The seasonal variabilities in phytoplankton-related bio-optical properties are also discussed. Finally, we consider the implications of short-term meteorological and oceanographic processes on optical variability.

The tangled dynamics of DOC, SPM, and Chla, evidenced by the scattered relationships between these variables (Fig. 6), illustrate the optical complexity of the underwater light field in the nearshore zones of the EGSL. This clearly demonstrates the need to improve our understanding of the relationships between IOPs and optically significant constituents for remote sensing applications in the nearshore zones. Overall, these results confirm the Case-2 nature (*sensu* Morel and Prieur, 1977) of the water masses encountered in our study areas.

1.6.1 Bio-optical variability

1.6.1.1 Dissolved organic matter

As expected, we found a strong relationship between $a_{\text{cdom}}(\lambda)$ and DOC, which followed a (quasi-) continuum from the fresh-to-marine environment (Fig. 7a, 7c). However, we observed consistently higher values of $a_{\text{cdom}}(350)$ per unit of DOC compared to the global relationship reported by Massicotte et al. (2017), which revealed higher $a_{\text{cdom}}^*(350)$ values in the boreal riverine endmembers of our study area. This was also confirmed by the relatively higher values found for the DOC-specific UV absorbance at 254 nm (SUVA_{254} , $\text{m}^2 \text{gC}^{-1}$) for rivers (4.86 ± 0.51) when compared to samples from freshwater ecosystems at approximately the same distance from the shoreline (also reported by Massicotte et al., 2017).

Briefly, $SUVA_{254}$ is a metric used as a proxy for assessing both chemical and biological reactivity of the DOM pool (Asmala et al., 2013; Massicotte et al., 2017; Weishaar et al., 2003) and may be related to the proximity of its sources. It is also important to note the lower absorption per unit of DOC of the samples collected in the middle of the lower estuary, at the PMZA-RIKI subregion (pink circles in Fig. 7a). This indicates that the endmember source of DOM in the central part of the estuary differs markedly from nearshore zones in MAN and BSI, or even that DOM is more degraded in water samples taken more offshore in the EGSL.

The relationship between $a_{\text{cdom}}^*(350)$ and $S_{275-295}$ also reinforces the dominance of terrigenous DOC in the DOM pool for our river-dominated coastal regions, as reported by Fichot and Benner (2012). One may note that the lower values of $S_{275-295}$ reported here (from 0.011 to 0.022 nm^{-1}), in comparison to those of Fichot and Benner (2012) in the northern Gulf of Mexico (their Fig. 7b; approximately 0.013 – 0.045 nm^{-1}), suggest that the DOM pool exported to the nearshore zones of the EGSL was subject to less photobleaching and was composed of a large fraction of terrigenous DOM, especially those samples coming from the small rivers that flow into the bay of the BSI subregion. This influence overcomes the potential interference of high phytoplankton productivity on the DOM pool (Danhie et al., 2017), even for subregions with relatively higher values of Chla (e.g., MAN). Nevertheless, some marine samples had higher values of $S_{275-295}$ compared to their local riverine endmembers, which suggests that DOM with higher molecular weights are found just after riverine waters enter the sea; this idea is supported by the studies of Fichot and Benner (2012) and Xie et al. (2012), in which slopes correlated negatively with DOM molecular weight. However, flocculation - a process known to occur in this interface - is expected to reduce the mean molecular weight of the DOM pool (Asmala et al., 2014).

We also found small regional differences in the relationship between $a_{\text{cdom}}^*(350)$ and $S_{275-295}$ (Fig. 7b); this is consistent with the findings of Fichot and Benner (2011), who compared Gulf of Mexico and Beaufort Sea samples. Despite this small regional difference, we reparametrized the model of Fichot and Benner (2011) for all subregions of the EGSL by dividing the dataset into two groups based on a threshold of $a_{\text{cdom}}(275)$ (i.e., 15 m^{-1}). The

very good performance of the model (Fig. 7c; Table 11, Annex 1) suggests that $a_{\text{cdom}}(\lambda)$, which is obtained by a relatively simpler and less expensive analysis than analytical DOC procedures, could be routinely used for an approximation of DOC. In addition to the lower range of $a_{\text{cdom}}(\lambda)$ in central parts of the EGSL (e.g., the PMZA-RIKI subregion), the same equations could also be applied to some extent these areas, since both $a_{\text{cdom}}(\lambda)$ and DOC are within the range of previously reported values (Barber et al., 2017; Çizmeli, 2008; Nieke et al., 1997; Tremblay and Gagné, 2009; Xie et al., 2012).

Our average of $S_{350-500}$ agrees with other values reported from around the world, although in the lower part of the range reported for coastal regions, for example, around Europe (Babin et al., 2003), the northwestern Mediterranean Sea (Para et al., 2010), and a subtropical estuary in Brazil (Noernberg et al., 2020). However, in the EGSL and especially in nearshore zones, the strong influence of riverine water discharge makes $S_{275-295}$ a more reliable descriptor of the DOM pool. The low CDOM spectral slopes reported here for both spectral ranges of the EGSL indicate that surface-water CDOM is dominated by large aromatic DOM from a terrestrial origin, which is consistent with chemical proxies reported in the literature (Barber et al., 2017; Tremblay and Gagné, 2009).

Relationships of $S_{275-295}$ values to salinity levels also differed between subregions. These results suggest that the terrestrial DOM pool inputs in MAN have lower molecular weights and may have been exposed to greater photobleaching compared to those in BSI. This interpretation is supported by other studies (Fichot and Benner, 2012; Helms et al., 2008), including that of Xie et al. (2012) in the EGSL. One possible explanation for these differences is the presence of dams on the rivers sampled in the MAN subregion, which increases the length of time DOM spends in the watershed and, consequently, increases its exposure to photobleaching and/or biodegradation processes. Indeed, the impact of dams on sedimentation processes was observed in cores in a region of the EGSL near BSI (Boyer-Villemare et al., 2013), and one would expect some effects to also occur in the pelagic system. Moreover, the presence of dams on major rivers of the EGSL's north shore was found

to alter natural cycling of the CDOM pool compared to CDOM conditions in undammed rivers (Jaegler, 2014).

It is important to note that the dissimilarities observed in the rivers sampled in this study may also be linked to individual watershed characteristics. For example, the four minor rivers in the BSI subregion (that flow into the bay) have consistently higher $a_{\text{cdom}}(\lambda)$ and lower $S_{275-295}$ values than the nearby Moisie River, one of the major rivers on the north shore. Those smaller watersheds are in lower areas of the north shore and may have relatively larger proportions of wetlands, a known source of DOM in the terrestrial environment (e.g., Mattsson et al., 2005), compared with the Moisie watershed, which drains higher areas.

As reported by previous studies on central regions of the EGSL (Nieke et al., 1997; Xie et al., 2012), we observed a conservative mixing behavior of the DOM pool (Fig. 8a; Table 10, Annex 1), but some caveats should be considered. Major regional differences were found, particularly in the nearshore BSI and MAN subregions, with a tighter relationship between $a_{\text{cdom}}(\lambda)$ and salinity in the latter. The higher variability found in this relationship for BSI is explained both by the more diverse sampling strategy (seasonal variability) and differences among the rivers' endmember values (salinity equal to 0), as shown by the inset of Figure 8a. In such conditions, the conservative mixing behavior should consider multiple endmembers, as for example in Stedmon et al. (2010).

The conservative mixing behavior of CDOM may be of particular interest for hydrodynamical and coupled ecological studies (Le Fouest et al., 2018; Stedmon et al., 2010). More importantly, these results indicate that satellite-derived $a_{\text{cdom}}(\lambda)$ may be used as a proxy for salinity to trace river runoff in nearshore environments, but local relationships must be determined even within the EGSL realms. Moreover, although we have found that conservative mixing of CDOM in the nearshore zones is a dominant process, it is important to emphasize that other processes that known to alter the DOM pool in such dynamic areas, such as flocculation (Asmala et al., 2014) and autochthonous phytoplankton production (Danheiz et al., 2017), may also have significantly impacts.

1.6.1.2 Suspended particulate matter

Suspended particulate matter was found to have a complex and heterogenous nature in nearshore waters along the north shore of the EGSL., as revealed by its dry-mass concentration (SPM and the inorganic and organic fractions, PIM and POM) and optical proxies (IOPs, i.e., absorption and backscattering coefficients).

The more complex nature of marine particle assemblages is revealed by the strong relationships obtained between particulate absorption proxies ($a_p(\lambda)$ and $a_{\text{nap}}(\lambda)$) and mass concentrations in river samples (square symbols in Fig. 9b, 10b, 10c; Table 3) in contrast to the weak relationships observed in marine samples. For example, the relationship between $a_{\text{nap}}(443)$ and SPM in the marine samples was unlike those from other locations around the world (see, for example, Babin et al., 2003; Bowers and Binding, 2006), and even for previous relationships reported for central parts of the EGSL (Çizmeli, 2008).

We speculate that this behavior, which occur in the continuum between rivers and nearshore EGSL waters, may be due to any of four possible processes: flocculation, sorption of organic matter onto mineral particles, biological transformation of the organic matter pool, and the heterogeneous nature of sediment resuspended from the bottom. Flocculation has major implications in the organic matter pool, and this aggregation process is particularly common in these transition zones (Asmala et al., 2014; Lisitsyn, 1995). The process of sorption between (dissolved and particulate) organic and (particulate) inorganic matter has several geochemical implications, and it commonly occurs in estuarine systems (Hedges and Keil, 1999). Organic matter decomposition by heterotrophic bacteria was found to be very important along the St. Lawrence Estuary and Saguenay Fjord (Bourgoin and Tremblay, 2010). Finally, sediment resuspension events increase the number of particles in the water column, and they will be consequently less sorted in terms of size, shape, and density, compared to riverine inputs. This latter process will be discussed later in subsection 4.2.3.

These four processes can all significantly alter particle size distributions as well as organic and inorganic matter pools in rivers and nearshore zones of EGSL, which has implications on the relationships between IOPs and optically significant constituents.

The spectral slope of non-algal particles (S_{nap} ; Fig. 10a) had consistently lower values compared with different localities around the globe, for example coastal waters of Europe (Babin et al., 2003), Northern Australia (Blondeau-Patissier et al., 2017), and a subtropical estuary in Brazil (Noernberg et al., 2020). In some cases, the reported values are comparable with our dataset, e.g., the MAN subregion and the Irish Sea (Bowers and Binding, 2006). Methodological differences in both the $a_{\text{nap}}(\lambda)$ analyses (e.g., integrating sphere versus transmission-reflectance technique) and the fitting procedures (e.g., spectral ranges, baseline correction, etc.) may also yield differences when comparisons with the literature are done. More importantly, the S_{nap} values in the marine samples agreed well with those of the riverine samples, and significant regional differences between the BSI and MAN subregions were also observable. This result indicates that the nature of particulate matter differs within the nearshore waters of the EGSL.

Although a relatively lower contributions of the $a_{\text{p}}(\lambda)$ is expected in the near-infrared (NIR) compared to the visible, we found non-negligible values in our dataset; this has also been found in several studies (e.g., Bowers and Binding, 2006; Röttgers et al., 2014; Stramski et al., 2007; Tzortziou et al., 2006). Furthermore, we found $a_{\text{p}}(\text{NIR})$ to be very well correlated with PIM, especially for the river samples. This result indicates that $a_{\text{p}}(\text{NIR})$ can be a useful proxy for the concentration of suspended inorganic particles but may be limited to situations where mineral composition does vary much.

The $b_{\text{bp}}(\lambda)$ values reported here span about three orders of magnitude and cover typical values found both in oceanic and coastal zones (Antoine et al., 2011; Neukermans et al., 2012; Reynolds et al., 2016). However, our values are more concentrated around the mean, indicating relatively lower variability, compared with these other studies.

By partitioning Arctic marine samples into three classes, from mineral- to organic-dominated particles with an intermediate class, Reynolds et al. (2016) investigated the influence of particle composition on $b_{bp}(\lambda)$. Considering the $b_{bp}(550)$ – SPM relationship, these authors found a general decreasing trend of lowering values in the exponent values (equivalent of coefficient B from the equation in Table 3) from mineral- to organic-dominated samples. The fitted value found in our study (Table 3) was about three times lower than the one reported by (Reynolds et al., 2016) for the organic-dominated samples.

Reynolds et al. (2016) also reported that these organic-dominated samples had generally higher (closer to 0) values for the spectral slope (γ) of $b_{bp}(\lambda)$. In comparison, the γ values we found in this study were higher, sometimes even greater than 0 (Fig. 10e). Taking this into consideration, we suggest that the $b_{bp}(\lambda)$ reported in this study was more influenced by organic matter than those previously reported in the literature. This can be partially supported by the CDOM-laden waters characteristic of the nearshore zones of EGSL, as previously discussed.

The relatively strong relationship observed between $b_{bp}^*(\lambda)$ and $a_{nap}^*(\lambda)$ has already been reported for regions in Australia (Blondeau-Patissier et al., 2017; Blondeau-Patissier et al., 2009). Although these variables differ to a similar degree, our data revealed lower $b_{bp}^*(\lambda)$ values in relation to the same $a_{nap}^*(\lambda)$ compared with these earlier studies (Fig. 10f). Nevertheless, a decreasing trend of $b_{bp}^*(\lambda)$ from mineral- to organic-dominant particles was also observed by Reynolds et al. (2016) (see their Table 2). For instance, our global mean values of $b_{bp}^*(550)$ was $0.0022 \text{ m}^2\text{g}^{-1}$ ($\sigma = \pm 0.0013$), which is less than three times the mean value reported by Reynolds et al. (2016) in their organic-dominant samples. This result shows the strong influence of organic particles on the low backscattering efficiency of particulate matter encountered in the nearshore zones of the EGSL.

The relatively poor relationships between IOPs and SPM make it difficult to estimate SPM from remote sensing. Given the complexity of the optical properties of particles found in the EGSL, particularly the distributions of SPM and POM to SPM ratios for nearshore

zones, we argue that more complete studies involving particle size distribution (PSD), composition (refractive indexes), and size-fractionated samples would help to better understand the role of optically significant constituents in IOPs (as in Koestner et al., 2020; Neukermans et al., 2012; Reynolds et al., 2016, for scattering properties), and consequently in the $R_{rs}(\lambda)$ signals.

1.6.1.3 Visible light absorption budget

The nearshore EGSL zones were high in CDOM throughout our sampling campaigns, and this is echoed by the large contribution of CDOM to the absorption budget (Fig. 11). The CDOM levels that we measured exceed measurements made in other coastal regions around the world, using the same ternary plot comparisons (Babin et al., 2003; Blondeau-Patissier et al., 2017; Noernberg et al., 2020), even in some regions that were reported to be CDOM-dominated, e.g., the central-east Arctic ocean (Gonçalves-Araujo et al., 2018). Similar ternary distributions were reported by Cannizzaro et al. (2013), for river plumes in the northeastern Gulf of Mexico, a situation very similar to what we encounter in the nearshore EGSL waters.

The study of Xie et al. (2012) showed that CDOM at 440 nm dominates the absorption budget in the estuarine region of the EGSL, while the phytoplankton ($a_{\text{phy}}(440)$) was dominant in the gulf stations. This major differences in IOPs between the estuary and gulf regions was already reported for specific absorption components, like $a_{\text{cdom}}(\lambda)$ and $a_{\text{phy}}(\lambda)$ (Babin et al., 1995, 1993; Nieke et al., 1997; Roy et al., 2008). Moreover, this may be related to the different hydrographic and oceanographic processes occurring in these areas (Fuentes-Yaco et al., 1997a; Koutitonsky and Bugden, 1991; Therriault and Levasseur, 1985).

Besides the generally higher contribution of $a_{\text{phy}}(\lambda)$ to the absorption budget for the gulf region, higher phytoplankton productivity and standing stock is expected for the Lower St. Lawrence Estuary throughout the summer (Therriault and Levasseur, 1985). Although

$a_{\text{cdom}}(\lambda)$ dominates the absorption budget in all subregions, the differences we encountered in BSI were marked by a relatively lower phytoplankton contribution compared to non-algal particles (Fig. 11), and this may be explained by their proximity to the Gulf of St. Lawrence. Because the other subregions are more under the influence of the Lower St. Lawrence Estuary, their higher phytoplankton contribution could be sustained by major differences in the adjacent *marine* endmembers (here we use *marine* in the sense of more offshore waters of the estuary and gulf regions, compared to the nearshore transition zones).

1.6.2 Seasonal and short-term bio-optical variability

1.6.2.1 Nearshore zones versus central parts of the EGSL

Compared to previously reported values of DOC for the St. Lawrence system (e.g., Barber et al., 2017; Tremblay and Gagné, 2009), the nearshore EGSL zones had higher than central parts of the lower estuary or the gulf, magnitudes similar to those reported for the Upper St. Lawrence Estuary, and values lower of those reported for surface waters of the Saguenay River. In addition, the consistently higher DOC values in the sampled boreal rivers suggests that they are the main DOM sources in these nearshore zones. Nevertheless, the $a_{\text{cdom}}(\lambda)$ values of nearshore marine surface samples that we present were consistently higher than other values reported for the EGSL (Çizmeli, 2008; Nieke et al., 1997; Xie et al., 2012), even for regions of the EGSL known to have higher DOM, such as the lower estuary near the mouth of the Saguenay River.

The $a_{\text{cdom}}(\lambda)$ distribution in EGSL is controlled by the major rivers. This will have an impact on the seasonal cycle, with the spring freshet being the main process controlling $a_{\text{cdom}}(\lambda)$ in central parts (Çizmeli, 2008). This seasonal pattern of riverine discharge also seems to be the main process controlling $a_{\text{cdom}}(\lambda)$ in the nearshore zones of the EGSL, but with a greater influence of local rivers. This is observable particularly in the BSI subregion, where the median $a_{\text{cdom}}(\lambda)$ values, at the stations visited in 2017 (Fig. 12d) follow the

discharge patterns of the Moisie River and the minor rivers (data not shown). In this way, when local river discharges peak, the nearshore zones will be more greatly influenced by water masses with lower salinity and higher $a_{\text{cdom}}(\lambda)$ levels. On contrary, the PMZA-RIKI subregion had consistently higher salinities, and consequently lower $a_{\text{cdom}}(\lambda)$ levels compared to the nearshore zones, although the seasonal signal was also noticeable. This result implies that central parts of the EGSL are more stable in terms of CDOM variability. Another interesting result is the relatively low $a_{\text{cdom}}(\lambda)$ levels found in the BSI samples in April. This result suggests that terrestrial DOM inputs in these regions are comparatively very limited during winter and early spring.

Chla variability observed in the nearshore EGSL zones was in the expected range, considering values reported in central areas of the EGSL (Çizmeli, 2008; Laliberté et al., 2018). In the lower estuary region, phytoplankton productivity and biomass are high throughout the summer (June to September) due to continuous nutrient replenishment to the euphotic zone via the upwelling zone (upstream of the Lower St Lawrence Estuary), and the maintenance of a stable mixed layer (Therriault and Levasseur, 1986, 1985; Vézina et al., 1995). In addition to the freshwater runoff, the gulf region exhibits a complex hydrodynamical circulation, with eddies, upwellings, and fronts (Koutitonsky and Bugden, 1991; Le Fouest et al., 2005). These characteristics give phytoplankton productivity in the gulf a more heterogeneous character (Fuentes-Yaco et al., 1997b; Levasseur et al., 1992), being generally more oligotrophic than the lower estuary region (Laliberté et al., 2018; Le Fouest et al., 2005).

These regional differences may explain the higher mean Chla values observed in the PMZA-RIKI, MAN, and especially the FV subregions compared to the BSI subregion. The high Chla ($>10 \text{ mg m}^{-3}$) encountered in the FV subregion in September 2017 might have been due to local upwelling along the north shore of the lower estuary. Another interesting feature of the gulf is the subsurface chlorophyll maximum that is nearly always present in summer (Vandeveldt et al., 1987). This feature was only observed at those stations farthest from the shore in the BSI subregion, and only early May 2017 field campaign (not shown).

In terms of SPM variability, the average values of the nearshore EGSL zones were lower than those reported for the maximum turbidity zone (Upper St. Lawrence Estuary), which varied from ~ 10 to as high as 300 g m^{-3} (Lucotte and D'Anglejan, 1986). In contrast, observed SPM values in nearshore subregions were higher than those reported by Larouche and Boyer-Villemare (2010), which covered a wide area of the whole EGSL, during spring, summer, and fall. This can be explained by differences in the sampling strategy since the stations in our study were considerably shallower overall. Interestingly, similar or lower values of SPM were found in boreal rivers samples compared to marine samples, indicating other sources of suspended particulate matter in the nearshore water column. The relatively conservative mixing of DOC (or CDOM) along the salinity gradient, the moderate R^2 revealed from regressions between DOC and SPM in the river samples (Fig. 6b), and the absence of such a correlation in the marine samples also reinforce this interpretation.

The variability of the POM fraction for our study areas was within the range of previously reported values for the EGSL, but with a lower mean value compared to offshore zones ($\sim 39\%$, Çizmeli, 2008). However, the mean SPM values we measured in nearshore waters ($\sim 9 \text{ g m}^{-3}$) were up to one order of magnitude greater compared to the 2008 study. In summary, although a lower percentage of POM was observed, the absolute concentration of organic matter in these areas greatly exceeded the values one would expect in offshore parts of the EGSL.

An inverse phase in variability can be observed between $a_{\text{cdom}}(350)$ and $a_{\text{phy}}/a_{\text{p}}$ (443) for the BSI subregion during the April-Oct. 2017 sampling season (Fig. 12d, 8e). We also noticed a somewhat lagged response for $a_{\text{phy}}/a_{\text{p}}$ (443) during mid May and early June sampling. These results indicate that the relative contribution of phytoplankton to the total particulate absorption covaries with CDOM levels in this region, emphasizing the importance of freshwater runoff on phytoplankton at this spatial scale. Interestingly, the samples obtained in April 2017 in the middle of the bay showed low $a_{\text{cdom}}(350)$ and high Chla and $a_{\text{phy}}/a_{\text{p}}$ (443), indicating that the phytoplankton spring bloom probably occurred prior to the spring freshet which, in turn, severely reduced light availability in these nearshore

waters. Future studies aiming at documenting the phytoplankton spring bloom should probably begin as early as March.

1.6.2.2 Phytoplankton

Phytoplankton variability was assessed using both pigment assemblage and its spectral absorption spectra ($a_{\text{phi}}(\lambda)$). In the EGSL, both the effects of size (Tremblay et al., 1997, 2000) and pigments (Roy et al., 2008, 1996) are expected to characterize phytoplankton communities and their adaptation to the light field exposure. However, Babin et al. (1995, 1993) examined the spatial variability of $a_{\text{phi}}^*(\lambda)$ in spring and found major differences, mainly between gulf estuary regions, while Roy et al. (2008) confirmed the hypothesis that cell size would be of greater importance during spring bloom periods, while pigment composition would play a more important role during other seasons, in response to light availability and water stratification, as expected.

We found evidence for strong seasonal variability for $a_{\text{phi}}(\lambda)$ and pigment-related variables (Table 4). This indicates phytoplankton communities underwent a seasonal succession in the nearshore areas; this was particularly noticeable in the BSI subregion. Seasonal variability of phytoplankton communities has already been observed in the lower estuary region, and pigment composition was found to be useful for their identification (Roy et al., 1996).

Although photoprotective to photosynthetic carotenoids ratios are mostly used to assess phytoplankton photoacclimation within communities (and mostly vertically), we found them useful for computing and comparing the results for our dataset, considering the objectives of this study. Interestingly, the stricter approach using only the pigments involved in the xanthophyll cycle in the PPC class (Kauko et al., 2019) provided better results when compared to other groups (not shown). This may be related to the high phytoplankton diversity found in the seasonal domain.

We observed a few instances synchronized variability between S_f and the pigment ratios (not shown), which suggests that the pigment packaging effect, given by the S_f parameter, reflects both the effect of cell size and the co-varying accessory pigments. This was particularly true for the stations with higher Chla, e.g., MAN subregion and during April-May for the BSI subregion. These results agree with observations during bloom events reported by Roy et al. (2008), where the effect of cell size was dominant for $a_{\text{phi}}(\lambda)$, and mostly related to diatoms. On the other hand, the lack of such a match in the remaining data suggests that pigments that do not covary with cell size may play an important role in shaping $a_{\text{phi}}(\lambda)$. These results emphasize that bio-optical studies addressing the seasonal variability of phytoplankton communities in the EGSL should consider both pigment concentrations and cell size distribution, along with microscopic identification, if possible, given the complexity of the issue.

Overall, the standing stock of nearshore surface phytoplankton communities was found not to be negligible, with mean Chla values always higher than 1 mg m^{-3} . Nevertheless, the phytoplankton grow in highly absorbing waters with relatively higher SPM (more turbid) conditions than are found in central parts of the EGSL. Based on the absorption and pigment proxies examined in this study, we found that seasonal phytoplankton succession occurs in these optically complex waters. However, a more complete understanding of the community structure and its role in the regional ecosystem's functioning is needed.

1.6.2.3 Short-term optical variability

Lastly, we have demonstrated that short-term temporal events (on the order of days; Fig. 12) can strongly modify IOPs in the water column within a very short time frame. For example, the relatively abundant precipitation observed in early June 2019 increased land runoff around BSI, dramatically increasing the CDOM and particulate inputs that reached the central part of the bay. In addition, the strong winds associated with the same event may have remobilized previously deposited sediments (particles), as suggested by the higher

$b_{bp}(550)$. Similarly, the effects of meteorological cold fronts were found to modify IOPs in a river-influenced coastal area in the Gulf of Mexico (D'Sa et al., 2006).

Along with seasonal variability and these episodic events, circadian fluctuations induced by tides also modulate hydrodynamical and biological processes (Shaw, 2019; Vandavelde et al., 1989). Consequently, we could also verify that tidal fluctuations rapidly (within hours) alter the IOPs in the central part of the bay (BSI subregion). This effect has spatial consequences in the surface waters (Fig. 13b, from a Eulerian perspective) and in the vertical stratification of the IOPs (Fig. 13c, 13d). Although beyond the scope of this work, vertical optical variability needs more in-depth investigations to provide details on its consequences to the underwater light regime, particularly to the attenuation coefficient of downwelling irradiance, which primarily affects the amount of light reaching the benthos. Coupled hydrodynamical models can be an asset in such matters, given the dominant conservative mixing behavior of $a_{cdom}(350)$ as well as its relative optical dominance on absorbing light. These short-term variations at a fixed coastal station have implications for monitoring programs based on sparse punctual sampling.

1.7 CONCLUSIONS

We have documented, for the first time, the spatial and seasonal variability of bio-optical properties in nearshore zones of the EGSL. The complexity of their relationships emphasizes the importance of considering regional differences and seasonality and reinforces our general premise that a more complete understanding of the optically-significant constituents that shape IOPs is needed for remote sensing applications. These considerations may well apply globally to nearshore areas in large estuaries.

The nearshore waters of the EGSL revealed an estuarine-like behavior, with the seawater (in this case, the water found in the middle of the estuary or gulf) being measurably diluted by freshwater from land runoff. In most cases dilution in the nearshore zones is not

confined to a semi-enclosed geomorphological feature, which contradicts the classic definition of an estuary (as in Pritchard, 1967). Notwithstanding, the circulation was found to be estuarine in nature at the mouth of the bay in the BSI subregion (Shaw, 2019).

We also confirmed the dominant conservative mixing behavior of CDOM in these areas, although differences among multiple riverine endmembers and other processes, such as flocculation and phytoplankton production products, need to be considered. The watersheds of local rivers are the main DOM sources of CDOM-dominated nearshore EGSL waters. We showed that the dynamics of resuspension events have a great influence on the magnitudes of certain IOPs.

The characteristics of CDOM-laden waters in these areas revealed the DOM pool to be a major factor in the underwater light environment. This has a great impact on the pelagic ecosystem, as we showed with the seasonal similarities between phytoplankton proxies and seasonal modulation of $a_{\text{cdom}}(350)$. A more in-depth analysis of the DOM pool, like using excitation-emission matrix spectroscopy (Coble, 1996; Stedmon et al., 2003), could provide further explanations of variability at the molecular level, since we surmised that there were molecular weight differences between the subregions of BSI and MAN, and also in the river-to-sea continuum, using the spectral slope $S_{275-295}$ as a proxy.

Globally, nearshore zones are known to be net heterotrophic systems, especially those influenced by large amounts of land runoff (Smith and Mackenzie, 1987). The particle-associated heterotrophic bacterial production was found to greatly contribute to total bacterial production in a coastal Arctic ecosystem and to positively correlate with temperature and POM concentrations (Garneau et al., 2009). Therefore, it is evident that particulate matter transformations - like the biological uptake together with flocculation and sorption processes - will have an important impact of the optical properties of non-algal particulate matter. State-of-art investigations of this variability are required to clarify these processes.

The separation of dry-mass concentration of particles into organic and inorganic fractions (POM and PIM, respectively) was found to be a useful descriptor of the optical

characteristics of assemblages. Also, interestingly, was the general flattening trend of $b_{bp}(\lambda)$ with increasing turbidity. Considering the very low $b_{bp}^*(\lambda)$ reported here, we concluded that particles in the nearshore waters of the EGSL (back)scatter less visible light per unit of particulate mass (SPM), compared to other regions worldwide, and this may have ecological implications. Specifically, we argue that this means that more light is available in the red region of the spectrum which, in turn, would benefit phytoplankton and other photosynthetic benthic organisms. Indeed, even with the relatively higher DOC and SPM values reported in this study (compared to central portions of the EGSL), the absolute Chla values were not negligible. This agrees with the idea that phytoplankton primary production in these regions is also an important component in local ocean budgets (Terhaar et al., 2021). Furthermore, a large portion of the intertidal and shallow subtidal areas are dominated by vegetated habitats, particularly seagrass meadows.

We found IOP characteristics and conditions similar to those reported for river-influenced coastal regions in the northeastern Gulf of Mexico (Cannizzaro et al., 2013; Le et al., 2015). Interestingly, the nearshore zones of this area are marked by the presence of continuous seagrass meadows (Cannizzaro et al., 2013), and IOP heterogeneity was found to be strongly linked with land use and land cover of the watersheds of the main rivers (Le et al., 2015). This highlights the importance of watershed management on controlling the nearshore processes, particularly at local scales of the EGSL.

The results presented here represent a first step towards developing local-scale remote sensing products for these regions (e.g., Mabit et al., 2022). For such products, radiometric data collected concomitantly with the present dataset will permit evaluation of empirical relationships as well as allow the verification of optical coherence between measured IOPs and AOPs through radiative transfer simulations (optical closure). Emerging satellite technologies and the synergy of using multi-resolution sensors will favor not only the scientific community investigating these environments, but also help to improve their management. The bio-optical investigation presented here brings new insights into the

variability of fundamental absorption and backscattering coefficients in these areas, which, in turn, will have consequences on satellite-based estimations of biogeochemical variables.

FUNDING SUPPORT

Funding for the collection of data used in this study was mainly from two interdisciplinary projects: the Canadian Healthy Oceans Network (CHONe-II), funded by the Natural Sciences and Engineering Research Council of Canada (NSERC) in partnership with Fisheries and Ocean Canada and INREST (representing the Port of Sept-Îles and City of Sept-Îles); and the WISE-Man Project (WaterSat Imaging Spectrometer Experiment [WISE] for Optically Shallow Inland and Coastal Waters Assessment), funded by the Canadian Space Agency through the FAST program and Fisheries and Oceans Canada through the Coastal Environmental Baseline Program. This study was also supported by SB's NSERC discovery grant (RGPIN-2019-06070). CASA was supported by Ph.D. scholarships from CHONe-II and the Fonds de Recherche du Québec – Nature et technologies (FRQNT), through a grant of the Merit Scholarship Program for Foreign Students (PBEEE, grant number 263427).

DECLARATION OF COMPETING INTEREST

The authors declare that they have no known competing financial interests or personal relationships that could have appeared to influence the work reported in this paper.

ACKNOWLEDGEMENTS

We acknowledge all persons involved in the field work campaigns and laboratory analyses, with special thanks to Dr. François-Pierre Danhiez, Alexandre Théberge and Zélie Schuhmacher. We extend our thanks to Dr. Claude Belzile for DOC analysis and Mélanie Simard and Julie Major for HPLC analysis. We are grateful to Drs. Dariusz Stramski and

Rick Reynolds for insightful discussions about the optical variability of particulate matter. We thank the editors of Estuarine, Coastal, and Shelf Science and three anonymous, independent reviewers for valuable feedback on earlier versions of this work that significantly improved the content and structure of this manuscript.

ARTICLE 2:

**ENVIRONMENTAL NICHEs AND SEASONAL SUCCESSION OF
PHYTOPLANKTON ASSEMBLAGES IN A SUBARCTIC COASTAL BAY:
APPLICATIONS TO REMOTE SENSING ESTIMATES**

Published in **Frontiers in Marine Science** (2022), 9: 1001098.

<https://doi.org/10.3389/fmars.2022.1001098>

Authors:

Carlos A.S. Araújo^{a,b}, Claude Belzile^c, Jean-Éric Tremblay^{b,d}, Simon Bélanger^{a,b}

^a Département de biologie, chimie et géographie et groupe BORÉAS, Université du Québec à Rimouski, Rimouski, QC G5L 3A1, Canada

^b Québec-Océan, groupe interinstitutionnel de recherches océanographiques du Québec, Québec, QC G1V 0A6, Canada

^c Institut des sciences de la mer de Rimouski, Université du Québec à Rimouski, Rimouski, QC G5L 2Z9, Canada

^d Département de biologie, Université Laval, Québec, QC G1V 0A6, Canada

The following sections correspond to the published article, with small modifications to suit the structure of the thesis.

2.1 ABSTRACT

The seasonal and spatial variability of surface phytoplankton assemblages and associated environmental niches regarding major nutrients, physical (temperature and salinity), and optical characteristics (inherent and apparent optical properties) were investigated in an anthropized subarctic coastal bay, in the Gulf of St. Lawrence: the Bay of Sept-Îles (BSI), Québec, Canada. Seven major phytoplankton assemblages were identified by applying a combined Principal Component Analysis and Hierarchical Cluster Analysis procedures, using pigment concentrations and $<20\ \mu\text{m}$ autotrophic cell abundances as inputs. The resulting phytoplankton groups from BSI ($n = 7$) were more diverse than at a station monitored in a central portion of the St. Lawrence Estuary ($n = 2$). The temporal distribution of the phytoplankton assemblages of BSI reflected the major seasonal (spring to fall) signal of a nearshore subarctic environment. Before the freshet, spring bloom was dominated by large (microphytoplankton) cells (diatoms), and the succession followed a shift towards nanophytoplankton and picophytoplankton cells throughout summer and fall. Most of the phytoplankton assemblages occupied significantly different environmental niches. Taking temperature and the bio-optical properties (ultimately, the remote sensing reflectance) as inputs, a framework to classify five major groups of phytoplankton in the BSI area is validated. The demonstrated possibility to retrieve major phytoplankton assemblages has implications for applying remote sensing imagery to monitoring programs.

Keywords: bio-optics, phytoplankton assemblages, phytoplankton phenology, nutrients, CDOM, HPLC, flow cytometry, remote sensing.

2.2 RÉSUMÉ

La variabilité saisonnière et spatiale des assemblages de phytoplancton de surface et des niches environnementales associées aux macronutriments, les caractéristiques physiques (température et salinité) et optiques (propriétés optiques intrinsèques et apparentes) ont été étudiées dans une baie côtière subarctique anthropisée, dans le golfe du Saint-Laurent : la baie de Sept-Îles (BSI), Québec, Canada. Sept principaux assemblages de phytoplancton ont été identifiés en appliquant une analyse en composantes principales et un regroupement hiérarchique, en utilisant des concentrations de pigments et des abondances de cellules autotrophes $<20 \mu\text{m}$ comme entrées. Les groupes de phytoplancton issus de BSI ($n = 7$) étaient plus diversifiés comparé aux eaux de la partie centrale de l'estuaire du Saint-Laurent ($n = 2$). La distribution temporelle des assemblages phytoplanctoniques de BSI reflète le signal saisonnier marqué (du printemps à l'automne) d'un environnement subarctique côtier. Avant la crue des rivières au printemps (mi-mai), l'efflorescence de phytoplancton était dominée par de grandes cellules (microphytoplancton; diatomées), et la succession a suivi un déplacement vers des cellules de nanophytoplancton et de picophytoplancton tout au long de l'été et de l'automne. La plupart des assemblages de phytoplancton occupaient des niches environnementales significativement différentes. En prenant la température et les propriétés bio-optiques (c-à-d, la réflectance de télédétection) comme entrées, une classification en cinq grands groupes de phytoplancton dans la zone BSI est proposée et validée. La possibilité de documenter les principaux assemblages de phytoplancton à l'aide de l'imagerie de télédétection est démontrée et pourrait être intégrée à un programme de surveillance à long terme de la baie.

Mots-clés : bio-optique, assemblages de phytoplancton, phénologie du phytoplancton, nutriments, CDOM, HPLC, cytométrie en flux, télédétection

“...phytoplankton (...), I still think are one of the best systems to study in ecology.”

Elena Lichtman, in ASLO’s 2021
G. Evelyn Hutchinson Award Talk

2.3 INTRODUCTION

Coastal and nearshore transitional zones host diverse productive ecosystems and are commonly associated with high biodiversity. While energy sources and trophic linkages are complex (Lindeman, 1942; McMahon et al., 2021), primary production by phytoplankton is an important component of such ecosystems (Cloern et al., 2014; Winder et al., 2017). The variability of composition, biomass and production of phytoplankton communities will have a wide range of spatial and temporal scales, with temperate and polar coastal regions presenting a markedly complex seasonal pattern (Carstensen et al., 2015; Cloern and Jassby, 2008).

Phytoplankton assemblages are of particular interest for biogeochemical models, as they are intrinsically related to ecological processes (Le Quéré et al., 2005). Ocean color products derived from Earth Observation platforms can provide information about phytoplankton assemblages composition or their ecological roles (IOCCG, 2014). However, from the remote sensing perspective, the optical complexity of coastal and nearshore waters, and the general greater contribution of the chromophoric dissolved organic matter (CDOM) and particles other than phytoplankton to the bulk optical variability often hinders the ability to extract quantitative (and qualitative) information about phytoplankton in these environments (Sathyendranath et al., 1989).

Notwithstanding, trait-based concepts can be successfully used to explain the distribution of major phytoplankton assemblages along environmental gradients (Litchman

et al., 2010; Roselli and Litchman, 2017). This approach may include diverse strategies of nutrient utilization (Litchman et al., 2007) that are modulated by temperature and light constraints (Edwards et al., 2016). Specifically, because various phytoplankton assemblages have different light requirements, the spectral quality of the light environment (or optical niches) will have consequences on shaping their composition (Hintz et al., 2021; Stomp et al., 2007).

In this study, we hypothesize that the composition of major phytoplankton assemblages in a nearshore coastal area will covary with temperature and the bulk optical properties of the environment. To test this hypothesis, the seasonal and spatial variability of the phytoplankton assemblages were investigated in a subarctic coastal bay (the Bay of Sept-Îles, Québec, Canada). The main objective was to identify the major assemblages and their respective environmental niches, in respect to nutrient concentrations, physical parameters (temperature and salinity), and bio-optical properties. We evaluated and demonstrated the potential of using sea surface temperature (SST, °C) and the remote sensing reflectance ($R_{rs}(\lambda)$, sr^{-1} , where λ indicates light wavelength), at selected wavelengths, to discriminate the major classes of phytoplankton assemblages found in the study area. SST and $R_{rs}(\lambda)$ are quantities that can be estimated by operational satellite sensors (see reviews of Minnett et al., 2019; and Werdell et al., 2018; respectively).

Understanding and predicting the effects of environmental change on natural communities and its consequences for ecosystem functioning is a major goal in ecology (Roselli and Litchman, 2017). In the context of climate change affecting coastal ecosystems (Harley et al., 2006), and particularly in Arctic and subarctic regions (Wassmann et al., 2011), the development of efficient tools to study and monitor phytoplankton assemblages is urgent. Furthermore, being subject of alteration of anthropogenic origin, problems related to phytoplankton such as eutrophication and harmful algal blooms in coastal zones are of major concern (Cloern, 2001; Glibert et al., 2005).

2.4 METHODS

2.4.1 Study area and sampling design

The study area comprises the region around and within the Bay of Sept-Îles (BSI), in the north shore of the Gulf of St. Lawrence (GSL), Canada (Figure 14). The BSI is a semi-enclosed bay with a relatively narrow (~5 km) connection to the gulf and sheltered by the Sept-Îles archipelago. The bay has approximately 100 km² and a great proportion of it (~40%) is occupied by intertidal zones and depths shallower than 2 m. BSI has a mesotidal regime (with an average amplitude of 2 m), which varies in semidiurnal cycles, while its circulation patterns is also influenced by the inflow of four small rivers (Shaw, 2019). The Moisie River outlet (annual average discharge of ~490 m³ s⁻¹), located ~20 km east of the bay, can also influence the nearshore waters of the region (Araújo and Bélanger, 2022; Normandeau et al., 2013). Besides, the BSI is considered as one of the coastal areas of the GSL likely to be most influenced by human activities, with the presence of harbors, major industrial ports and fisheries (Dreujou et al., 2021). Moreover, the BSI is a known region of occurrence of the toxic dinoflagellate *Alexandrium catenella* (previously known as *Alexandrium tamarense*, see Boivin-Rioux et al., 2021; John et al., 2014) in summer months, which was found to be linked to the Moisie River runoff (Weise et al., 2002).

The dataset used in this study consist of in situ profiles and discrete surface water samples collected on an array of stations, within the scope of the interdisciplinary project Canadian Healthy Oceans Network (CHONe2; see Ferrario et al., 2022, for further details about the project). More details about the sampling strategy and methods are found in Araújo and Bélanger (2022). The dataset provided a unique opportunity to investigate the spatial – order of 10⁰ to 10¹ km – and seasonal variability of phytoplankton and bio-optical conditions of the nearshore environment of BSI (Figure 14; Table 5). The stations (Figure 14C) were sampled during seven field campaigns from late spring to early fall 2017 (BSI-1 to BSI-7, from early May to October), and one time in 2019 (BSI-8, early June). For comparison purposes, we also included a station in the middle of the St. Lawrence Estuary (the AZMP –

Atlantic Zone Monitoring Program – buoy location, at Rimouski (RIKI) station, Figure 14B), visited on eleven occasions from July to October 2015 (described in Bélanger et al., 2017).

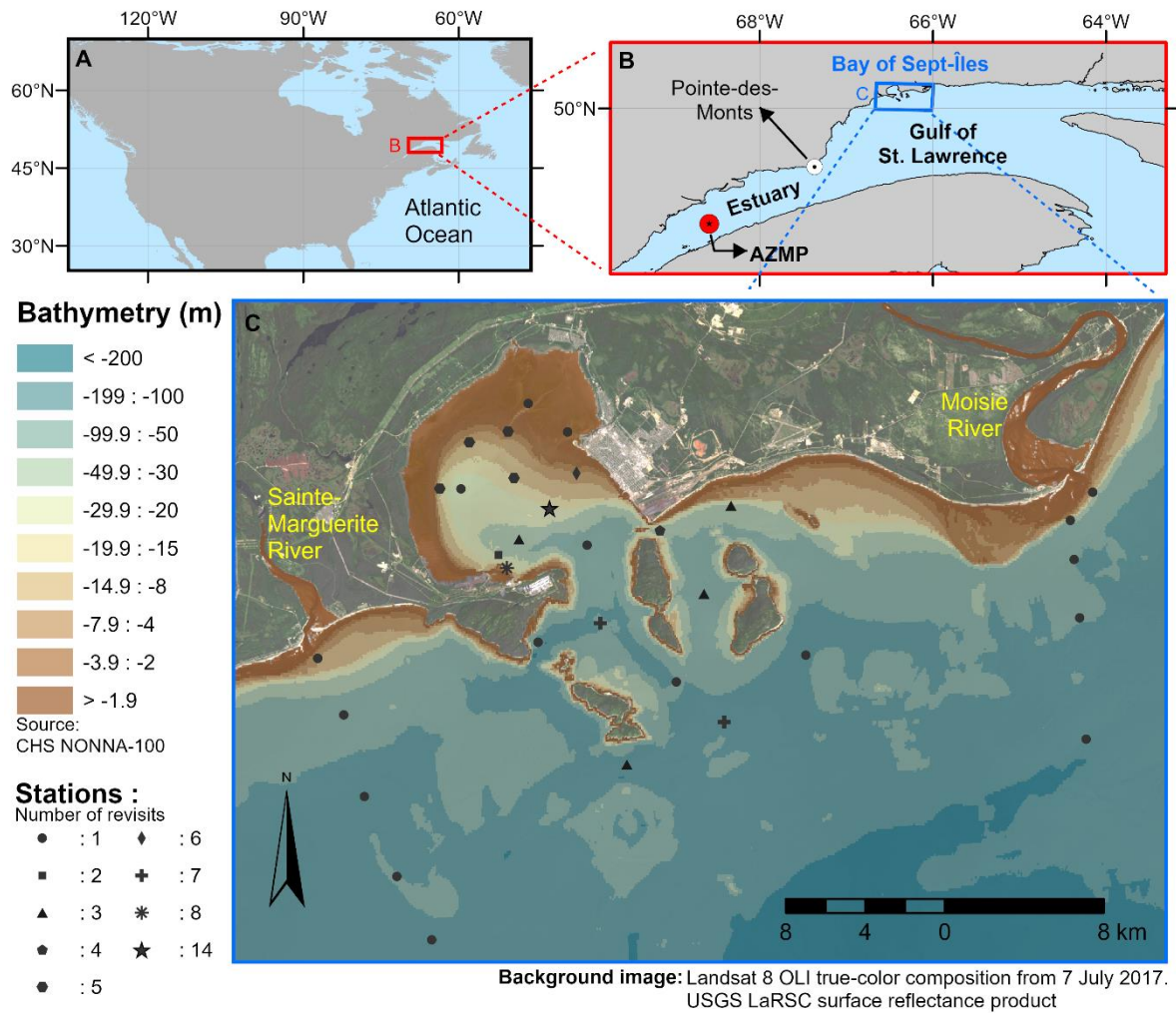


Figure 14. (A) The Estuary and Gulf of St. Lawrence in the North America context, and (B) study area sampling locations: the Bay of Sept-Îles and the AZMP buoy. (C) Spatial distribution and number of revisits of the sampling stations in the Bay of Sept-Îles

Table 5

Summary of the sampling strategy: dates and number of water samples. AZMP is the acronym for the Atlantic Zone Monitoring Program buoy location, and BSI is for the Bay of Sept-Îles

Key to field campaign location and survey: period of sampling	Number of samples (<i>n</i>)
AZMP: from 23 July to 24 October 2015	11
BSI-1: early May (4 and 5) 2017	13
BSI-2: mid-May (21 and 22) 2017	13
BSI-3: early June (6 and 7) 2017	14
BSI-4: mid-June (22 and 23) 2017	10
BSI-5: July (18) 2017	5
BSI-6: September (6) 2017	6
BSI-7: October (7) 2017	6
BSI-8: June (1, 2, 4 and 5) 2019	30
Total	108

The discrete surface water samples were collected with a Niskin bottle (or bucket) and were kept cool in dark conditions until further laboratory procedures, which were made each day immediately after the cruise and consisted mainly of filtration operations. Optical and biogeochemical parameters obtained using in situ vertical profiles were matched to the closest measure of the depth of the discrete water sampling. A total of 108 samples was considered in this study (Table 5).

2.4.2 Phytoplankton assemblages

Phytoplankton assemblages were identified using a combined Principal Component Analysis (PCA) and Hierarchical Cluster Analysis (HCA) procedures, using pigment concentrations and cell abundances grouped in size classes as primary inputs.

Phytoplankton pigments were determined using High Performance Liquid Chromatography (HPLC), following the procedure described by Zapata et al. (2000). Briefly, water samples were filtered through 25 mm (or 47 mm) GF/F glass fiber filters, flash frozen in liquid nitrogen, and stored in cryogenic vials at -80°C until further analysis. The pigment extraction was made using methanol, followed by sonification and centrifugation procedures, before placing the samples in the HPLC analyzer (Agilent Technologies 1200 series). Detection and quantification of the pigments were estimated as described in Bidigare et al. (2005).

A total of twenty accessory pigments were considered in the analysis: chlorophylls *b* (Chl*b*), *c*₁, *c*₂ and *c*₃, Mg 2,4 divinyl pheoporphyrin a₅ monomethyl ester (MgDVP), peridinin (Peri), 19'-butanoyloxyfucoxanthin (But), fucoxanthin (Fuco), neoxanthin, prasinoxanthin, violaxanthin, 19'-hexanoyloxyfucoxanthin (Hex), diadinoxanthin, alloxanthin (Allo), diatoxanthin, zeaxanthin (Zea), lutein, crocoxanthin, alfa and beta-carotene. Total chlorophyll-*a* (Chl*a*) was considered as the sum of monovinyl chlorophyll-*a*, chlorophyllids and the allomeric and epimeric forms of chlorophyll-*a*.

Autotrophic cells (i.e., phycoerythrin- and phycocyanin-containing cyanobacteria and autotrophic eukaryotes) abundances (in cells mL^{-1}) were measured by flow cytometry. Duplicate 4 mL samples were placed in cryovials and fixed with glutaraldehyde Grade I (Sigma; 0.1% final concentration) in the dark at room temperature for 15 min, flash-frozen in liquid nitrogen, and then stored at -80°C until analysis. The analysis was made using a CytoFLEX flow cytometer (Beckman Coulter) fitted with a blue (488 nm) and a red laser (638 nm). The forward scatter, side scatter, orange fluorescence from phycoerythrin (582/42 nm BP) and red fluorescence from chlorophyll (690/50 nm BP) were measured using the blue

laser. The red laser was used to excite the red fluorescence of phycocyanin (660/20 nm BP). Polystyrene microspheres of 2 μm diameter (Fluoresbrite YG, Polysciences) were added to each sample as an internal standard. Pico- ($<2 \mu\text{m}$) and nano-autotrophs (2-20 μm) were discriminated based on a forward scatter calibration using algal cultures. Since the abundance of phycocyanin-containing cyanobacteria was generally low (i.e., $<100 \text{ cells mL}^{-1}$), they were not included in the analysis.

Prior to applying the PCA/HCA algorithms, each pigment was normalized by Chla and, together with cell abundances (pico- and nano-autotrophs), were standardized (z-scores), given the different nature (units) of inputs. The normalized and standardized data were then submitted to the PCA and the number of Principal Components (PCs) that explained most of the variability ($> 80\%$) were selected to proceed to the HCA.

The HCA method classifies objects (i.e., phytoplankton pigments and size class abundances) into groups (or clusters) that are similar. In this study, the clustering approach using Ward's minimum variance method (Ward, 1963) and paired Euclidean linkage distances was applied (as in Neukermans et al., 2016; and Reynolds and Stramski, 2019). The output of the HCA is a dendrogram in which the user defines a linkage distance cutoff value, which, in turn, will determine the number of clusters. For the optimal linkage distance value retrieval, we used the iterative L method procedure (Neukermans et al., 2016; Salvador and Chan, 2004). We also report the cophenetic correlation (Sokal and Rohlf, 1962), as a measure of how accurately a dendrogram maintains the pairwise distance between data objects.

2.4.2.1 Size-classes contribution to biomass

The fractional contribution of different size classes of phytoplankton to Chla – f_{pico} (picophytoplankton, mean diameter $[D] < 2 \mu\text{m}$); f_{nano} (nanophytoplankton, $D = 2$ to $20 \mu\text{m}$); and f_{micro} (microphytoplankton, $D > 20 \mu\text{m}$) – was examined using two different

approaches. The first approach (as in Uitz et al., 2006) uses the weighted contributions of seven diagnostic pigments concentrations (Fuco, Peri, Allo, But, Hex, Zea, and Chlb) to determine $f_{\text{pico}}^{\text{HPLC}}$, $f_{\text{nano}}^{\text{HPLC}}$, and $f_{\text{micro}}^{\text{HPLC}}$. For comparison, a second approach used picophytoplankton cell abundances (cells mL⁻¹) obtained from flow cytometry analysis. It includes eukaryotes and cyanobacteria cell abundances (A_{euk} and A_{cy} , respectively), with Chla cell quotas taken for the prasinophyte *Micromonas pusilla* (Q_{Mic} , equal to 2×10^{-8} $\mu\text{g Chl cell}^{-1}$; Montagnes et al., 1994) and the cyanobacteria *Synechococcus sp.* (Q_{Syn} , equal to 1×10^{-9} $\mu\text{g Chl cell}^{-1}$; Morel et al., 1993), respectively. Thus, the fractional contribution of picophytoplankton, $f_{\text{pico}}^{\text{FC}}$, was determined by $f_{\text{pico}}^{\text{FC}} = 10^3 [(A_{\text{euk}} \times Q_{\text{Mic}}) + (A_{\text{cy}} \times Q_{\text{Syn}})] / \text{Chla}$.

2.4.2.2 Taxonomic analysis by light microscopy

Phytoplankton cell identification was performed on selected samples ($n = 16$) to the lower rank possible (groups, genus, and species). Samples were preserved in acidic Lugol's solution and kept in the dark at 4°C until analysis. The counting of cells $>2 \mu\text{m}$ was performed using an inverted fluorescence microscope (Zeiss Axiovert 10) following the Utermöhl method with settling columns of 25 mL (Lund et al., 1958). A minimum of 400 cells were counted over at least three transects of 20 mm. Autotrophic phytoplankton were distributed in 10 taxonomic groups plus a group of unidentified flagellates. Unidentified cells accounted for an average of 20% of total cells abundance and, from those, ~60% were smaller than 5 μm .

2.4.4 Major nutrients and physical parameters

Concentrations of nitrite (NO_2^-), nitrate (NO_3^-) + NO_2^- , phosphate (PO_4^{3-}), and silicate (Si(OH)_4^{4-}) were determined using a colorimetric method with an Autoanalyzer 3 (Bran +

Luebbe), as described in Bluteau et al. (2021). Prior to analytical procedures, water samples were filtered through 25 mm GF/F filters in acid-wash syringes and Swinnex. Concentrations of NO_3^- were determined by difference.

High-precision salinity (± 0.0003 , in practical salinity units, PSU) was measured on discrete water samples using a calibrated Portasal salinometer (model 8410A, Guildline Instruments, Smiths Falls, ON). In situ vertical profiles of temperature and conductivity were taken using a calibrated CTD probe (SBE19, Sea-Bird Scientific, Bellevue, WA).

2.4.5 Inherent and apparent optical properties

The spectral backscattering and absorption coefficients ($b_b(\lambda)$ and $a(\lambda)$, respectively, in m^{-1}) are inherent optical properties (IOPs) that are related to the remote-sensing reflectance ($R_{rs}(\lambda)$), an apparent optical property, by the means of $R_{rs}(\lambda) \propto b_b(\lambda)/a(\lambda)$ (Morel and Prieur, 1977). Hence, the characterization of the IOPs is a primary requirement for discriminating phytoplankton assemblages when considering optical approaches (Reynolds and Stramski, 2019).

The total absorption coefficient, $a(\lambda)$, is decomposed by the additive contributions of pure water itself ($a_w(\lambda)$), chromophoric dissolved organic matter ($a_{\text{cdom}}(\lambda)$), non-algal particles ($a_{\text{nap}}(\lambda)$), and phytoplankton ($a_{\text{phy}}(\lambda)$) (eq. 7). Similarly, $b_b(\lambda)$ is decomposed in backscattering of pure water ($b_{\text{bw}}(\lambda)$) and particulate matter ($b_{\text{bp}}(\lambda)$) (eq. 8).

$$a(\lambda) = a_w(\lambda) + a_{\text{cdom}}(\lambda) + a_{\text{nap}}(\lambda) + a_{\text{phy}}(\lambda) \quad , \quad (7)$$

$$b_b(\lambda) = b_{\text{bw}}(\lambda) + b_{\text{bp}}(\lambda) \quad , \quad (8)$$

The determination of the above IOPs for the present dataset is described in Araújo and Bélanger (2022). Briefly, $a_{\text{cdom}}(\lambda)$, $a_{\text{nap}}(\lambda)$, and $a_{\text{phy}}(\lambda)$ were determined using a benchtop PerkinElmer Lambda-850 spectrophotometer, equipped with an integrating sphere (used for

particles only). The in situ b_{bp} was determined at six wavelengths using a HydroScat-6P (HS6) backscattering meter (HOBI Labs Inc., Bellevue, WA), and was corrected for salinity variations and loss due to attenuation along the pathlength. The spectral dependency of b_{bp} was modelled (non-least-squares algorithm) using a power-law function, as $b_{bp}(\lambda) = b_{bp}(\lambda_0)[\lambda/\lambda_0]^\gamma$, where γ is a dimensionless parameter describing the spectral dependency of b_{bp} relative to a reference wavelength (λ_0 ; defined as equal to 550 nm in this study). Low residual differences (means < 5%) between measured and modelled values of b_{bp} assured the validity of this equation on describing its spectral shape in the study area (Araújo and Bélanger, 2022). Seawater absorption and backscattering coefficients were retrieved from tabulated values available in the literature (IOCCG, 2018; Morel, 1974; Zhang et al., 2009).

The $R_{rs}(\lambda)$ was derived from in situ radiometric measurements using a Compact Optical Profiling System (C-OPS; Biospherical Instruments Inc., San Diego, CA), and followed the procedures described in Bélanger et al. (2017) and Mabit et al. (2022). Briefly, the system was equipped with sensors that measured the above-water downwelling irradiance, $E_d(\lambda, 0^+)$, and the upwelling radiance from vertical profiles in the water column, $L_u(\lambda, z)$. The processing schema included the extrapolation of $L_u(\lambda, z)$ to assess the water-leaving radiance, $L_w(\lambda, 0^+)$. The $R_{rs}(\lambda)$ is then calculated using $R_{rs}(\lambda) = L_w(\lambda, 0^+)/E_d(\lambda, 0^+)$. C-OPS radiometry data are collected at 19 wavelengths, thus, $R_{rs}(\lambda)$ was interpolated using a piecewise cubic polynomial function to obtain 1-nm resolution, while preserving its spectral shape (Reynolds and Stramski, 2019).

2.4.6 Statistical analysis

Descriptive statistics (mean and standard deviation) and one-way Analysis of Variance (ANOVA) were used to quantitatively compare the populations identified by the clusters obtained by the PCA / HCA procedures. Data were confirmed to exhibit normal distributions using the Lilliefors (or Kolmogorov-Smirnov) test prior to all ANOVAs, and differences

between pairs of means (pairwise comparisons) were assessed using the Tukey Honest Significant Difference (Tukey's HSD) criterion post-hoc test. In the following, when a population of data presents *significant difference*, it means that ANOVA presented a *p-value* less than 5% of significance level ($p < 0.05$). Additionally, when individual groups (clusters) are compared to others (pairwise comparisons), the Tukey's HSD criterion is used. All data manipulations and statistics were done using Matlab (MathWorks) software.

2.5 RESULTS

2.5.1 Clusters of phytoplankton assemblages

The normalized and standardized phytoplankton pigments concentrations ($n = 20$) and pico- and nano-autotrophic cell abundances (eukaryotic and cyanobacteria; $n = 4$) were submitted to the Principal Component Analysis (PCA), and the seven first principal components explained 80.3% of the variance in the data set. In sequence, the projections of the original data on the principal component vector space (scores) were computed and the seven first columns were used as input in the Hierarchical Cluster Analysis (HCA). Figure 15 shows the dendrogram as obtained by HCA, as well as the procedure used to determine the linkage distance and subsequent number of clusters (L method; Salvador and Chan, 2004).

The inset of Figure 15A shows the reductional approach necessary to obtain a lower number of groups, consisting of applying the L method to a limited range of possible clusters (Neukermans et al., 2016; Salvador and Chan, 2004). This approach revealed to be more adequate to our analysis, since the obtained linkage distance cutoff (Figure 15B) divided the dataset in seven groups, containing between 8 and 26 samples, in each individual cluster. The cophenetic correlation value for the HCA was 0.62, comparable to other reported values in the literature (e.g., Neukermans et al., 2016).

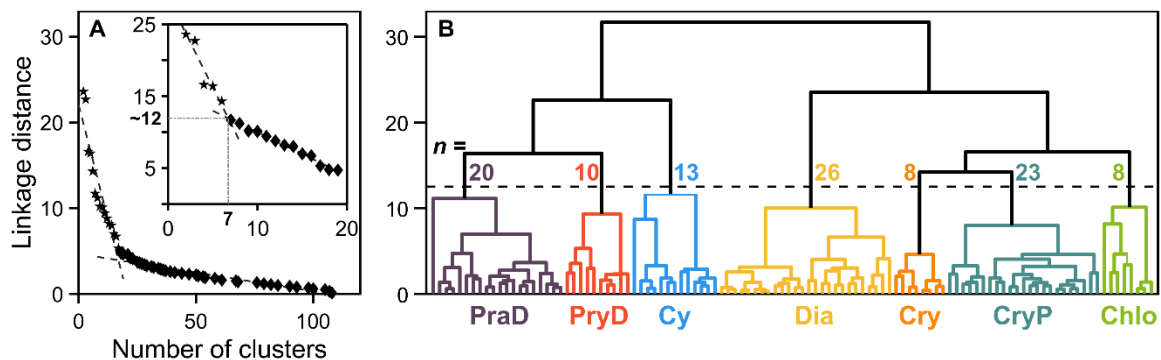


Figure 15. (A) Linkage distance as a function of the number of clusters obtained from the dendrogram (shown in (B)). The L-method (Salvador and Chan 2004) is first applied considering all dataset ($n = 108$), and then to a restricted range for the number of clusters (inset). The resulting “knee” corresponds to a linkage distance cutoff of 11.9, which divides the input dataset in seven clusters. (B) Dendrogram obtained from the Hierarchical Cluster Analysis. The dashed line corresponds to the linkage distance cutoff, and the number above each cluster shows the corresponding number of samples. The clusters are denoted by PraD (purple), PryD (red), Cy (blue), Dia (yellow), Cry (orange), CryP (teal) and Chlo (green)

The variability of selected inputs is shown in Figure 16, whereas the mean and standard deviation of all 24 inputs are presented in Table 13 (Annex2). Only the pigment 19' butanoyloxyfucoxanthin (But) did not present significant difference considering the seven classes of phytoplankton assemblages (one-way ANOVA, $p > 0.05$). The analysis of cell abundances and pigments to Chla ratios within the groups revealed a complex co-occurrence of diverse phytoplankton groups, as the assignment of taxonomic classes from pigment signatures is not always a straight-forward task (Roy et al., 1996). Despite these inherent limitations, we assessed characteristics of each group that could be used to distinguish them from the others. For such analysis, we used available information compiled in the literature that links phytoplankton pigments to taxonomic classes (e.g., Roy et al., 1996; Gibb et al., 2000; Kramer and Siegel, 2019).

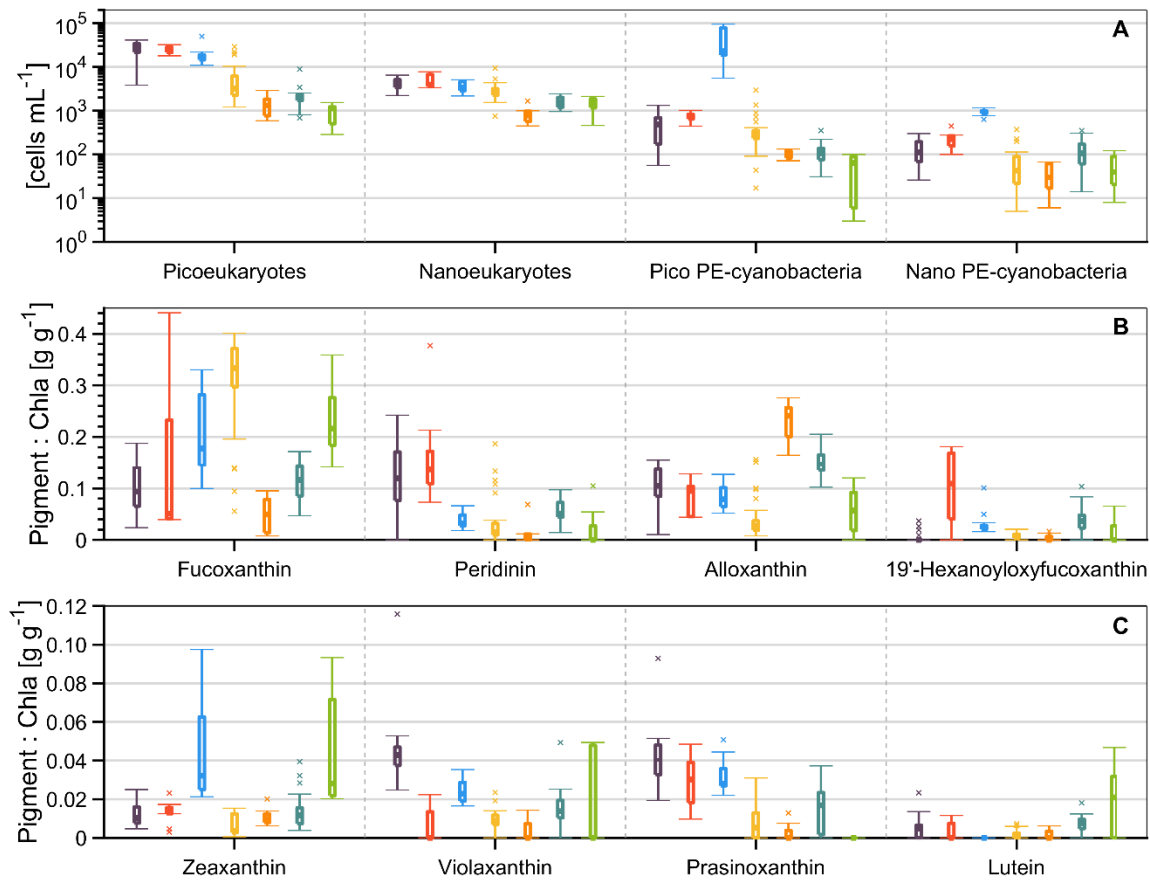


Figure 16. Variability (median, 25th and 75th percentiles, minimum, maximum and outliers) of (A) four classes of phytoplankton cell abundances (B and C) and eight accessory pigments to Chla ratios concentrations. The autotrophic cells concentration is separated by eukaryotes and phycoerythrin-containing (PE-) cyanobacteria, and by pico- (<2 μm) and nano-size (>2 and <20 μm) classes. The color code, associated to each cluster group, is the same as in Figure 15

The relative distribution of phytoplankton groups identified by light microscopy (LM) are presented in Figure 32 (Annex 2). The correspondence between the seven clusters and the taxonomic analysis by LM was not straight-forward since it is nearly impossible to discriminate and identify cells smaller than 3 μm as this cell size is close to the resolution of LM and because the strong coloration of the acidic Lugol's solution, used to preserve the samples, make it difficult to distinguish autotrophic from heterotrophic cells (see Tremblay

et al., 2009). On the contrary, HPLC pigment concentrations and flow cytometry measurements both account for autotrophic cells of this size. Moreover, a high number of unidentified cells (average 20%) and, specifically, unidentified flagellates (between 25 and 50%, Figure 32) were assigned by the LM technique. Besides, LM analysis revealed the presence of important species that helped in the interpretation of the composition of the phytoplankton assemblages.

The first cluster (purple) presented the highest means (and significantly higher than almost all other groups) picoeukaryotes cell counts and Chl_a-normalized pigment concentrations of neoxanthin, prasinoxanthin, violaxanthin, and Chl *b*. Moreover, there were significantly higher means (although not the highest) concentrations of nanoeukaryotes, Chl *c*₁, β-carotene and Perid. From these characteristics, we related this group to the presence of prasinophytes (possibly *Micromonas sp.*) and dinoflagellates (hereafter referred to as PraD). From the LM analysis, the prasinophyte *Pyramimonas spp.* was representative for the group PraD.

The second cluster (red) presented the highest means of nanoeukaryotes, Perid, Hex, and diadinoxanthin, while picoeukaryotes, Chl *c*₁ and *c*₂, prasinoxanthin and β-carotene were also significantly higher than other groups (but not the highest). We related this group to a relative dominance of prymnesiophytes and dinoflagellates (PryD). The LM analysis confirmed the presence and a relative high abundance of the prymnesiophyte *Chrysocromulina spp.* in this group. The dinoflagellates *Gymnodinium spp.* and *Heterocapsa rotundata* were always representative in samples of groups PraD and PryD, while the toxic *Alexandrium catenella* was also identified in these groups. Interestingly, the maximum concentration of *A. catenella* (2920 cells L⁻¹) was observed in an anomalous sample (PryD-B; Figure 32, Annex 2) with a very high concentration of the diatom *Skeletonema costatum*.

The third cluster (blue) presented the highest means of pico- and nano-phycoerythrin-containing cyanobacteria, Zea, Chl *c*₃, and β-carotene, but also higher picoeukaryotes, neoxanthin, prasinoxanthin and Chl *b*. Thus, this group was related to a marked characteristic of occurrence of cyanobacteria (Cy), possibly *Synechococcus sp.* While presenting relatively

high Fucoxanthin to Chl_a, the LM revealed in this group high abundances of the diatoms *Lennoxia faveolata*, *Leptocylindrus minimus*, *Skeletonema costatum*, *Thalassiosira conferta*, and *Chaetoceros spp.*, but also the dinoflagellate *H. rotundata*.

The fourth (yellow) and most numerous cluster ($n = 26$) presented the highest means of Fuco, Chl c_1 and c_2 , and was attributed to a dominance of diatoms (Dia). Cells enumerated by LM analysis revealed high abundances of the genus *Chaetoceros* (*C. debilis*, *C. convolutes*, *C. gelidus*, and *Chaetoceros spp.*) and the species *Thalassiosira nordenskiöldii*. Furthermore, the taxonomic groups identification of samples from group Dia revealed higher dominance of diatoms in relation to others (>50%, Figure 32), as expected.

The fifth (orange) and sixth (teal) clusters both presented the highest means of Allo and crocoxanthin, but the former had the highest means of α -carotene, while the latter had the highest means of MgDVP. We attributed these groups to be related to a marked presence of cryptophytes, but the sixth group had some important contribution from prasinophytes. Therefore, these groups were denoted as Cry and CryP, respectively, with *Hemiselmis virescens* and *Plagioselmis prolunga* var. *nordica* being a representative species. Moreover, these two groups were the most similar based on the dendrogram (Figure 15B). Finally, the seventh (green) cluster presented the highest mean of lutein, but also significantly higher concentrations of Zea than other groups (except Cy). We attributed this group to a relatively greater contribution of chlorophytes (Chlo) to the phytoplankton assemblages.

The numerical abundance of micro-, nano-, and pico-phytoplankton size classes were examined in Figure 33 (Annex2). First, nanophytoplankton abundances obtained from flow cytometric measurements were compared to those obtained by light microscopy (LM), including unidentified cells (Figure 33A). Both measurements are comparable in terms of absolute values, but LM systematically underestimates the number of cells, comparatively, indicating a limitation of the former method to adequately account for this size class. Furthermore, a comparison of distribution of the three size classes abundances (Figure 33B, with microphytoplankton abundances retrieved from the LM analysis) revealed a strong

numerical dominance of picophytoplankton in all samples, except 5 samples where picophytoplankton represented ~50% of total cell abundance.

The fractional contribution of phytoplankton size classes to Chla (f_{pico} , f_{nano} , and f_{micro}) are shown in Figure 17. The two methods used to estimate f_{pico} ($f_{\text{pico}}^{\text{FC}}$ and $f_{\text{pico}}^{\text{HPLC}}$) were compared (Figure 17A) and presented a coefficient of determination (R^2) of 0.35. In general, the correspondences between the two methods presented different patterns when considering the different groups, with $f_{\text{pico}}^{\text{FC}}$ underestimating f_{pico} in comparison to $f_{\text{pico}}^{\text{HPLC}}$, especially for the groups Dia, Cry, CryP, and Chlo, which were restricted to the lower range of variability (<25%). Nevertheless, the groups with higher values of f_{pico} , PraD and Cy, were noticeable in both methods.

Although the Uitz et al. (2006) method (used to determine f^{HPLC}) was developed using global relationships and may have constraints on applying to a coastal / nearshore dataset, as the one presented in this study, we investigated the size fractioned contributions of phytoplankton in the ternary diagram presented in Figure 17B. The different clustering groups presented distinguishable patterns of distribution. Most samples presented $f_{\text{micro}}^{\text{HPLC}}$ higher than 50%, with the most noticeable contribution of this fraction for Dia. Specifically, the groups PraD and Cy presented a dispersion from $f_{\text{micro}}^{\text{HPLC}}$ towards $f_{\text{pico}}^{\text{HPLC}}$, while this dispersion for the groups CryP, PryD, and, particularly for Cry, were towards $f_{\text{nano}}^{\text{HPLC}}$.

Overall, the phytoplankton communities were well discriminated by the PCA / HCA procedures. Despite the picophytoplankton numerical dominance, the total biomass was dominated by microphytoplankton, with some variations within clusters.

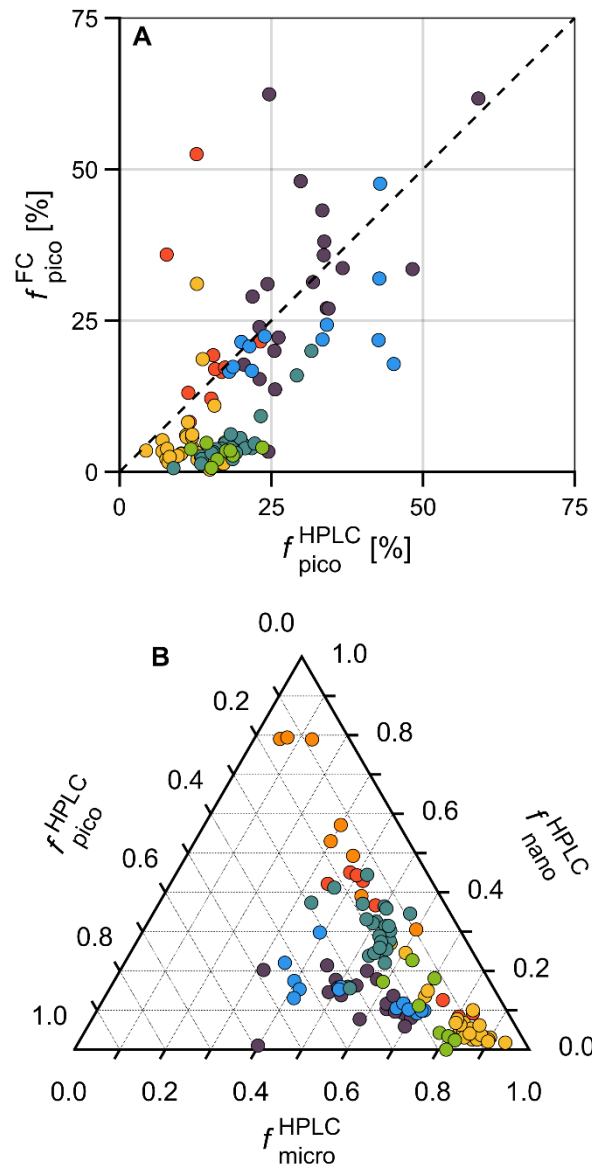


Figure 17. Relative (or fractional, f) contributions of phytoplankton size classes to Chla, for each phytoplankton cluster. **(A)** Two methods to obtain the picophytoplankton fractional contribution to chlorophyll- a (f_{pico}): f_{pico}^{FC} and f_{pico}^{HPLC} (see text for details). **(B)** Ternary plot of f_{pico}^{HPLC} , f_{nano}^{HPLC} , and f_{micro}^{HPLC} . This approach (pigment-based) considers a global relationship using seven diagnostic pigments as inputs (Uitz et al. 2006). The color code is the same as in Figure 15

2.5.2 Seasonal and spatial variability

The Chla biomass, the seasonal succession, and spatial variabilities within phytoplankton clusters are shown in Figure 18. In Bay of Sept-Îles (BSI), Chla medians were always between 1 and 3 mg m⁻³ for all groups, except for Chlo whose median is 0.66 mg m⁻³ (Figure 18A). No group is significantly different from the others, but PryD and Dia presented higher means of Chla. In comparison, only two groups were present at AZMP (Dia and PraD) in the middle of the Lower St. Lawrence Estuary, during the period from July to October 2015, and Chla values were generally higher than in BSI, with values ranging from 1.02 to 11.43 mg m⁻³ (Figure 18B).

The seasonal evolution of the phytoplankton clusters of BSI are shown in Figure 18C, where the bars represent the relative contribution of each group during each campaign. Firstly, in early May 2017 (BSI-1) only the group Dia was found in BSI surface waters. About two weeks later (BSI-2), the group Dia was replaced mainly by the groups Cry, CryP, and Chlo. Interestingly, the dominance of groups CryP and Chlo (but also some samples from Dia) was also observed in the field campaign of early June 2019 (BSI-8). In June 2017 (BSI-3 and 4) only groups PraD and PryD were found in BSI, followed in July (BSI-5) by the occurrence of PryD, Dia, and Cy. Finally, only group Cy was found in fall (BSI-6 and 7).

Although BSI-1, 6, and 7 were characterized by a single group, the other field campaigns presented heterogeneity regarding the phytoplankton assemblages, and their spatial distribution is shown in Figures 18D-H. The dominant groups in BSI-2, Cry and CryP, were generally found inside and outside the bay, respectively (Figure 18D). This spatial separation was even clearer in BSI-3 for the groups PraD (inside) and PryD (outside). In BSI-5, the sample correspondent to Cy is in a station outside the bay. In the 2019 campaign (BSI-8), beside the dominance of CryP, the group Chlo was distributed in the riverine (freshwater) plumes, while two Dia samples are distributed in-between the islands east of the bay. These results evidence the seasonal succession of phytoplankton assemblages, but also reveal that the spatial variability, at this scale, is also important.

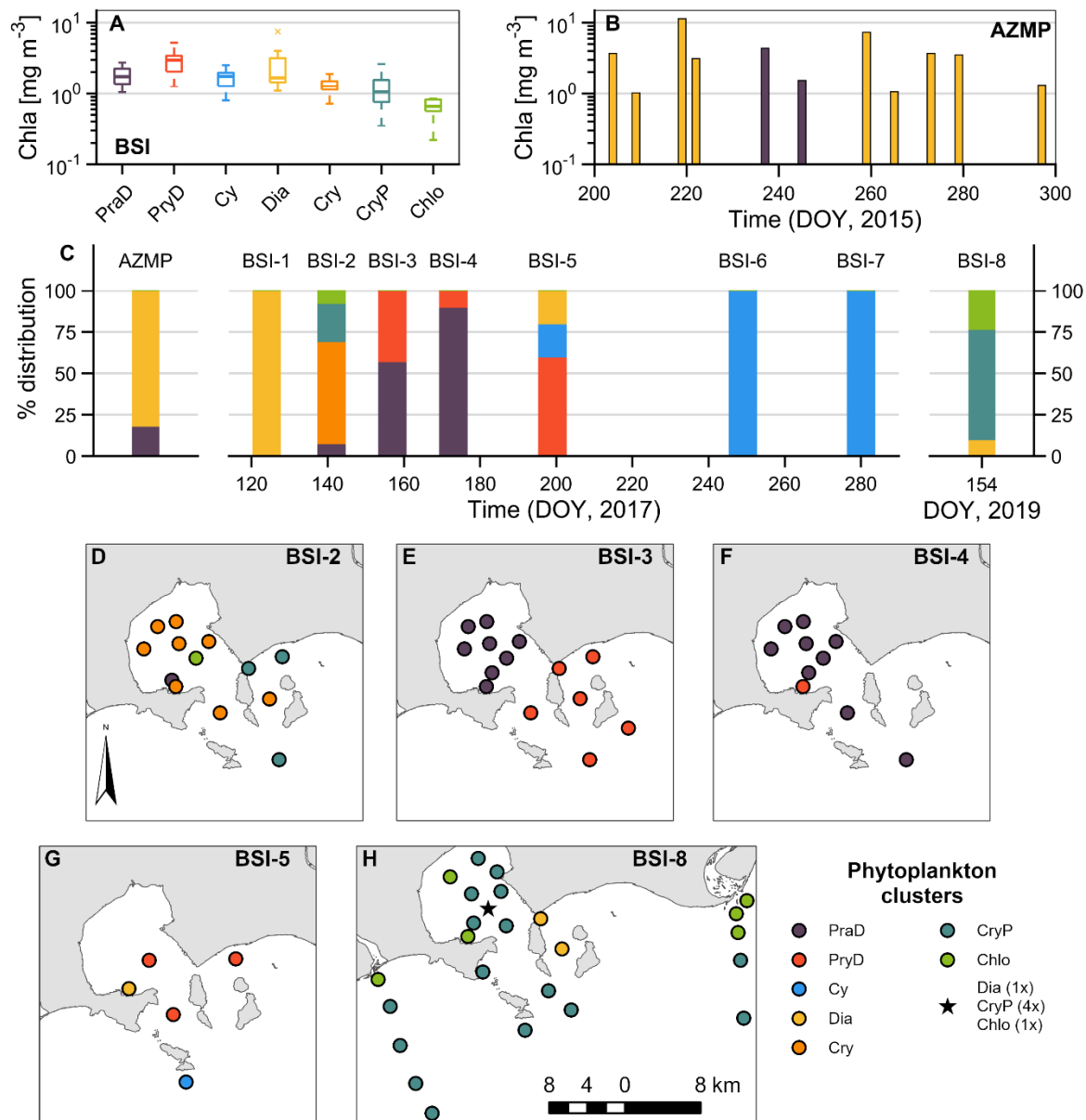


Figure 18. Temporal and spatial variability of the phytoplankton clusters. (A) Boxplots showing the variability of Chla for each cluster, for the Bay of Sept-Îles (BSI). (B) Bars showing the temporal variability of Chla in the AZMP buoy station (DOY = Day of Year). The color of the bars corresponds to the class of phytoplankton clusters. (C) Relative distribution of phytoplankton clusters for AZMP and for the temporal series in BSI (BSI-1 to 8; Table 5). (D-H) Spatial distribution for each campaign that presented noticeable variability of phytoplankton clusters

2.5.3 Major nutrients and physical environment

The relationships between major nutrient concentrations, associated to each phytoplankton assemblage, are shown in Figures 19A and 19B, and the physical environment, as determined by temperature and salinity, are shown in Figure 19C. The mean and standard deviation of each variable for the Bay of Sept-Îles (BSI) of Figure 19 (plus nitrite and nutrient concentrations ratios) are summarized in Table 6. Samples from the Lower St. Lawrence Estuary (AZMP, squares in Figure 19) were differentiated from those of BSI. In addition, other samples from BSI were considered as outliers. First, two samples from the group Dia, in the campaign BSI-8 (Figure 18H), had environmental (and optical) characteristics typical of those from the group Chlo. This might be related to lateral advection of phytoplankton cells. Secondly, few samples from groups Chlo (2) and CryP (1) were found to have anomalous values of physical and optical (not shown) variables. These samples were obtained in turbulent hydrodynamic conditions close to riverine discharges. Water sampling might not reflect the same conditions as the data acquired by the in situ instrumentation (CTD, HS6, C-OPS). In the following, these outliers are not considered.

The nutrients and physical environment at the Lower St. Lawrence Estuary station (AZMP) are markedly different from those of BSI, when considering the same phytoplankton groups of these two locations. Nitrate and phosphate concentrations values were higher for AZMP (Figure 19B), while silicate concentrations were similar (Figure 19A). However, if only the group Dia is considered, silicate concentrations were also higher at AZMP (except for one sample). Interestingly, the Dia samples from AZMP were also associated with higher temperatures (mean of 8.2°C) than the ones from BSI, but with slightly lower salinities (mean of 27.6) (Figure 19C).

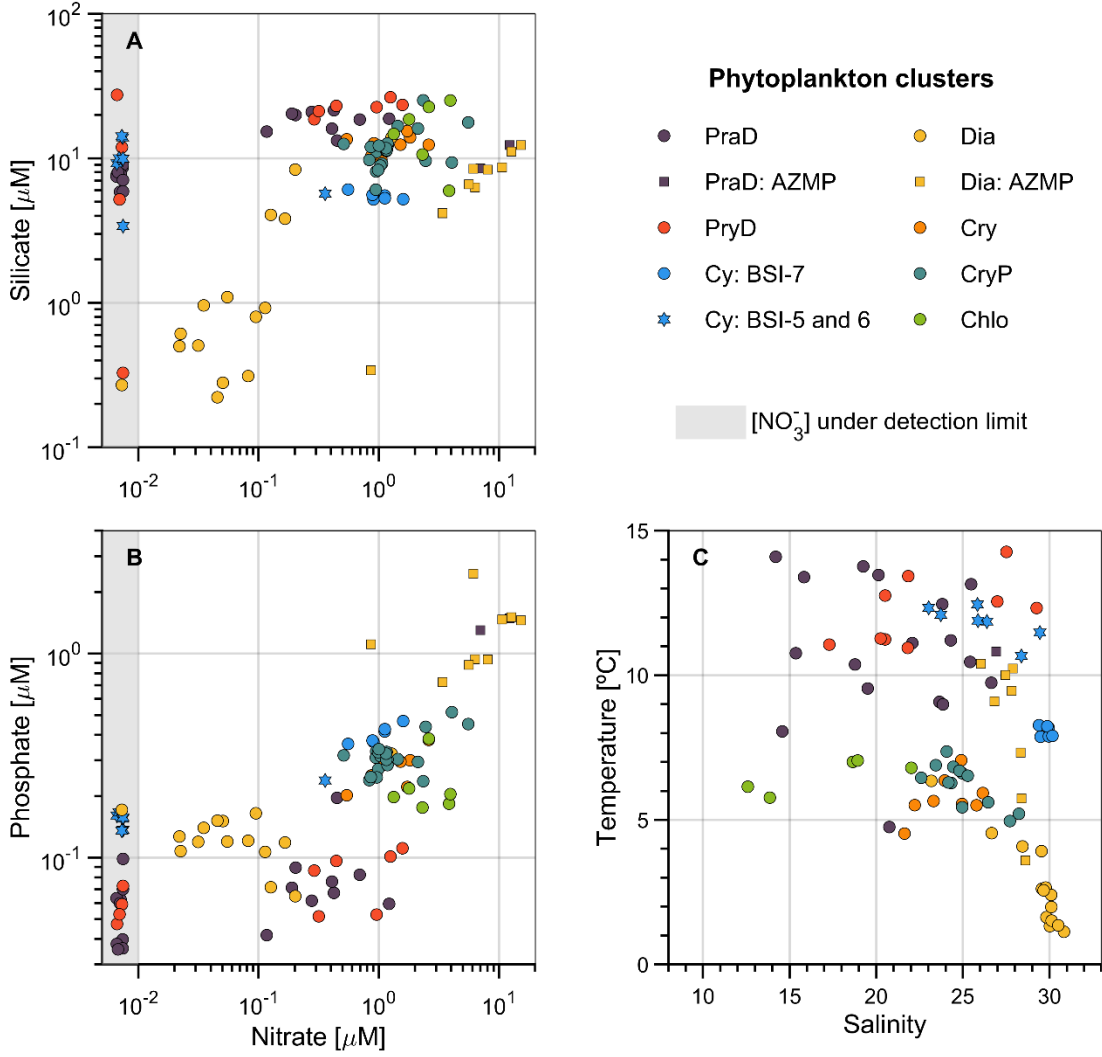


Figure 19. Nutrient concentrations and physical parameters relationships associated with each phytoplankton cluster. (A) Silicate ($[\text{Si}(\text{OH})_4^-]$) versus nitrate ($[\text{NO}_3^-]$); (B) phosphate ($[\text{PO}_4^{3-}]$) versus nitrate concentrations; and (C) temperature versus salinity. Samples from the Lower St. Lawrence Estuary station (AZMP) are presented by squares, and outliers from the Bay of Sept-Îles (BSI) are presented by diamonds. The gray-shaded area corresponds to undetectable nitrate levels ($\sim 0 \mu\text{M}$)

Table 6

Mean and (plus or minus) standard deviation of nutrient concentrations and physical parameters for each of the seven clusters of phytoplankton (PraD, PryD, Cy, Dia, Cry, CryP, and Chlo), for the Bay of Sept-Îles (BSI) region

Environmental variable	PraD	PryD	Cy	Dia	Cry	CryP	Chlo
Nitrate, [NO ₃ ⁻] (µM)	0.22 ±0.32	0.49 ±0.58	0.51 ±0.56	0.16 ±0.32	1.38 ±0.67	1.54 ±0.18	2.64 ±1.07
Nitrite, [NO ₂ ⁻] (µM)	0.10 ±0.04	0.09 ±0.03	0.17 ±0.05	0.03 ±0.04 *	0.09 ±0.02	0.08 ±0.04	0.12 ±0.04
Silicate [†] , [Si(OH) ₄ ⁴⁻] (µM)	12.89 ±5.93	18.01 ±9.18	7.63 ±3.49	2.44 ±3.88 *	12.57 ±1.84	11.97 ±4.07	16.28 ±7.28
Phosphate, [PO ₄ ³⁻] (µM)	0.07 ±0.04 *	0.07 ±0.02 *	0.27 ±0.13	0.14 ±0.06	0.28 ±0.05	0.32 ±0.07	0.23 ±0.08
([NO ₃ ⁻] + [NO ₂ ⁻]) : [Si(OH) ₄ ⁴⁻] (dim.)	0.02 ±0.02	0.04 ±0.04	0.12 ±0.12	0.15 ±0.16	0.12 ±0.05	0.14 ±0.09	0.23 ±0.22
([NO ₃ ⁻] + [NO ₂ ⁻]) : [PO ₄ ³⁻] (dim.)	4.87 ±5.02	7.27 ±6.50	2.00 ±1.13	1.21 ±1.30	5.21 ±1.89	4.84 ±2.57	13.07 ±6.60
Salinity [†] (PSU)	21.11 ±4.14	22.43 ±4.08	27.81 ±2.53	29.11 ±1.94	24.11 ±1.63	24.13 ±3.82	16.82 ±3.62 *
Temperature [†] (°C)	10.85 ±2.44	12.20 ±1.17	10.09 ±2.00	2.72 ±1.50 *	5.76 ±0.74	6.24 ±0.72	6.55 ±0.57

All variables presented significantly difference (one-way ANOVA, $p < 0.05$). Bold values indicate groups that were significantly higher (Tukey's HSD criterion) than at least four or more other groups. Conversely, the asterisk (*) indicate when a group of samples were significantly lower than at least four or more other groups.

[†] Smirnov-Kolmogorov test rejects the null hypothesis at the 5% significance level, but Lilliefors test does not.

All nutrient concentrations, nutrient ratios, and physical parameters were significantly different for the seven phytoplankton clusters (one-way ANOVA, $p < 0.05$). Samples from BSI-4, BSI-5, and BSI-6 (stars in Figure 19) field campaigns (Figure 18C, from mid-June to early September 2017) presented undetectable nitrate concentration ($\sim 0 \mu\text{M}$). Thus, depleted nitrate conditions were noticeable for samples of groups PraD, PryD and Cy (right side of Figs. 19a and 19b). Although we do not differentiate these samples from others of the same group in Table 6, silicate concentrations values for these population of samples were generally lower for PraD and PryD (comparing to the same groups in BSI-3), and higher for Cy (comparing to the same group in BSI-7). Notwithstanding, phosphate concentrations values (in the nitrate-depleted conditions) were comparable with others of PraD and PryD, and slightly lower for Cy. A single sample from group Cy (BSI-6) presented a nitrate concentration much higher than the detection limit ($\sim 0.36 \mu\text{M}$), and it corresponded to the station farthest from the shore.

The nitrate concentrations associated to the different groups in BSI, as analyzed by pairwise comparisons (Tukey's HSD criterion), revealed that Chlo has higher concentration than all other groups, while CryP was higher than PraD, PryD, Cy, and Dia. Nitrite concentrations was higher in Cy than all other groups (except Chlo), while Dia has significantly lower concentrations than all other groups.

In non-depleted $[\text{NO}_3^-]$ conditions, silicate concentrations (Figure 19A; Table 6) in groups PraD, PryD, and Cy presented very low variability. In Dia, silicate concentrations were significantly lower than all other groups (except Cy). Two groups, PraD and PryD, presented significantly lower values of phosphate concentrations (Figure 19B, Table 6) than others (Cy, Cry, CryP, and Chlo). Moreover, $[\text{PO}_4^{3-}]$ in Chlo was significantly higher than Dia (besides Prad and PryD).

Nutrient ratios are commonly used to assess elemental limitation for phytoplankton production. The nitrate (plus nitrite) to silicate and the nitrate (plus nitrite) to phosphate ratios (dimensionless) are presented in Table 6. The $[\text{NO}_3^-] + [\text{NO}_2^-]: [\text{Si}(\text{OH})_4^{4-}]$ means were lower for groups PraD and PryD and highest for group Chlo. Nevertheless, Chlo also presented

higher $[\text{NO}_3^-] + [\text{NO}_2^-]:[\text{PO}_4^{3-}]$ means than all other groups (minus PryD), while Dia was significantly lower than Chlo and PryD.

The groups PraD, PryD, and Cy were found in warmer waters than the other groups (Figure 19C, Table 6). Conversely, the group Dia presented significantly lower temperatures when compared to all other groups. Dia and Cy (specifically the blue circles in Figure 19) were found in saltier waters (>28), while group Chlo presented significantly lower salinities than all other groups but PraD. Also noticeable is the narrow range of temperature (~ 8 °C) and salinity (~ 30) of some samples of group Cy, which were collected on BSI-7 (October 2017, Figure 18C). The groups associated with the presence of cryptophytes, Cry and CryP, and Chlo, presented low variability of temperatures (small standard deviation, Table 6).

The separation of group Cy between campaigns BSI-5 and 6 (stars in Figure 19) and BSI-7 were done because of the different environmental conditions in which the two sets of samples were found (e.g., nitrate depletion, temperature, salinity). The set of samples of group Cy in BSI-5 and 6 presented more similar environmental conditions to those of groups PraD and PryD. Similarly, optical conditions of group Cy from BSI-5 and 6 were close related to these groups (not shown). Therefore, in the following presentation of results only the set of BSI-7 are considered for the group Cy.

2.5.4 Optical characterization

The total and component-specific spectral absorption and backscattering coefficients are presented in Figure 20. For each graph (A-F), each phytoplankton group curve is represented by the sample having the highest counts of median values (mode), calculated for unitary wavelength within the visible spectral range (400 to 700 nm). Descriptive statistics and tests for some optical properties shown in Figures 20 and 21 are presented in Table 7, for selected wavelengths, in the perspective of satellite remote sensing applications.

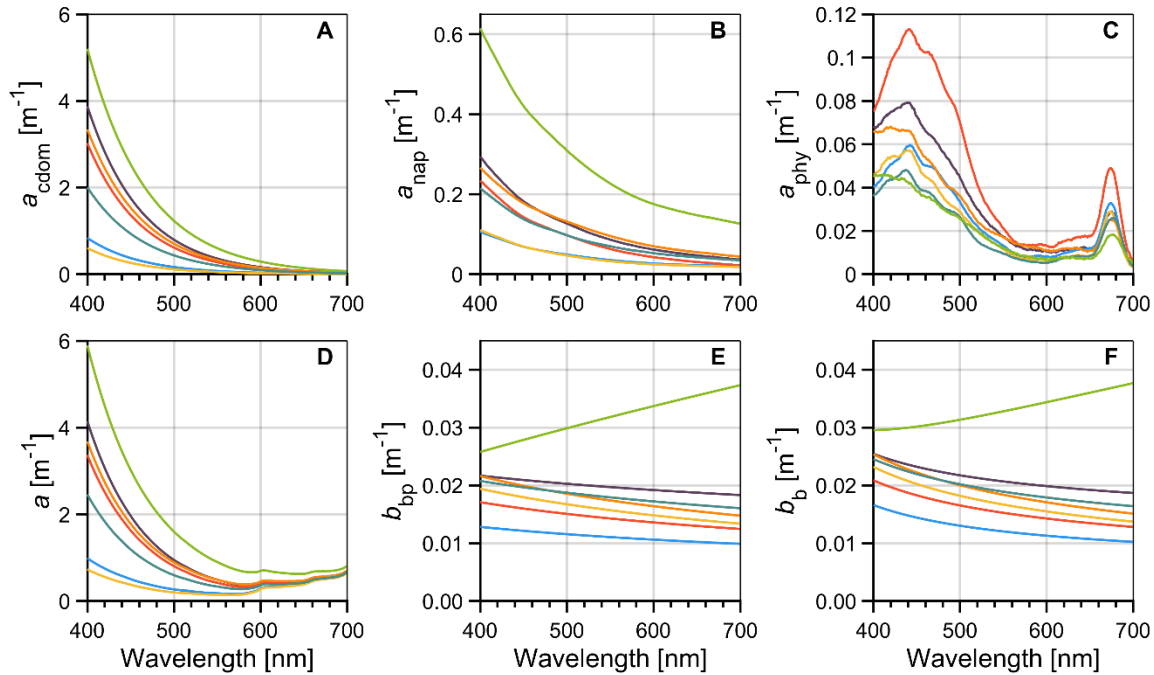


Figure 20. Inherent optical properties spectra: absorption coefficients of (A) chromophoric dissolved organic matter ($a_{\text{cdom}}(\lambda)$); (B) non-algal particles ($a_{\text{nap}}(\lambda)$); and (C) phytoplankton ($a_{\text{phy}}(\lambda)$); (D) total absorption coefficient ($a(\lambda)$); (E) particulate backscattering ($b_{\text{bp}}(\lambda)$); and (F) total backscattering coefficient $b_{\text{b}}(\lambda)$. For each graph, the different lines represent the median spectra for each cluster of phytoplankton groups, and the color code is the same as in Figure 15

For most phytoplankton assemblages, CDOM absorption coefficient (a_{cdom} , Figure 20A) was approximately one order of magnitude higher than the other absorption components in wavelengths shorter than 500 nm. As expected, the group Chlo, found in fresher waters (Table 6) presented significantly higher $a_{\text{cdom}}(465)$ than other groups, minus PraD and CryP (Table 7). In contrast, groups likely to be more related to marine end-member waters (with saltier characteristics), such as Dia and Cy, presented lower values of $a_{\text{cdom}}(\lambda)$.

The non-algal particles absorption (a_{nap} , Figure 20B) spectra were much lower than a_{cdom} , but had similar relative magnitudes when considering individual groups of phytoplankton, suggesting a co-variation between these two optical components. For

example, $a_{\text{nap}}(465)$ in group Chlo was significantly higher than all others, while Dia and Cy values were significantly lower than for PraD and Cry.

The phytoplankton absorption coefficient spectra (a_{phy} , Figure 20C) were also much lower than a_{cdom} or a_{nap} and, thus, its influence in the total absorption coefficient (a , Figure 20D) are minimal (see also Araújo and Bélanger, 2022). For example, the fractional contribution of a_{phy} to the non-water absorption coefficient ($= a_{\text{cdom}} + a_{\text{nap}} + a_{\text{phy}}$) was maximal in the blue peak of a_{phy} (~465 nm), but higher mean values reached only 6.2 and 5.4% for groups Dia and Cy. Nevertheless, significantly higher values of $a_{\text{phy}}(465)$ and $a_{\text{phy}}(665)$ were found for group PryD, which also presented higher Chla values (Figure 18A).

As expected, the $a(\lambda)$ reflects the additive effects of a_{cdom} and a_{nap} , especially in the blue and green regions of the spectrum, while in the red the pure water absorption (a_{w}) dominates the absorption budget.

The particulate (b_{bp}) and total (b_{b}) backscattering coefficients are shown in Figures 20E-F. Most phytoplankton groups presented similar spectral characteristics of b_{bp} (and b_{b}), but group Chlo was higher than others in all wavelength ranges. Interestingly, the spectral variability of b_{bp} from group Chlo presented an odd behavior compared to the others, with increasing values with increasing wavelength. This group has significantly higher values of the spectral slope (γ) of b_{bp} , resulting in significantly higher $b_{\text{bp}}(655)$ (Table 7).

Table 7

Mean and (plus or minus) standard deviation of temperature, inherent optical properties (including ratios), and remote sensing reflectance, at selected wavelengths, for each of the seven clusters of phytoplankton (PraD, PryD, Cy, Dia, Cry, CryP, and Chlo)

Optical parameters	PraD	PryD	Cy (BSI-7)	Dia	Cry	CryP	Chlo
$a_{\text{cdom}}(465)$ [m^{-1}]	1.45 \pm 0.76	1.05 \pm 0.49	0.29 \pm 0.04	0.34 \pm 0.27 *	1.29 \pm 0.43	0.88 \pm 0.52	2.18 \pm0.71
$b_{\text{bp}}(665)$ [m^{-1}]	1.80 \pm 0.64	1.28 \pm 0.16	1.10 \pm 0.43	1.67 \pm 1.13	1.81 \pm 0.54	1.73 \pm 0.95	3.64 \pm1.64
b_{b}/a (465) [$\cdot 10^2$, dim.]	1.48 \pm 0.76	1.13 \pm 0.16	3.46 \pm 0.77	5.34 \pm1.71	1.61 \pm 0.54	2.34 \pm 0.78	1.61 \pm 0.97
b_{b}/a (566) [$\cdot 10^2$, dim.]	4.68 \pm 2.09	3.63 \pm 0.49	7.14 \pm 1.98	10.41 \pm3.16	4.81 \pm 1.64	6.03 \pm 2.24	5.86 \pm 2.60
b_{b}/a (665) [$\cdot 10^2$, dim.]	3.22 \pm 1.10	2.35 \pm 0.21	2.31 \pm 0.83	3.37 \pm 2.00	3.30 \pm 0.91	3.23 \pm 1.59	6.81 \pm1.81
$R_{\text{rs}}(465)$ [$\cdot 10^3$, sr^{-1}]	0.67 \pm 0.34	0.46 \pm 0.18	2.04 \pm0.36	2.60 \pm0.93	0.74 \pm 0.19	0.98 \pm 0.31	0.57 \pm 0.47
$R_{\text{rs}}(566)$ [$\cdot 10^3$, sr^{-1}]	1.81 \pm 0.72	1.54 \pm 0.38	3.58 \pm 0.61	4.67 \pm1.47	2.03 \pm 0.37	2.41 \pm 0.78	2.60 \pm 1.07
$R_{\text{rs}}(665)$ [$\cdot 10^3$, sr^{-1}]	1.34 \pm 0.40	1.25 \pm 0.22	1.17 \pm 0.26	1.75 \pm 1.01	1.48 \pm 0.39	1.61 \pm 0.85	3.12 \pm0.96

All variables presented significantly difference (one-way ANOVA, $p < 0.05$). Bold values indicate groups that were significantly higher (Tukey's HSD criterion) than at least four or more other groups. Conversely, the asterisk (*) indicate when a group of samples were significantly lower than at least four or more other groups.

The spectra of backscattering to total absorption coefficient ratio (b_b/a) and the remote sensing reflectance (R_{rs}) are shown in Figure 21, for each phytoplankton assemblage. As for individual IOPs (Figure 20) the b_b/a and R_{rs} shown for each group corresponds to the mode (spectral domain) of median values for individual wavelengths. Although similarities are expected when comparing these two variables, it is important to note that inelastic scattering by water molecules (Raman) and by CDOM and phytoplankton pigments (fluorescence) are not considered in b_b/a . Furthermore, the approach we used does not consider changes in IOPs along the water column, that could result in changes in the light field in highly stratified waters (particularly in L_w , and consequently in R_{rs}). Notwithstanding, this latter situation is likely to happen under some circumstances in our study area (Araújo and Bélanger, 2022).

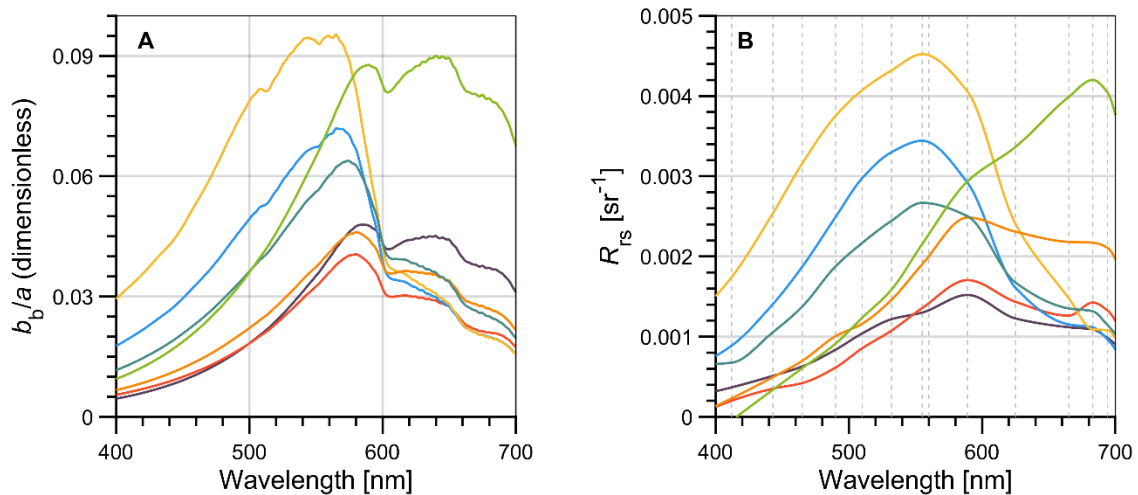


Figure 21. Spectra of (A) the ratio of total backscattering to total absorption coefficients ($b_b/a(\lambda)$), and (B) the measured remote sensing reflectance ($R_{rs}(\lambda)$). The vertical gray dashed lines on (B) indicates the original spectral bands of the C-OPS instrument used to derive R_{rs} . For each graph, the different lines represent the median spectra for each cluster of phytoplankton groups, and the color code is the same as in Figure 15

Most phytoplankton groups presented similar shape and magnitudes of the b_b/a spectra, which was observed in all wavelength ranges. The two exceptions were for groups Dia and Chlo that peak in green (~560 nm) and red (~640 nm) regions, respectively. The

combination of lower a and at-average b_b values give significant higher values of b_b/a in the blue (465) and green (566) regions for group Dia (Table 7). Similarly, the significantly higher values of b_b/a (665) for the group Chlo is explained by the high b_{bp} in the red region associated with this group, which is found in waters heavily influenced by terrigenous inputs.

Dissimilarities between b_b/a and R_{rs} were observable mainly in the red spectral range (>620 nm) and are mostly due to inelastic scattering processes affecting R_{rs} . However, the characteristics of b_b/a spectra that are distinguishable for the phytoplankton groups Dia and Chlo are also observed in R_{rs} (Figure 21B, Table 7).

2.5.5 Seasonal succession and framework for remote sensing estimations

The variability of phytoplankton assemblages and nutrient concentrations, physical parameters, and optical properties revealed a clear seasonal signal, as summarized in Figure 22. Since riverine discharges are a major controlling factor in the optical environment in the BSI region (Araújo and Bélanger, 2022), the Moisie River discharge for years 2017, 2019, and the climatological median (1965-2021) is depicted in Figure 22A. It is expected to reflect the seasonality of the smaller rivers discharging directly into the bay (i.e., rivières Hall, des Rapides, aux-foins, Poste). The mean value of the discharge peaks of 2017 and 2019 (~2,500 m³ s⁻¹) were 60 % higher than the historical median (from 1965 to 2021).

The group Dia occurred in BSI in April - early May (Figure 22B), before the spring freshet, and is related to the spring bloom, a common feature at high latitude estuaries (Carstensen et al., 2015). Lower water temperatures and the lowest absorbing characteristics (due to lower a_{cdom} and a_{nap}) are found.

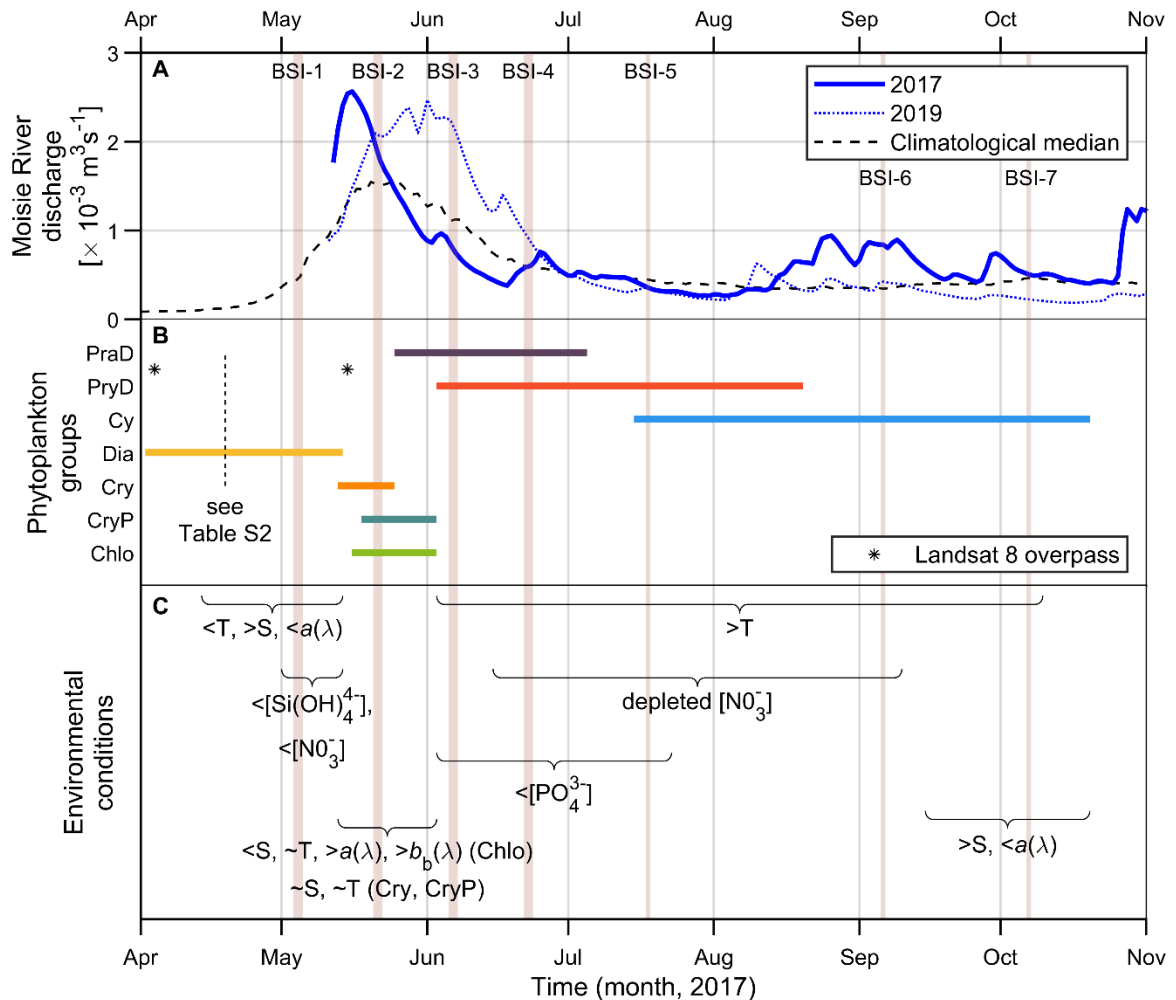


Figure 22. Seasonal succession of phytoplankton assemblages in the Bay of Sept-Îles. **(A)** Moisie River discharge for years 2017, 2019, and climatological median (1965-2021). Source: Ministère de l'Environnement et de la Lutte contre les changements climatiques (<https://www.cehq.gouv.qc.ca/>). **(B)** Phytoplankton assemblages distribution (see Table 13 in Annex 2 for details of samples collected in April 19); and **(C)** environmental conditions as showed by nutrient concentrations and physical parameters (Temperature and Salinity, T and S) along the year 2017. The durations of the events of both occurrence of phytoplankton assemblages and environmental conditions are extrapolated from punctual field campaigns (BSI-1 to BSI-7, refer to Table 5), represented by vertical transparent lines

Our interpretation of the spring bloom starting in the BSI region earlier than BSI-1 campaign (early May) is supported by samples collected in mid-April 2017 (Table 13, Annex

2; not used in this study due to incomplete dataset), where biomass (Chla) and Fucoxantin to Chla ratio were among the highest. The Dia samples observed in campaign BSI-1 were likely related to the end of the spring bloom, as indicated by the low nitrate and silicate concentrations. The presence of a subsurface chlorophyll maximum (SCM), a common feature in the Gulf of St. Lawrence (Vandavelde et al., 1987), was observed during field campaign BSI-1 (see Figure 34; Annex 2), with similar phytoplankton composition despite much higher Chla values (Table 13). Silicate and phosphate concentrations were comparable at the surface and within SCM, although SCM nitrate levels were one order of magnitude higher than surface samples.

The groups associated with cryptophytes, Cry and CryP, occurred approximately in phase with the peaks of the spring freshet (Figure 22B), and were characterized by an increase in temperature and decreasing salinities. As expected, the freshet increased the amount of CDOM and non-algal particles in the water column, increasing its absorbing and backscattering characteristics. Samples collected in the 2019 field campaign (BSI-8), in early June, had similar characteristics of those collected in BSI-2 (mid-May 2017), reflecting the timing of freshet peaks in each year.

The group Chlo was also dominant during the spring freshet and was found in the vicinity of river plumes (Figure 18H), characterized by lower salinities. This group was characterized by lower Chla values than others and was associated with very turbulent conditions (field observation). The significantly higher nitrate to phosphate ratio in this group (Table 6) reflects the generally higher values of $[\text{NO}_3^-]$ in the riverine endmembers (data not shown), in comparison to marine samples. Moreover, the suspended sediment- and CDOM-laden waters of river plumes generate the highest absorption and backscattering coefficient values of BSI. The highest b_b (b_{bp}) values in the red portion of the spectrum characteristic of Chlo are explained by higher values of the spectral slope of b_{bp} (γ), which likely reflects higher concentrations of particulate organic matter (Araújo and Bélanger, 2022).

After the spring freshet, as water temperature continue to increase, the groups PraD and PryD occupied the BSI region, and this last throughout the summer. Significant lower phosphate concentrations were found to be associated with these two groups (Table 6), while nitrate depletion occurred a few days after their appearance (in-between BSI-3 and BSI-4 campaigns, Figure 22B). The nitrate-depleted conditions then continued in summer up to early fall.

The group dominated by PE-containing cyanobacteria, Cy, began dominating BSI waters in early fall, although its presence was already noted in mid-summer at the station farthest from the shore (BSI-5, Figure 18G). In mid-fall (BSI-7) nitrate concentrations are restored (Figure 19A, Table 6).

The shape and relative magnitudes of remote sensing reflectance ($R_{rs}(\lambda)$) reflected the importance of the bio-optical environment for the determination of phytoplankton assemblages in nearshore waters of BSI. Strong differences in R_{rs} (Figure 21B; Table 7), in the blue, green, and red bands (465, 566, and 665 nm, respectively), and in SST (Figure 19C; Table 6) between assemblages of phytoplankton suggested the potential of using multispectral and thermal infrared radiometer sensors onboard Earth Observation platforms to infer about them. An inverse framework where hypothetical satellite-derived SST and $R_{rs}(465)$, $R_{rs}(566)$, and $R_{rs}(665)$ are used as inputs in the classification of BSI waters is therefore proposed (Figure 23).

Firstly, the group Chlo presented the highest values of $a_{cdom}(465)$ and $b_{bp}(665)$, resulting in low values of $R_{rs}(465)$ and very high values of $R_{rs}(665)$ and, consequently, were found in more reddish waters. Considering this, using a simple threshold of the ratio $R_{rs}(665)/R_{rs}(465)$, the group Chlo can be separated from others. Secondly, the lowest values of a_{cdom} and a_{nap} for group Dia resulted in the highest values of $R_{rs}(465)$ and $R_{rs}(566)$, comparatively to other groups. Thus, the sum of R_{rs} in these two wavelengths is used to target group Dia, and SST is also included to better distinguish it from group Cy.

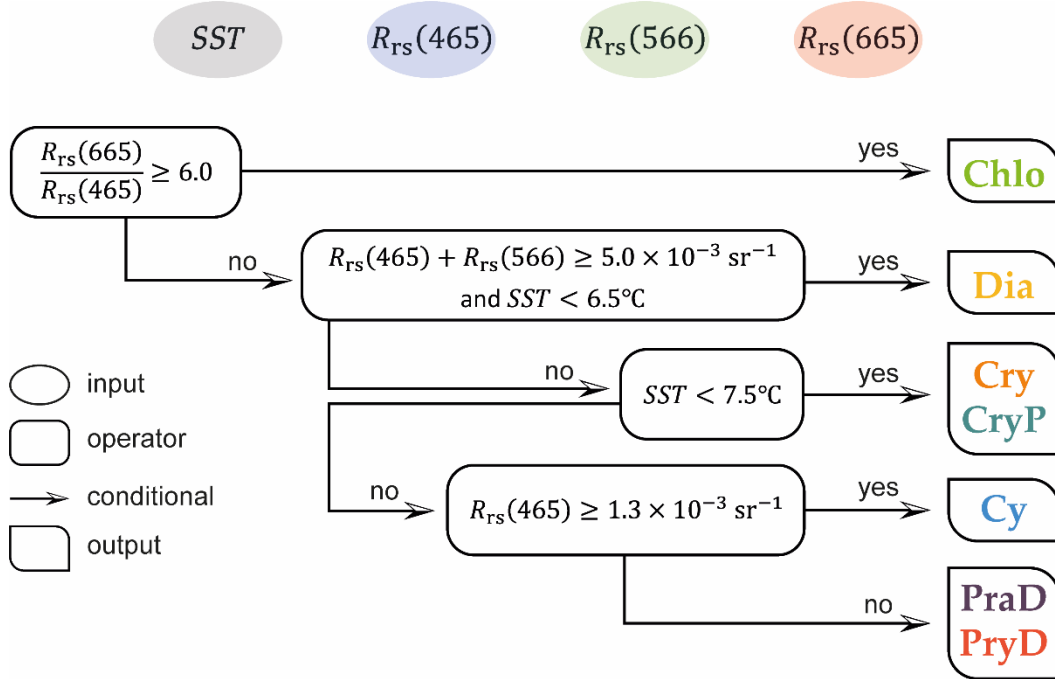


Figure 23. Idealized framework to separate the different phytoplankton assemblages using satellite-derived sea surface temperature (SST) and remote sensing reflectance in the blue ($R_{rs}(465)$), green ($R_{rs}(566)$), and red ($R_{rs}(665)$) regions of the spectrum

In a third step, taking advantage of different temperature niches occupied by the phytoplankton assemblages, another threshold is used to separate groups Cry and CryP from groups Cy, PraD, and PryD. Finally, the lower a_{cdom} of Cy, and its influence on $R_{rs}(465)$, is used to separate this group from PraD and PryD (Figure 23).

In a simple validation exercise, the presented framework was applied to the in situ R_{rs} and SST measurements to verify its coherence. When compared to the original discrimination of the seven phytoplankton assemblages (re-grouped in five, as in Figure 23; $n = 72$) determined by the PCA/HCA method, the result of this empirical inversion succeeds 92%. The samples where this procedure failed refer mainly to some isolated groups in the context of other dominant groups in the same field campaign, as for example a single PraD (Figure 18D) and a Dia sample (Figure 18H).

To test the applicability of this framework in real imagery, we processed two Landsat 8 images from 2017 (April 4 and May 15, stars in Figure 22B), downloaded as Level-1 Collection 2 data and distributed by the United States Geological Survey (USGS). The $R_{rs}(\lambda)$ thresholds presented in Figure 23 were tested and adjusted while contemplating the Spectral Response Function of the Operational Land Imager (OLI) of bands 2 (blue), 3 (green), and 4 (red). The two images were atmospherically-corrected using the dark spectrum fitting algorithm implemented in ACOLITE software (Vanhellemont, 2020a, 2019). For SST retrieval, the images of the Thermal Infrared Sensor (TIRS) were processed using the Thermal Atmospheric Correction Tool (TACT), also implemented in ACOLITE (Vanhellemont, 2020b, 2020c).

The application of the proposed framework in the two images (Figure 24) successfully targeted the dominance of group Dia in early April, as both R_{rs} values in the blue and green were higher than 0.005 sr^{-1} and SST values were the lowest when compared to other periods. Following the freshet, the classification of the image from mid-May also could detect the presence of the group Cry/CryP in nearshore waters of BSI, while the group Dia were more restricted to offshore waters. The occurrence of group Cy at this period of the year is probably a misclassification due to the overestimation of R_{rs} in the blue region from the atmospheric correction procedure (see Mabit et al., 2022). In this case, the classified group Cy would actually represent a dominance of phytoplankton assemblages from groups PraD/PryD. Nevertheless, the application of the framework in remote sensing imagery showed to be suitable.

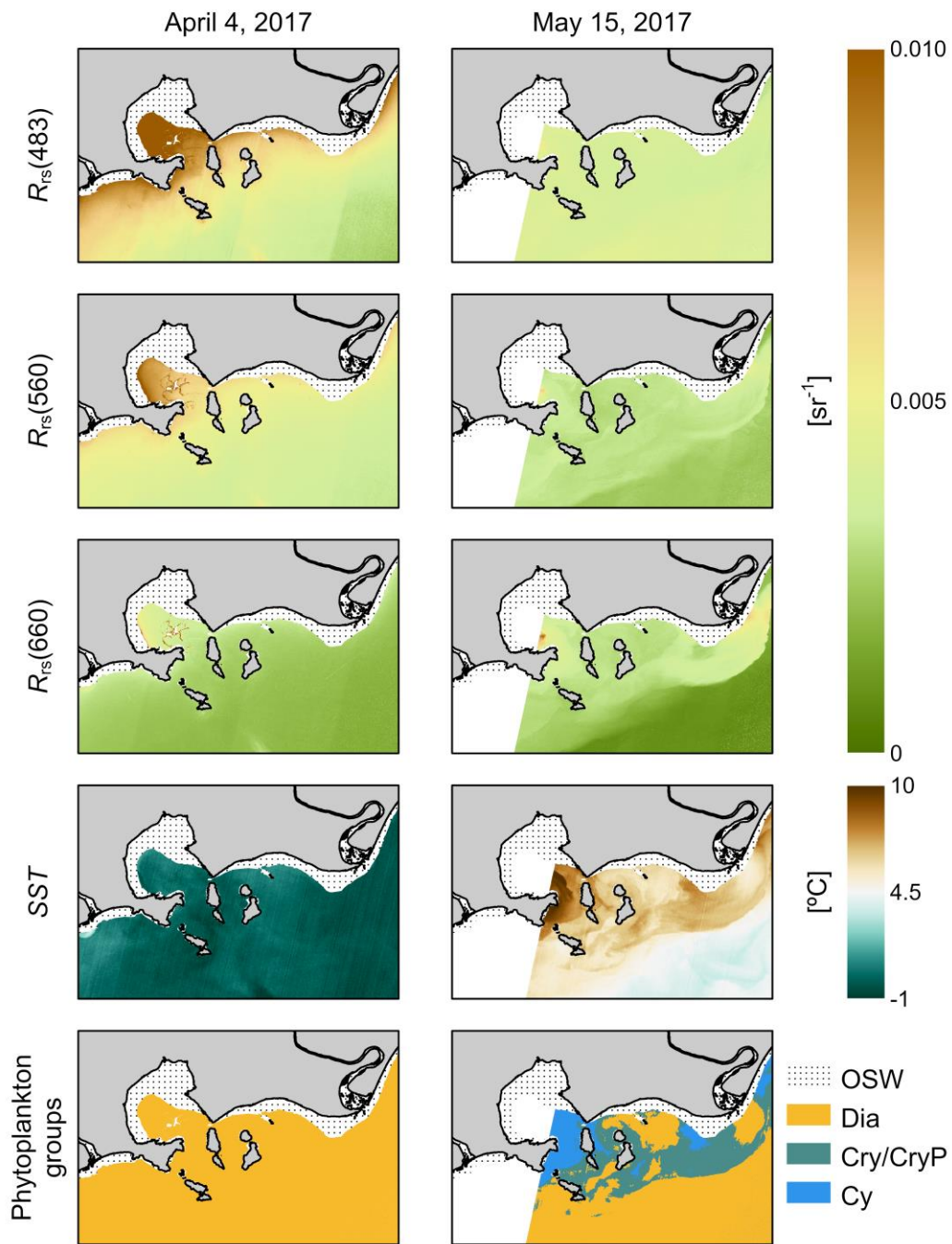


Figure 24. Application of the exposed framework shown in Figure 23 in satellite images of the Operational Land Imager (OLI) and the Thermal Infrared Sensor (TIRS) of Landsat 8. The atmospherically corrected images of the blue, green, and red bands, the sea surface temperature, and the resulting classification of the groups of phytoplankton assemblages are shown for two dates: April 4 and May 15, 2017

2.6 DISCUSSION

The potential for identification of major phytoplankton assemblages from pigment concentrations and <20 µm autotrophic cell abundances, in a dynamic nearshore subarctic environment, was evaluated. The combined PCA and HCA techniques applied to these proxies demonstrated to be a good indicator of distinctive communities of phytoplankton in the studied area, and it was confirmed, to some extent, by the LM taxonomy analysis. This dataset was comprehensive in terms of temporal (seasonal, from mid-spring to early fall) and spatial (order of 10⁰ to 10¹ km) scales. However, winter conditions, early phytoplankton spring bloom and pre-bloom (March-April), and mid-summer (August) conditions are missing.

The seven clusters revealed relevant characteristics associated to the following groups (Figure 16; Table 13, Annex 2): prasinophytes and dinoflagellates (PraD); prymnesiophytes and dinoflagellates (PryD); cyanobacterias (Cy); diatoms (Dia); cryptophytes (Cry); cryptophytes and prasinophytes (CryP); and chlorophytes (Chlo). These phytoplankton assemblages have been reported elsewhere in subarctic and temperate estuaries and coastal areas (Blais et al., 2022; Roy et al., 1996; Vallières et al., 2008; Vaultot et al., 2008). However, the nomenclature adopted in this study reflects pigment ratios characteristics used to distinguish the major phytoplankton assemblages but are not necessarily related to higher biomass or numerical dominance of one or another taxonomic class.

The combination of flow cytometry and HPLC pigment analysis revealed complementary to each other on assigning the major classes of phytoplankton assemblages. For example, the presence of certain pigments (e.g., prasinoxanthin, 19'-hexanoyloxyfucoxanthin) allowed the determination of groups PraD and PryD, and they also presented a high number of picoeukaryotes (Figure 16). *Micromonas pusilla* and *Chrysocromulina sp.* are candidate species to be representative of these clusters, respectively, as they are ubiquitous in cold marine environments (see review of Vaultot et al., 2008). In addition, the ability to count the phycoerythrin-containing cyanobacteria) using flow

cytometry, while phycoerythrin is a pigment not detected by standard HPLC method, was an asset to identify assemblages dominated by cyanobacteria (group Cy), which is probably related to *Synechococcus sp.*

The biomass variability along the size spectrum of phytoplankton communities brings with them relevant ecological information (Cloern, 2018; and references therein). The approach of Uitz et al. (2006) partitioned the relative contribution to Chla of three different size classes, and it showed coherency with our interpretation of community structure of the seven identified groups. The fractional contribution of picophytoplankton to Chla (f_{pico}) estimated from HPLC pigments ($f_{\text{pico}}^{\text{HPLC}}$) and from flow cytometry ($f_{\text{pico}}^{\text{FC}}$) were coherent, especially for groups PraD and Cy (Figure 17A).

The overall dominance of $f_{\text{micro}}^{\text{HPLC}}$ over other fractions was noticeable for most of the phytoplankton assemblages, and comparable to other boreal coastal regions, such as in the Western English Channel and North Sea (Barnes et al., 2014). The general higher contribution of f_{micro} is expected in areas with relatively high biomass (Chla) and replenished nutrient conditions (Brewin et al., 2019; Cloern, 2018). The dispersion from f_{micro} (right corner of the ternary diagram shown in Figure 17B) towards f_{nano} (upper corner), for Cry, Cryp, and PryD, and towards f_{pico} (left corner), for PraD and Cy, agreed with the inferred characteristics of each group.

The samples from the middle of the Lower St. Lawrence Estuary (at PMZA station), collected from mid-summer to fall season (Table 5), presented only two phytoplankton assemblages (Dia and PraD), but relatively higher biomass compared to BSI. The nearshore BSI region has more variability in terms of physical and optical conditions than the PMZA location and, consequently, a more diverse microbial community, including phytoplankton, is expected. Although Dia and PraD assemblages were found in both PMZA and BSI, their nutrient and physical environment were very distinctive (Figure 19, Table 6). The higher concentrations of all nutrients and high salinity values at PMZA are due to upwelled waters

in the Lower St. Lawrence Estuary (Therriault et al., 1990) while BSI is influenced by the Gulf of St. Lawrence waters (see Koutitonsky and Bugden, 1991).

The seasonal variability of the phytoplankton assemblages is a common feature in temperate and polar coastal waters and estuaries (e.g., Ansotegui et al., 2003; Trefault et al., 2021). In addition, local river discharge in these environments is a major driver of phytoplankton composition (Domingues et al., 2005), biomass and production, particularly during the spring freshet (Malone et al., 1988). Overall, we found that the seasonal succession of the phytoplankton assemblages in surface waters of BSI is intrinsically related to changes in the environmental niches that are largely driven by bio-optical conditions and sea surface temperature.

Before the spring freshet, the group Dia fully occupied BSI surface waters, as expected for high-latitude spring blooms dominated by large cells (diatoms) (Carstensen et al., 2015; Tremblay et al., 2006). The low nutrient concentrations found during BSI-1 campaign suggest that phytoplankton growth was nutrient-limited at the time. While silicate depletion has been found to be responsible for the termination of an Arctic diatom bloom (Krause et al., 2019), the fact that silicate concentrations of $\sim 0.2 - 1.1 \mu\text{M}$ persisted after nitrate had reached extremely low values of $< 0.1 \mu\text{M}$ indicates that the latter presumably drives bloom termination in the surface waters of BSI (Figure 19). A major shift in the coastal light environment occurs when freshet brings massive concentration of terrigenous optical constituents.

During higher riverine discharges, the assemblages associated with cryptophytes (Cry and CryP) occupy the waters of BSI. The assemblages associated with chlorophytes (Chlo) were also found during the spring freshet and, due to the proximity of the riverine discharges, the highest absorbing and turbid conditions conferred to them less biomass compared to other assemblages.

After freshet and with warmer temperatures in surface waters, the assemblages composed by dinoflagellates co-occurring with smaller phytoplankton cells (PraD and PryD)

replace groups Cry and CryP in BSI. These assemblages were characterized by nitrate-depleted conditions just after their first appearance in BSI-3 (Figure 22), and with lower concentration of phosphate. Nitrate-depleted conditions were also found to be associated with phytoplankton communities related to small prymnesiophytes and prasinophytes in the North Atlantic and Chukchi Sea (Hill et al., 2005; Sieracki et al., 1993). Notably, the occurrence, or even blooms, of the toxic dinoflagellate *A. catenella* are likely associated to these two groups, as previously reported in summer for BSI (Weise et al., 2002) and the Lower St. Lawrence Estuary (Fauchot et al., 2008; Roy et al., 2021).

At the end of summer and throughout fall, the assemblage associated with a high abundance of PE-containing cyanobacteria (Cy) dominates BSI waters. However, the environmental niche they occupy is distinguishable from those of PraD and PryD only by fall (BSI-7), when nitrate concentration levels are replenished, and salty (and less absorbing) waters from the Gulf of St. Lawrence are found.

The seasonal variability of surface nutrients followed the general pattern of the Gulf of St. Lawrence, especially regarding the establishment of nitrate-depleted conditions in the summer (Blais et al., 2019; Tremblay et al., 2000). Nutrient concentrations in the nearshore and coastal areas of the Bay of Sept-Îles were consistently lower than those of upwelled waters in the Lower St. Lawrence Estuary (AZMP buoy, Blais et al., 2019).

The ratio $[\text{NO}_3^-]:[\text{PO}_4^{3-}]$ was consistently lower than the Redfield value (16:1) but showed large differences between phytoplankton assemblages (Table 6). The lowest values observed for this ratio here are typical of coastal areas, including estuaries, indicating that N is generally the limiting factor for phytoplankton growth (Howarth et al., 2021; and references therein). Moreover, Howarth et al. (2021) also demonstrated that, in addition to the contribution of continental runoff to nutrient loads in coastal areas, the adjacent ocean also strongly affects nutrient availability in these areas. This scenario is consistent with our results for nitrate concentrations in BSI during late fall.

The seasonal (spring to fall) succession of phytoplankton assemblages in BSI region exhibit a shift from large cells, in the spring bloom (group Dia), to smaller ones (nano- and pico-phytoplankton size classes) from summer to fall. This shift started after the spring freshet, towards nanophytoplankton (cryptophytes, groups Cry and CryP), followed by pico- and nano-eukaryotes such as those of groups PraD and PryD, coexisting with dinoflagellates, and finally cyanobacteria (group Cy).

The CDOM-laden characteristic of the nearshore waters of BSI makes the a_{cdom} a determining IOP in shaping the R_{rs} , especially at shorter wavelengths ($\sim <600$ nm). Another characteristic of BSI waters (and other nearshore zones of the St. Lawrence Estuary; see Araújo and Bélanger, 2022) is the generally flatter spectral shape of the particulate backscattering coefficient (approximately $-1 < \gamma < 0.5$) comparatively to other coastal waters (e.g., Antoine et al., 2011). Furthermore, the specific $b_{\text{bp}}(\lambda)$ in relation to dry-mass concentration of suspended particles is very low compared to other regions, a characteristic of the particulate and dissolved organic-rich waters of BSI (Araújo and Bélanger, 2022). This is also reflected in the relatively lower $R_{\text{rs}}(\lambda)$, particularly in the red region of the spectrum, expected for a determined concentration of particles, when compared to other regions (Mabit et al., 2022).

Phytoplankton absorption (a_{phy}) represents a small fraction of the total absorption budget in BSI and, consequently, $R_{\text{rs}}(\lambda)$ signals are more sensitive to other optically active constituents than phytoplankton itself. This result implies that algorithms used to discriminate major phytoplankton assemblages that rely only on phytoplankton optical properties may have limited applications in BSI, as it is the case for other optically complex waters (e.g., Arctic ocean; Reynolds and Stramski, 2019). Nevertheless, significant differences in a_{phy} spectra between some groups were found. Moreover, analysis of the spectral shape of a_{phy} and the Chla-specific a_{phy} also revealed significant differences in the seasonal domain (Araújo and Bélanger, 2022). Taking these results into consideration, the phytoplankton absorption can be an asset to assess the major phytoplankton assemblages in

BSI, as demonstrated for diverse locations by other studies (e.g., Hoepffner and Sathyendranath, 1991, 1993; Devred et al., 2006; Oliveira et al., 2021; Sun et al., 2022).

Recent satellite missions and respective sensors covers the blue (~465 nm), green (~566 nm), and red (~665 nm) region of the spectrum, and with a relevant spatial resolution (order of $\sim 10^1$ m) for the scale of this study (see review of Werdell et al., 2018), allowing the retrieval of the remote sensing reflectance (R_{rs}) in these spectral bands. Another common satellite-derived parameter is the sea surface temperature (Minnett et al., 2019). Temperature is a major controlling factor of phytoplankton phenology (e.g., Trombetta et al., 2019) and it was found to explain well the phytoplankton primary production in the estuary and Gulf of St. Lawrence, under low nutrient concentration circumstances (Babin et al., 1991). The results of the framework shown in Figure 23 and its application in remote sensing imagery (Figure 24) demonstrated that sensors onboard Earth Observation platforms can be used to infer about the general seasonal pattern of the major phytoplankton assemblages in the BSI region.

Although the proposed approach is empirical in nature, its foundations remits to the general bio-optical background and physical environment in which each assemblage is contextualized. Operational satellite missions such as the Landsat 8-9, carrying the Operational Land Imager (OLI) and the Thermal Infrared Sensor (TIRS), Sentinel-2, carrying the MultiSpectral Instrument (MSI), and Sentinel-3, carrying the Ocean and Land Colour Instrument (OLCI), are examples of sensors that could be used to investigate the variability of the phytoplankton assemblages in coastal zones. The suitability of application of this approach was shown in two scenes collected by Landsat 8 OLI/TIRS (Figure 24). However, inherent constraints to optical remote sensing such as persistent cloud cover over target regions and difficulties in atmospheric correction (a necessary step to obtain R_{rs} from top-of-atmosphere radiances) in highly absorbing waters, as it is the case of nearshore regions of the estuary and Gulf of St. Lawrence (Mabit et al., 2022), will limit their application. Another important constrain to consider is the potential difference of temperatures used in this study,

collected by in situ thermometers, to those collected by satellite radiometers, which are related to the sea surface skin temperature (see Donlon et al., 2002; Minnett et al., 2011).

Our general hypothesis that the composition of major assemblages in a coastal area will covary with temperature and the bulk optical environment (IOPs) is confirmed. Furthermore, the premise that the IOPs characterization is a necessary step to investigate the phytoplankton assemblages using optical approaches (as in Reynolds and Stramski, 2019) in a coastal area was also confirmed. Nevertheless, the composition of phytoplankton assemblages likely reflected major traits that were shaped by different environmental niches.

2.7 CONCLUSIONS

Given the intrinsic dynamic of coastal and estuarine areas, understanding the ecology of phytoplankton is a major challenge for scientists and, consequently, are often overlooked by stakeholders, managers, and policy makers. The application of the proposed framework to retrieve major phytoplankton assemblages using satellite imagery would favor the monitoring of Essential Biodiversity Variables in coastal ecosystems (Muller-Karger et al., 2018), deriving information about their distribution and with potential to extend it to functional traits. Although developed in the context of the subarctic Bay of Sept-Îles, similar approaches could be successfully implemented in other coastal regions, especially those that experience strong seasonal variability.

In view of ecological modelling (coupled with hydrodynamical modelling, as for an aquatic system), the information about major phytoplankton assemblages derived by satellite could be integrated into a monitoring program including automated buoys to collect high frequency meteorological and oceanographic data (Eulerian perspective), and regular (space and time) field campaigns to collect target biogeochemical and optical parameters.

Global warming has an important role in restructuring major phytoplankton assemblages (Benedetti et al., 2021) and developing new tools to systematically monitor

these microorganisms that are key to coastal ecosystems are urged. Moreover, bringing the scientific knowledge developed in this study into a broader context, such as its mapping onto a Social-Ecological-Environmental System, as presented by Ferrario et al. (2022), would bring benefits to society.

DATA AVAILABILITY STATEMENT

The datasets generated and analyzed for this study can be found in the St. Lawrence Global Observatory repository (<https://ogsl.ca/en/home-slgo/>), under the CHONe II project dataset.

AUTHOR CONTRIBUTIONS

CA and SB designed the study. CB was responsible for the flow cytometry analysis. J-ÉT was responsible for the nutrient analysis. SB contributed to fundraising, fieldwork, and software development for optical data processing. CA conducted fieldwork, laboratory analysis, curated the data, and wrote the first draft of the manuscript. All authors contributed to manuscript revision, read and approved the submitted version.

FUNDING

The data used in this study was mainly supported by the interdisciplinary project “Canadian Healthy Oceans Network” (CHONe-2), funded by the Natural Sciences and Engineering Research Council of Canada (NSERC) and its partners: Department of Fisheries and Ocean Canada and INREST (representing the Port of Sept-Îles and the city of Sept-Îles). CA was supported by PhD scholarships from CHONe-2 and the Fond de Recherche du Québec – Nature et technologies (FRQNT), through a grant of the Merit Scholarship Program for Foreign Students (PBEEE, grant number 263427). This study was also supported by a NSERC Discovery Grant of SB (RGPIN-2019-0670).

ACKNOWLEDGEMENTS

We acknowledge all people involved in the field work campaigns and laboratory analysis, with special thanks to Alexandre Théberge, Zélie Schuhmacher, and Dr. François-Pierre Danhiez. Thanks to Mélanie Simard and Julie Major for pigment analysis, to Sylvie Lessard for the phytoplankton identification and enumeration by light microscopy, to Gabrièle Deslongchamps and Jonathan Gagnon for nutrient analysis, to Raphaël Mabit for the C-OPS data processing, and to ARCTUS Inc. for kindly providing SST images processed using the TACT algorithm implemented in ACOLITE. CA also acknowledges Drs. Rick Reynolds and Michel Gosselin for insightful discussions in early versions of this manuscript.

CONFLICT OF INTEREST

The authors declare that the research was conducted in the absence of any commercial or financial relationships that could be construed as a potential conflict of interest.

ARTICLE 3 :

**MASSIVE AREAL COVERAGE INCREASES OF THE FOUNDATION
SPECIES *ZOSTERA MARINA* L. IN A LARGE ESTUARINE SYSTEM
REVEALED BY LANDSAT TIME SERIES IMAGERY**

Article in preparation.

Authors:

Carlos A.S. Araújo^{a,b}, Simon Bélanger^{a,b}, Pascal Bernatchez^{a,b}, Mathieu Cusson^{b,c}

^a Département de biologie, chimie et géographie et groupe BORÉAS, Université du Québec à Rimouski, Rimouski, QC G5L 3A1, Canada

^b Québec-Océan, groupe interinstitutionnel de recherches océanographiques du Québec, Québec, QC G1V 0A6, Canada

^c Département de sciences fondamentales, Université du Québec à Chicoutimi, Chicoutimi, QC G7H 2B1, Canada

3.1 ABSTRACT

The ecosystem services and functions of seagrass meadows are indisputable. In this study, the dynamics of surface area coverage of eelgrass (*Zostera marina* L.) meadows at broad spatial scales (meters to kilometers) and at an annual to decadal temporal scales were investigated in four relatively contrasting subregions of the estuary and Gulf of Saint Lawrence (EGSL), Eastern Canada, encompassing cold temperate and subarctic environments. To achieve this, Landsat imagery reflectance products from the Thematic Mapper (TM), the Enhanced Thematic Mapper Plus (ETM+), and the Operational Land Imager (OLI) sensors were accessed and processed through a freely cloud computing platform (Google Earth Engine). The meadows in all subregions occur mainly in intertidal zones, and the processing of the images considered the restrictions imposed by tidal and water optical properties variabilities, as well as limitations by the sensors design. The classified polygons encompass at least a 25% coverage of eelgrass in a determined patch, while the classification accuracy showed very good agreement (overall accuracy of 91% and kappa coefficient of 0.81) when compared to coastal ecosystem habitats maps generated by photointerpretation (and with field verification). From the 39-year period analyzed (1984 – 2022), the surface area coverage of the meadows presented a dramatic increase reaching 10 to 20-fold. For some subregions, the expansion of meadows was towards land – i.e., starting closer to subtidal areas. However, relative short-term losses (interannual scale) can occur differently among the subregions. While remaining an open question, the relationship between the dynamical coverage of eelgrass at interannual and decennial scales with environmental variables should be targeted for better understanding these complex nearshore systems. Overall, the results revealed these nearshore EGSL zones as important areas for biodiversity, while the (blue) carbon sequestration rate remains to be quantified. Notwithstanding, recent advances in Earth Observation satellites can be an asset in quantifying seagrass stocks in coastal zones.

Keywords: eelgrass meadows, remote sensing, Landsat, subarctic, nearshore environment, intertidal areas, Google Earth Engine

3.2 RÉSUMÉ

Les services écosystémiques et les fonctions des herbiers marins sont incontestables. Dans cette étude, la dynamique de la couverture de la superficie des herbiers de zostère (*Zostera marina* L.) à de larges échelles spatiales (mètres à kilomètres) et à des échelles temporelles annuelles à décennales a été étudiée dans quatre sous-régions relativement contrastées de l'estuaire et du golfe de Saint-Laurent. Lawrence (EGSL), Est du Canada, englobant les environnements tempérés froids et subarctiques. Pour ce faire, les produits de réflectance des images Landsat des capteurs Thematic Mapper (TM), Enhanced Thematic Mapper Plus (ETM+) et Operational Land Imager (OLI) ont été consultés et traités via une plate-forme d'infonuagique gratuite (Google Earth Engine). Les herbiers de toutes les sous-régions se trouvent principalement dans les zones intertidales, et le traitement des images a pris en compte les restrictions imposées par les variabilités des propriétés optiques de la marée et de l'eau, ainsi que les limitations de la conception des capteurs. Les polygones classés englobent au moins 25 % de couverture de zostère dans une parcelle déterminée, tandis que la précision de la classification a montré un très bon accord (précision globale de 91 % et coefficient kappa de 0,81) par rapport aux cartes d'habitats des écosystèmes côtiers générées par photo-interprétation (et avec vérification sur le terrain). Sur la période de 39 ans analysée (1984 – 2022), la superficie couverte par les herbiers a présenté une augmentation spectaculaire atteignant 10 à 20 fois. Pour certaines sous-régions, l'expansion des herbiers s'est déroulée vers la terre – c'est-à-dire en commençant plus près des zones infralittorales. Toutefois, les pertes relatives à court terme (échelle interannuelle) peuvent survenir différemment selon les sous-régions. Tout en restant une question ouverte, la relation entre la couverture dynamique de zostère aux échelles interannuelles et décennales et les variables environnementales devrait être ciblée pour une meilleure compréhension de ces systèmes complexes près du littoral. Dans l'ensemble, les résultats ont révélé que ces zones littorales du EGSL sont importantes pour la biodiversité, tandis que le taux de séquestration du carbone (bleu) reste à quantifier. Néanmoins, les progrès récents des satellites d'observation de la

Terre peuvent constituer un atout pour quantifier les stocks d'herbiers marins dans les zones côtières.

Mots-clés : herbiers de zostères, télédétection, Landsat, subarctique, environnement littoral, zones intertidales, Google Earth Engine

3.3 INTRODUCTION

Seagrasses are recognized as foundation species, i.e., they modify their environments to create singular habitats, and constitute highly productive areas in coastal and nearshore environments, providing valuable ecosystem services and functions, such as habitat for various species (including exploited ones), coastline protection, improvement of water quality and (blue) carbon storage (Beck et al., 2001; Duarte, 2017; Henderson et al., 2019; Holmer, 2019; Ondiviela et al., 2014; Röhr et al., 2018; Unsworth et al., 2019b; Whitfield, 2017). Historically, seagrass has been negatively affected by human activities, while the effect of multiple stressors is commonly a matter of consideration (Dunic and Côté, 2023; Lefcheck et al., 2017; Lotze et al., 2006; Orth et al., 2006). Notwithstanding, conservational and monitoring efforts targeting best management practices of seagrass meadows are delineated worldwide (Grech et al., 2012; Unsworth et al., 2019a, 2015).

From a global perspective, seagrass meadows present a general declining trend in extent, although high variability is observed at regional and temporal scales (Dunic et al., 2021; Waycott et al., 2009). As highlighted by Gallagher et al. (2022), global estimates of seagrass coverage can vary 10-fold, either considering a compiled and verified dataset (McKenzie et al., 2020) or a predictive habitat model (Jayathilake and Costello, 2018), which suggests possible gaps of knowledge. However, knowledge about the distribution and extent of seagrass meadows is a minimum requirement for management practices, yet not publicly available in many coastal regions.

The heterogeneity of meadows at broad (meters to kilometers) spatial scales are complexly related to ecological processes (seagrass landscapes; *sensu* Boström et al., 2006; Turner, 1989). At these spatial scales, the yearly and decadal variations in the areal cover of seagrass meadows have also broad ecological relevance. In combination with traditional knowledge, including fieldwork, Earth Observation technologies are the most reliable method to assess information at broad temporal and spatial scales (see reviews of Hossain and Hashim, 2019; Veetil et al., 2020).

Canada has the longest coastline of the world and eelgrass (*Zostera marina* L.) meadows is a major habitat in nine of its twelve bioregions (Murphy et al., 2021). In the estuary and Gulf of the St. Lawrence (EGSL), which connects the Great Lakes with the North Atlantic ocean and encompasses one of the largest estuaries in the world (El-Sabh and Silverberg, 1990b), eelgrass meadows were abundant and commercially exploited (Michaud, 1985) before the so-called “wasting disease” (see Den Hartog 1987; Short et al. 1988). The latter is a pathogen attributed to a marine slime mold-like protist, *Labyrinthula zosterae* Porter and Muehlstein (Muehlstein et al., 1991), attributed as the cause of devastation of most eelgrass along the North Atlantic Coast by the end of the 1920’s. Punctual inventories and local knowledge reveal the reappearance of eelgrass in nearshore waters of EGSL at the end of the 20th century and relatively extensive meadows in recent years (e.g.; Lemieux and Lalumière 1995; Provencher and Deslandes 2012; Jobin et al. 2021). Notwithstanding, the distribution of eelgrass meadows in EGSL at broad spatial scales and considering a yearly to decadal time frame has not been reported. This is particularly true for the St. Lawrence Estuary and northern part of the gulf.

In this context, the following questions arise: Is eelgrass ubiquitous along EGSL coast? Is the rate of recovery similar in contrasting coastal setups? Do we observe linear trends or there are significant interannual variability? To answer these questions, the primary objective of this study was to build a long-term dataset of eelgrass distribution in ecologically significant areas (subregions) of EGSL, assessing its spatial and areal changes. A 39-year long time series of eelgrass coverage was built using the freely-available Landsat imagery archive (Wulder et al., 2022) and a free cloud computing platform (Google Earth Engine; Gorelick et al., 2017).

3.4 MATERIAL AND METHODS

3.4.1 Study areas

The four study sites (subregions; Fig. 25) are between temperate and subarctic zones with a climate classified as cold, without dry season, and with either warm or cold summer, but with trends indicating future warmer conditions (Köppen-Geiger classification; Beck et al., 2018). The subregions were chosen because eelgrass meadows are the dominant vegetated habitat present in relatively extensive tidal flats (Fig. 25B-E). In addition, each subregion is subject to dissimilarities in terms of environmental conditions, such as the degree of wave exposure, hydrodynamic regime, and optical properties of water.

From downstream to upstream (or from Northeast to Southwest) of EGSL, the subregions are the Bay of Sept-Îles (BSI), the Manicouagan Peninsula (MAN), the Rimouski bay (RIB), and the L'Isle-Verte bay (IVE, including a National Wildlife Area of Canada). The presence of large tidal flats in these regions (Fig. 25) is associated with a lowstand sea level followed by the Laurentian transgression in the mid-Holocene (Dionne, 2001), and to relatively sheltered positions in relation to central parts of the EGSL. Salt marshes (*Spartina alterniflora* Loisel) often occupy the upper limit of the tidal flats in BSI, RIB and IVE subregions, while sandy beaches are found along MAN subregion. Other depositional facies within the intertidal zones include deltas and tidal channels, and they can also be colonized by eelgrass, especially in MAN subregion. Scattered boulders and cobbles, in both intertidal and subtidal (infralittoral) zones, support the presence of diverse and abundant macroalgal assemblages, and the heterogenous seabed of the subtidal zones is more likely occupied by macroalgae than other vegetated substrate (Ferrario et al., 2022; Jobin et al., 2021).

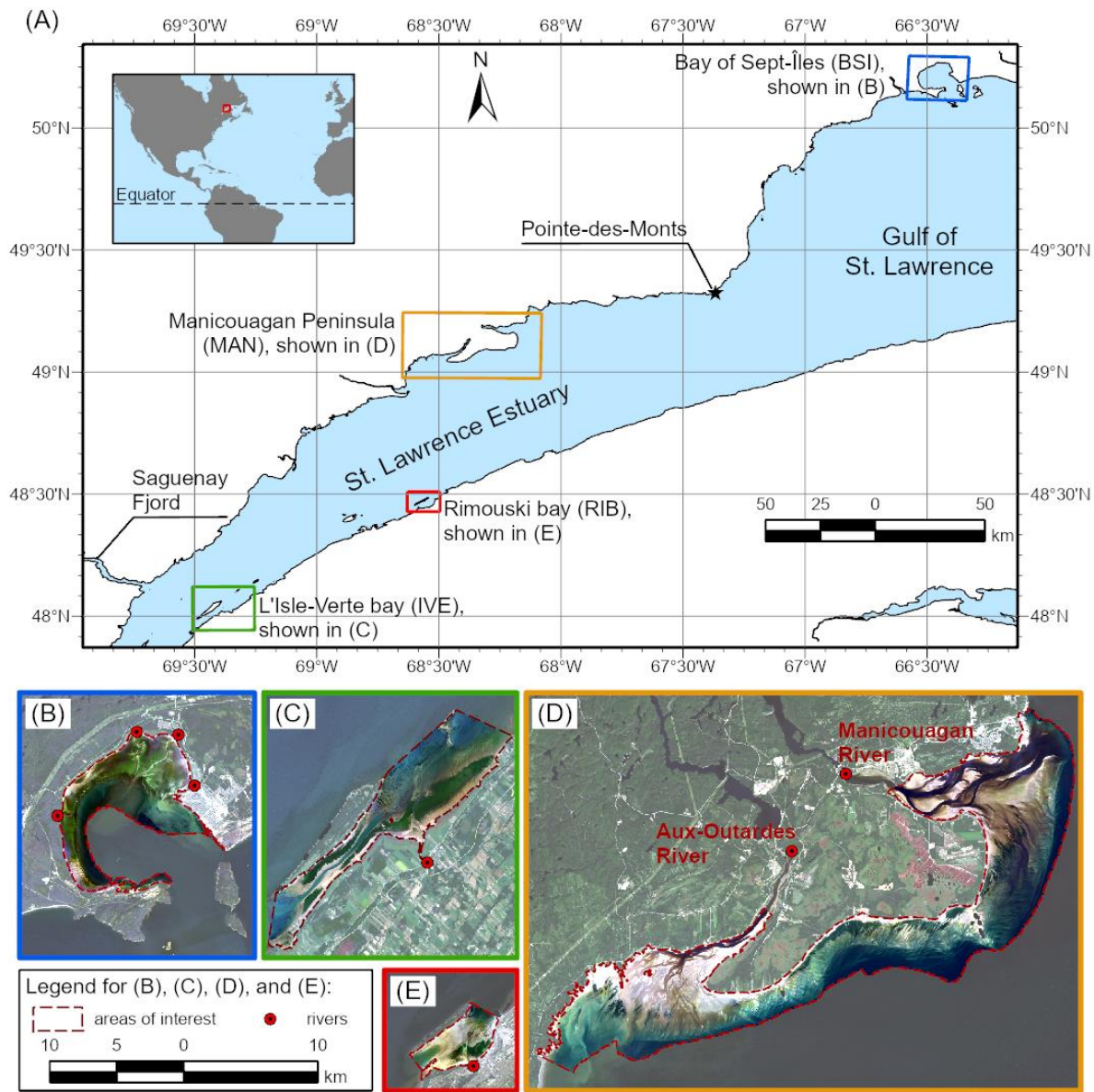


Figure 25. (A) Study areas (subregions) locations in the Estuary and Gulf of St. Lawrence (EGSL). The inset shows EGSL in North America context. Primary delimitation of areas of interest (red dashed lines) for the (B) Bay of Sept-Îles (BSI), (C) L'Isle-Verte bay (IVE), (D) Manicouagan Peninsula (MAN), and Rimouski bay (RIB). The main local riverine outlets are indicated for each subregion and the background images are a true-color composition of a recent (2020s) Landsat 8 (or 9) OLI scenes (USGS L2SP)

Besides different oceanographic characteristics of the Lower St. Lawrence Estuary (approximately from the mouth of the Saguenay Fjord to Pointe-des-Monts, Fig. 25), surrounding MAN, RIB and IVE, and the Gulf of St. Lawrence, surrounding BSI, all four subregions are under the influence of major and local riverine discharges. Firstly, the waters in nearshore zones of BSI are influenced by four rivers that outflow inside the bay (Fig. 25B, Araújo and Bélanger, 2022; Shaw et al., 2022). Secondly, the adjacency of MAN is under the influence of the river plumes of the Betsiamites, Aux-Outardes and Manicouagan (Fig. 25D, Therriault et al., 1990). Lastly, RIB and IVE, besides receiving waters from local riverine discharges, are also influenced by flushed waters along the south shore corresponding to the outflow of the Saguenay Fjord and the Upper St. Lawrence Estuary (Figs. 25E and 25C; El-Sabh et al., 1982; Therriault et al., 1990). The contrasting sea surface temperature and water optical conditions of the surrounding coastal environment of each subregion will be further examined in the results section.

The primary delimitation of the studied areas (highlighted portion of images in Fig. 25B-E) was performed using coastline extraction through satellite imagery, and bathymetry from the Canadian Hydrographic Service (CHS) Non-Navigational (NONNA) Bathymetric Data. For each subregion, a cloud-free Landsat 8-9 OLI scene (Collection 2, Level 2, available from the United States Geological Survey - USGS) acquired at high tide were used to delineate the upper boundary of the intertidal zone. The Modified Normalized Difference Water Index was calculated using the green and the shortwave infrared 1 (SWIR 1) surface reflectance (SR) values as (MNDWI; Xu, 2006):

$$MNDWI = \frac{SR_{Green} - SR_{SWIR1}}{SR_{Green} + SR_{SWIR1}}, \quad (9)$$

MNDWI values of approximately “0” were selected as a threshold to separate the nearshore zones (intertidal and adjacent subtidal) from land. Subsequently, the outer (lower) limit of BSI and MAN subregions were determined using the isobath of 15 meters, while the northeast and southwest limits of islands were used for RIB (Île Saint-Barnabé and Îlet Canuel) and IVE (Isle Verte and Île aux Pommes) subregions. An exploratory analysis of

Landsat time-series imagery at low-tide conditions assured that the areas of interest included continuous eelgrass meadows and that they were suitable for classification using sensors with a spatial resolution of 30 m. However, it should be noticed that this primary delimitation goes far below the intertidal zone. Next, we present the reasons to limit our study areas to intertidal zones.

3.4.1.1 Regional characteristics and rationale for image selection

The knowledge about variability of water optical properties, tides and reflectance of nearshore vegetation are primary requirements for mapping seagrass using optical approaches, including multispectral satellite imagery. In EGSL, eelgrass meadows occupy mainly intertidal and, to a lesser extent, shallow subtidal zones (Fig. 26). Fig. 26A shows a typical meadow found in L'Isle-Verte bay subregion.

The optical properties of nearshore waters of the northern part of EGSL are influenced by high Coloured Dissolved Organic Matter (CDOM) content and moderate Suspended Particulate Matter concentration (SPM) conditions (average of $\sim 10 \text{ mg L}^{-1}$) (Araújo and Bélanger, 2022). To illustrate the effect of optically significant constituents of the water in EGSL, the spectral diffuse attenuation coefficient of downwelling irradiance ($K_d(\lambda)$) and the light penetration depth ($Z_{90}(\lambda)$); as defined by Gordon and McCluney, 1975) are shown in Fig. 26C (mean \pm standard deviation). First, $K_d(\lambda)$ was calculated from *in situ* profiles of the downwelling diffuse irradiance ($E_d(\lambda)$), using a Compact Optical Profiling System (C-OPS, Biospherical Instruments Inc., San Diego) and taken in several field campaigns in BSI and MAN subregions (for details, see Araújo et al., 2022; Araújo and Bélanger, 2022). The $K_d(\lambda)$ was then used to determine $Z_{90}(\lambda)$ as:

$$Z_{90}(\lambda) = \frac{1}{K_d(\lambda)}, \quad (10)$$

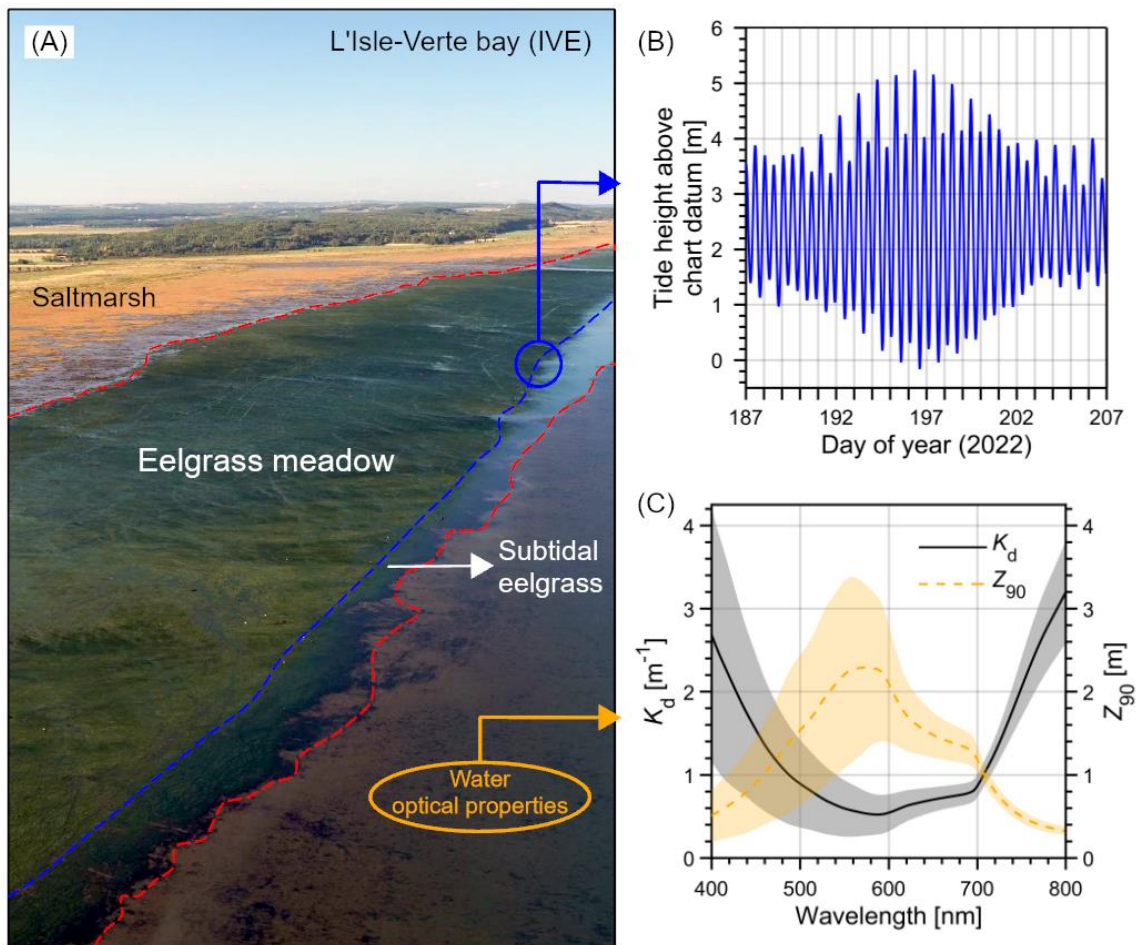


Figure 26. General characteristics of eelgrass meadows in the Estuary and Gulf of St. Lawrence and physical processes affecting their distribution. (A) Oblique aerial photograph taken in the L'Isle-Verte bay subregion at low-tide conditions (image courtesy from the *Laboratoire de dynamique et de gestion intégrée des zones côtières*, UQAR). (B) Tidal variability for a 20-day period in 2022 (tidal gauge in Baie-Sainte-Catherine, mouth of Saguenay Fjord - data available from the Canadian Hydrographic Service). (C) Some optical characteristics of the water column surrounding meadows: the spectral diffuse attenuation coefficient of downwelling irradiance ($K_d(\lambda)$) and the light penetration depth ($Z_{90}(\lambda)$). The solid and dashed lines indicate the mean values of K_d and Z_{90} , respectively, and the shaded areas indicate the (\pm) standard deviation.

Briefly, K_d will determine the amount of light that reaches the benthic substrate (Beer-Lambert law), with higher values meaning less light being transmitted to deeper layers, and

it can be related to the maximum depth of occurrence of meadows (Duarte, 1991). The Z_{90} can be defined as the depth above which 90% of light (i.e., the diffuse irradiance) is reflected (Gordon and McCluney, 1975). The Z_{90} values can roughly be associated to the depth in which a sensor can obtain information (in optically deep waters) from remote sensing. Lower values of Z_{90} (reaching less than 1 m) was observed at shorter wavelengths in the blue (<460 nm) and in the near-infrared regions (>700 nm). The maximum value of Z_{90} was observed around 570 nm (~2.3 m). It is important to note, however, the high variability of these parameters in the visible domain (400 to 700 nm), which reflects the importance of the seasonality in governing the optical properties.

Tidal variability will also affect the amount of light reaching the canopy of seagrass meadows. In EGSL, the tides are predominantly semidiurnal, with daily inequalities, and fortnightly cycles (spring and neap tides) are a marked feature (Fig. 26B). Typical range of neap and spring tides values are given for BSI subregion as 0.54 and 3.50 m, respectively (Shaw et al., 2022), but tidal amplitudes are higher upstream EGSL (see El-Sabh and Murty, 1990). Thus, at MAN and RIB subregions the amplitudes will be higher than in BSI, and even higher in IVE (reaching 5 m, in the example of Fig. 26C).

Besides the dynamic character of tides and water optical properties acting over the meadows and restricting their ease to map, another physical constraint to consider is the characteristics and limitations of Landsat sensors. Although the 30-m spatial resolution and similar spectral resolutions (similar center wavelengths, but varying bandwidths) across the different Landsat collections, there were significant improvements in radiometric quality from Landsat 4 TM to Landsat 9 OLI. TM and ETM+ sensors have 8-bit quantization, while OLI has 12 and 14-bits, for Landsat 8 and 9, respectively. This increment in radiometric precision improves overall signal-to-noise ratios (SNRs) and increases the performance of algorithms for earth science applications (Schott et al., 2016). Specifically, the lower radiometric quality of TM and ETM+ sensors implies in poor atmospheric correction performances to retrieve SR (or remote sensing reflectance) for applications to water color (Xu et al., 2020). Consequently, the information of eelgrass meadows that are flooded by

tides are also compromised. Moreover, low reflectance values of nearshore waters of EGSL due to their strongly light-absorbing and weakly light-scattering character (Araújo and Bélanger, 2022) makes the application of atmospheric correction methods challenging, even for Landsat 8 OLI or Sentinel 2 MSI sensors (see Mabit et al., 2022).

Nevertheless, the seasonal aspect of growth of the nearshore vegetation should also be considered for mapping the intertidal meadows. During boreal winter, ice and snow cover limits the growth of eelgrass in EGSL, but also the ability to map them using optical remote sensing approaches. Moreover, along the beginning of the growing season (approximately early May), the variability of reflectance values between different types of vegetation present in the intertidal zone are not significant, limiting their separability using multispectral imagery (Légaré et al., 2022).

3.4.2 Image repository and selection criteria

The mapping of eelgrass meadows was made using the Landsat Collection 2 (C2) Tier 1 (T1) Level 2 Science Product (L2SP). This collection embraces the satellites (sensors) Landsat 4, 5 (Thematic Mapper, TM), 7 (Enhanced Thematic Mapper Plus, ETM+), 8 and 9 (Operational Land Imager, OLI), and the surface reflectance (*SR*) products are generated by the Land Surface Reflectance Code (LaSRC, for Landsat 8-9; USGS, 2023) and by the Landsat Ecosystem Disturbance Adaptive Processing System (LEDAPS, for Landsat 4-5,7; Masek et al., 2006; USGS, 2021). The products are generated at 30-meter spatial resolution and cover a time-span of more than 40 years, while being fully-available in the catalog of Google Earth Engine (GEE) cloud computing platform.

The polygons of the primary delimitation areas of the four subregions were uploaded in GEE and used to crop each Landsat scene (a methodological flowchart is shown in Fig. 27). The collection of images was constrained between June to October (because of the ice, snow and vegetation reflectance phenology) and the scaling factors were applied to each *SR*

band (blue, green, red, near infrared, shortwave infrared 1 and shortwave infrared 2). Pixel quality attributes (namely the “*Dilated Cloud*” and “*Cloud*” attributes) generated from the CFMASK algorithm (Foga et al., 2017; Zhu and Woodcock, 2012) were selected and used to flag the *SR* bands. The cropped images with more than 50% of pixels masked by this procedure were discarded and not used in the following analysis.

Because of the limitations to access subtidal eelgrass meadows and to establish a concise analysis across all Landsat collections, only emerged (or non-flooded) pixels were considered for the classification procedure. A series of image processing techniques were implemented in GEE to extract emerged pixels. The near infrared band (SR_{NIR}) are sensitive to flooded areas because of the high absorption of water in this spectral region (e.g., Smith and Baker, 1981), and it was found to be empirically-related to tidal variability in nearshore EGSL (data not shown). Therefore, SR_{NIR} was used as input to separate *flooded* and *non-flooded* areas. Firstly, for noise removal, a filter (*convolve* function in GEE) was first applied considering a Gaussian kernel of radius equal to 3 pixels. The resulting images were then subject to a segmentation procedure, which consisted of a superpixel clustering based on SNIC (Simple Non-Iterative Clustering; Achanta and Susstrunk, 2017), available in GEE. Zonal statistics, namely the mean SR_{NIR} value of each segment was computed, and a threshold (~ 0.05) was used to separate the emerged areas of each image of the collections. This procedure presented good consistency with field observations and shallow bathymetric knowledge.

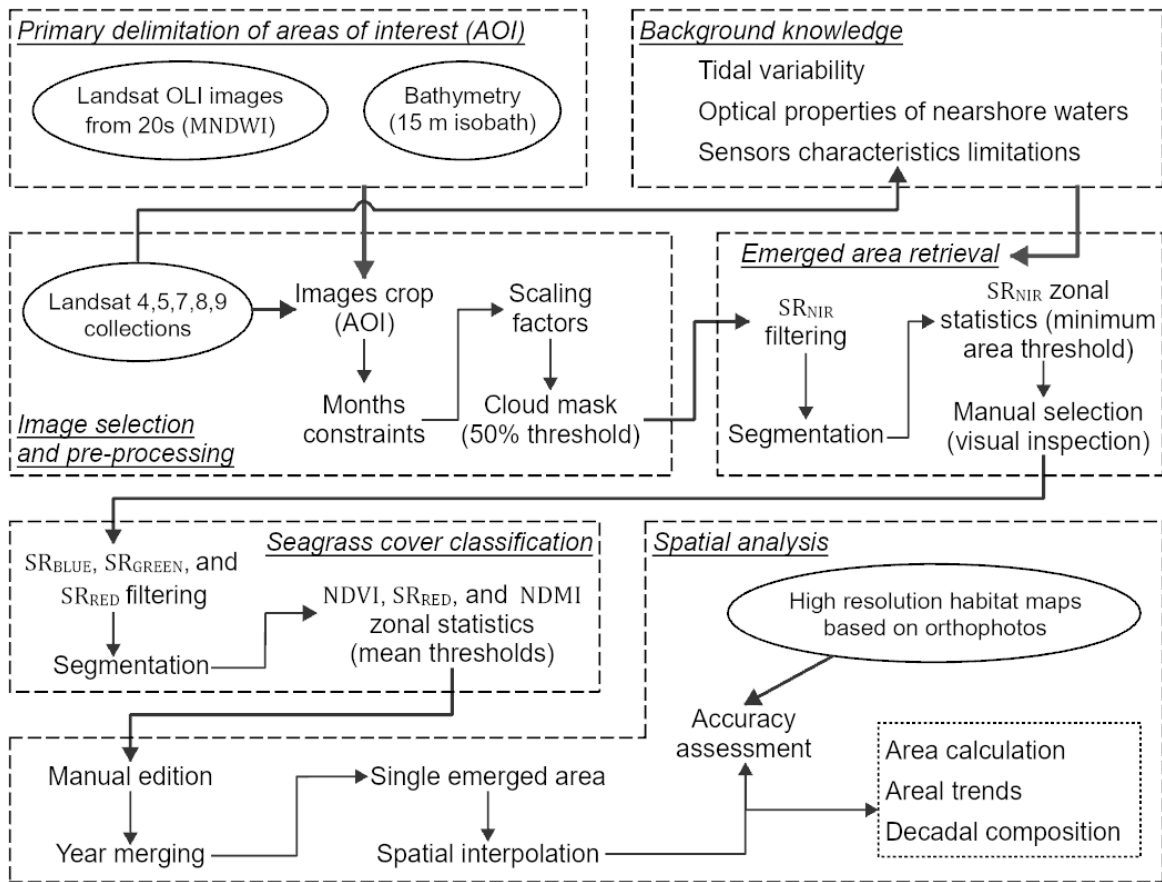


Figure 27. Methodological flowchart of the processing and analysis chain to assess the yearly and decadal variability of intertidal eelgrass meadows coverage in four subregions of the Estuary and Gulf of St. Lawrence

Considering only the emerged areas from the resulting images, a minimum number of pixels was established as thresholds for selecting images with a reasonable emerged area. For example, an image with lower number of pixels than the threshold value means that more pixels were considered as flooded, and therefore it was not selected for the following classification. The thresholds varied by subregion and were empirically determined so that a minimum of images was representative of the yearly variability of intertidal (and emerged) eelgrass meadows coverage for the period between 1984 to 2022. Finally, a manual selection based on visual inspection of individual images was made to avoid problems related to clouds

not detected by the masking procedure (e.g., cirrus), but also to not exceed more than four images in a single year.

3.4.3 Eelgrass cover classification

The final selected images were then classified to obtain eelgrass coverage. From the previous procedures, each image is only a fraction of the original primary delimitation areas, corresponding to emerged areas at the time of acquisition.

As for the emerged areas delimitation, the polygons of eelgrass meadows were obtained by segmentation and classification by object-based image analysis. Firstly, the blue, green and red bands were filtered (Gaussian kernel) and segmented using SNIC algorithm. The zonal statistics (mean values in each segment) were computed for each SR and selected vegetation and water indices. After testing several indices, we found that the Normalized Difference Vegetation Index (NDVI; Tucker, 1979) and the Normalized Difference Moisture Index (NDMI; Wilson and Sader, 2002) were the most useful on discriminating the eelgrass polygons in intertidal EGSL zones. The spectral indices are calculated as:

$$NDVI = \frac{SR_{NIR} - SR_{Red}}{SR_{NIR} + SR_{Red}}, \quad (11)$$

$$NDMI = \frac{SR_{NIR} - SR_{SWIR 1}}{SR_{NIR} + SR_{SWIR 1}}, \quad (12)$$

In short, the NDVI is used to assess vegetation greenness, while the NDMI is used to access the moisture level of either soil or vegetation. The mean values of NDVI, SR_{Red} and NDMI were used as thresholds in the rule-based classification scheme of the segmented images. The polygons were classified as eelgrass when (approximately) mean values of $NDVI \geq 0.3$, “AND” $SR_{Red} \leq 0.05$, “AND” $NDMI \geq 0.3$. The rationale to use these indices (or bands) and respective thresholds are further discussed in subsection 3.5.1.

The polygons classified as eelgrass and the (total) emerged areas of each image were exported from GEE, and a few of them required manual edition (because of reasons that will be further discussed).

3.4.4 Eelgrass cover analysis and accuracy assessment

For each subregion, the resulting polygons of eelgrass patches and emerged areas were grouped and merged by year. The merging process considered the maximum area occupied by all polygons (of the two classes) by each year. The number of images per year varied from 1 to 4, and years without images were not considered in the analysis. A final emerged area was calculated considering that a same pixel location was classified as “emerged” at least 70% of the total number of years that were analyzed. Finally, if the emerged area of a specific year did not cover the final (single) emerged area of the subregion, the missing areas were considered as being equal to the closest classified year (either *eelgrass* or *no eelgrass* classes).

The verification of the classification procedure was performed by direct comparison with maps of nearshore habitats based on orthophotos with a spatial resolution of 30 cm (Jobin et al., 2021; SIGEC, 2023). The orthophotos, acquired by Fisheries and Oceans Canada (DFO), were taken at low tide conditions in September or October in the years 2015 (RIB and IVE) and 2016 (BSI and MAN), and were composed by four bands (RGB + NIR). In short, the orthophoto images were first submitted to a segmentation algorithm in PCI Geomatica software, and the segments were classified based on visual interpretation by experts, using oblique aerial photos and fieldwork recognition as auxiliary data. For the comparison, only the segments classified as predominantly eelgrass and with at least 25% coverage were considered.

The spatial accuracy statistics were calculated through the computation of the confusion matrix (Congalton and Green, 2019), built considering the two classes and only in

the final emerged area polygon for each subregion. The metrics include the Producer's accuracy (% of each reference class mapped correctly), the User's accuracy (% of each map class that were correct in the reference), the overall accuracy (% of reference sites mapped correctly), and the Cohen's kappa coefficient (which shows the strength of agreement between two variables [reference and mapped data], with 0 indicating no agreement, and 1 complete agreement).

The final area of eelgrass meadows (per subregion and per year) was calculated by multiplying the number of classified pixels by the area of unitary pixel (equal to 900 m²). Similarly, the percentage of the area covered by the meadows in relation to the total emerged area was also calculated. Decadal changes of eelgrass meadows coverage were accessed by grouping the yearly patches by each decade, in a similar procedure of the yearly composition of the original classified images. Long term trend analysis of the meadows was investigated by dividing the area of meadows (of each subregion and year) by their initial area (from 1984). Nevertheless, the decadal (80s, 90s, 00s, 10s, 20s) compositions were compared to a reference year, which was the last year an image was classified for each subregion. Meadows that were present anytime of the analyzed period and that were not present in the reference year were also obtained.

All algebra of images described in this subsection were made using MATLAB software (MathWorks[®]), while final maps (presented as figures in this study) and the manual selection of polygons were made using ArcGIS Pro software (ESRI[™]).

3.4.5 Environmental variables

For comparing the different environmental background of the four subregions of EGSL, climatological means (and standard deviation) of sea surface temperature (SST, °C) and optical properties, namely the attenuation coefficient of downwelling irradiance, integrated over the photosynthetically available radiation (400 to 700 nm, PAR; $K_d(\text{PAR})$;

in m^{-1}) were accessed. These environmental variables are known to affect the spatial distribution of seagrass meadows.

The climatology of SST was retrieved from the Ocean Color SMI - Standard Mapped Image MODIS Aqua and Terra Data - processed by NASA's Ocean Biology Processing Group and available in GEE platform, available from 2000 to 2022. Each dataset (Aqua and Terra) is available on a daily-basis, and they were constrained only for the month of August, where the highest SST values are expected and the peak of growing of meadows are observed.

The $K_d(\text{PAR})$ were downloaded from the GlobColour project (<http://globcolour.info>), corresponding to a merged product of different satellite sensors (MERIS, MODIS Aqua, SeaWiFS, and VIIRS; see Maritorena et al. 2010), and encompassed the period from 1997 to 2022. Briefly, the normalized remote sensing reflectance obtained from the merged product is first used to compute the K_d at 490 nm, through the semi-analytical method of Lee et al. (2005), followed by an extrapolation for the estimation of $K_d(\text{PAR})$ using the method described in Saulquin et al. (2013). We assessed the monthly averages and only for the month of August. For both SST and $K_d(\text{PAR})$ the original spatial resolution of the datasets is 4 km, and the values for each subregion were obtained by taking a pixel outside the influence of land.

3.5 RESULTS

3.5.1 Image selection and classification accuracy

The first selection of images (cropped and monthly-constrained images; see Fig. 27) varied by subregion and was mainly related to the position of the areas of interest related to the orbit (path and row) of the Landsat satellites. As a result, L'Isle-Verte (IVE) subregion presented the highest number of images, while the other subregions presented similar

numbers (Table 8). The application of the cloud mask and the area threshold criteria (for image selection) reduced the previous selection by an average of 50%. From this selection, the minimal area threshold applied to the classification of the emerged areas reduced the number of images to only 10% (MAN subregion) to 31% (IVE). This reduction evidences the negative effect of high tidal levels on selecting the images suitable for classification (only *emerged pixels* criteria). Nonetheless, the manual selection removed between 30 (MAN) and 70% (IVE) of the remaining images.

A total of 215 Landsat images were used to classify the eelgrass meadows coverage in the four subregions. Table 8 presents the number of images separated by subregion and by Landsat sensors. The lowest number of images was for MAN (31), while the one with highest was IVE (65). The MAN subregion was found to have the lowest width (perpendicular to the coast) of emerged pixels. The yearly-coverage of the selected images was representative for the analyzed period (average of 67% of the years). The maximum number of consecutive years without images was five (from 2012 to 2016, in RIB subregion), while all other gaps oscillated between 1 to 3 years.

Table 8

Percentage of years mapped in relation to the 39-year period (1984 to 2022) and number of images per subregion and per Landsat sensor

Subregion	Percentage of years mapped (coverage period)	Number of TM images (Landsat 4 or 5)	Number of ETM+ images (Landsat 7)	Number of OLI images (Landsat 8 or 9)
BSI	69 (1984-2021)	29	9	4
MAN	59 (1984-2021)	24	5	2
RIB	64 (1984-2022)	29	5	6
IVE	77 (1984-2022)	24	23	18

As previously mentioned, the classification of the eelgrass meadows was made through an object-based image analysis, using mean NDVI, SR_{Red} , and NDMI values of individual polygons (segments). The contrasting higher NDVI and lower SR_{Red} values of the meadows in comparison to surrounding bare sediment was effective in separating these two coverage types. In addition, mean NDMI values were effective in separating some salt marshes from eelgrass meadows. A possible explanation is the lower content of water present in salt marshes at low tide compared to eelgrass meadows. The threshold values were determined on a single-image basis, mainly because of oscillations of reflectance values that could be related to natural causes (vegetation phenology) or atmospheric correction issues and differences in solar viewing geometry. The manual edition of the classified polygons of eelgrass coverage was only necessary in specific situations. For example, isolated patches of known macroalgae beds were removed manually in RIB and IVE subregions on a few images.

When more than one image was available for a given year, a yearly merging was performed for the eelgrass coverage and respective emerged areas (incorporating both *eelgrass* and *no eelgrass* classes). However, obtaining a single emerged area for each subregion, considering the whole time series, was a critical step to establish a common baseline of comparison. Therefore, the determination of the threshold of 70% of each emerged pixel present in the whole time series was adequate so that only a maximum of 30% of an eelgrass coverage map of a determined year could be interpolated, thus decreasing classification uncertainties. The surface area of the emerged polygons of BSI, MAN, RIB, and IVE subregions was 21, 43, 12, and 31 km², respectively. It is important to note that the emerged polygons encompass only the upper part of the intertidal area of each subregion, with relatively smaller intertidal and adjacent subtidal areas being omitted in the following analysis. Moreover, it is important to note that the SR_{NIR} threshold used to separate the emerged pixels may also include very shallow (< 1m) submerged areas (see Fig. 26C).

The confusion matrix and accuracy assessment results, as analyzed by comparing the corresponding classified year (eelgrass coverage) with the high resolution habitat maps, is

presented in Table 9 (considering the sum of the four subregions). An overall accuracy of 91% and a kappa coefficient (κ) of 0.81 reveal a very good agreement of the classification procedure applied in the Landsat images of the years used for direct comparison. More importantly, the accuracy assessment exercise assured that the classification procedure developed in this study classifies meadows with at least 25% areal coverage. Furthermore, since the general image processing procedures were systematic for the whole Landsat time series, we assume that the classification procedure was valid for the whole analyzed period.

Table 9

Confusion matrix and accuracy assessment of eelgrass coverage. The values shown correspond to the sum of areas (in km²) of all four subregions considered in this study

Classified cover map	Reference cover map			User's accuracy (%)
	Eelgrass	No eelgrass	Total	
Eelgrass	32.47	5.12	37.59	86
No eelgrass	3.78	62.28	66.06	94
Total	36.25	67.40	103.65	
Producer's accuracy (%)	90	92		
Overall accuracy (%)	91		$\kappa = 0.81$	

The kappa coefficient (κ) is presented separately and is out of context in the table.

The degree of misclassification areas varied by subregion (see Table 14, Annex 3) and was mainly related to regions where eelgrass meadows were mixed with other vegetation types and where its coverage was close to the threshold of 25%. For example, in BSI subregion (overall accuracy = 81% and $\kappa = 0.54$) there was a sector in the reference map with a coverage classified as a mixed type with eelgrass and brown algae (*Fucus sp.*) and therefore not included in the accuracy assessment. However, the same sector was considered as eelgrass in the classification procedure of the Landsat imagery. Still in BSI, a sector known

to be with a sparse eelgrass coverage (~25% in the reference map) was not classified in the Landsat workflow. These types of misclassifications were common, to a lesser degree, in the other subregions (overall accuracy > 90% and $\kappa > 0.8$). Nonetheless, misclassifications at the edge of the polygons were also observed and attributed to the discrepancy of two orders of magnitude between the spatial resolution of Landsat (30 m) and the aerial photographs (30 cm) used in the reference maps.

3.5.2 Eelgrass coverage, area, trends, and decennial changes

The analysis of the eelgrass coverage in the intertidal zone of the studied areas (subregions) revealed a highly dynamic character at yearly and decennial time scales. Figure 28 shows selected Landsat images of the approximately initial year of analysis, and the approximately year of maximum coverage for each subregion. A first remark is the abrupt gain, in all subregions, of the area occupied by the meadows relative to bare sediment (or meadows with less coverage), when comparing recent years to 1980's images.

The shape and area of the emerged zones retrieved from the processing chain reflected the major geomorphological aspects of each subregion. The emerged area of BSI followed the shape of the bay and varied about 1 to 2.5 km in width (perpendicular to the coast). Two major types of emerged areas were observed in MAN subregion. The first, associated with the peninsula feature coastline and corresponding to half of the total emerged area, presented a typical width of about 1 km and was the main area of eelgrass occurrence. The areas corresponding to the other half were associated with the mouth of Aux-Outardes and Manicouagan rivers, while being less occupied by eelgrass meadows. Nevertheless, the emerged areas of RIB and IVE occupied the zones between land and the barrier islands, while sometimes forming a contiguous area reaching up to 3 km wide (as for RIB subregion).

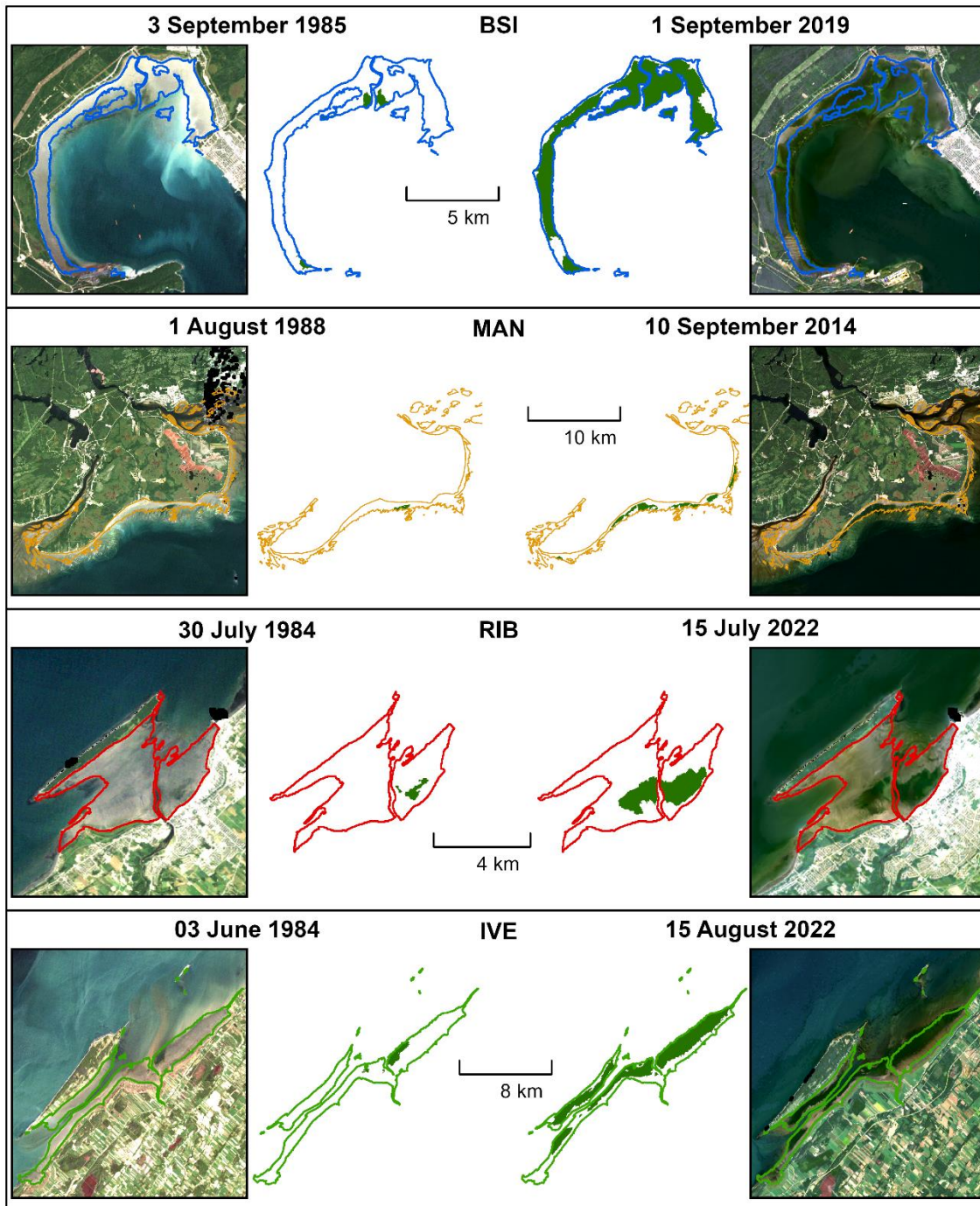


Figure 28. Examples of Landsat images used in the classification process of eelgrass meadows (green patches) inside the polygons of the emerged areas (solid lines with varying colors for subregions: blue for BSI, yellow for MAN, red for RIB, and green for IVE). Images on the left (right) correspond to the approximately years of minimum (maximum) area of meadows

The temporal evolution of areal cover of the meadows and their respective relative occupation of the emerged zone (in percentage) is presented in Figure 29. In all subregions, the initial area of the meadows (in 1984) were the lowest of the whole period and did not reach 1 km² (except for IVE, with an initial area of ~1.5 km²). All subregions experienced a significant areal increase of meadows coverage along the years, reaching the highest areas in BSI and IVE subregions (~16.5 km²) at the end of the analyzed period. The highest area of RIB was also observed by the end of the time series, reaching ~2.4 km². In contrast, MAN subregion reached its maximum in 2014 (~7.4 km²), followed by an almost linear decline since then (~2 km² loss from 2014 to 2021). It is important to note the different orders of magnitude of the absolute area values (*y-axis* in Fig. 29) for each subregion, which, for example, varied eight-fold from RIB to BSI. Small fluctuations in the areal increase trends were observed in the whole time series, and for all subregions. A noticeable decrease is also observed from 2002 to 2006 in RIB (~1 km² loss).

The percentage of meadows coverage relative to total emerged areas (values in parenthesis in Fig. 29) also varied by subregion. Firstly, BSI presented the highest value of relative coverage, reaching 80% of the total emerged area. In contrast, the meadows coverage in MAN and RIB subregions have reached only ~20% of the intertidal emerged area. Nonetheless, IVE presented an intermediate relative coverage, with a value of ~55%. The initial relative cover of all subregions was below 5%. These results evidence a relative saturation of space of emerged areas in BSI subregion for eelgrass expansion, considering that some areas are also occupied by saltmarshes. The lower occupation rate of meadows in MAN subregion can be associated with the high proportion of the emerged areas being present in more dynamical areas such as the mouths of the rivers.

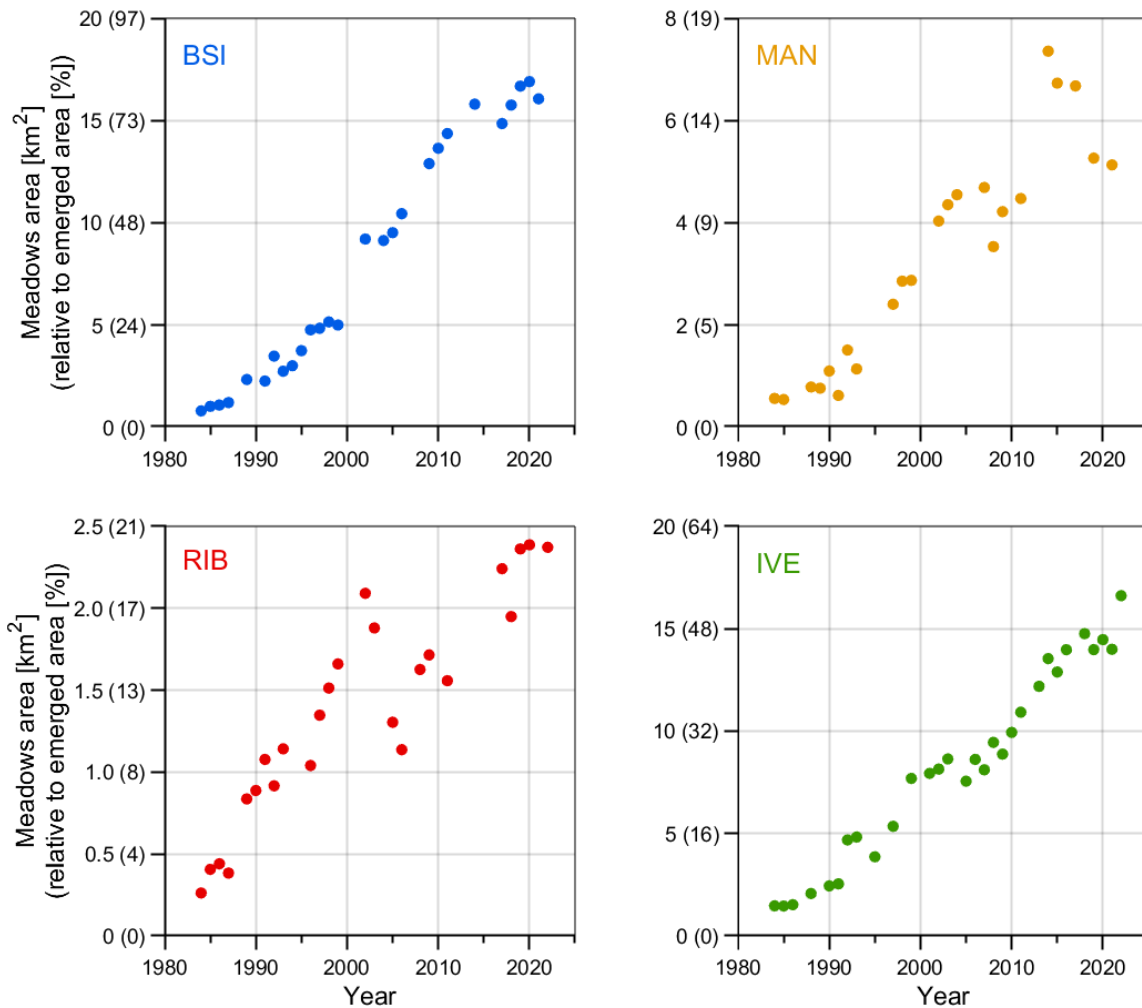


Figure 29. Temporal evolution of areal cover of eelgrass meadows in the four subregions. The values in parenthesis in y-axis are the percentage of the eelgrass areal cover in relation to the total emerged area. The color codes for the subregions are the same as in Fig. 28

The seagrass areal trends for EGSL are plotted in Figure 30. Here, the yearly areal eelgrass coverage was normalized by the initial area (1984) for comparison between subregions. The solid line curves were obtained by fitting a 4th degree polynomial equation in the log10-transformed to illustrate the relative areal trends in the four subregions. A comparison was also made on including the curves of North Atlantic Ocean, from both East

and West coasts, and using the (world bioregions; see Short et al., 2007) data compiled by Dunic et al. (2021). The data was also normalized by the area of 1984.

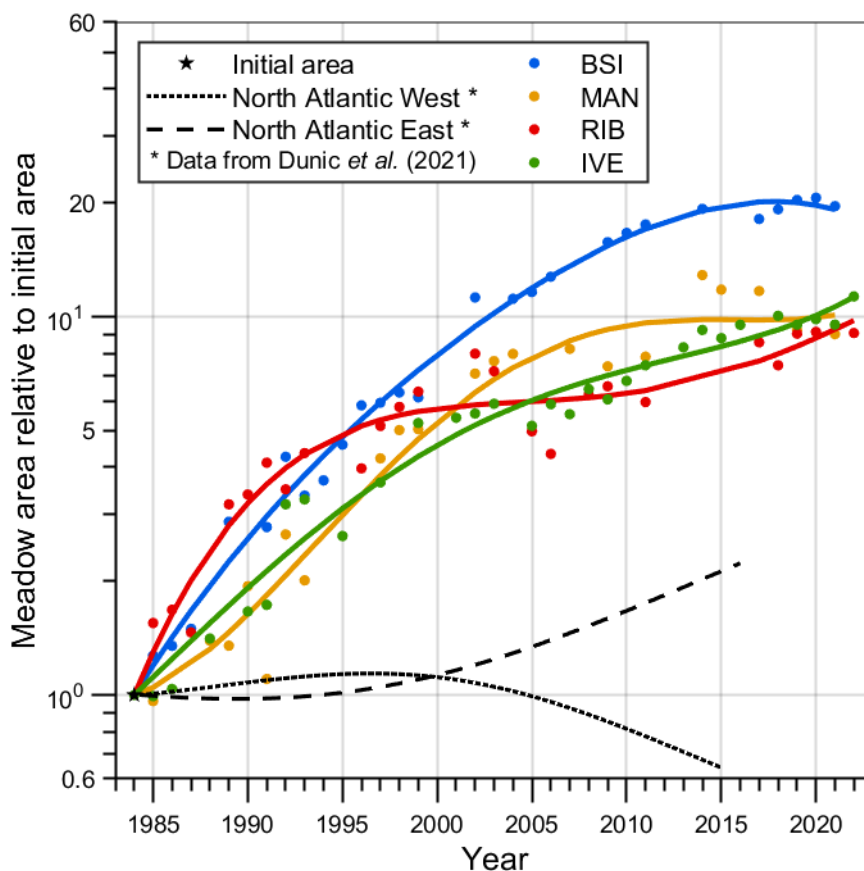


Figure 30. Eelgrass meadows areal trends in the Estuary and Gulf of St. Lawrence in the last four decades, and comparison with other seagrass areal trends in the North Atlantic West (East Europe) and East (West North America) coasts.

The general trends were very similar for all subregions, reaching as much as 20-fold increase for BSI and 10-fold increases for the other subregions. When compared to global bioregional trends, EGSL experienced about one order of magnitude of higher increases than in North Atlantic East. Nevertheless, EGSL also showed to have an opposite trend when

compared to other southern North Atlantic West meadows (see Figure 1 of Dunic et al., 2021).

The spatial dynamics of eelgrass meadows expansion over the last decades are shown in Figure 31. The comparison of a reference year with the coverage over the decades allowed the identification of when and where the meadows first appeared (or disappeared). In general, the expansion started in small patches and were located mostly closer to the outer limit (i.e., offshore direction) of the emerged areas. This indicates that the expansion generally started from areas farthest from the coast and expanded towards land. This spatial pattern is more evident in BSI and MAN subregions, in the north coast of EGSL. Moreover, areas where the meadows were present at any time in the analyzed period, but for some reason disappeared (relative to the reference year), is also shown in Figure 31 (light red patches). Specifically, these “loss” patches in MAN and RIB subregions correspond to the period of area declining previously mentioned and shown in the areal evolution (Fig. 29).

3.5.3 Environmental variables

The climatological mean and standard deviation values comparing the environmental variables of the four subregions of EGSL is shown in Table 10. The SST values were the highest for BSI and the lowest for MAN subregions, with a difference of 4.2 °C in the mean values, indicating warmer conditions in the gulf domain in August. BSI also presented the lowest $K_d(\text{PAR})$ for the same period (August), while the highest values were for RIB subregion. It is important to note that the coarse spatial resolution (4 km) of the products for both SST and $K_d(\text{PAR})$ were retrieved from pixels far enough of the coast to avoid its contamination by land and may not reflect the nearshore water conditions that are over the meadows. However, we found these products adequate for comparing the general background of these parameters for the different subregions, attempting to the fact that the values presented reflect their surrounding offshore conditions.

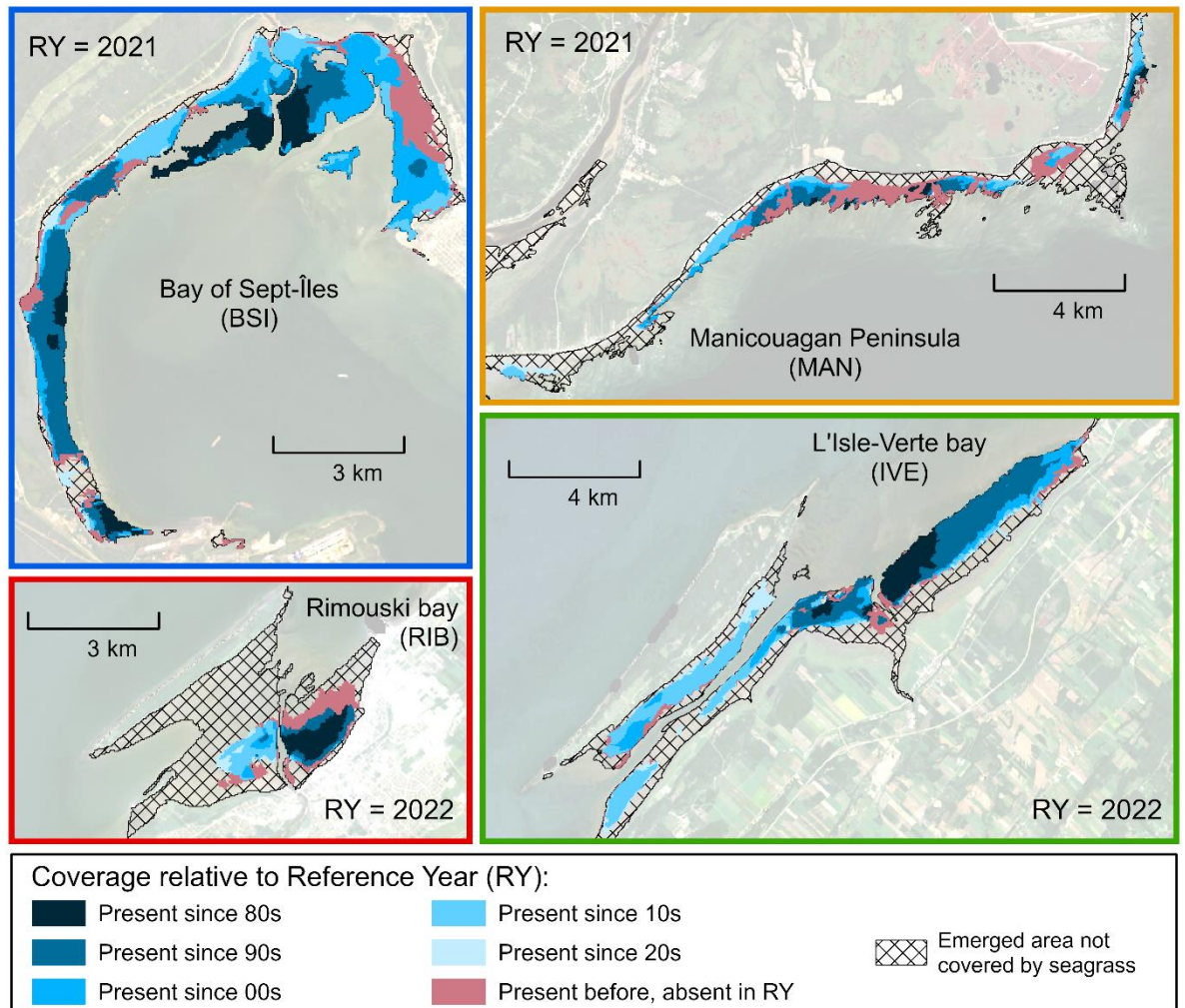


Figure 31. Decadal spatial changes of eelgrass patches in the four subregions of the Estuary and Gulf of St. Lawrence

Table 10

Climatological comparisons of environmental variables (mean \pm standard deviation) surrounding eelgrass meadows of the different subregions of the estuary and Gulf of St Lawrence

Subregion	SST [°C] (August)	K_d(PAR) [m⁻¹] (August)
BSI	14.2 \pm 2.6	0.26 \pm 0.04
MAN	10.0 \pm 1.8	0.40 \pm 0.07
RIB	12.7 \pm 2.2	0.42 \pm 0.10
IVE	10.6 \pm 2.0	0.36 \pm 0.08

3.6 DISCUSSION AND CONCLUSIONS

The spatial variability of eelgrass meadows at an annual to decadal time frame was investigated in one of the largest estuarine systems of the world: the Estuary and Gulf of St. Lawrence (EGSL). A massive increase in the areal coverage of meadows in intertidal areas was demonstrated in four contrasting subregions of EGSL using Landsat historical images and the freely cloud-computing platform Google Earth Engine (GEE).

The advent of GEE together with the availability of optical imagery products (archives) allowed the development of several seagrass mapping efforts worldwide, either considering time series analysis (e.g., Lizcano-Sandoval et al. 2022; Sebastian et al. 2023) or actual inventories (e.g.; Kovacs et al. 2022; Traganos et al. 2022a; b; Li et al. 2022). The advantages of combining these two facilities include increased capabilities for mapping very large areas with relatively low computational costs, bringing agility in accessing meadows coverage. Moreover, the analysis-ready data available through the repositories permits the access of a large number of images and favors its utilization by end-users, while minimizing the requirements of applications of more complicated image processing techniques such as

atmospheric correction procedures. However, it is important to note that high spatial resolution (<30 m) products specifically designed for water color applications would favor not only the retrieval of water quality parameters but also optically-shallow benthic coverage information, including seagrass mapping.

Limiting the classification to exposed macrophytes in low tide conditions present advantages and is a common procedure applied to optical imagery (e.g.; Zoffoli et al. 2020; Carlson et al. 2023). The restriction of the analysis to intertidal areas was a necessary step to avoid map uncertainties due to variability in water optical properties, sun and sky glint, and allowed the classification of the eelgrass meadows by the application of vegetation indices. Nevertheless, the knowledge of spectral signatures of the different types of coverage occurring in the tidal flats is a primary requirement for developing classification tools. It is important to note, however, the limitations of multispectral imagery on discriminating different types of vegetation (e.g., seagrass and macroalgae), as could be observed in a few intertidal areas of EGSL (e.g., Légaré et al., 2022).

The legacy of the Landsat program provide a unique opportunity to establish a baseline of seagrass distribution at yearly to decadal temporal scales, as demonstrated by several studies worldwide (Calleja et al., 2017; Dekker et al., 2005; Fernandes et al., 2022; Gullström et al., 2006; Lyons et al., 2013). Although inherent limitations to access subtidal seagrass in highly-absorbing and turbid waters with TM and ETM+ sensors, advances in the capabilities of satellite and airborne sensors proved to be adequate to overcome or minimize this issue (Dierssen et al., 2019; Krause et al., 2021; Kuhwald et al., 2022). Therefore, recent and planned satellite missions are promising to extrapolate the mapping of eelgrass meadows in subtidal areas of EGSL.

Furthermore, the so-called depth of colonization of seagrass, i.e., the light-limited maximum depth to which seagrass grows (M. W. Beck et al., 2018) are strictly related to (absolute or relative) irradiance levels reaching the underwater benthic substrate (Dennison et al., 1993; Ralph et al., 2007). From experimental results made with eelgrass shoots harvested in RIB subregion, light limitation was found to occur below $200 \mu\text{mol m}^{-2} \text{s}^{-1}$ (in

PAR units) and the Minimum Quantum Requirements (i.e., the light intensity where leaf productivity equals the respiratory demands of the whole plant) was found to be $13.7 \mu\text{mol m}^{-2} \text{s}^{-1}$ (Léger-Daigle et al., 2022). Thus, combining the retrieval of water quality parameters such as diffuse attenuation coefficient (e.g., $K_d(\text{PAR})$) with photoacclimation and light thresholds can be used to access the depth limits of the meadows. Moreover, since the depth of colonization is subject of anthropogenic pressures affecting water clarity, the development of inverse modeling tools applied to remote sensing imagery to retrieve $K_d(\text{PAR})$ (e.g., Xu et al., 2023) and (water) subsurface PAR can be an asset for monitoring purposes.

The eelgrass meadows coverage in EGSL showed a dramatic increasing trajectory over the last four decades, contrary to global declining trends and particularly comparing to previous inventories in temperate North Atlantic West regions (Dunic et al., 2021; Waycott et al., 2009). These results revealed the recolonization of the tidal flats after the catastrophic decline in the 1930's caused by the wasting disease, placing these nearshore zones of EGSL as ecologically significant habitats (*Z. marina* was recognized as an Ecologically Significant Species in Canada; DFO, 2009, 2007). This trend reversal (recovery of seagrass meadows coverage) has been reported by few recent studies in temperate North Atlantic East regions (western Europe), southwest Florida, and south Australia (de los Santos et al., 2019; Fernandes et al., 2022; Lizcano-Sandoval et al., 2022; Tomasko et al., 2018). Overall, these studies associate the increase followed by an overall improvement of water quality (less nutrient input in coastal areas leading to less eutrophication and turbid conditions) and to relative success of transplantation programs. However, overall meadows increase of the dwarf eelgrass (*Zostera noltei* Hornemann) was also observed in intertidal areas of North Atlantic East (Bourgneuf Bay, at $\sim 46^{\circ}60'N$; Zoffoli et al., 2021). In this case, and for intertidal eelgrass meadows of EGSL, light limitation caused by overlaying waters in high tide conditions are unlikely, since subaerial conditions may satisfy the light requirements for growth of seagrass (for example, see Cussioli et al. 2019).

The trajectories of eelgrass meadows coverage in cold temperate and subarctic environments vary highly within regional context. In James Bay (a water body extend from the Arctic Ocean) a major decline is reported between 1995 and 1999, followed by a limited recovery (Leblanc et al., 2023). In contrast, a region in the south Gulf of St. Lawrence (Tabusintac Estuary) presented a relatively stable condition of meadows coverage over more than three decades (Leblanc et al., 2021). It should be noted that both meadows contemplated in these studies are subtidal. Even though, the nearshore areas contemplated in our study, located between these two regions and reaching over 300 km of distance from each other (BSI and IVE), presented a consistent and significant areal increase. Despite relatively contrasting conditions of sea surface temperature and water clarity, the four subregions of EGSL presented similar increasing trajectories, considering their initial area (Fig. 30).

However, despite the overall increase from the point of view of the whole period, a marked interannual variability was noticeable. Particularly, this was more evident in the meadows losses from MAN and RIB subregions. In general, the increase (or recovery) pattern is slower than the loss, which was more abrupt. Again, a similar pattern was noticed in Bourgneuf Bay for the intertidal dwarf eelgrass (Zoffoli et al., 2021). These observations highlight the need for the understanding of the mechanisms driving the short term losses and recovery, and their possible link with environmental variables. The level of exposure of the meadows to the action of waves, intensity and frequency of storms, high sedimentation rates, and the phenology and dynamics of landfast ice are examples of local processes affecting the interannual variability of the meadows and are worth investigating.

The similar areal trends over the almost four decades suggest major regional control and, like the short interannual variability, need to be further investigated in terms of environmental variables and their combinations (multiple stressors). Notwithstanding, some hypotheses to explain the increase of the meadows can be drawn up and could be further tested, such as the causal responses to the reduction in ice cover (e.g., Krause-Jensen and Duarte, 2014) and to adaptation to changes in the mean relative sea level (e.g., Kairis and Rybczyk, 2010). Understanding the underlying mechanisms of seagrass meadows spatial and

temporal patterns are of major importance in the context of global climate change and other anthropogenic stressors.

GENERAL CONCLUSION

The main findings of this study were achieved because of a combined use of ship-based (*in situ*) and remote sensing approaches to address some important spatial and temporal variability phenomena of primary producers in nearshore environments of the estuary and Gulf of St Lawrence (EGSL).

The bio-optical properties of nearshore waters of the north part of EGSL are under the influence of discharges of major (or local) CDOM-rich rivers that drained boreal forests watersheds. Consequently, these nearshore waters are more strongly affected by the seasonality of watershed and oceanographic processes, compared to offshore EGSL waters. This also has implications in the succession of major phytoplankton assemblages. The possibility to retrieve information about the distribution of phytoplankton assemblages from Earth Observation satellites (EOS) was demonstrated. Using EOS and background knowledge about optical properties and tidal variability, the interannual and decennial variability of seagrass meadows coverage in intertidal and ecologically relevant habitats (subregions) of EGSL were assessed. A massive increase in areal coverage of eelgrass meadows were observed in all subregions along the last decades. In summary, a baseline of knowledge about the variability of optical properties and remote sensing tools were developed to investigate primary producers in nearshore waters of subarctic and cold temperate environments, achieving the primary objectives of this thesis.

The general premise that a baseline knowledge of bio-optical properties in nearshore environments is necessary to take advantage of EOS on retrieving information about the distribution of primary producers was confirmed. This premise might be valid for nearshore zones in coastal areas worldwide and, therefore, the *in situ* (ship-based) sampling framework developed in this study could be applied elsewhere. Specifically, the variability of inherent

optical properties (IOPs) is central on understanding the reflectance signals obtained by EOS for water quality and optically shallow waters applications.

The bio-optical database built in the scope of this thesis is available at an online repository (the Saint Lawrence Global Observatory - <https://ogsl.ca/en/home-slgo/>) and served as support for the development of EOS algorithms for the retrieval of water quality parameters (see Mabit et al., 2022). The application of these algorithms was tested on Sentinel-2 MSI and Landsat 8 OLI sensors. Notwithstanding, exploring time-series images and applications in other current (e.g., PRISMA and EnMAP) or planned sensors (e.g., Landsat NEXT) can also advantage of this dataset. Although Articles 2 and 3 explored the usage of the high spatial resolution of Landsat, the application of such algorithms in sensors with similar spatial resolutions and improved temporal coverage and spectral resolutions are promising for coastal and nearshore applications. Furthermore, the bio-optical dataset can also be used as baseline knowledge for more detailed studies of optical characterizations in nearshore zones of EGSL. Nevertheless, the EOS applications can include studies of dissolved organic matter (DOM) pool stocks, fluxes and transformations (see review of Fichot et al., 2023); composition and size distribution of suspended particles; phytoplankton composition, biomass, and phenology; and monitoring and quantifying stocks of nearshore vegetated habitats.

In Article 1, through the *in-situ* approach only, we showed that CDOM absorption ($a_{\text{cdom}}(\lambda)$) strongly dominates the absorption budget in nearshore waters of north EGSL. These waters also present extremely low values of suspended particulate matter concentration-specific backscattering coefficient ($b_{\text{bp}}^*(\lambda)$). These factors characterize a strongly light-absorbing and weakly light-scattering medium, resulting in low reflectance values and with major implications to optical remote sensing approaches. In particular, the molar and dry-mass concentrations and IOPs relationships revealed interesting and complex patterns, which could be further explored.

The dissolved organic matter (DOM) pool in the studied areas is mainly of terrigenous sources and showed a dominant conservative mixing behaviour. The $a_{\text{cdom}}(\lambda)$ was highly correlated with the concentration of dissolved organic carbon (DOC). A potential application for $a_{\text{cdom}}(\lambda)$ retrievals are the development of DOM mixing models (e.g.; Fichot and Benner, 2012; Stedmon et al., 2010) and its possibility to link with hydrodynamical modeling. Also important is the characterization of $a_{\text{cdom}}(\lambda)$ and DOC relationships within different watersheds that outflow in nearshore EGSL areas (e.g., riverine endmembers). However, transformation process such as photobleaching, flocculation, and sorption, besides autochthonous production (e.g., by phytoplankton), are likely to co-occur in the river-to-sea aquatic continuum.

A more in-depth investigation of the chemical composition and structure of the molecules of organic matter (e.g., lignin, tannin, humic and fulvic acids) and their relationships with $a_{\text{cdom}}(\lambda)$ and DOC (and derived proxies, like $S_{275-195}$) in nearshore EGSL would enlighten the understanding of DOM sources and lability, either mediated by microbial or photochemical processes (see Del Vecchio and Blough, 2004; Fichot et al., 2023; Hansell, 2013; Holmes et al., 2008; Tzortziou et al., 2007). In this context, measurements of fluorescence excitation-emission matrices (EEMs) can be an asset to characterize the DOM pool (Coble, 1996; Stedmon et al., 2003). Moreover, inelastic scattering processes such as the fluorescence of chlorophyll-*a* and DOM are also a matter of consideration on shaping water reflectance, including R_{rs} (for example, see differences in the shapes of curves from the two graphics of Figure 21). Notwithstanding, DOM fluorescence was found to be significant in a optical closure exercise for the Manicoaugan Peninsula subregion (Mukherjee et al., 2023).

The optical characterization of suspended particulate matter (SPM) was made in terms of both non-algal particles absorption coefficient (a_{nap}) and the particulate backscattering coefficient (b_{bp}), and its relationships with dry-mass concentration of SPM. Its separation (in terms of composition) in either inorganic or organic fractions revealed to be a markedly characteristic affecting the IOPs. Therefore, a more complete characterization of the

composition of SPM (e.g., types of minerals, phytoplankton, bacteria, organic detritus, particulate organic carbon concentration) and its relationships with optical properties can provide more insights about this relationship (Babin and Stramski, 2004; Koestner et al., 2020; Stramski et al., 2007, 2004).

Besides the composition of SPM, a more complete description of SPM can be in terms of the particle size distribution (PSD), which describes the average concentration of particles within discrete size intervals for a given volume of suspension (Reynolds and Stramski, 2021; Stramski and Kiefer, 1991). Since the particle concentration can be described by multiple ways (e.g., particle number, cross-sectional area), the relationships of PSD metrics and IOPs (particularly the volume scattering function, $\beta(\lambda, \psi)$) is worth of more investigation in EGSL and nearshore zones worldwide.

Nevertheless, it is also important to account to processes affecting SPM and with consequences to optical properties. For example, given the massive contribution of organic matter (dissolved and particulate) by riverine inputs, it would be interesting to investigate what proportion (quality and quantity) of them are incorporated in the trophic chain. Flocculation and sorption are other examples of processes that, besides affecting the DOM pool, could also affect the PSD and $\beta(\lambda, \psi)$. However, to tackle these problems may require state-of-art optical equipment that are in constant development, either considering the range of *in situ* (e.g., radiometry profilers and gliders, hyperspectral b_b) or laboratory-based ones (e.g., VSF, $\beta(\lambda, \psi)$ as many angles and wavelengths as possible).

Although this study documented, for the first time, the characterization of bio-optical properties in the northern part of EGSL, other nearshore areas still lack information (e.g., southern part of the Lower St. Lawrence Estuary). A major recommendation built upon Article 1 is that inverse models applied to (EGSL) nearshore areas, including remote sensing approaches, should focus in IOPs then directly to a biogeochemical quantity (e.g., dry-mass concentrations) of an optically active constituent.

The article 2 documented the seasonal succession of phytoplankton assemblages in a subarctic bay, and showed that their temperature, nutritive, and optical niches can be significantly different. The possibility to retrieve information about their distribution from EOS was demonstrated, although atmospheric corrections issues are of major concern. Phytoplankton are among the organisms most sensible to environmental variability, thus developing tools to better assess information about them, such as the distribution of the major assemblages, can be an asset.

A first remark in the approach used to assess the different phytoplankton assemblages is the inherent limitations of the HPLC and flow cytometry techniques to assign them to lower taxonomic levels. Notwithstanding, our analysis revealed a relative importance of some picophytoplankton classes, which is impossible to assess by optical microscopy techniques. In this case, single cells sorting by flow cytometry (e.g.; Marie et al., 2017) and the possibility to further characterization by metabarcoding and metagenomics approaches (e.g. for the global oceans; de Vargas et al., 2015; Sunagawa et al., 2015) are worth of investigating.

The *in situ* sampling strategy used to characterize the phytoplankton assemblages and their associated environmental variables was adequate to observe a seasonal succession. However, a more frequent (order of weeks) sampling would reveal more details about these relationships, besides more insights about phenology metrics of individual assemblages, such as duration and biomass peak. For example, a sampling design covering late winter and early spring would be necessary to fully capture the phytoplankton spring bloom dominated by diatoms. Another potential field to study is the characterization of selected communities to the lower taxonomic level and further relating their ecological metrics (e.g., abundance, species richness, and diversity) with the major phytoplankton assemblages. A practical example could be the identification (by an expert) of diatoms and dinoflagellates, only in the microphytoplankton size class, using optical microscopy.

Since the diversity of the phytoplankton assemblages co-varied with environmental variables, one may expect that ecological processes may also differ among them. For

example, the different assemblages may have different photophysiological parameters and require different parametrization of photosynthesis-irradiance ($P-E$) curves (see Bouman et al., 2018). The retrieval of proxies for phytoplankton biomass, like chlorophyll- a concentration (Chl a), are also a key parameter to be further explored from EOS applications (see reviews of Blondeau-Patissier et al., 2014; Odermatt et al., 2012) in optically deep nearshore waters of EGSL. Notwithstanding, chlorophyll- a (and other pigments) fluorescence is also a proxy for Chl a and, like DOM, affects $R_{rs}(\lambda)$ shapes and magnitudes.

Although not explored in this thesis, the coupled retrieval of phytoplankton assemblages and biomass estimations from EOS would represent, together with the photophysiological parameters and estimations of solar radiation at the surface of water, a first step towards modeling phytoplankton primary production in nearshore EGSL at unprecedented temporal and spatial scales.

Nevertheless, trait-based approaches capture the form (morphological) and function (functional traits) of an organism and can be used to reveal the mechanisms underpinning phytoplankton community composition and dynamics, and that are straightly related to environmental drivers (Edwards et al., 2016, 2013; Litchman et al., 2010, 2007; Litchman and Klausmeier, 2008; Wentzky et al., 2020). Therefore, a more in-depth investigation of functional traits and trade-offs might reveal details about the ecological function of each phytoplankton assemblage in nearshore EGSL, with the possibility to extend this knowledge to take advantage of sampling by EOS.

Article 3 applied a remote sensing approach to address the yearly and decadal variability of seagrass coverage (specifically eelgrass, *Zostera marina* L.) in intertidal areas of EGSL. The area of the meadows presented a significantly increase trend in all subregions. These results are relevant at global scales and reveal these nearshore EGSL zones as important areas for biodiversity. Multiple stressors, such as light and temperature constraints, may act together over the dynamics of population growth rate of eelgrass meadows (Dunic

and Côté, 2023; Lefcheck et al., 2017). The littoral zone where the nearshore intertidal areas were analyzed may be also constrained by sea surface temperature (SST) and, to a lesser extent, water clarity. However, air temperature and ice cover may also be important factors. In this context, using the results from Article 3 and extending its objectives beyond, quantitative relationships relating the increase of meadows coverage with environmental variables could be used to build an ecological model, with possible applications to monitoring purposes.

Background information about optical properties and tidal variabilities helped to constrain the final delimitation areas of the studied subregions of EGSL. From the remote sensing perspective, a more detailed information about seagrass distribution were mainly limited by the characteristics of the sensors used in the study, which made it difficult to address the status of the submerged aquatic vegetation. For example, Landsat TM and ETM+ have very low radiometric quality for water quality applications. In turn, the radiometric requirements of the strongly light-absorbing and weakly light-scattering medium found in nearshore waters of EGSL are particularly critical. Furthermore, as showed in Article 2 (but see also Mabit et al., 2022), atmospheric correction is still challenging even for sensors with relatively higher radiometry quality. However, the application of inverse models (for both optically deep and shallow waters) relies in accurate reflectance retrievals, which reinforces the idea of obtaining a successful atmospheric correction. In such scenario, further studies could focus in atmospheric corrections algorithms verifications with *in situ* radiometric measurements, but also consider the implementation of more robust aerosol retrievals (e.g., see Ahmad et al., 2011) and accounting for adjacency effects (e.g.; see Pan et al., 2022; Santer and Schmechtig, 2000).

As previously discussed, sensors with characteristics intersecting *H4 imaging* (Muller-Karger et al., 2018) are a reality in recent advances of EOS. Notwithstanding, overpassing the atmospheric correction problem, the possibility to assess ecological information about submerged aquatic vegetation in EGSL can be further explored. This can include (but may not be limited to) the determination of the major habitat (e.g., seagrass, macroalgae) and

(blue) carbon budget studies. Moreover, integrating information about IOPs, bathymetry, and benthic reflectance, could enlighten the knowledge about the light budget (quantity and quality) reaching the canopy of nearshore benthic primary producers. These information could be used to understand the optical niche affecting the distribution of patches of submerged vegetation communities (Thoral et al., 2023), but also help to build primary production models for these nearshore vegetated habitats (e.g., Daggars et al., 2018; Dierssen et al., 2010; Hill et al., 2014).

Bringing the concept of spatial and temporal patterns present in nearshore zones developed in the Introduction to this Conclusion, one may note that this idea is central in the development of the three research articles. Taking only the Bay of Sept-Îles subregion as example (which is present in the three articles), the Article 1 used an *in situ*-based approach addressing spatial variability in the order of 10^0 to 10^1 km, and temporal variability in the order of 10^1 to 10^2 days (seasonal). Article 2 used the same ship-based approach and linked it with EOS, showing the possibility to extend the approach to a spatial order of 10^{-2} to 10^2 km and temporal coverage of (10^0) days to (10^1) years (for example, using Landsat OLI and Sentinel-2 MSI sensors). Finally, Article 3 used a satellite-based approach to address a spatial variability in the order of 10^{-2} to 10^2 km, and a temporal variability ranging from 10^0 to 10^1 years.

The spatial and temporal scales addressed in the Articles 1 and 2 corresponds to the intersection of the ship and satellite-based approaches, shown in the Stommel diagram of Figure 2. Once a link between the two approaches is well established, the observer may have the benefit of taking the advantages that both approaches can offer. Nevertheless, although not used in this thesis, the same principle can apply to mooring approaches, which can offer unprecedented data at high frequency acquisition (temporal resolution, see Fig. 2). It is evident that modeling exercises could take advantage of the three approaches and their intersectionality to better achieve prediction (and verification) of ecological processes acting in nearshore zones.

This thesis focused on the retrieval of ecosystem state variables (for example the distribution of phytoplankton assemblages and seagrass meadows) that are fundamental “stocks” of nearshore environments. It is important to note, however, that there is still a long path to incorporate these variables in regional ecosystem models and integrate them in ecosystem-based management. Howsoever, this thesis represents a first step towards a more representative sampling of these stocks on considering nearshore variability.

The dimension of multiple stressors acting in nearshore social ecological systems (SES) is of major concern for either the pelagic and benthic habitat, and are key to understand potential tipping points, i.e., shifts in ecosystem state (Carrier-Belleau et al., 2022; Folt et al., 1999; Gunderson et al., 2016; Regier and Kay, 1996). Global climate change is a major challenge in the Anthropocene era and developing new tools that help better understand the relationship between human and nature is mandatory. Nearshore zones host important ecosystems worldwide and it is important to consider both watershed and oceanographic processes affecting them. Notwithstanding, the incorporation of satellite-based approaches in models of SES applied to nearshore zones enables addressing fundamental but complex processes. This, in turn, may facilitate dealing with multiple stressors and predicting potential tipping points scenarios.

ANNEX I

-

ARTICLE 1: SUPPLEMENTARY MATERIAL

Table 11

Summary of fitted regressions and associated errors for the optical properties of dissolved organic matter. The reported metrics are the mean absolute error, *MAE* (and the mean absolute percentage error, *MAPE*); *bias* (and the percentage bias, *P – bias*); coefficient of determination, R^2 ; and the root mean square error, *RMSE*. The considered subset of the data and the corresponding scatterplot figure are also indicated

Ref.	Equation	Dependent variable (y)	Independent variable (x)	Locale or subset type	Ref. Fig.
1	$y = A + Bx$	$a_{\text{cdom}}(350)$	DOC	all data	7a
2	$y = e^{(A-Bx)} + e^{(C-Dx)}$	$a_{\text{cdom}}^*(350)$	$S_{275-295}$	BSI (marine)	7b
3	$y = e^{(A-Bx)} + e^{(C-Dx)}$	$a_{\text{cdom}}^*(350)$	$S_{275-295}$	MAN (marine)	7b
4	$\ln y = A + B \ln x_1 + C \ln x_2$	DOC	$x_1, a_{\text{cdom}}(275)$ $x_2, a_{\text{cdom}}(295)$	$x_1 < 15$	7c
5	$\ln y = A + B \log x_1 + C \ln x_2$	DOC	$x_1, a_{\text{cdom}}(275)$ $x_2, a_{\text{cdom}}(295)$	$x_1 \geq 15$	7c
6	$y = A + Bx$	$a_{\text{cdom}}(350)$	Salinity	BSI	8a
7	$y = A + Bx$	$a_{\text{cdom}}(350)$	Salinity	MAN	8a
8	$y = Ax^B + C$	$S_{275-295}$	Salinity	BSI	8b
9	$y = Ax^B + C$	$S_{275-295}$	Salinity	MAN	8b

Table 11 (cont.)

Ref.	Coefficients				<i>MAE</i> (<i>MAPE</i>)	<i>bias</i> <i>P-bias</i>	<i>R</i> ²	<i>RMSE</i>
	<i>A</i>	<i>B</i>	<i>C</i>	<i>D</i>				
1	-4.2·10 ⁰	4.4·10 ⁻²	-	-	1.2·10 ⁰ (20%)	4.7·10 ⁻¹⁶ (5%)	0.98	2.2·10 ⁰
2	-1.9·10 ¹	1.2·10 ¹	-1.3·10 ⁰	2.0·10 ²	3.3·10 ⁻³ (13%)	-2.0·10 ⁻³ (6%)	0.80	4.2·10 ⁻³
3	-1.9·10 ¹	-6.7·10 ²	-6.6·10 ⁻¹	2.0·10 ²	3.7·10 ⁻³ (18%)	3.0·10 ⁻³ (15%)	0.71	5.1·10 ⁻³
4	4.1·10 ⁰	2.9·10 ⁻¹	1.3·10 ⁻¹	-	1.2·10 ¹ (8%)	-2.7·10 ⁰ (< 1%)	0.69	1.6·10 ¹
5	2.9·10 ⁰	9.8·10 ⁻¹	-1.4·10 ⁻¹	-	3.0·10 ¹ (5%)	-1.2·10 ¹ (2%)	0.98	5.8·10 ¹
6	2.8·10 ¹	-9.1·10 ⁻¹	-	-	1.3·10 ⁰ (25%)	-7.1·10 ⁻¹⁵ (1%)	0.85	2.1·10 ⁰
7	1.7·10 ¹	-5.5·10 ⁻¹	-	-	3.5·10 ⁻¹ (12%)	7.1·10 ⁻¹⁶ (4%)	0.96	5.7·10 ⁻¹
8	1.2·10 ⁻¹⁶	9.3·10 ⁰	1.3·10 ⁻²	-	7.4·10 ⁻⁴ (5%)	6.6·10 ⁻⁵ (< 1%)	0.84	9.5·10 ⁻⁴
9	1.3·10 ⁻¹³	7.2·10 ⁰	1.4·10 ⁻²	-	5.1·10 ⁻⁴ (3%)	-1.1·10 ⁻⁴ (< 1%)	0.78	8.1·10 ⁻⁴

Please refer to **Table 1** of the main text for acronyms and units of variables.

The column “Ref.” contains the reference for the same line presented in different pages.

ANNEX II

-

ARTICLE 2: SUPPLEMENTARY MATERIAL

Table 12

Mean and (plus or minus) standard deviation of phytoplankton pigments concentrations (normalized by Chla) and pico- and nano-cells (eukaryotic and cyanobacteria) abundances, for each of the seven clusters obtained by the Hierarchical Cluster Analysis (PraD, PryD, Cy, Dia, Cry, CryP, and Chlo)

Phytoplankton counts (cell mL⁻¹) and pigments to Chla ratios ($\times 10^2$ g g⁻¹)	PraD	PryD	Cy	Dia	Cry	CryP	Chlo
Picoeukaryotes	26917 ± 9541	24646 ± 4389	19094 ± 9800	6418 ± 7490	1417 ± 804	2234 ± 1569	944 ± 449
Nanoeukaryotes	4238 ± 1233	4833 ± 1825	3703 ± 982	2980 ± 1615	844 $\pm 392^*$	1618 $\pm 454^*$	1457 $\pm 542^*$
Pico phycoerythrin- containing cyanobacteria	478 ± 367	744 ± 166	46894 ± 33257	4400 ± 585	101 ± 22	120 ± 70	53 ± 42
Nano phycoerythrin- containing cyanobacteria	132 ± 81	226 ± 98	920 ± 145	75 ± 82	36 ± 24	131 ± 94	53 ± 42
Chlorophyll <i>c</i> ₃	0.76 $\pm 0.63^*$	2.76 ± 1.27	3.39 ± 1.04	2.13 ± 1.25	0.34 $\pm 0.72^*$	1.81 ± 0.96	0.5 $\pm 0.94^*$
Mg 2,4 divinyl pheoporphyrin <i>a</i> 5 monomethyl ester (MgDVP)	0.11 ± 0.33	0 ± 0	1.19 ± 0.74	0.59 ± 0.65	0 ± 0	1.40 ± 1.05	0.49 ± 1.40
Chlorophyll <i>c</i> ₂	9.54 ± 2.24	12.23 ± 2.31	9.62 ± 1.58	12.80 ± 3.37	8.10 ± 0.99	7.67 ± 1.58	2.64 $\pm 4.39^*$

Table 12 (cont.)

Phytoplankton counts (cell mL⁻¹) and pigments to Chla ratios ($\times 10^2$ g g⁻¹)	PraD	PryD	Cy	Dia	Cry	CryP	Chlo
Chlorophyll <i>c</i> ₁	2.23 ±1.40	2.39 ±0.94	1.08 ±0.57	3.01 ±0.86	0.34 ±0.96	0.38 ±0.59	0.33 ±0.16
Peridinin	12.11 ±6.58	16.02 ±8.58	3.83 ±1.42	3.76 ±4.78	1.26 ±2.33	5.18 ±2.31	1.99 ±3.92
19'- Butanoyloxyfucoxanthin	0.02 ±0.11	0.46 ±0.53	0.54 ±1.45	0.38 ±0.47	0 ±0	0.10 ±0.29	0 ±0
Fucoxanthin	10.17 ±4.97	13.04 ±4.29	21.00 ±8.04	30.12 ±9.72	4.84 ±3.47*	11.52 ±3.53	23.14 ±7.10
Neoxanthin	2.09 ±0.63	1.00 ±0.33	1.36 ±0.55	0.66 ±0.38	0 ±0*	0.20 ±0.41*	0 ±0*
Prasincoxanthin	4.20 ±1.50	2.96 ±1.24	3.22 ±0.81	0.79 ±0.87	0.26 ±0.49	1.54 ±1.15	0 ±0*
Violaxanthin	4.51 ±1.80	0.67 ±0.90	2.40 ±0.59	1.00 ±0.50	0.36 ±0.55	1.50 ±1.03	1.81 ±2.50
19'- Hexanoyloxyfucoxanthin	0.45 ±1.04	10.16 ±6.92	3.04 ±2.28	0.71 ±0.56	0.37 ±0.70	3.70 ±2.46	1.49 ±2.78
Diadinoxanthin	8.50 ±2.96	14.41 ±2.97	5.43 ±1.21	7.12 ±1.96	3.29 ±1.74*	5.34 ±1.37	7.32 ±2.01
Alloxanthin [†]	10.61 ±3.57	8.25 ±3.32	8.20 ±2.30	4.21 ±4.11*	22.94 ±3.82	15.34 ±2.59	5.69 ±4.31
Diatoxanthin	1.33 ±0.68	1.51 ±0.67	0.48 ±0.30	1.02 ±0.38	0.38 ±0.34	0.56 ±0.59	1.83 ±2.27
Zeaxanthin	1.20 ±0.61	1.32 ±0.58	4.57 ±2.50	0.65 ±0.50	1.08 ±0.44	1.39 ±0.91	4.46 ±3.09
Lutein	0.47 ±0.57	0.32 ±0.47	0 ±0	0.17 ±0.22	0.16 ±0.24	0.69 ±0.47	1.90 ±1.77
Crocoxanthin	0.76 ±0.26	0.64 ±0.38	0.62 ±0.34	0.36 ±0.38	1.83 ±0.29	1.31 ±0.30	0.17 ±0.48

Table 12 (cont.)

Phytoplankton counts (cell mL⁻¹) and pigments to Chla ratios ($\times 10^2$ g g⁻¹)	PraD	PryD	Cy	Dia	Cry	CryP	Chlo
Chlorophyll <i>b</i>	15.66 ±5.16	8.70 ±2.01	14.39 ±3.47	5.53 ±1.78	2.63 ±1.49*	7.53 ±2.39	4.56 ±2.76
α -Carotene	1.59 ±2.75	2.56 ±3.10	1.93 ±2.17	1.00 ±1.85	15.15 ±10.67	0.99 ±1.99	0 ±0
β -Carotene	4.06 ±0.62	4.30 ±0.89	4.37 ±0.76	2.74 ±0.68	1.08 ±0.75*	2.21 ±0.47	2.27 ±1.23

All variables presented significantly difference (one-way ANOVA, $p < 0.05$). Bold values indicate groups that were significantly higher (Tukey's HSD criterion) than at least four or more other groups. Conversely, the asterisk (*) indicate when a group of samples were significantly lower than at least four or more other groups.

† Smirnov-Kolmogorov test rejects the null hypothesis at the 5% significance level, but Lilliefors test does not.

Table 13

Pigment and nutrient concentrations from samples collected in the phytoplankton spring bloom (April-May), including surface and deep waters in selected stations of the Bay of Sept-Îles

Station (Lat. / Long.)	Depth (m)	Date of sampling (2017)	Chla (mg m ⁻³)	Fuco:Chla (w w ⁻¹)	[NO ₃ ⁻] (μM)	[Si(OH) ₄ ⁴⁻] (μM)	[PO ₄ ³⁻] (μM)
PT-02 (50.14° / -66.40°)	0	19 April	12.92	0.32	-	-	-
PT-01 (50.19° / -66.43°)	0	19 April	5.45	0.41	-	-	-
PT-5.1 (50.07° / -66.38°)	0	4 May	3.21	0.39	0.03	0.96	0.14
PT-5.1	27	4 May	5.51	0.45	0.15	0.67	0.22
PT-02	0	4 May	1.67	0.34	0.05	1.09	0.12
PT-02	41	4 May	8.76	0.46	0.66	1.09	0.28

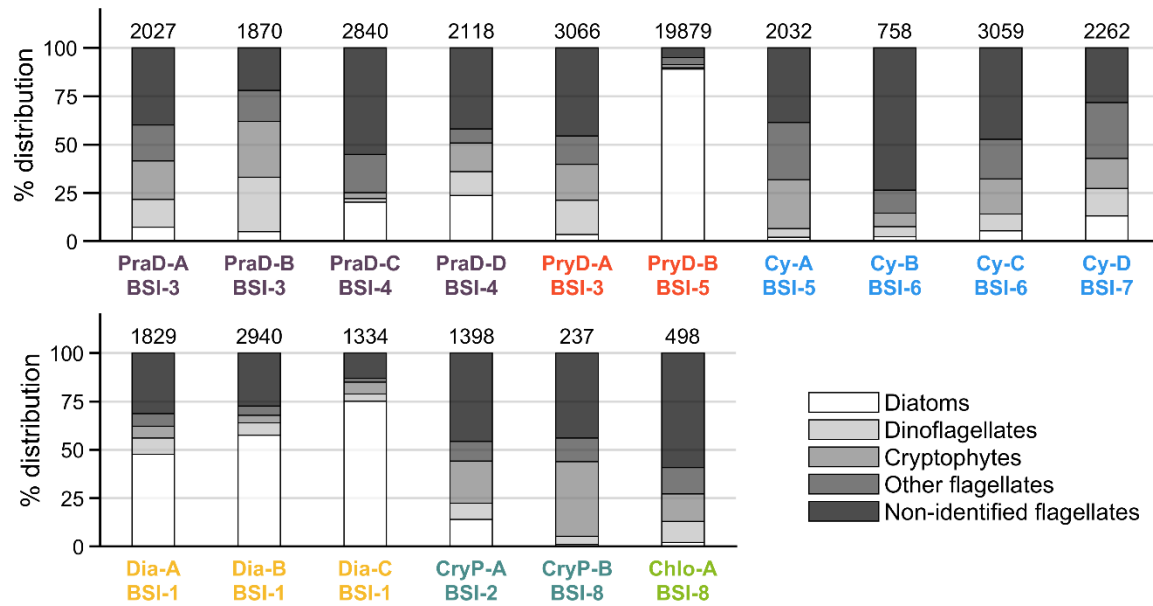


Figure 32. Bar plots showing the percentage distribution of phytoplankton classes as assigned by the light microscopy technique. The names in the x-axis refer to the phytoplankton groups and respective field campaigns (refer to **Table 5**). The number above each bar is the total phytoplankton cell count (in cells L⁻¹). Other flagellates include chlorophytes, chrysophytes, dictyophytes, euglenophytes, prasinophytes, prymnesiophytes and raphidophytes

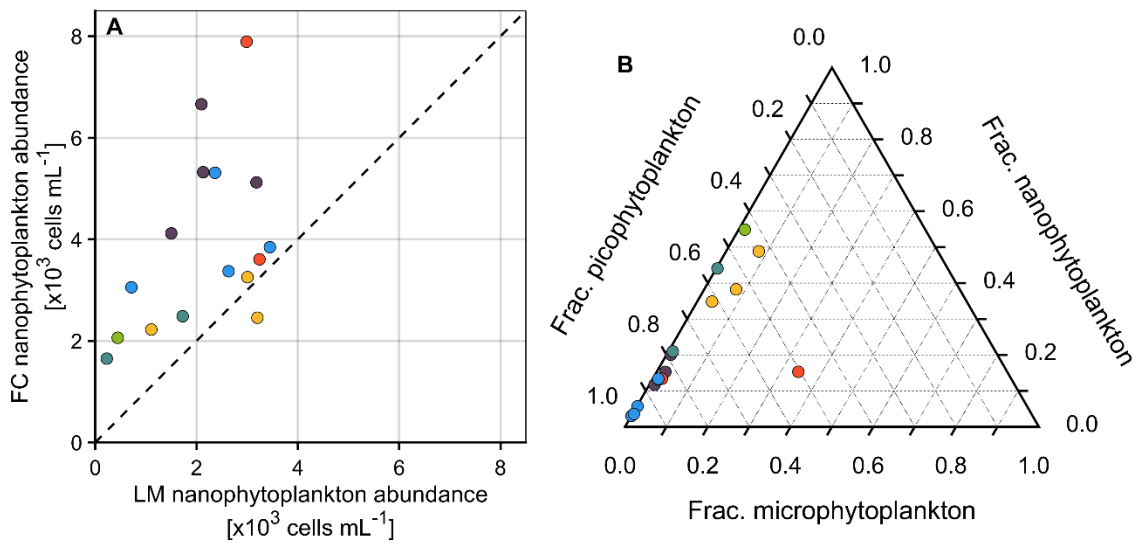


Figure 33. **(A)** Cells concentration comparison of nanophytoplankton counts from flow cytometry (FC) versus light microscopy (LM) methods. Unidentified cells with sizes lower than 20 μm were included in the LM nanophytoplankton abundances. **(B)** Ternary plot showing the relative contribution (or fraction) of phytoplankton size classes to total cell concentration and for each phytoplankton cluster. Concentration of cells was derived from flow cytometry measurements for the pico- and nano-size classes, while micro-size classes concentration was obtained by counts using LM technique ($n = 16$). The phytoplankton clusters are denoted by PraD (purple), PryD (red), Cy (blue), Dia (yellow), Cry (orange), CryP (teal), and Chlo (green)

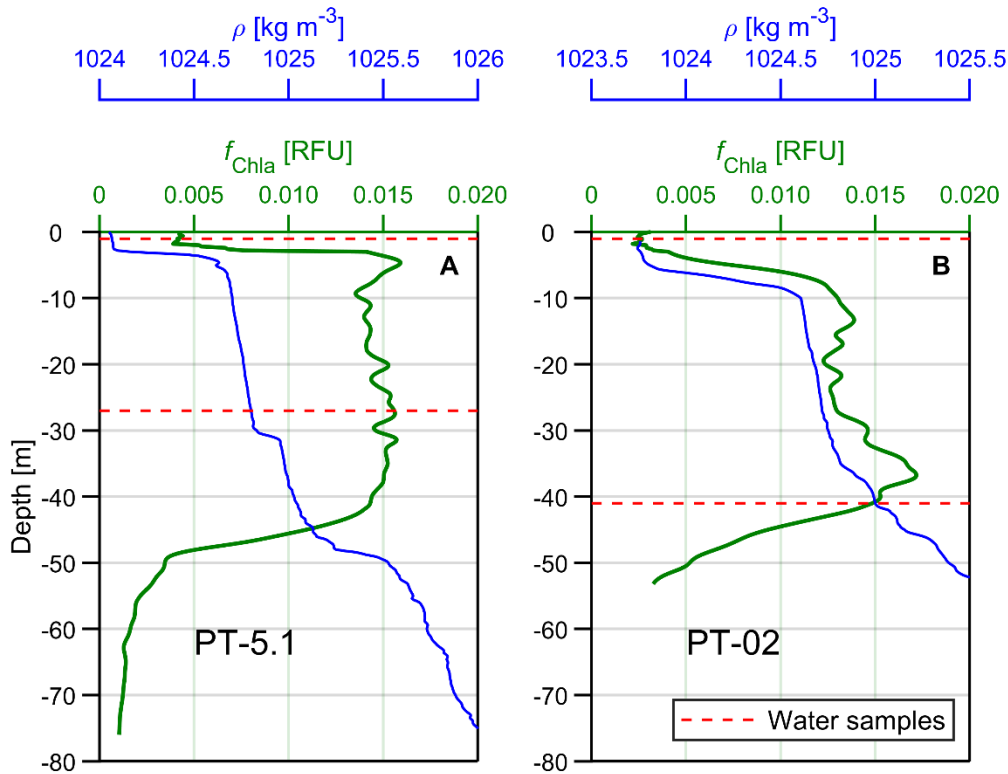


Figure 34. Vertical profiles of density of sea water ($\rho = \rho(S, T, p)$) and chlorophyll-*a* fluorescence (f_{Chla} , in Relative Fluorescence Units, RFU, as measured by the HS6 instrument). Captions (A) and (B) refer to two stations from 4 May 2017 (BSI-1 campaign), where the presence of a subsurface chlorophyll maximum (SCM) can be noticed. From these two stations, the concentrations of Chla, major nutrients, and the Fucoxanthin to Chla ratio are found in **Table 12**, for water samples collected at two different depths

ANNEX III

-

ARTICLE 3: SUPPLEMENTARY MATERIAL

Table 14

Confusion matrix and accuracy assessment of eelgrass coverage for the four subregions of the Estuary and Gulf of St. Lawrence. The values shown correspond to the sum of areas (in km²)

Classified cover map	Reference cover map			User's accuracy (%)
	Eelgrass	No eelgrass	Total	
<i>Bay of Sept-Îles (BSI)</i>				
Eelgrass	12.67	2.02	14.69	86
No eelgrass	1.82	3.97	5.79	69
Total	14.49	5.99	20.48	
Producer's accuracy (%)	87	66		
Overall accuracy (%)	81		$\kappa = 0.54$	
<i>Manicouagan Peninsula (MAN)</i>				
Eelgrass	5.88	0.80	6.68	88
No eelgrass	1.25	35.27	36.52	97
Total	7.13	36.07	43.20	
Producer's accuracy (%)	82	98		
Overall accuracy (%)	95		$\kappa = 0.82$	
<i>Rimouski bay (RIB)</i>				
Eelgrass	1.84	0.40	2.24	82
No eelgrass	0.16	9.56	9.72	98
Total	2.0	9.96	11.96	
Producer's accuracy (%)	92	96		
Overall accuracy (%)	95		$\kappa = 0.84$	

Table 14 (cont.)

Classified cover map	Reference cover map			User's accuracy (%)
	Eelgrass	No eelgrass	Total	
<i>L'Isle-Verte bay (IVE)</i>				
Eelgrass	12.08	1.90	13.98	86
No eelgrass	0.55	16.48	17.03	97
Total	12.63	18.38	31.01	
Producer's accuracy (%)	96	90		
Overall accuracy (%)	92		$\kappa = 0.84$	

The kappa coefficient (κ) is presented separately for each subregion and is out of context in the table.

REFERENCES

- Achanta, R., Susstrunk, S., 2017. Superpixels and Polygons Using Simple Non-iterative Clustering, in: 2017 IEEE Conference on Computer Vision and Pattern Recognition (CVPR). IEEE, Honolulu, HI, pp. 4895–4904. <https://doi.org/10.1109/CVPR.2017.520>
- Ahmad, Z., Franz, B.A., McClain, C.R., Kwiatkowska, E.J., Werdell, J., Shettle, E.P., Holben, B.N., 2011. New aerosol models for the retrieval of aerosol optical thickness and normalized water-leaving radiances from the SeaWiFS and MODIS sensors over coastal regions and open oceans: publisher's note. *Appl. Opt.* 50, 626. <https://doi.org/10.1364/AO.50.000626>
- Albert, A., Mobley, C., 2003. An analytical model for subsurface irradiance and remote sensing reflectance in deep and shallow case-2 waters. *Opt. Express* 11, 2873. <https://doi.org/10.1364/OE.11.002873>
- Ansotegui, A., Sarobe, A., Trigueros, J.M., Urrutxurtu, I., Orive, E., 2003. Size distribution of algal pigments and phytoplankton assemblages in a coastal--estuarine environment: contribution of small eukaryotic algae. *J. Plankton Res.* 25, 341–355. <https://doi.org/10.1093/plankt/25.4.341>
- Antoine, D., André, J.-M., Morel, A., 1996. Oceanic primary production: 2. Estimation at global scale from satellite (Coastal Zone Color Scanner) chlorophyll. *Global Biogeochem. Cycles* 10, 57–69. <https://doi.org/10.1029/95GB02832>
- Antoine, D., Siegel, D.A., Kostadinov, T., Maritorena, S., Nelson, N.B., Gentili, B., Vellucci, V., Guillocheau, N., 2011. Variability in optical particle backscattering in contrasting bio-optical oceanic regimes. *Limnol. Oceanogr.* 56, 955–973. <https://doi.org/10.4319/lo.2011.56.3.0955>
- Araújo, C.A.S., Bélanger, S., 2022. Variability of bio-optical properties in nearshore waters of the estuary and Gulf of St. Lawrence: Absorption and backscattering coefficients. *Estuar. Coast. Shelf Sci.* 264, 107688. <https://doi.org/10.1016/j.ecss.2021.107688>
- Araújo, C.A.S., Belzile, C., Tremblay, J.-É., Bélanger, S., 2022. Environmental niches and seasonal succession of phytoplankton assemblages in a subarctic coastal bay: Applications to remote sensing estimates. *Front. Mar. Sci.* 9, 1–23. <https://doi.org/10.3389/fmars.2022.1001098>
- Asmala, E., Autio, R., Kaartokallio, H., Pitkänen, L., Stedmon, C.A., Thomas, D.N., 2013.

- Bioavailability of riverine dissolved organic matter in three Baltic Sea estuaries and the effect of catchment land use. *Biogeosciences* 10, 6969–6986. <https://doi.org/10.5194/bg-10-6969-2013>
- Asmala, E., Bowers, D.G., Autio, R., Kaartokallio, H., Thomas, D.N., 2014. Qualitative changes of riverine dissolved organic matter at low salinities due to flocculation. *J. Geophys. Res. Biogeosciences* 119, 1919–1933. <https://doi.org/10.1002/2014JG002722>
- Audet, R., 2012. L'écologie humaine de Pierre Dansereau et la métaphore du paysage intérieur. *Natures Sci. Sociétés* 20, 30–38. <https://doi.org/10.1051/nss/2012009>
- Babin, M., Stramski, D., 2004. Variations in the mass-specific absorption coefficient of mineral particles suspended in water. *Limnol. Oceanogr.* 49, 756–767. <https://doi.org/10.4319/lo.2004.49.3.0756>
- Babin, M., Stramski, D., Ferrari, G.M., Claustre, H., Bricaud, A., Obolensky, G., Hoepffner, N., 2003. Variations in the light absorption coefficients of phytoplankton, nonalgal particles, and dissolved organic matter in coastal waters around Europe. *J. Geophys. Res.* 108, 3211. <https://doi.org/10.1029/2001JC000882>
- Babin, M., Therriault, J.-C., Legendre, L., 1991. Potential utilization of temperature in estimating primary production from remote sensing data in coastal and estuarine waters. *Estuar. Coast. Shelf Sci.* 33, 559–579. [https://doi.org/10.1016/0272-7714\(91\)90041-9](https://doi.org/10.1016/0272-7714(91)90041-9)
- Babin, M., Therriault, J.-C., Legendre, L., Condal, A., 1993. Variations in the specific absorption coefficient for natural phytoplankton assemblages: Impact on estimates of primary production. *Limnol. Oceanogr.* 38, 154–177. <https://doi.org/10.4319/lo.1993.38.1.0154>
- Babin, M., Therriault, J.-C., Legendre, L., Nieke, B., Reuter, R., Condal, A., 1995. Relationship between the maximum quantum yield of carbon fixation and the minimum quantum yield of chlorophyll a in vivo fluorescence in the Gulf of St. Lawrence. *Limnol. Oceanogr.* 40, 956–968. <https://doi.org/10.4319/lo.1995.40.5.0956>
- Barber, A., Sirois, M., Chaillou, G., Gélinas, Y., 2017. Stable isotope analysis of dissolved organic carbon in Canada's eastern coastal waters. *Limnol. Oceanogr.* 62, S71–S84. <https://doi.org/10.1002/lno.10666>
- Barnes, M., Tilstone, G., Smyth, T., Suggett, D., Astoreca, R., Lancelot, C., Kromkamp, J., 2014. Absorption-based algorithm of primary production for total and size-fractionated phytoplankton in coastal waters. *Mar. Ecol. Prog. Ser.* 504, 73–89. <https://doi.org/10.3354/meps10751>
- Beck, H.E., Zimmermann, N.E., McVicar, T.R., Vergopolan, N., Berg, A., Wood, E.F., 2018. Present and future Köppen-Geiger climate classification maps at 1-km resolution. *Sci.*

Data 5, 180214. <https://doi.org/10.1038/sdata.2018.214>

- Beck, M.W., Hagy, J.D., Le, C., 2018. Quantifying Seagrass Light Requirements Using an Algorithm to Spatially Resolve Depth of Colonization. *Estuaries and Coasts* 41, 592–610. <https://doi.org/10.1007/s12237-017-0287-1>
- Beck, M.W., Heck, K.L., Able, K.W., Childers, D.L., Eggleston, D.B., Gillanders, B.M., Halpern, B., Hays, C.G., Hoshino, K., Minello, T.J., Orth, R.J., Sheridan, P.F., Weinstein, M.P., 2001. The identification, conservation, and management of estuarine and marine nurseries for fish and invertebrates. *Bioscience* 51, 633–641.
- Behrenfeld, M.J., Falkowski, P.G., 1997. Photosynthetic rates derived from satellite-based chlorophyll concentration. *Limnol. Oceanogr.* 42, 1–20. <https://doi.org/10.4319/lo.1997.42.1.0001>
- Behrenfeld, M.J., O'Malley, R.T., Siegel, D.A., McClain, C.R., Sarmiento, J.L., Feldman, G.C., Milligan, A.J., Falkowski, P.G., Letelier, R.M., Boss, E.S., 2006. Climate-driven trends in contemporary ocean productivity. *Nature* 444, 752–755. <https://doi.org/10.1038/nature05317>
- Bélanger, S., Carrascal-Leal, C., Jaegler, T., Larouche, P., Galbraith, P., 2017. Assessment of radiometric data from a buoy in the St. Lawrence Estuary. *J. Atmos. Ocean. Technol.* 34, 877–896. <https://doi.org/10.1175/JTECH-D-16-0176.1>
- Benedetti, F., Vogt, M., Elizondo, U.H., Righetti, D., Zimmermann, N.E., Gruber, N., 2021. Major restructuring of marine plankton assemblages under global warming. *Nat. Commun.* 12, 5226. <https://doi.org/10.1038/s41467-021-25385-x>
- Bidigare, R.R., Van Heukelem, L., Trees, C.C., 2005. Analysis of algal pigments by high-performance liquid chromatography, in: Andersen, R.A. (Ed.), *Algal Culturing Techniques*. Elsevier Academic Press, Burlington, MA, pp. 327–345. <https://doi.org/10.1016/b978-012088426-1/50021-4>
- Bissett, P., Arnone, R., Davis, C., Dickey, T., Dye, D., Kohler, D., Gould, R., 2004. From Meters to Kilometers: A Look at Ocean-Color Scales of Variability, Spatial Coherence, and the Need for Fine-Scale Remote Sensing in Coastal Ocean Optics. *Oceanography* 17, 32–43. <https://doi.org/10.5670/oceanog.2004.45>
- Blais, M.-A., Matveev, A., Lovejoy, C., Vincent, W.F., 2022. Size-fractionated microbiome structure in subarctic rivers and a coastal plume across DOC and salinity gradients. *Front. Microbiol.* 12. <https://doi.org/10.3389/fmicb.2021.760282>
- Blais, M., Galbraith, P.S., Plourde, S., Scarratt, M., Devine, L., Lehoux, C., 2019. Chemical and biological oceanographic conditions in the Estuary and Gulf of St. Lawrence during 2018. DFO Can. Sci. Advis. Sec. Res. Doc.

- Blondeau-Patissier, D., Gower, J.F.R., Dekker, A.G., Phinn, S.R., Brando, V.E., 2014. A review of ocean color remote sensing methods and statistical techniques for the detection, mapping and analysis of phytoplankton blooms in coastal and open oceans. *Prog. Oceanogr.* 123, 123–144. <https://doi.org/10.1016/j.pocean.2013.12.008>
- Blondeau-Patissier, D., Schroeder, T., Clementson, L.A., Brando, V.E., Purcell, D., Ford, P., Williams, D.K., Doxaran, D., Anstee, J., Thapar, N., Tovar-Valencia, M., 2017. Bio-Optical properties of two neighboring coastal regions of tropical northern Australia: The Van Diemen Gulf and Darwin Harbour. *Front. Mar. Sci.* 4, 1–27. <https://doi.org/10.3389/fmars.2017.00114>
- Blondeau-Patissier, D., Brando, V.E., Oubelkheir, K., Dekker, A.G., Clementson, L.A., Daniel, P., 2009. Bio-optical variability of the absorption and scattering properties of the Queensland inshore and reef waters, Australia. *J. Geophys. Res.* 114, C05003. <https://doi.org/10.1029/2008JC005039>
- Bluteau, C.E., Galbraith, P.S., Bourgault, D., Villeneuve, V., Tremblay, J.-É., 2021. Winter observations alter the seasonal perspectives of the nutrient transport pathways into the lower St. Lawrence Estuary. *Ocean Sci.* 17, 1509–1525. <https://doi.org/10.5194/os-17-1509-2021>
- Boivin-Rioux, A., Starr, M., Chassé, J., Scarratt, M., Perrie, W., Long, Z., 2021. Predicting the Effects of Climate Change on the Occurrence of the Toxic Dinoflagellate *Alexandrium catenella* Along Canada's East Coast. *Front. Mar. Sci.* 7, 1–20. <https://doi.org/10.3389/fmars.2020.608021>
- Boström, C., Jackson, E.L., Simenstad, C.A., 2006. Seagrass landscapes and their effects on associated fauna: A review. *Estuar. Coast. Shelf Sci.* 68, 383–403. <https://doi.org/10.1016/j.ecss.2006.01.026>
- Bouman, H.A., Platt, T., Doblin, M., Figueiras, F.G., Gudmundsson, K., Gudfinnsson, H.G., Huang, B., Hickman, A., Hiscock, M., Jackson, T., Lutz, V.A., Mélin, F., Rey, F., Pepin, P., Segura, V., Tilstone, G.H., van Dongen-Vogels, V., Sathyendranath, S., 2018. Photosynthesis–irradiance parameters of marine phytoplankton: synthesis of a global data set. *Earth Syst. Sci. Data* 10, 251–266. <https://doi.org/10.5194/essd-10-251-2018>
- Bourgoin, L.-H., Tremblay, L., 2010. Bacterial reworking of terrigenous and marine organic matter in estuarine water columns and sediments. *Geochim. Cosmochim. Acta* 74, 5593–5609. <https://doi.org/10.1016/j.gca.2010.06.037>
- Bowers, D.G., Binding, C.E., 2006. The optical properties of mineral suspended particles: A review and synthesis. *Estuar. Coast. Shelf Sci.* 67, 219–230. <https://doi.org/10.1016/j.ecss.2005.11.010>
- Boyer-Villemare, U., St-Onge, G., Bernatchez, P., Lajeunesse, P., Labrie, J., 2013. High-

resolution multiproxy records of sedimentological changes induced by dams in the Sept-Îles area (Gulf of St. Lawrence, Canada). *Mar. Geol.* 338, 17–29. <https://doi.org/10.1016/j.margeo.2012.11.012>

Brando, V.E., Dekker, A.G., Park, Y.J., Schroeder, T., 2012. Adaptive semianalytical inversion of ocean color radiometry in optically complex waters. *Appl. Opt.* 51, 2808. <https://doi.org/10.1364/AO.51.002808>

Brewin, R.J.W., Morán, X.A.G., Raitos, D.E., Gittings, J.A., Calleja, M.L., Viegas, M., Ansari, M.I., Al-Otaibi, N., Huete-Stauffer, T.M., Hoteit, I., 2019. Factors regulating the relationship between total and size-fractionated chlorophyll-a in coastal waters of the Red Sea. *Front. Microbiol.* 10, 1–16. <https://doi.org/10.3389/fmicb.2019.01964>

Bricaud, A., Babin, M., Morel, A., Claustre, H., 1995. Variability in the chlorophyll-specific absorption coefficients of natural phytoplankton: Analysis and parameterization. *J. Geophys. Res.* 100, 13321. <https://doi.org/10.1029/95JC00463>

Bricaud, A., Morel, A., Babin, M., Allali, K., Claustre, H., 1998. Variations of light absorption by suspended particles with chlorophyll a concentration in oceanic (case 1) waters: Analysis and implications for bio-optical models. *J. Geophys. Res. Ocean.* 103, 31033–31044. <https://doi.org/10.1029/98JC02712>

Bricaud, A., Morel, A., Prieur, L., 1981. Absorption by dissolved organic matter of the sea (yellow substance) in the UV and visible domains. *Limnol. Oceanogr.* 26, 43–53. <https://doi.org/10.4319/lo.1981.26.1.0043>

Browman, H.I., Stergiou, K.I., 2004. Perspectives on ecosystem-based approaches to the management of marine resources. *Mar. Ecol. Prog. Ser.* 274, 269–303. <https://doi.org/10.3354/meps274269>

Brown, A.G., Tooth, S., Bullard, J.E., Thomas, D.S.G., Chiverrell, R.C., Plater, A.J., Murton, J., Thorndycraft, V.R., Tarolli, P., Rose, J., Wainwright, J., Downs, P., Aalto, R., 2017. The geomorphology of the Anthropocene: emergence, status and implications. *Earth Surf. Process. Landforms* 42, 71–90. <https://doi.org/10.1002/esp.3943>

Calleja, F., Galván, C., Silió-Calzada, A., Juanes, J.A., Ondiviela, B., 2017. Long-term analysis of *Zostera noltei*: A retrospective approach for understanding seagrasses' dynamics. *Mar. Environ. Res.* 130, 93–105. <https://doi.org/10.1016/j.marenvres.2017.07.017>

Cannizzaro, J.P., Carlson, P.R., Yarbro, L.A., Hu, C., 2013. Optical variability along a river plume gradient: Implications for management and remote sensing. *Estuar. Coast. Shelf Sci.* 131, 149–161. <https://doi.org/10.1016/j.ecss.2013.07.012>

Carder, K.L., Steward, R.G., Harvey, G.R., Ortner, P.B., 1989. Marine humic and fulvic

- acids: Their effects on remote sensing of ocean chlorophyll. *Limnol. Oceanogr.* 34, 68–81. <https://doi.org/10.4319/lo.1989.34.1.0068>
- Carlson, D.F., Vivó-Pons, A., Treier, U.A., Mätzler, E., Meire, L., Sejr, M., Krause-Jensen, D., 2023. Mapping intertidal macrophytes in fjords in Southwest Greenland using Sentinel-2 imagery. *Sci. Total Environ.* 865, 161213. <https://doi.org/10.1016/j.scitotenv.2022.161213>
- Carrier-Belleau, C., Pascal, L., Nozais, C., Archambault, P., 2022. Tipping points and multiple drivers in changing aquatic ecosystems: A review of experimental studies. *Limnol. Oceanogr.* 67, S312–S330. <https://doi.org/10.1002/lno.11978>
- Carstensen, J., Klais, R., Cloern, J.E., 2015. Phytoplankton blooms in estuarine and coastal waters: Seasonal patterns and key species. *Estuar. Coast. Shelf Sci.* 162, 98–109. <https://doi.org/10.1016/j.ecss.2015.05.005>
- Christensen, N.L., Bartuska, A.M., Brown, J.H., Carpenter, S., D’Antonio, C., Francis, R., Franklin, J.F., MacMahon, J.A., Noss, R.F., Parsons, D.J., Peterson, C.H., Turner, M.G., Woodmansee, R.G., 1996. The Report of the Ecological Society of America Committee on the Scientific Basis for Ecosystem Management. *Ecol. Appl.* 6, 665–691. <https://doi.org/10.2307/2269460>
- Ciotti, A.M., Bricaud, A., 2006. Retrievals of a size parameter for phytoplankton and spectral light absorption by colored detrital matter from water-leaving radiances at SeaWiFS channels in a continental shelf region off Brazil. *Limnol. Oceanogr. Methods* 4, 237–253. <https://doi.org/10.4319/lom.2006.4.237>
- Ciotti, Á.M., Lewis, M.R., Cullen, J.J., 2002. Assessment of the relationships between dominant cell size in natural phytoplankton communities and the spectral shape of the absorption coefficient. *Limnol. Oceanogr.* 47, 404–417. <https://doi.org/10.4319/lo.2002.47.2.0404>
- Çizmeli, S.A., 2008. Parameterization, regionalization and radiative transfer coherence of optical measurements acquired in the St-Lawrence ecosystem. Ph.D. Diss. Université de Sherbrooke, Québec, Canada.
- Cloern, J.E., 2018. Why large cells dominate estuarine phytoplankton. *Limnol. Oceanogr.* 63, S392–S409. <https://doi.org/10.1002/lno.10749>
- Cloern, J.E., 2001. Our evolving conceptual model of the coastal eutrophication problem. *Mar. Ecol. Prog. Ser.* 210, 223–253. <https://doi.org/10.3354/meps210223>
- Cloern, J.E., Foster, S.Q., Kleckner, A.E., 2014. Phytoplankton primary production in the world’s estuarine-coastal ecosystems. *Biogeosciences* 11, 2477–2501. <https://doi.org/10.5194/bg-11-2477-2014>

- Cloern, J.E., Jassby, A.D., 2008. Complex seasonal patterns of primary producers at the land-sea interface. *Ecol. Lett.* 11, 1294–1303. <https://doi.org/10.1111/j.1461-0248.2008.01244.x>
- Coble, P.G., 1996. Characterization of marine and terrestrial DOM in seawater using excitation-emission matrix spectroscopy. *Mar. Chem.* 51, 325–346. [https://doi.org/10.1016/0304-4203\(95\)00062-3](https://doi.org/10.1016/0304-4203(95)00062-3)
- Congalton, R.G., Green, K., 2019. Assessing the accuracy of remotely sensed data: Principles and practices, 3rd editio. ed. CRC Press, Boca Raton, Florida, USA.
- Corbisier, T.N., Petti, M.A. V., Skowronski, R.S.P., Brito, T.A.S., 2004. Trophic relationships in the nearshore zone of Martel Inlet (King George Island, Antarctica): $\delta^{13}\text{C}$ stable-isotope analysis. *Polar Biol.* 27, 75–82. <https://doi.org/10.1007/s00300-003-0567-z>
- Costanza, R., de Groot, R., Sutton, P., van der Ploeg, S., Anderson, S.J., Kubiszewski, I., Farber, S., Turner, R.K., 2014. Changes in the global value of ecosystem services. *Glob. Environ. Chang.* 26, 152–158. <https://doi.org/10.1016/j.gloenvcha.2014.04.002>
- Cussioli, M.C., Bryan, K.R., Pilditch, C.A., de Lange, W.P., Bischof, K., 2019. Light penetration in a temperate meso-tidal lagoon: Implications for seagrass growth and dredging in Tauranga Harbour, New Zealand. *Ocean Coast. Manag.* 174, 25–37. <https://doi.org/10.1016/j.ocecoaman.2019.01.014>
- D'Sa, E.J., Miller, R.L., Del Castillo, C., 2006. Bio-optical properties and ocean color algorithms for coastal waters influenced by the Mississippi River during a cold front. *Appl. Opt.* 45, 7410. <https://doi.org/10.1364/AO.45.007410>
- Daggers, T.D., Kromkamp, J.C., Herman, P.M.J., van der Wal, D., 2018. A model to assess microphytobenthic primary production in tidal systems using satellite remote sensing. *Remote Sens. Environ.* 211, 129–145. <https://doi.org/10.1016/j.rse.2018.03.037>
- Danhiez, F.P., Vantrepotte, V., Cauvin, A., Lebourg, E., Loisel, H., 2017. Optical properties of chromophoric dissolved organic matter during a phytoplankton bloom. Implication for DOC estimates from CDOM absorption. *Limnol. Oceanogr.* 62, 1409–1425. <https://doi.org/10.1002/lno.10507>
- Dansereau, P., 1957. Biogeography: An ecological perspective. Ronald Press Company, New York, NY, USA.
- de Jonge, V.N., 2000. Importance of temporal and spatial scales in applying biological and physical process knowledge in coastal management, an example for the Ems estuary. *Cont. Shelf Res.* 20, 1655–1686. [https://doi.org/10.1016/S0278-4343\(00\)00042-X](https://doi.org/10.1016/S0278-4343(00)00042-X)

- de los Santos, C.B., Krause-Jensen, D., Alcoverro, T., Marbà, N., Duarte, C.M., van Katwijk, M.M., Pérez, M., Romero, J., Sánchez-Lizaso, J.L., Roca, G., Jankowska, E., Pérez-Lloréns, J.L., Fournier, J., Montefalcone, M., Pergent, G., Ruiz, J.M., Cabaço, S., Cook, K., Wilkes, R.J., Moy, F.E., Trayter, G.M.-R., Arañó, X.S., de Jong, D.J., Fernández-Torquemada, Y., Auby, I., Vergara, J.J., Santos, R., 2019. Recent trend reversal for declining European seagrass meadows. *Nat. Commun.* 10, 3356. <https://doi.org/10.1038/s41467-019-11340-4>
- de Vargas, C., Audic, S., Henry, N., Decelle, J., Mahé, F., Logares, R., Lara, E., Berney, C., Le Bescot, N., Probert, I., Carmichael, M., Poulain, J., Romac, S., Colin, S., Aury, J.-M., Bittner, L., Chaffron, S., Dunthorn, M., Engelen, S., Flegontova, O., Guidi, L., Horák, A., Jaillon, O., Lima-Mendez, G., Lukeš, J., Malviya, S., Morard, R., Mulot, M., Scalco, E., Siano, R., Vincent, F., Zingone, A., Dimier, C., Picheral, M., Searson, S., Kandels-Lewis, S., Acinas, S.G., Bork, P., Bowler, C., Gorsky, G., Grimsley, N., Hingamp, P., Iudicone, D., Not, F., Ogata, H., Pesant, S., Raes, J., Sieracki, M.E., Speich, S., Stemann, L., Sunagawa, S., Weissenbach, J., Wincker, P., Karsenti, E., Boss, E., Follows, M., Karp-Boss, L., Krzic, U., Reynaud, E.G., Sardet, C., Sullivan, M.B., Velayoudon, D., 2015. Eukaryotic plankton diversity in the sunlit ocean. *Science* (80-.). 348, 1261605–1/11. <https://doi.org/10.1126/science.1261605>
- Defoin-Platel, M., Chami, M., 2007. How ambiguous is the inverse problem of ocean color in coastal waters? *J. Geophys. Res.* 112, C03004. <https://doi.org/10.1029/2006JC003847>
- Dekker, A.G., Brando, V.E., Anstee, J.M., 2005. Retrospective seagrass change detection in a shallow coastal tidal Australian lake. *Remote Sens. Environ.* 97, 415–433. <https://doi.org/10.1016/j.rse.2005.02.017>
- Dekker, A.G., Pinnel, N., Gege, P., Broittet, X., Court, A., Peters, S., Turpie, K.R., Sterckx, S., Costa, M., Giardino, C., Brando, V.E., Braga, F., Bergeron, M., Heege, T., Pflug, B., 2018. Feasibility Study for an Aquatic Ecosystem Earth Observing System Version 1.2. Committee on Earth Observation Satellites (CEOS).
- Del Vecchio, R., Blough, N. V., 2004. On the Origin of the Optical Properties of Humic Substances. *Environ. Sci. Technol.* 38, 3885–3891. <https://doi.org/10.1021/es049912h>
- Den Hartog, C., 1987. “Wasting disease” and other dynamic phenomena in *Zostera* beds. *Aquat. Bot.* 27, 3–14. [https://doi.org/10.1016/0304-3770\(87\)90082-9](https://doi.org/10.1016/0304-3770(87)90082-9)
- Dennison, W.C., Orth, R.J., Moore, K.A., Stevenson, J.C., Carter, V., Kollar, S., Bergstrom, P.W., Batiuk, R.A., 1993. Assessing Water Quality with Submersed Aquatic Vegetation. *Bioscience* 43, 86–94. <https://doi.org/10.2307/1311969>
- Devred, E., Sathyendranath, S., Stuart, V., Maass, H., Ulloa, O., Platt, T., 2006. A two-component model of phytoplankton absorption in the open ocean: Theory and

- applications. *J. Geophys. Res.* 111, C03011. <https://doi.org/10.1029/2005JC002880>
- Dierssen, H., Zimmerman, R., Drake, L., Burdige, D., 2010. Benthic ecology from space: optics and net primary production in seagrass and benthic algae across the Great Bahama Bank. *Mar. Ecol. Prog. Ser.* 411, 1–15. <https://doi.org/10.3354/meps08665>
- Dierssen, H.M., Bostrom, K.J., Chlus, A., Hammerstrom, K., Thompson, D.R., Lee, Z., 2019. Pushing the limits of seagrass remote sensing in the turbid waters of Elkhorn Slough, California. *Remote Sens.* 11, 13–15. <https://doi.org/10.3390/rs11141664>
- Dionne, J.-C., 2001. Relative sea-level changes in the St. Lawrence estuary from deglaciation to present day, in: Weddle, T.K., Retelle, M.J. (Eds.), *Deglacial History and Relative Sea-Level Changes, Northern New England and Adjacent Canada*. Geological Society of America, Denver, CO, USA, pp. 271–284. <https://doi.org/10.1130/0-8137-2351-5.271>
- Domingues, R.B., Barbosa, A., Galvão, H., 2005. Nutrients, light and phytoplankton succession in a temperate estuary (the Guadiana, south-western Iberia). *Estuar. Coast. Shelf Sci.* 64, 249–260. <https://doi.org/10.1016/j.ecss.2005.02.017>
- Doney, S.C., 2010. The growing human footprint on coastal and open-ocean biogeochemistry. *Science* (80-.). 328, 1512–1516. <https://doi.org/10.1126/science.1185198>
- Donlon, C.J., Minnett, P.J., Gentemann, C., Nightingale, T.J., Barton, I.J., Ward, B., Murray, M.J., 2002. Toward improved validation of satellite sea surface skin temperature measurements for climate research. *J. Clim.* 15, 353–369. [https://doi.org/10.1175/1520-0442\(2002\)015<0353:TIVOSS>2.0.CO;2](https://doi.org/10.1175/1520-0442(2002)015<0353:TIVOSS>2.0.CO;2)
- Doxaran, D., Leymarie, E., Nechad, B., Dogliotti, A., Gernez, P., Knaeps, E., 2016. Improved correction methods for field measurements of particulate light backscattering in turbid waters. *Opt. Express* 24, 5415–5436. <https://doi.org/10.1364/OE.24.003615>
- Dreujou, E., Desroy, N., Carrière, J., Tréau de Coeli, L., McKindsey, C.W., Archambault, P., 2021. Determining the ecological status of benthic coastal communities: A case in an anthropized sub-arctic area. *Front. Mar. Sci.* 8, 1–16. <https://doi.org/10.3389/fmars.2021.637546>
- Duarte, C.M., 2017. Reviews and syntheses: Hidden forests, the role of vegetated coastal habitats in the ocean carbon budget. *Biogeosciences* 14, 301–310. <https://doi.org/10.5194/bg-14-301-2017>
- Duarte, C.M., 1991. Seagrass depth limits. *Aquat. Bot.* 40, 363–377. [https://doi.org/10.1016/0304-3770\(91\)90081-F](https://doi.org/10.1016/0304-3770(91)90081-F)

- Dunic, J.C., Brown, C.J., Connolly, R.M., Turschwell, M.P., Côté, I.M., 2021. Long-term declines and recovery of meadow area across the world's seagrass bioregions. *Glob. Chang. Biol.* 27, 4096–4109. <https://doi.org/10.1111/gcb.15684>
- Dunic, J.C., Côté, I.M., 2023. Management thresholds shift under the influence of multiple stressors: Eelgrass meadows as a case study. *Conserv. Lett.* 1–9. <https://doi.org/10.1111/conl.12938>
- Edwards, K.F., Litchman, E., Klausmeier, C.A., 2013. Functional traits explain phytoplankton community structure and seasonal dynamics in a marine ecosystem. *Ecol. Lett.* 16, 56–63. <https://doi.org/10.1111/ele.12012>
- Edwards, K.F., Thomas, M.K., Klausmeier, C.A., Litchman, E., 2016. Phytoplankton growth and the interaction of light and temperature: A synthesis at the species and community level. *Limnol. Oceanogr.* 61, 1232–1244. <https://doi.org/10.1002/lno.10282>
- El-Sabh, M.I., Lie, H.-J., Koutitonsky, V.G., 1982. Variability of the near-surface residual current in the lower St. Lawrence estuary. *J. Geophys. Res.* 87, 9589. <https://doi.org/10.1029/JC087iC12p09589>
- El-Sabh, M.I., Murty, T.S., 1990. Mathematical modelling of tides in the St. Lawrence Estuary, in: El-Sabh, M., Silverberg, N. (Eds.), *Oceanography of a Large-Scale Estuarine System*. pp. 10–50. <https://doi.org/10.1029/ce039p0010>
- El-Sabh, M.I., Silverberg, N., 1990a. The St. Lawrence Estuary: Introduction, in: El-Sabh, M., Silverberg, N. (Eds.), *Oceanography of a Large-Scale Estuarine System*. Springer New York, New York, NY, pp. 1–9. https://doi.org/10.1007/978-1-4615-7534-4_1
- El-Sabh, M.I., Silverberg, N., 1990b. *Oceanography of a Large-Scale Estuarine System*. Springer New York, New York, NY. <https://doi.org/10.1007/978-1-4615-7534-4>
- Ellis, E.C., Klein Goldewijk, K., Siebert, S., Lightman, D., Ramankutty, N., 2010. Anthropogenic transformation of the biomes, 1700 to 2000. *Glob. Ecol. Biogeogr.* 19, no-no. <https://doi.org/10.1111/j.1466-8238.2010.00540.x>
- Environment and natural resources Canada [WWW Document], n.d. URL <https://climat.meteo.gc.ca/> (accessed 2.19.21).
- Fauchot, J., Saucier, F.J., Levasseur, M., Roy, S., Zakardjian, B., 2008. Wind-driven river plume dynamics and toxic *Alexandrium tamarense* blooms in the St. Lawrence estuary (Canada): A modeling study. *Harmful Algae* 7, 214–227. <https://doi.org/10.1016/j.hal.2007.08.002>
- Fernandes, M.B., Hennessy, A., Law, W.B., Daly, R., Gaylard, S., Lewis, M., Clarke, K., 2022. Landsat historical records reveal large-scale dynamics and enduring recovery of

seagrasses in an impacted seascape. *Sci. Total Environ.* 813, 152646. <https://doi.org/10.1016/j.scitotenv.2021.152646>

- Ferrario, F., Araújo, C.A.S., Bélanger, S., Bourgault, D., Carrière, J., Carrier-Belleau, C., Dreujou, E., Johnson, L.E., Juniper, S.K., Mabit, R., McKindsey, C.W., Ogston, L., Picard, M.M.M., Saint-Louis, R., Saulnier-Talbot, É., Shaw, J.-L., Templeman, N., Therriault, T.W., Tremblay, J.-E., Archambault, P., 2022. Holistic environmental monitoring in ports as an opportunity to advance sustainable development, marine science, and social inclusiveness. *Elem. Sci. Anthr.* 10, 1–21. <https://doi.org/10.1525/elementa.2021.00061>
- Ferreira, A., Ciotti, Á.M., Mendes, C.R.B., Uitz, J., Bricaud, A., 2017. Phytoplankton light absorption and the package effect in relation to photosynthetic and photoprotective pigments in the northern tip of Antarctic Peninsula. *J. Geophys. Res. Ocean.* 122, 7344–7363. <https://doi.org/10.1002/2017JC012964>
- Fichot, C.G., Benner, R., 2012. The spectral slope coefficient of chromophoric dissolved organic matter (S₂₇₅₋₂₉₅) as a tracer of terrigenous dissolved organic carbon in river-influenced ocean margins. *Limnol. Oceanogr.* 57, 1453–1466. <https://doi.org/10.4319/lo.2012.57.5.1453>
- Fichot, C.G., Benner, R., 2011. A novel method to estimate DOC concentrations from CDOM absorption coefficients in coastal waters. *Geophys. Res. Lett.* 38, L03610. <https://doi.org/10.1029/2010GL046152>
- Fichot, C.G., Tzortziou, M., Mannino, A., 2023. Remote sensing of dissolved organic carbon (DOC) stocks, fluxes and transformations along the land-ocean aquatic continuum: advances, challenges, and opportunities. *Earth-Science Rev.* 242, 104446. <https://doi.org/10.1016/j.earscirev.2023.104446>
- Field, C.B., Behrenfeld, M.J., Randerson, J.T., Falkowski, P., 1998. Primary Production of the Biosphere: Integrating Terrestrial and Oceanic Components. *Science* (80-.). 281, 237–240. <https://doi.org/10.1126/science.281.5374.237>
- Fisheries and Oceans Canada, (DFO), 2009. Does eelgrass (*Zostera marina*) meet the criteria as an ecologically significant species? *Can. Sci. Advis. Secr. Sci. Advis. Rep.* 2009/018 11 p.
- Fisheries and Oceans Canada, (DFO), 2007. Guidance document on identifying conservation priorities and phrasing conservation objectives for large ocean management areas. *DFO Can. Sci. Advis. Secr. Sci. Advis. Rep.* 2007/010 13 p.
- Foga, S., Scaramuzza, P.L., Guo, S., Zhu, Z., Dilley, R.D., Beckmann, T., Schmidt, G.L., Dwyer, J.L., Joseph Hughes, M., Laue, B., 2017. Cloud detection algorithm comparison and validation for operational Landsat data products. *Remote Sens. Environ.* 194, 379–

390. <https://doi.org/10.1016/j.rse.2017.03.026>

Folke, C., Hahn, T., Olsson, P., Norberg, J., 2005. Adaptive governance of social-ecological systems. *Annu. Rev. Environ. Resour.* 30, 441–473. <https://doi.org/10.1146/annurev.energy.30.050504.144511>

Folke, C., Polasky, S., Rockström, J., Galaz, V., Westley, F., Lamont, M., Scheffer, M., Österblom, H., Carpenter, S.R., Chapin, F.S., Seto, K.C., Weber, E.U., Crona, B.I., Daily, G.C., Dasgupta, P., Gaffney, O., Gordon, L.J., Hoff, H., Levin, S.A., Lubchenco, J., Steffen, W., Walker, B.H., 2021. Our future in the Anthropocene biosphere. *Ambio* 50, 834–869. <https://doi.org/10.1007/s13280-021-01544-8>

Folt, C.L., Chen, C.Y., Moore, M. V., Burnaford, J., 1999. Synergism and antagonism among multiple stressors. *Limnol. Oceanogr.* 44, 864–877. https://doi.org/10.4319/lo.1999.44.3_part_2.0864

Fuentes-Yaco, C., Vézina, A.F., Larouche, P., Gratton, Y., Gosselin, M., 1997a. Phytoplankton pigment in the Gulf of St. Lawrence, Canada, as determined by the Coastal Zone Color Scanner—Part II: multivariate analysis. *Cont. Shelf Res.* 17, 1441–1459. [https://doi.org/10.1016/S0278-4343\(97\)00022-8](https://doi.org/10.1016/S0278-4343(97)00022-8)

Fuentes-Yaco, C., Vézina, A.F., Larouche, P., Vigneau, C., Gosselin, M., Levasseur, M., 1997b. Phytoplankton pigment in the Gulf of St. Lawrence, Canada, as determined by the Coastal Zone Color Scanner—Part I: spatio-temporal variability. *Cont. Shelf Res.* 17, 1421–1439. [https://doi.org/10.1016/S0278-4343\(97\)00021-6](https://doi.org/10.1016/S0278-4343(97)00021-6)

Gallagher, A.J., Brownscombe, J.W., Alsudairy, N.A., Casagrande, A.B., Fu, C., Harding, L., Harris, S.D., Hammerschlag, N., Howe, W., Huertas, A.D., Kattan, S., Kough, A.S., Musgrove, A., Payne, N.L., Phillips, A., Shea, B.D., Shipley, O.N., Sumaila, U.R., Hossain, M.S., Duarte, C.M., 2022. Tiger sharks support the characterization of the world's largest seagrass ecosystem. *Nat. Commun.* 13, 6328. <https://doi.org/10.1038/s41467-022-33926-1>

Gallegos, C.L., Davies-Colley, R.J., Gall, M., 2008. Optical closure in lakes with contrasting extremes of reflectance. *Limnol. Oceanogr.* 53, 2021–2034. <https://doi.org/10.4319/lo.2008.53.5.2021>

Garneau, M.-È., Vincent, W.F., Terrado, R., Lovejoy, C., 2009. Importance of particle-associated bacterial heterotrophy in a coastal Arctic ecosystem. *J. Mar. Syst.* 75, 185–197. <https://doi.org/10.1016/j.jmarsys.2008.09.002>

Gibb, S., Barlow, R., Cummings, D., Rees, N., Trees, C., Holligan, P., Suggett, D., 2000. Surface phytoplankton pigment distributions in the Atlantic Ocean: an assessment of basin scale variability between 50°N and 50°S. *Prog. Oceanogr.* 45, 339–368. [https://doi.org/10.1016/S0079-6611\(00\)00007-0](https://doi.org/10.1016/S0079-6611(00)00007-0)

- Glibert, P., Anderson, D., Gentien, P., Granéli, E., Sellner, K., 2005. The global, complex phenomena of harmful algal blooms. *Oceanography* 18, 136–147. <https://doi.org/10.5670/oceanog.2005.49>
- Gonçalves-Araujo, R., Rabe, B., Peeken, I., Bracher, A., 2018. High colored dissolved organic matter (CDOM) absorption in surface waters of the central-eastern Arctic Ocean: Implications for biogeochemistry and ocean color algorithms. *PLoS One* 13, e0190838. <https://doi.org/10.1371/journal.pone.0190838>
- Gordon, H.R., Brown, O.B., Evans, R.H., Brown, J.W., Smith, R.C., Baker, K.S., Clark, D.K., 1988. A semianalytic radiance model of ocean color. *J. Geophys. Res. Atmos.* 93, 10909–10924. <https://doi.org/10.1029/JD093iD09p10909>
- Gordon, H.R., Brown, O.B., Jacobs, M.M., 1975. Computed Relationships Between the Inherent and Apparent Optical Properties of a Flat Homogeneous Ocean. *Appl. Opt.* 14, 417. <https://doi.org/10.1364/AO.14.000417>
- Gordon, H.R., McCluney, W.R., 1975. Estimation of the depth of sunlight penetration in the sea for remote sensing. *Appl. Opt.* 14, 413. <https://doi.org/10.1364/AO.14.000413>
- Gorelick, N., Hancher, M., Dixon, M., Ilyushchenko, S., Thau, D., Moore, R., 2017. Google Earth Engine: Planetary-scale geospatial analysis for everyone. *Remote Sens. Environ.* 202, 18–27. <https://doi.org/10.1016/j.rse.2017.06.031>
- Graff, J.R., Westberry, T.K., Milligan, A.J., Brown, M.B., Dall’Olmo, G., Reifel, K.M., Behrenfeld, M.J., 2016. Photoacclimation of natural phytoplankton communities. *Mar. Ecol. Prog. Ser.* 542, 51–62. <https://doi.org/10.3354/meps11539>
- Grech, A., Chartrand-Miller, K., Erfteimeijer, P., Fonseca, M., McKenzie, L., Rasheed, M., Taylor, H., Coles, R., 2012. A comparison of threats, vulnerabilities and management approaches in global seagrass bioregions. *Environ. Res. Lett.* 7, 024006. <https://doi.org/10.1088/1748-9326/7/2/024006>
- Gullström, M., Lundén, B., Bodin, M., Kangwe, J., Öhman, M.C., Mtolera, M.S.P., Björk, M., 2006. Assessment of changes in the seagrass-dominated submerged vegetation of tropical Chwaka Bay (Zanzibar) using satellite remote sensing. *Estuar. Coast. Shelf Sci.* 67, 399–408. <https://doi.org/10.1016/j.ecss.2005.11.020>
- Gunderson, A.R., Armstrong, E.J., Stillman, J.H., 2016. Multiple Stressors in a Changing World: The Need for an Improved Perspective on Physiological Responses to the Dynamic Marine Environment. *Ann. Rev. Mar. Sci.* 8, 357–378. <https://doi.org/10.1146/annurev-marine-122414-033953>
- Hansell, D.A., 2013. Recalcitrant Dissolved Organic Carbon Fractions. *Ann. Rev. Mar. Sci.* 5, 421–445. <https://doi.org/10.1146/annurev-marine-120710-100757>

- Harley, C.D.G., Randall Hughes, A., Hultgren, K.M., Miner, B.G., Sorte, C.J.B., Thornber, C.S., Rodriguez, L.F., Tomanek, L., Williams, S.L., 2006. The impacts of climate change in coastal marine systems. *Ecol. Lett.* 9, 228–241. <https://doi.org/10.1111/j.1461-0248.2005.00871.x>
- Hedges, J.I., Keil, R.G., 1999. Organic geochemical perspectives on estuarine processes: sorption reactions and consequences. *Mar. Chem.* 65, 55–65. [https://doi.org/10.1016/S0304-4203\(99\)00010-9](https://doi.org/10.1016/S0304-4203(99)00010-9)
- Helms, J.R., Stubbins, A., Ritchie, J.D., Minor, E.C., Kieber, D.J., Mopper, K., 2008. Absorption spectral slopes and slope ratios as indicators of molecular weight, source, and photobleaching of chromophoric dissolved organic matter. *Limnol. Oceanogr.* 53, 955–969. <https://doi.org/10.4319/lo.2008.53.3.0955>
- Henderson, C.J., Stevens, T., Lee, S.Y., Gilby, B.L., Schlacher, T.A., Connolly, R.M., Warnken, J., Maxwell, P.S., Olds, A.D., 2019. Optimising seagrass conservation for ecological functions. *Ecosystems* 22, 1368–1380. <https://doi.org/10.1007/s10021-019-00343-3>
- Hill, V., Cota, G., Stockwell, D., 2005. Spring and summer phytoplankton communities in the Chukchi and Eastern Beaufort Seas. *Deep. Res. Part II Top. Stud. Oceanogr.* 52, 3369–3385. <https://doi.org/10.1016/j.dsr2.2005.10.010>
- Hill, V.J., Zimmerman, R.C., Bissett, W.P., Dierssen, H., Kohler, D.D.R., 2014. Evaluating Light Availability, Seagrass Biomass, and Productivity Using Hyperspectral Airborne Remote Sensing in Saint Joseph’s Bay, Florida. *Estuaries and Coasts* 37, 1467–1489. <https://doi.org/10.1007/s12237-013-9764-3>
- Hintz, N.H., Zeising, M., Striebel, M., 2021. Changes in spectral quality of underwater light alter phytoplankton community composition. *Limnol. Oceanogr.* 66, 3327–3337. <https://doi.org/10.1002/lno.11882>
- Hoepffner, N., Sathyendranath, S., 1993. Determination of the major groups of phytoplankton pigments from the absorption spectra of total particulate matter. *J. Geophys. Res.* 98, 22789. <https://doi.org/10.1029/93JC01273>
- Hoepffner, N., Sathyendranath, S., 1991. Effect of pigment composition on absorption properties of phytoplankton. *Mar. Ecol. Prog. Ser.* 73, 11–23. <https://doi.org/10.3354/meps073011>
- Holmer, M., 2019. Productivity and biogeochemical cycling in seagrass ecosystems, in: Perillo, G.M.E., Wolanski, E., Cahoon, D.R., Hopkinson, C.S. (Eds.), *Coastal Wetlands: An Integrated Approach*. Elsevier, pp. 443–477. <https://doi.org/10.1016/B978-0-444-63893-9.00013-7>

- Holmes, R.M., McClelland, J.W., Raymond, P.A., Frazer, B.B., Peterson, B.J., Stieglitz, M., 2008. Lability of DOC transported by Alaskan rivers to the Arctic Ocean. *Geophys. Res. Lett.* 35, L03402. <https://doi.org/10.1029/2007GL032837>
- Hossain, M.S., Hashim, M., 2019. Potential of Earth Observation (EO) technologies for seagrass ecosystem service assessments. *Int. J. Appl. Earth Obs. Geoinf.* 77, 15–29. <https://doi.org/10.1016/j.jag.2018.12.009>
- Howarth, R.W., Chan, F., Swaney, D.P., Marino, R.M., Hayn, M., 2021. Role of external inputs of nutrients to aquatic ecosystems in determining prevalence of nitrogen vs. phosphorus limitation of net primary productivity. *Biogeochemistry* 154, 293–306. <https://doi.org/10.1007/s10533-021-00765-z>
- IOCCG, 2023a. Current Ocean-Colour Sensors [WWW Document]. Int. Ocean Colour Coord. Gr. URL <https://ioccg.org/resources/missions-instruments/current-ocean-colour-sensors/> (accessed 4.25.23).
- IOCCG, 2023b. Scheduled Ocean-Colour Sensors [WWW Document]. Int. Ocean Colour Coord. Gr. <https://doi.org/25 April 2023>
- IOCCG, 2020. Synergy between ocean colour and biogeochemical/ecosystem models. International Ocean Colour Coordinating Group, Dartmouth, NS, Canada. <https://doi.org/10.25607/OBP-711>
- IOCCG, 2018. Ocean optics and biogeochemistry protocols for satellite ocean colour sensor validation. Volume 1: Inherent optical property measurements and protocols: absorption coefficient. IOCCG, Dartmouth, Canada. <https://doi.org/10.25607/OBP-119>
- IOCCG, 2014. Phytoplankton functional types from space, Phytoplankton functional types from space. Reports of the International Ocean Colour Coordinating Group. IOCCG, Dartmouth, Canada.
- IOCCG, 2008. Why ocean colour? The societal benefits of ocean-colour technology, Reports of the International Ocean-Colour Coordinating Group, No. 7. IOCCG, Dartmouth, NS, Canada.
- IPCC, 2022. Climate Change 2022: Impacts, Adaptation and Vulnerability. Contrib. Work. Gr. II Contrib. to Sixth Assess. Rep. Intergovernmental Panel Clim. Chang. <https://doi.org/10.1017/9781009325844>
- Jaegler, T., 2014. Variabilité Spatiale et Temporelle des Propriétés Optiques et Chimiques de la Matière Organique Dissoute dans les Rivières de la Côte-Nord, Québec, Canada. M.Sc. Thesis. Université du Québec à Rimouski, Canada.
- Jayatilake, D.R.M., Costello, M.J., 2018. A modelled global distribution of the seagrass

- biome. *Biol. Conserv.* 226, 120–126. <https://doi.org/10.1016/j.biocon.2018.07.009>
- Jerlov, N.G., 1968. *Optical oceanography*. Elsevier, New York.
- Jobin, A., Marquis, G., Provencher-Nolet, L., Gabaj Castrillo, M.J., Trubiano, C., Drouet, M., Eustache-Létourneau, D., Drejza, S., Fraser, C., Marie, G., Bernatchez, P., 2021. Cartographie des écosystèmes côtiers du Québec maritime - Rapport méthodologique. Chaire de recherche en géoscience côtière, Laboratoire de dynamique et de gestion intégrée des zones côtières, Université du Québec à Rimouski. Rapport remis au ministère de l'Environnement et de la Lutte contre les changements climatiques, Rimouski, QC, Canada.
- John, U., Litaker, R.W., Montresor, M., Murray, S., Brosnahan, M.L., Anderson, D.M., 2014. Formal Revision of the *Alexandrium tamarense* Species Complex (Dinophyceae) Taxonomy: The Introduction of Five Species with Emphasis on Molecular-based (rDNA) Classification. *Protist* 165, 779–804. <https://doi.org/10.1016/j.protis.2014.10.001>
- Kairis, P.A., Rybczyk, J.M., 2010. Sea level rise and eelgrass (*Zostera marina*) production: A spatially explicit relative elevation model for Padilla Bay, WA. *Ecol. Modell.* 221, 1005–1016. <https://doi.org/10.1016/j.ecolmodel.2009.01.025>
- Kaiser, M.J., Attrill, M.J., Jennings, S., Thomas, D.N., Barnes, D.K.A., Brierley, A.S., Graham, N.A.J., Hiddink, J.G., Howell, K., Kaartokallio, H., 2020. *Marine ecology: Processes, Systems, and Impacts*, Third edit. ed. Oxford University Press, New York, NY, USA.
- Kauko, H.M., Pavlov, A.K., Johnsen, G., Granskog, M.A., Peeken, I., Assmy, P., 2019. Photoacclimation State of an Arctic Underice Phytoplankton Bloom. *J. Geophys. Res. Ocean.* 124, 1750–1762. <https://doi.org/10.1029/2018JC014777>
- Kay, J.J., Regier, H.A., Boyle, M., Francis, G., 1999. An ecosystem approach for sustainability: addressing the challenge of complexity. *Futures* 31, 721–742. [https://doi.org/10.1016/S0016-3287\(99\)00029-4](https://doi.org/10.1016/S0016-3287(99)00029-4)
- Kirk, J.T.O., 2011. *Light and Photosynthesis in Aquatic Ecosystems*, Third. ed. Cambridge University Press, New York.
- Kishino, M., Takahashi, M., Okami, N., Ichimura, S., 1985. Estimation of the spectral absorption coefficients of phytoplankton in the sea. *Bull. Mar. Sci.* 37, 634–642.
- Klemas, V., 2010. Remote sensing techniques for studying coastal ecosystems: An overview. *J. Coast. Res.* 27, 2–17. <https://doi.org/10.2112/JCOASTRES-D-10-00103.1>
- Koestner, D., Stramski, D., Reynolds, R.A., 2020. Assessing the effects of particle size and

- composition on light scattering through measurements of size-fractionated seawater samples. *Limnol. Oceanogr.* 65, 173–190. <https://doi.org/10.1002/lno.11259>
- Konovalov, B. V., Kravchishina, M.D., Belyaev, N.A., Novigatsky, A.N., 2014. Determination of the concentration of mineral particles and suspended organic substance based on their spectral absorption. *Oceanology* 54, 660–667. <https://doi.org/10.1134/S0001437014040067>
- Koutitonsky, V.G., Bugden, G.L., 1991. The physical oceanography of the Gulf of St. Lawrence: A review with emphasis on the synoptic variability of the motion. *Can. Spec. Publ. Fish. Aquat. Sci.* 113, 57–90.
- Kovacs, E.M., Roelfsema, C., Udy, J., Baltais, S., Lyons, M., Phinn, S., 2022. Cloud Processing for Simultaneous Mapping of Seagrass Meadows in Optically Complex and Varied Water. *Remote Sens.* 14, 1–9. <https://doi.org/10.3390/rs14030609>
- Kramer, S.J., Siegel, D.A., 2019. How can phytoplankton pigments be best used to characterize surface ocean phytoplankton groups for ocean color remote sensing algorithms? *J. Geophys. Res. Ocean.* 124, 7557–7574. <https://doi.org/10.1029/2019JC015604>
- Krause-Jensen, D., Duarte, C.M., 2014. Expansion of vegetated coastal ecosystems in the future Arctic. *Front. Mar. Sci.* 1. <https://doi.org/10.3389/fmars.2014.00077>
- Krause, J.R., Hinojosa-Corona, A., Gray, A.B., Watson, E.B., 2021. Emerging sensor platforms allow for seagrass extent mapping in a turbid estuary and from the meadow to ecosystem scale. *Remote Sens.* 13, 1–15. <https://doi.org/10.3390/rs13183681>
- Krause, J.W., Schulz, I.K., Rowe, K.A., Dobbins, W., Winding, M.H.S., Sejr, M.K., Duarte, C.M., Agustí, S., 2019. Silicic acid limitation drives bloom termination and potential carbon sequestration in an Arctic bloom. *Sci. Rep.* 9, 1–11. <https://doi.org/10.1038/s41598-019-44587-4>
- Kuhwald, K., Schneider von Deimling, J., Schubert, P., Oppelt, N., 2022. How can Sentinel-2 contribute to seagrass mapping in shallow, turbid Baltic Sea waters? *Remote Sens. Ecol. Conserv.* 8, 328–346. <https://doi.org/10.1002/rse2.246>
- Laliberté, J., Larouche, P., Devred, E., Craig, S., 2018. Chlorophyll-a Concentration Retrieval in the Optically Complex Waters of the St. Lawrence Estuary and Gulf Using Principal Component Analysis. *Remote Sens.* 10, 265. <https://doi.org/10.3390/rs10020265>
- Larouche, P., Boyer-Villemare, U., 2010. Suspended particulate matter in the St. Lawrence estuary and Gulf surface layer and development of a remote sensing algorithm. *Estuar. Coast. Shelf Sci.* 90, 241–249. <https://doi.org/10.1016/j.ecss.2010.09.005>

- Le, C., Lehrter, J.C., Hu, C., Schaeffer, B., MacIntyre, H., Hagy, J.D., Beddick, D.L., 2015. Relation between inherent optical properties and land use and land cover across Gulf Coast estuaries. *Limnol. Oceanogr.* 60, 920–933. <https://doi.org/10.1002/lno.10065>
- Le Fouest, V., Matsuoka, A., Manizza, M., Shernetsky, M., Tremblay, B., Babin, M., 2018. Towards an assessment of riverine dissolved organic carbon in surface waters of the western Arctic Ocean based on remote sensing and biogeochemical modeling. *Biogeosciences* 15, 1335–1346. <https://doi.org/10.5194/bg-15-1335-2018>
- Le Fouest, V., Zakardjian, B., Saucier, F.J., 2005. Seasonal versus synoptic variability in planktonic production in a high-latitude marginal sea: The Gulf of St. Lawrence (Canada). *J. Geophys. Res.* 110, C09012. <https://doi.org/10.1029/2004JC002423>
- Le Quéré, C., Harrison, S.P., Colin Prentice, I., Buitenhuis, E.T., Aumont, O., Bopp, L., Claustre, H., Cotrim Da Cunha, L., Geider, R., Giraud, X., Klaas, C., Kohfeld, K.E., Legendre, L., Manizza, M., Platt, T., Rivkin, R.B., Sathyendranath, S., Uitz, J., Watson, A.J., Wolf-Gladrow, D., 2005. Ecosystem dynamics based on plankton functional types for global ocean biogeochemistry models. *Glob. Chang. Biol.* 11, 2016–2040. <https://doi.org/10.1111/j.1365-2486.2005.1004.x>
- Leblanc, M.-L., LaRocque, A., Leblon, B., Hanson, A., Humphries, M.M., 2021. Using Landsat time-Series to monitor and inform seagrass dynamics: A case study in the Tabusintac estuary, New Brunswick, Canada. *Can. J. Remote Sens.* 47, 65–82. <https://doi.org/10.1080/07038992.2021.1893672>
- Leblanc, M., O'Connor, M.I., Kuzyk, Z.Z.A., Noisette, F., Davis, K.E., Rabbitskin, E., Sam, L., Neumeier, U., Costanzo, R., Ehn, J.K., Babb, D., Idrobo, C.J., Gilbert, J., Leblon, B., Humphries, M.M., 2023. Limited recovery following a massive seagrass decline in subarctic eastern Canada. *Glob. Chang. Biol.* 29, 432–450. <https://doi.org/10.1111/gcb.16499>
- Lee, Z.-P., Du, K.-P., Arnone, R., 2005. A model for the diffuse attenuation coefficient of downwelling irradiance. *J. Geophys. Res.* 110, C02016. <https://doi.org/10.1029/2004JC002275>
- Lefcheck, J.S., Wilcox, D.J., Murphy, R.R., Marion, S.R., Orth, R.J., 2017. Multiple stressors threaten the imperiled coastal foundation species eelgrass (*Zostera marina*) in Chesapeake Bay, USA. *Glob. Chang. Biol.* 23, 3474–3483. <https://doi.org/10.1111/gcb.13623>
- Légaré, B., Bélanger, S., Singh, R.K., Bernatchez, P., Cusson, M., 2022. Remote sensing of coastal vegetation phenology in a cold temperate intertidal system: Implications for classification of coastal habitats. *Remote Sens.* 14, 3000. <https://doi.org/10.3390/rs14133000>

- Léger-Daigle, R., Noisette, F., Bélanger, S., Cusson, M., Nozais, C., 2022. Photoacclimation and Light Thresholds for Cold Temperate Seagrasses. *Front. Plant Sci.* 13, 1–14. <https://doi.org/10.3389/fpls.2022.805065>
- Lemieux, C., Lalumière, R., 1995. Répartition de la zostère marine (*Zostera marina*) dans l'estuaire du fleuve Saint-Laurent et dans la Baie des Chaleurs (1994). *Rapp. présenté au Serv. Can. la faune, Environ. Canada, pépapré par le Groupe-conseil Génivar inc.* 58.
- Leslie, H.M., McLeod, K.L., 2007. Confronting the challenges of implementing marine ecosystem-based management. *Front. Ecol. Environ.* 5, 540–548. <https://doi.org/10.1890/060093>
- Levasseur, M., Fortier, L., Therriault, J.-C., Harrison, P., 1992. Phytoplankton dynamics in a coastal jet frontal region. *Mar. Ecol. Prog. Ser.* 86, 283–295. <https://doi.org/10.3354/meps086283>
- Levin, S.A., 1992. The Problem of Pattern and Scale in Ecology: The Robert H. MacArthur Award Lecture. *Ecology* 73, 1943–1967. <https://doi.org/10.2307/1941447>
- Lewis, S.L., Maslin, M.A., 2015. Defining the Anthropocene. *Nature* 519, 171–180. <https://doi.org/10.1038/nature14258>
- Li, Q., Jin, R., Ye, Z., Gu, J., Dan, L., He, J., Christakos, G., Agusti, S., Duarte, C.M., Wu, J., 2022. Mapping seagrass meadows in coastal China using GEE. *Geocarto Int.* 37, 12602–12617. <https://doi.org/10.1080/10106049.2022.2070672>
- Lindeman, R.L., 1942. The trophic-dynamic aspect of ecology. *Ecology* 23, 399–417. <https://doi.org/10.2307/1930126>
- Lisitsyn, A.P., 1995. The marginal filter of the ocean. *Oceanology* 34, 671–682.
- Litchman, E., de Tezanos Pinto, P., Klausmeier, C.A., Thomas, M.K., Yoshiyama, K., 2010. Linking traits to species diversity and community structure in phytoplankton. *Hydrobiologia* 653, 15–28. <https://doi.org/10.1007/s10750-010-0341-5>
- Litchman, E., Klausmeier, C.A., 2008. Trait-Based Community Ecology of Phytoplankton. *Annu. Rev. Ecol. Evol. Syst.* 39, 615–639. <https://doi.org/10.1146/annurev.ecolsys.39.110707.173549>
- Litchman, E., Klausmeier, C.A., Schofield, O.M., Falkowski, P.G., 2007. The role of functional traits and trade-offs in structuring phytoplankton communities: Scaling from cellular to ecosystem level. *Ecol. Lett.* 10, 1170–1181. <https://doi.org/10.1111/j.1461-0248.2007.01117.x>
- Lizcano-Sandoval, L., Anastasiou, C., Montes, E., Raulerson, G., Sherwood, E., Muller-

- Karger, F.E., 2022. Seagrass distribution, areal cover, and changes (1990–2021) in coastal waters off West-Central Florida, USA. *Estuar. Coast. Shelf Sci.* 279, 108134. <https://doi.org/10.1016/j.ecss.2022.108134>
- Lo Prejato, M., McKee, D., Mitchell, C., 2020. Inherent Optical Properties-Reflectance Relationships Revisited. *J. Geophys. Res. C Ocean.* 125, 1–20. <https://doi.org/10.1029/2020JC016661>
- Lohrenz, S.E., Weidemann, A.D., Tuel, M., 2003. Phytoplankton spectral absorption as influenced by community size structure and pigment composition. *J. Plankton Res.* 25, 35–61. <https://doi.org/10.1093/plankt/25.1.35>
- Longhurst, A., Sathyendranath, S., Platt, T., Caverhill, C., 1995. An estimate of global primary production in the ocean from satellite radiometer data. *J. Plankton Res.* 17, 1245–1271. <https://doi.org/10.1093/plankt/17.6.1245>
- Lotze, H.K., Lenihan, H.S., Bourque, B.J., Bradbury, R.H., Cooke, R.G., Kay, M.C., Kidwell, S.M., Kirby, M.X., Peterson, C.H., Jackson, J.B.C., 2006. Depletion, Degradation, and Recovery Potential of Estuaries and Coastal Seas. *Science (80-)*. 312, 1806–1809. <https://doi.org/10.1126/science.1128035>
- Lucotte, M., D'Anglejan, B., 1986. Seasonal control of the Saint-Lawrence maximum turbidity zone by tidal-flat sedimentation. *Estuaries* 9, 84. <https://doi.org/10.2307/1351940>
- Lund, J.W.G., Kipling, C., Le Cren, E.D., 1958. The inverted microscope method of estimating algal numbers and the statistical basis of estimations by counting. *Hydrobiologia* 11, 143–170. <https://doi.org/10.1007/BF00007865>
- Lyons, M.B., Roelfsema, C.M., Phinn, S.R., 2013. Towards understanding temporal and spatial dynamics of seagrass landscapes using time-series remote sensing. *Estuar. Coast. Shelf Sci.* 120, 42–53. <https://doi.org/10.1016/j.ecss.2013.01.015>
- Mabit, R., Araújo, C.A.S., Singh, R.K., Bélanger, S., 2022. Empirical remote sensing algorithms to retrieve SPM and CDOM in québec coastal waters. *Front. Remote Sens.* 3, 834908. <https://doi.org/10.3389/frsen.2022.834908>
- Maffione, R.A., Dana, D.R., 1997. Instruments and methods for measuring the backward-scattering coefficient of ocean waters. *Appl. Opt.* 36, 6057. <https://doi.org/10.1364/AO.36.006057>
- Malone, T.C., Crocker, L.H., Pike, S.E., Wendler, B.W., 1988. Influences of river flow on the dynamics of phytoplankton production in a partially stratified estuary. *Mar. Ecol. Prog. Ser.* 48, 235–249.

- Marie, D., Le Gall, F., Edern, R., Gourvil, P., Vaultot, D., 2017. Improvement of phytoplankton culture isolation using single cell sorting by flow cytometry. *J. Phycol.* 53, 271–282. <https://doi.org/10.1111/jpy.12495>
- Maritorena, S., D'Andon, O.H.F., Mangin, A., Siegel, D.A., 2010. Merged satellite ocean color data products using a bio-optical model: Characteristics, benefits and issues. *Remote Sens. Environ.* 114, 1791–1804. <https://doi.org/10.1016/j.rse.2010.04.002>
- Masek, J.G., Vermote, E.F., Saleous, N.E., Wolfe, R., Hall, F.G., Huemmrich, K.F., Gao, F., Kutler, J., Lim, T.-K., 2006. A Landsat Surface Reflectance Dataset for North America, 1990–2000. *IEEE Geosci. Remote Sens. Lett.* 3, 68–72. <https://doi.org/10.1109/LGRS.2005.857030>
- Massicotte, P., Asmala, E., Stedmon, C., Markager, S., 2017. Global distribution of dissolved organic matter along the aquatic continuum: Across rivers, lakes and oceans. *Sci. Total Environ.* 609, 180–191. <https://doi.org/10.1016/j.scitotenv.2017.07.076>
- Matsuoka, A., Bricaud, A., Benner, R., Para, J., Sempéré, R., Prieur, L., Bélanger, S., Babin, M., 2012. Tracing the transport of colored dissolved organic matter in water masses of the Southern Beaufort Sea: relationship with hydrographic characteristics. *Biogeosciences* 925–940. <https://doi.org/10.5194/bg-9-925-2012>
- Mattsson, T., Kortelainen, P., Räike, A., 2005. Export of DOM from Boreal Catchments: Impacts of Land Use Cover and Climate. *Biogeochemistry* 76, 373–394. <https://doi.org/10.1007/s10533-005-6897-x>
- McClain, C.R., 2009. A Decade of Satellite Ocean Color Observations. *Ann. Rev. Mar. Sci.* 1, 19–42. <https://doi.org/10.1146/annurev.marine.010908.163650>
- McKenzie, L.J., Nordlund, L.M., Jones, B.L., Cullen-Unsworth, L.C., Roelfsema, C., Unsworth, R.K.F., 2020. The global distribution of seagrass meadows. *Environ. Res. Lett.* 15, 074041. <https://doi.org/10.1088/1748-9326/ab7d06>
- McMahon, K.W., Ambrose, W.G., Reynolds, M.J., Johnson, B.J., Whiting, A., Clough, L.M., 2021. Arctic lagoon and nearshore food webs: Relative contributions of terrestrial organic matter, phytoplankton, and phytobenthos vary with consumer foraging dynamics. *Estuar. Coast. Shelf Sci.* 257, 107388. <https://doi.org/10.1016/j.ecss.2021.107388>
- Meadows, D.H., 2008. *Thinking in systems: A primer*. Chelsea Green Publishing Company, White River Junction, VT, USA.
- Michaud, R., 1985. *La mousse de mer : de L'Isle-Verte à la Baie des Chaleurs*. Leméac, Montréal, QC, Canada.

- Minnett, P.J., Alvera-Azcárate, A., Chin, T.M., Corlett, G.K., Gentemann, C.L., Karagali, I., Li, X., Marsouin, A., Marullo, S., Maturi, E., Santoleri, R., Saux Picart, S., Steele, M., Vazquez-Cuervo, J., 2019. Half a century of satellite remote sensing of sea-surface temperature. *Remote Sens. Environ.* 233, 111366. <https://doi.org/10.1016/j.rse.2019.111366>
- Minnett, P.J., Smith, M., Ward, B., 2011. Measurements of the oceanic thermal skin effect. *Deep Sea Res. Part II Top. Stud. Oceanogr.* 58, 861–868. <https://doi.org/10.1016/j.dsr2.2010.10.024>
- Mobley, C.D., 1994. *Light and Water: Radiative Transfer in Natural Waters*. Academic Press, San Diego, CA, USA.
- Mohammadpour, G., Gagné, J.-P., Larouche, P., Montes-Hugo, M.A., 2017. Optical properties of size fractions of suspended particulate matter in littoral waters of Québec. *Biogeosciences* 14, 5297–5312. <https://doi.org/10.5194/bg-14-5297-2017>
- Mohammadpour, G., Montes-Hugo, M.A., Stavn, R., Gagné, J.-P., Larouche, P., 2015. Particle composition effects on MERIS-derived SPM: A case study in the Saint Lawrence Estuary. *Can. J. Remote Sens.* 41, 515–524. <https://doi.org/10.1080/07038992.2015.1110012>
- Montagnes, D.J.S., Berges, J.A., Harrison, P.J., Taylor, F.J.R., 1994. Estimating carbon, nitrogen, protein, and chlorophyll a from volume in marine phytoplankton. *Limnol. Oceanogr.* 39, 1044–1060. <https://doi.org/10.4319/lo.1994.39.5.1044>
- Montes-Hugo, M.A., Mohammadpour, G., 2012. Biogeo-optical modeling of SPM in the St. Lawrence Estuary. *Can. J. Remote Sens.* 38, 197–209. <https://doi.org/10.5589/m12-033>
- Montes-Hugo, M., Xie, H., 2015. An inversion model based on salinity and remote sensing reflectance for estimating the phytoplankton absorption coefficient in the Saint Lawrence estuary. *J. Geophys. Res. Ocean.* 120, 6958–6970. <https://doi.org/10.1002/2015JC011079>
- Morel, A., 1974. Optical properties of pure water and pure seawater, in: Jerlov, N.G., Steeman-Nielsen, E. (Eds.), *Optical Aspects of Oceanography*. Academic Press, New York, NY, pp. 1–24.
- Morel, A., Ahn, Y.-H., Partensky, F., Vaultot, D., Claustre, H., 1993. *Prochlorococcus* and *Synechococcus*: A comparative study of their optical properties in relation to their size and pigmentation. *J. Mar. Res.* 51, 617–649. <https://doi.org/10.1357/0022240933223963>
- Morel, A., Prieur, L., 1977. Analysis of variations in ocean color. *Limnol. Oceanogr.* 22, 709–722. <https://doi.org/10.4319/lo.1977.22.4.0709>

- Moses, W.J., Ackleson, S.G., Hair, J.W., Hostetler, C.A., Miller, W.D., 2016. Spatial scales of optical variability in the coastal ocean: Implications for remote sensing and in situ sampling. *J. Geophys. Res. Ocean.* 121, 4194–4208. <https://doi.org/10.1002/2016JC011767>
- Muehlstein, L.K., Porter, D., Short, F.T., 1991. *Labyrinthula Zosteræ* Sp. Nov., The Causative Agent of Wasting Disease of Eelgrass, *Zostera Marina*. *Mycologia* 83, 180–191. <https://doi.org/10.1080/00275514.1991.12025994>
- Mukherjee, S., Hedley, J.D., Fichot, C.G., Laliberté, J., Bélanger, S., 2023. Optical closure in highly absorptive coastal waters: significance of inelastic scattering processes. *Opt. Express* 31, 35178. <https://doi.org/10.1364/OE.501732>
- Muller-Karger, F.E., Hestir, E., Ade, C., Turpie, K., Roberts, D.A., Siegel, D., Miller, R.J., Humm, D., Izenberg, N., Keller, M., Morgan, F., Frouin, R., Dekker, A.G., Gardner, R., Goodman, J., Schaeffer, B., Franz, B.A., Pahlevan, N., Mannino, A.G., Concha, J.A., Ackleson, S.G., Cavanaugh, K.C., Romanou, A., Tzortziou, M., Boss, E.S., Pavlick, R., Freeman, A., Rousseaux, C.S., Dunne, J., Long, M.C., Klein, E., McKinley, G.A., Goes, J., Letelier, R., Kavanaugh, M., Roffer, M., Bracher, A., Arrigo, K.R., Dierssen, H., Zhang, X., Davis, F.W., Best, B., Guralnick, R., Moisan, J., Sosik, H.M., Kudela, R., Mouw, C.B., Barnard, A.H., Palacios, S., Roesler, C., Drakou, E.G., Appeltans, W., Jetz, W., 2018. Satellite sensor requirements for monitoring essential biodiversity variables of coastal ecosystems. *Ecol. Appl.* 28, 749–760. <https://doi.org/10.1002/eap.1682>
- Murphy, G.E.P., Dunic, J.C., Adamczyk, E.M., Bittick, S.J., Côté, I.M., Cristiani, J., Geissinger, E.A., Gregory, R.S., Lotze, H.K., O'Connor, M.I., Araújo, C.A.S., Rubidge, E.M., Templeman, N.D., Wong, M.C., 2021. From coast to coast to coast: ecology and management of seagrass ecosystems across Canada. *FACETS* 6, 139–179. <https://doi.org/10.1139/facets-2020-0020>
- Murphy, G.E.P., Wong, M.C., Lotze, H.K., 2019. A human impact metric for coastal ecosystems with application to seagrass beds in Atlantic Canada. *FACETS* 4, 210–237. <https://doi.org/10.1139/facets-2018-0044>
- Neukermans, G., Loisel, H., Mériaux, X., Astoreca, R., McKee, D., 2012. In situ variability of mass-specific beam attenuation and backscattering of marine particles with respect to particle size, density, and composition. *Limnol. Oceanogr.* 57, 124–144. <https://doi.org/10.4319/lo.2012.57.1.0124>
- Neukermans, G., Reynolds, R.A., Stramski, D., 2016. Optical classification and characterization of marine particle assemblages within the western Arctic Ocean. *Limnol. Oceanogr.* 61, 1472–1494. <https://doi.org/10.1002/lno.10316>
- Nieke, B., Reuter, R., Heuermann, R., Wang, H., Babin, M., Therriault, J.C., 1997. Light

- absorption and fluorescence properties of chromophoric dissolved organic matter (CDOM), in the St. Lawrence Estuary (Case 2 waters). *Cont. Shelf Res.* 17, 235–252. [https://doi.org/10.1016/S0278-4343\(96\)00034-9](https://doi.org/10.1016/S0278-4343(96)00034-9)
- Noernberg, M.A., Mizerkowski, B.D., Mafra, L.L., Freitas, F.H., 2020. Seasonal evolution of particulate and dissolved absorption coefficients in a subtropical estuary. *Estuar. Coast. Shelf Sci.* 244, 106907. <https://doi.org/10.1016/j.ecss.2020.106907>
- Nordstrom, D.K., 2012. Models, validation, and applied geochemistry: Issues in science, communication, and philosophy. *Appl. Geochemistry* 27, 1899–1919. <https://doi.org/10.1016/j.apgeochem.2012.07.007>
- Normandeau, A., Lajeunesse, P., St-Onge, G., 2013. Shallow-water longshore drift-fed submarine fan deposition (Moisie River Delta, Eastern Canada). *Geo-Marine Lett.* 33, 391–403. <https://doi.org/10.1007/s00367-013-0336-0>
- Odermatt, D., Gitelson, A., Brando, V.E., Schaeppman, M., 2012. Review of constituent retrieval in optically deep and complex waters from satellite imagery. *Remote Sens. Environ.* 118, 116–126. <https://doi.org/10.1016/j.rse.2011.11.013>
- Oliveira, A.L., Rudorff, N., Kämpel, M., Sathyendranath, S., Pompeu, M., Detoni, A.M.S., Cesar, G.M., 2021. Phytoplankton assemblages and optical properties in a coastal region of the South Brazil Bight. *Cont. Shelf Res.* 227, 104509. <https://doi.org/10.1016/j.csr.2021.104509>
- Ondiviela, B., Losada, I.J., Lara, J.L., Maza, M., Galván, C., Bouma, T.J., van Belzen, J., 2014. The role of seagrasses in coastal protection in a changing climate. *Coast. Eng.* 87, 158–168. <https://doi.org/10.1016/j.coastaleng.2013.11.005>
- Orth, R.J., Dennison, W.C., Duarte, C.M., Fourqurean, J.W., Heck, K.L., Hughes, A.R., Kendrick, G.A., Kenworthy, W.J., Short, F.T., Waycott, M., Williams, S.L., 2006. A global crisis for seagrass ecosystems. *Bioscience* 56, 987–996.
- Ostrom, E., 2009. A General Framework for Analyzing Sustainability of Social-Ecological Systems. *Science* (80-.). 325, 419–422. <https://doi.org/10.1126/science.1172133>
- Pan, Y., Bélanger, S., Huot, Y., 2022. Evaluation of Atmospheric Correction Algorithms over Lakes for High-Resolution Multispectral Imagery: Implications of Adjacency Effect. *Remote Sens.* 14, 2979. <https://doi.org/10.3390/rs14132979>
- Para, J., Coble, P.G., Charrière, B., Tedetti, M., Fontana, C., Sempéré, R., 2010. Fluorescence and absorption properties of chromophoric dissolved organic matter (CDOM) in coastal surface waters of the northwestern Mediterranean Sea, influence of the Rhône River. *Biogeosciences* 7, 4083–4103. <https://doi.org/10.5194/bg-7-4083-2010>

- Parsons, T.R., Maita, Y., Lalli, C.M., 1984. A manual of chemical and biological methods for seawater analysis. Pergamon Press, Toronto, Canada. <https://doi.org/10.1016/C2009-0-07774-5>
- Pereira, H.M., Ferrier, S., Walters, M., Geller, G.N., Jongman, R.H.G., Scholes, R.J., Bruford, M.W., Brummitt, N., Butchart, S.H.M., Cardoso, A.C., Coops, N.C., Dulloo, E., Faith, D.P., Freyhof, J., Gregory, R.D., Heip, C., Hoft, R., Hurtt, G., Jetz, W., Karp, D.S., McGeoch, M.A., Obura, D., Onoda, Y., Pettorelli, N., Reyers, B., Sayre, R., Scharlemann, J.P.W., Stuart, S.N., Turak, E., Walpole, M., Wegmann, M., 2013. Essential Biodiversity Variables. *Science* (80-.). 339, 277–278. <https://doi.org/10.1126/science.1229931>
- Preisendorfer, R.W., 1976. Hydrologic Optics. Volume I. National Oceanic and Atmospheric Administration, Environmental Research Laboratories, Pacific Marine Environmental Laboratory, Honolulu, HI, USA.
- Pritchard, D.W., 1967. What is an estuary: Physical viewpoint, in: Lauff, G.H. (Ed.), *Estuaries*. American Association for the Advancement of Science, Washington, DC, pp. 3–5.
- Provencher, L., Deslandes, S., 2012. Utilisation d’images satellitaires pour évaluer la superficie, l’étendue et la densité de l’herbier de la zostère marine (*Zostera marina*) de la péninsule de Manicouagan (Québec). *Rapp. Tech. Can. des Sci. halieutiques Aquat.* 2988 16.
- Ralph, P.J., Durako, M.J., Enríquez, S., Collier, C.J., Doblin, M.A., 2007. Impact of light limitation on seagrasses. *J. Exp. Mar. Bio. Ecol.* 350, 176–193. <https://doi.org/10.1016/j.jembe.2007.06.017>
- Redman, C.L., Grove, J.M., Kuby, L.H., 2004. Integrating Social Science into the Long-Term Ecological Research (LTER) Network: Social Dimensions of Ecological Change and Ecological Dimensions of Social Change. *Ecosystems* 7, 161–171. <https://doi.org/10.1007/s10021-003-0215-z>
- Regier, H.A., Kay, J.J., 1996. An heuristic model of transformations of the aquatic ecosystems of the Great Lakes-St. Lawrence River Basin. *J. Aquat. Ecosyst. Heal.* 5, 3–21. <https://doi.org/10.1007/BF00691726>
- Reynolds, R.A., Stramski, D., 2021. Variability in Oceanic Particle Size Distributions and Estimation of Size Class Contributions Using a Non-parametric Approach. *J. Geophys. Res. Ocean.* 126. <https://doi.org/10.1029/2021JC017946>
- Reynolds, R.A., Stramski, D., 2019. Optical characterization of marine phytoplankton assemblages within surface waters of the western Arctic Ocean. *Limnol. Oceanogr.* 64, 2478–2496. <https://doi.org/10.1002/lno.11199>

- Reynolds, R.A., Stramski, D., Neukermans, G., 2016. Optical backscattering by particles in Arctic seawater and relationships to particle mass concentration, size distribution, and bulk composition. *Limnol. Oceanogr.* 61, 1869–1890. <https://doi.org/10.1002/lno.10341>
- Röhr, M.E., Holmer, M., Baum, J.K., Björk, M., Boyer, K., Chin, D., Chalifour, L., Cimon, S., Cusson, M., Dahl, M., Deyanova, D., Duffy, J.E., Eklöf, J.S., Geyer, J.K., Griffin, J.N., Gullström, M., Hereu, C.M., Hori, M., Hovel, K.A., Hughes, A.R., Jorgensen, P., Kiriakopolos, S., Moksnes, P.-O., Nakaoka, M., O’Connor, M.I., Peterson, B., Reiss, K., Reynolds, P.L., Rossi, F., Ruesink, J., Santos, R., Stachowicz, J.J., Tomas, F., Lee, K.-S., Unsworth, R.K.F., Boström, C., 2018. Blue Carbon Storage Capacity of Temperate Eelgrass (*Zostera marina*) Meadows. *Global Biogeochem. Cycles* 32, 1457–1475. <https://doi.org/10.1029/2018GB005941>
- Roselli, L., Litchman, E., 2017. Phytoplankton traits, functional groups and community organization. *J. Plankton Res.* 39, 491–493. <https://doi.org/10.1093/plankt/fbx019>
- Röttgers, R., Dupouy, C., Taylor, B.B., Bracher, A., Woźniak, S.B., 2014. Mass-specific light absorption coefficients of natural aquatic particles in the near-infrared spectral region. *Limnol. Oceanogr.* 59, 1449–1460. <https://doi.org/10.4319/lo.2014.59.5.1449>
- Röttgers, R., Gehnke, S., 2012. Measurement of light absorption by aquatic particles: improvement of the quantitative filter technique by use of an integrating sphere approach. *Appl. Opt.* 51, 1336. <https://doi.org/10.1364/AO.51.001336>
- Roy, S., Blouin, F., Jacques, A., Therriault, J.C., 2008. Absorption properties of phytoplankton in the Lower Estuary and Gulf of St. Lawrence (Canada). *Can. J. Fish. Aquat. Sci.* 65, 1721–1737. <https://doi.org/10.1139/F08-089>
- Roy, S., Chanut, J., Gosselin, M., Sime-Ngando, T., 1996. Characterization of phytoplankton communities in the lower St. Lawrence Estuary using HPLC-detected pigments and cell microscopy. *Mar. Ecol. Prog. Ser.* 142, 55–73. <https://doi.org/10.3354/meps142055>
- Roy, S., Pitcher, Grant C., Kudela, R.M., Smith, M.E., Bernard, S., Mazeran, C., 2021. Ocean colour remote sensing of dinoflagellate blooms associated with paralytic shellfish poisoning, in: Bernard, S., Kudela, R.M., Robertson Lain, L., Pitcher, G.C. (Eds.), *Observation of Harmful Algal Blooms with Ocean Colour Radiometry*. International Ocean Colour Coordinating Group, Dartmouth, Canada, pp. 39–50. <https://doi.org/10.25607/OBP-1042>
- Salvador, S., Chan, P., 2004. Determining the number of clusters/segments in hierarchical clustering/segmentation algorithms, in: 16th IEEE International Conference on Tools with Artificial Intelligence. *IEEE Comput. Soc*, pp. 576–584. <https://doi.org/10.1109/ICTAI.2004.50>

- Santer, R., Schmechtig, C., 2000. Adjacency effects on water surfaces: primary scattering approximation and sensitivity study. *Appl. Opt.* 39, 361. <https://doi.org/10.1364/AO.39.000361>
- Sathyendranath, S., Prieur, L., Morel, A., 1989. A three-component model of ocean colour and its application to remote sensing of phytoplankton pigments in coastal waters. *Int. J. Remote Sens.* 10, 1373–1394. <https://doi.org/10.1080/01431168908903974>
- Saulquin, B., Hamdi, A., Gohin, F., Populus, J., Mangin, A., D’Andon, O.F., 2013. Estimation of the diffuse attenuation coefficient KdPAR using MERIS and application to seabed habitat mapping. *Remote Sens. Environ.* 128, 224–233. <https://doi.org/10.1016/j.rse.2012.10.002>
- Schott, J.R., Gerace, A., Woodcock, C.E., Wang, S., Zhu, Z., Wynne, R.H., Blinn, C.E., 2016. The impact of improved signal-to-noise ratios on algorithm performance: Case studies for Landsat class instruments. *Remote Sens. Environ.* 185, 37–45. <https://doi.org/10.1016/j.rse.2016.04.015>
- Sebastian, T., Sreenath, K.R., Sreeram, M.P., Ranith, R., 2023. Dwindling seagrasses: A multi-temporal analysis on Google Earth Engine. *Ecol. Inform.* 74, 101964. <https://doi.org/10.1016/j.ecoinf.2022.101964>
- Seegers, B.N., Stumpf, R.P., Schaeffer, B.A., Loftin, K.A., Werdell, P.J., 2018. Performance metrics for the assessment of satellite data products: an ocean color case study. *Opt. Express* 26, 7404. <https://doi.org/10.1364/OE.26.007404>
- Shaw, J.-L., 2019. Hydrodynamique de la baie de Sept-Îles. M.Sc. Thesis. Université du Québec à Rimouski.
- Shaw, J.-L., Bourgault, D., Dumont, D., Lefaivre, D., 2022. Hydrodynamics of the Bay of Sept-Îles. *Atmosphere-Ocean* 0, 1–17. <https://doi.org/10.1080/07055900.2022.2141605>
- Short, F., Carruthers, T., Dennison, W., Waycott, M., 2007. Global seagrass distribution and diversity: A bioregional model. *J. Exp. Mar. Bio. Ecol.* 350, 3–20. <https://doi.org/10.1016/j.jembe.2007.06.012>
- Short, F.T., Ibelings, B.W., Den Hartog, C., 1988. Comparison of a current eelgrass disease to the wasting disease in the 1930s. *Aquat. Bot.* 30, 295–304. [https://doi.org/10.1016/0304-3770\(88\)90062-9](https://doi.org/10.1016/0304-3770(88)90062-9)
- Sieracki, M.E., Verity, P.G., Stoecker, D.K., 1993. Plankton community response to sequential silicate and nitrate depletion during the 1989 North Atlantic spring bloom. *Deep. Res. Part II* 40, 213–225. [https://doi.org/10.1016/0967-0645\(93\)90014-E](https://doi.org/10.1016/0967-0645(93)90014-E)
- SIGEC, 2023. Système Intégré de Gestion de l’Environnement Côtier (SIGEC Web) [WWW

Document]. Lab. Dyn. Gest. intégrée des Zo. côtières. URL <https://ldgizc.uqar.ca/Web/sigecweb> (accessed 4.25.23).

SLGO [WWW Document], n.d. URL <https://ogsl.ca/en/home-slgo/> (accessed 2.19.21).

Small, C., Nicholls, R.J., 2003. A Global Analysis of Human Settlement in Coastal Zones. *J. Coast. Res.* 19, 584–589.

Smith, R.C., Baker, K.S., 1981. Optical properties of the clearest natural waters (200–800 nm). *Appl. Opt.* 20, 177. <https://doi.org/10.1364/AO.20.000177>

Smith, S. V., Mackenzie, F.T., 1987. The ocean as a net heterotrophic system: Implications from the carbon biogeochemical cycle. *Global Biogeochem. Cycles* 1, 187–198. <https://doi.org/10.1029/GB001i003p00187>

Sokal, R.R., Rohlf, F.J., 1962. The comparison of dendrograms by objective methods. *Taxon* 11, 33–40. <https://doi.org/10.2307/1217208>

St. Pierre, K.A., Oliver, A.A., Tank, S.E., Hunt, B.P. V., Giesbrecht, I., Kellogg, C.T.E., Jackson, J.M., Lertzman, K.P., Floyd, W.C., Korver, M.C., 2020. Terrestrial exports of dissolved and particulate organic carbon affect nearshore ecosystems of the Pacific coastal temperate rainforest. *Limnol. Oceanogr.* 65, 2657–2675. <https://doi.org/10.1002/lno.11538>

Stedmon, C.A., Markager, S., Bro, R., 2003. Tracing dissolved organic matter in aquatic environments using a new approach to fluorescence spectroscopy. *Mar. Chem.* 82, 239–254. [https://doi.org/10.1016/S0304-4203\(03\)00072-0](https://doi.org/10.1016/S0304-4203(03)00072-0)

Stedmon, C.A., Osburn, C.L., Kragh, T., 2010. Tracing water mass mixing in the Baltic–North Sea transition zone using the optical properties of coloured dissolved organic matter. *Estuar. Coast. Shelf Sci.* 87, 156–162. <https://doi.org/10.1016/j.ecss.2009.12.022>

Stommel, H., 1963. Varieties of oceanographic experience: The ocean can be investigated as a hydrodynamical phenomenon as well as explored geographically. *Science* (80-). 139, 572–576. <https://doi.org/10.1126/science.139.3555.572>

Stomp, M., Huisman, J., Stal, L.J., Matthijs, H.C.P., 2007. Colorful niches of phototrophic microorganisms shaped by vibrations of the water molecule. *ISME J.* 1, 271–282. <https://doi.org/10.1038/ismej.2007.59>

Stramski, D., Babin, M., Woźniak, S.B., 2007. Variations in the optical properties of terrigenous mineral-rich particulate matter suspended in seawater. *Limnol. Oceanogr.* 52, 2418–2433. <https://doi.org/10.4319/lo.2007.52.6.2418>

- Stramski, D., Boss, E., Bogucki, D., Voss, K.J., 2004. The role of seawater constituents in light backscattering in the ocean. *Prog. Oceanogr.* 61, 27–56. <https://doi.org/10.1016/j.pocean.2004.07.001>
- Stramski, D., Kiefer, D.A., 1991. Light scattering by microorganisms in the open ocean. *Prog. Oceanogr.* 28, 343–383. [https://doi.org/10.1016/0079-6611\(91\)90032-H](https://doi.org/10.1016/0079-6611(91)90032-H)
- Stramski, D., Reynolds, R.A., Kaczmarek, S., Uitz, J., Zheng, G., 2015. Correction of pathlength amplification in the filter-pad technique for measurements of particulate absorption coefficient in the visible spectral region. *Appl. Opt.* 54, 6763. <https://doi.org/10.1364/AO.54.006763>
- Sun, X., Shen, F., Brewin, R.J.W., Li, M., Zhu, Q., 2022. Light absorption spectra of naturally mixed phytoplankton assemblages for retrieval of phytoplankton group composition in coastal oceans. *Limnol. Oceanogr.* 67, 946–961. <https://doi.org/10.1002/lno.12047>
- Sunagawa, S., Coelho, L.P., Chaffron, S., Kultima, J.R., Labadie, K., Salazar, G., Djahanschiri, B., Zeller, G., Mende, D.R., Alberti, A., Cornejo-Castillo, F.M., Costea, P.I., Cruaud, C., D’Ovidio, F., Engelen, S., Ferrera, I., Gasol, J.M., Guidi, L., Hildebrand, F., Kokoszka, F., Lepoivre, C., Lima-Mendez, G., Poulain, J., Poulos, B.T., Royo-Llonch, M., Sarmiento, H., Vieira-Silva, S., Dimier, C., Picheral, M., Searson, S., Kandels-Lewis, S., Bowler, C., de Vargas, C., Gorsky, G., Grimsley, N., Hingamp, P., Iudicone, D., Jaillon, O., Not, F., Ogata, H., Pesant, S., Speich, S., Stemmann, L., Sullivan, M.B., Weissenbach, J., Wincker, P., Karsenti, E., Raes, J., Acinas, S.G., Bork, P., Boss, E., Bowler, C., Follows, M., Karp-Boss, L., Krzic, U., Reynaud, E.G., Sardet, C., Sieracki, M., Velayoudon, D., 2015. Structure and function of the global ocean microbiome. *Science (80-.)*. 348, 1–10. <https://doi.org/10.1126/science.1261359>
- Terhaar, J., Lauerwald, R., Regnier, P., Gruber, N., Bopp, L., 2021. Around one third of current Arctic Ocean primary production sustained by rivers and coastal erosion. *Nat. Commun.* 12, 169. <https://doi.org/10.1038/s41467-020-20470-z>
- Tett, P., Carreira, C., Mills, D.K., van Leeuwen, S., Foden, J., Bresnan, E., Gowen, R.J., 2008. Use of a Phytoplankton Community Index to assess the health of coastal waters. *ICES J. Mar. Sci.* 65, 1475–1482. <https://doi.org/10.1093/icesjms/fsn161>
- Therriault, J.-C., Legendre, L., Demers, S., 1990. Oceanography and ecology of phytoplankton in the St.Lawrence Estuary, in: El-Sabh, M., Silverberg, N. (Eds.), *Oceanography of a Large-Scale Estuarine System*. pp. 269–295. https://doi.org/10.1007/978-1-4615-7534-4_12
- Therriault, J.-C., Levasseur, M., 1986. Freshwater Runoff Control of the Spatio-Temporal Distribution of Phytoplankton in the Lower St.Lawrence Estuary (Canada), in: *The Role of Freshwater Outflow in Coastal Marine Ecosystems*. Springer Berlin, pp. 251–260. https://doi.org/10.1007/978-3-642-70886-2_17

- Therriault, J.C., Levasseur, M., 1985. Control of phytoplankton production in the Lower St. Lawrence Estuary: Light and Freshwater runoff. *Nat. Can.* 112, 77–96.
- Thoral, F., Pinkerton, M.H., Tait, L.W., Schiel, D.R., 2023. Spectral light quality on the seabed matters for macroalgal community composition at the extremities of light limitation. *Limnol. Oceanogr.* 68, 902–916. <https://doi.org/10.1002/lno.12318>
- Tomasko, D., Alderson, M., Burnes, R., Hecker, J., Leverone, J., Raulerson, G., Sherwood, E., 2018. Widespread recovery of seagrass coverage in Southwest Florida (USA): Temporal and spatial trends and management actions responsible for success. *Mar. Pollut. Bull.* 135, 1128–1137. <https://doi.org/10.1016/j.marpolbul.2018.08.049>
- Traganos, D., Lee, C.B., Blume, A., Poursanidis, D., Čížmek, H., Deter, J., Mačić, V., Montefalcone, M., Pergent, G., Pergent-Martini, C., Ricart, A.M., Reinartz, P., 2022a. Spatially Explicit Seagrass Extent Mapping Across the Entire Mediterranean. *Front. Mar. Sci.* 9, 1–13. <https://doi.org/10.3389/fmars.2022.871799>
- Traganos, D., Pertiwi, A.P., Lee, C.B., Blume, A., Poursanidis, D., Shapiro, A., 2022b. Earth observation for ecosystem accounting: spatially explicit national seagrass extent and carbon stock in Kenya, Tanzania, Mozambique and Madagascar. *Remote Sens. Ecol. Conserv.* 8, 778–792. <https://doi.org/10.1002/rse2.287>
- Trefault, N., De la Iglesia, R., Moreno-Pino, M., Lopes dos Santos, A., Gériques Ribeiro, C., Parada-Pozo, G., Cristi, A., Marie, D., Vaultot, D., 2021. Annual phytoplankton dynamics in coastal waters from Fildes Bay, Western Antarctic Peninsula. *Sci. Rep.* 11, 1368. <https://doi.org/10.1038/s41598-020-80568-8>
- Tremblay, G., Belzile, C., Gosselin, M., Poulin, M., Roy, S., Tremblay, J., 2009. Late summer phytoplankton distribution along a 3500 km transect in Canadian Arctic waters: strong numerical dominance by picoeukaryotes. *Aquat. Microb. Ecol.* 54, 55–70. <https://doi.org/10.3354/ame01257>
- Tremblay, J.-É., Legendre, L., Therriault, J.-C., 1997. Size-differential Effects of Vertical Stability on the Biomass and Production of Phytoplankton in a Large Estuarine System. *Estuar. Coast. Shelf Sci.* 45, 415–431. <https://doi.org/10.1006/ecss.1996.0223>
- Tremblay, J.-É., Legendre, L., Klein, B., Therriault, J.-C., 2000. Size-differential uptake of nitrogen and carbon in a marginal sea (Gulf of St. Lawrence, Canada): significance of diel periodicity and urea uptake. *Deep. Res. Part II Top. Stud. Oceanogr.* 47, 489–518. [https://doi.org/10.1016/S0967-0645\(99\)00116-2](https://doi.org/10.1016/S0967-0645(99)00116-2)
- Tremblay, J.-É., Michel, C., Hobson, K.A., Gosselin, M., Price, N.M., 2006. Bloom dynamics in early opening waters of the Arctic Ocean. *Limnol. Oceanogr.* 51, 900–912. <https://doi.org/10.4319/lo.2006.51.2.0900>

- Tremblay, L., Gagné, J.-P., 2009. Organic matter distribution and reactivity in the waters of a large estuarine system. *Mar. Chem.* 116, 1–12. <https://doi.org/10.1016/j.marchem.2009.09.006>
- Trombetta, T., Vidussi, F., Mas, S., Parin, D., Simier, M., Mostajir, B., 2019. Water temperature drives phytoplankton blooms in coastal waters. *PLoS One* 14, 1–28. <https://doi.org/10.1371/journal.pone.0214933>
- Tucker, C.J., 1979. Red and photographic infrared linear combinations for monitoring vegetation. *Remote Sens. Environ.* 8, 127–150. [https://doi.org/10.1016/0034-4257\(79\)90013-0](https://doi.org/10.1016/0034-4257(79)90013-0)
- Turner, M.G., 1989. Landscape Ecology: The Effect of Pattern on Process. *Annu. Rev. Ecol. Syst.* 20, 171–197. <https://doi.org/10.1146/annurev.es.20.110189.001131>
- Turner, R.K., Subak, S., Adger, W.N., 1996. Pressures, trends, and impacts in coastal zones: Interactions between socioeconomic and natural systems. *Environ. Manage.* 20, 159–173. <https://doi.org/10.1007/BF01204001>
- Tzortziou, M., Herman, J.R., Gallegos, C.L., Neale, P.J., Subramaniam, A., Harding, L.W., Ahmad, Z., 2006. Bio-optics of the Chesapeake Bay from measurements and radiative transfer closure. *Estuar. Coast. Shelf Sci.* 68, 348–362. <https://doi.org/10.1016/j.ecss.2006.02.016>
- Tzortziou, M., Osburn, C.L., Neale, P.J., 2007. Photobleaching of Dissolved Organic Material from a Tidal Marsh-Estuarine System of the Chesapeake Bay†. *Photochem. Photobiol.* 83, 782–792. <https://doi.org/10.1111/j.1751-1097.2007.00142.x>
- Uitz, J., Claustre, H., Morel, A., Hooker, S.B., 2006. Vertical distribution of phytoplankton communities in open ocean: An assessment based on surface chlorophyll. *J. Geophys. Res.* 111, C08005. <https://doi.org/10.1029/2005JC003207>
- Unsworth, R.K.F., Collier, C.J., Waycott, M., McKenzie, L.J., Cullen-Unsworth, L.C., 2015. A framework for the resilience of seagrass ecosystems. *Mar. Pollut. Bull.* 100, 34–46. <https://doi.org/10.1016/j.marpolbul.2015.08.016>
- Unsworth, R.K.F., McKenzie, L.J., Collier, C.J., Cullen-Unsworth, L.C., Duarte, C.M., Eklöf, J.S., Jarvis, J.C., Jones, B.L., Nordlund, L.M., 2019a. Global challenges for seagrass conservation. *Ambio* 48, 801–815. <https://doi.org/10.1007/s13280-018-1115-y>
- Unsworth, R.K.F., Nordlund, L.M., Cullen-Unsworth, L.C., 2019b. Seagrass meadows support global fisheries production. *Conserv. Lett.* 12, e12566. <https://doi.org/10.1111/conl.12566>

- USGS, 2023. Landsat 8-9 Level 2 Science Product (L2SP) Guide.
- USGS, 2021. Landsat 4-7 Level 2 Science Product (L2SP) Guide.
- Vallières, C., Retamal, L., Ramlal, P., Osburn, C.L., Vincent, W.F., 2008. Bacterial production and microbial food web structure in a large arctic river and the coastal Arctic Ocean. *J. Mar. Syst.* 74, 756–773. <https://doi.org/10.1016/j.jmarsys.2007.12.002>
- Van Assche, K., Verschraegen, G., Valentinov, V., Gruezmacher, M., 2019. The social, the ecological, and the adaptive. Von Bertalanffy's general systems theory and the adaptive governance of social-ecological systems. *Syst. Res. Behav. Sci.* 36, 308–321. <https://doi.org/10.1002/sres.2587>
- Van der Linde, D.W., 1998. Protocol for determination of total suspended matter in oceans and coastal zones. JRC Technical note I.98.182.
- Vance, T.C., Doel, R.E., 2010. Graphical Methods and Cold War Scientific Practice: The Stommel Diagram's Intriguing Journey from the Physical to the Biological Environmental Sciences. *Hist. Stud. Nat. Sci.* 40, 1–47. <https://doi.org/10.1525/hsns.2010.40.1.1>
- Vandavelde, T., Legendre, L., Demers, S., Therriault, J.C., 1989. Circadian variations in photosynthetic assimilation and estimation of daily phytoplankton production. *Mar. Biol.* 100, 525–531. <https://doi.org/10.1007/BF00394829>
- Vandavelde, T., Legendre, L., Therriault, J.-C., Demers, S., Bah, A., 1987. Subsurface chlorophyll maximum and hydrodynamics of the water column. *J. Mar. Res.* 45, 377–396. <https://doi.org/10.1357/002224087788401151>
- Vanhellemont, Q., 2020a. Sensitivity analysis of the dark spectrum fitting atmospheric correction for metre- and decametre-scale satellite imagery using autonomous hyperspectral radiometry. *Opt. Express* 28, 29948. <https://doi.org/10.1364/OE.397456>
- Vanhellemont, Q., 2020b. Automated water surface temperature retrieval from Landsat 8/TIRS. *Remote Sens. Environ.* 237, 111518. <https://doi.org/10.1016/j.rse.2019.111518>
- Vanhellemont, Q., 2020c. Combined land surface emissivity and temperature estimation from Landsat 8 OLI and TIRS. *ISPRS J. Photogramm. Remote Sens.* 166, 390–402. <https://doi.org/10.1016/j.isprsjprs.2020.06.007>
- Vanhellemont, Q., 2019. Adaptation of the dark spectrum fitting atmospheric correction for aquatic applications of the Landsat and Sentinel-2 archives. *Remote Sens. Environ.* 225, 175–192. <https://doi.org/10.1016/j.rse.2019.03.010>
- Vaulot, D., Eikrem, W., Viprey, M., Moreau, H., 2008. The diversity of small eukaryotic

- phytoplankton ($\leq 3 \mu\text{m}$) in marine ecosystems. *FEMS Microbiol. Rev.* 32, 795–820. <https://doi.org/10.1111/j.1574-6976.2008.00121.x>
- Veettil, B.K., Ward, R.D., Lima, M.D.A.C., Stankovic, M., Hoai, P.N., Quang, N.X., 2020. Opportunities for seagrass research derived from remote sensing: A review of current methods. *Ecol. Indic.* 117, 106560. <https://doi.org/10.1016/j.ecolind.2020.106560>
- Vézina, A.F., Gratton, Y., Vinet, P., 1995. Mesoscale physical—biological variability during a summer phytoplankton bloom in the lower St. Lawrence Estuary. *Estuar. Coast. Shelf Sci.* 41, 393–411. [https://doi.org/10.1016/0272-7714\(95\)90001-2](https://doi.org/10.1016/0272-7714(95)90001-2)
- von Bertalanffy, L., 1950. An outline of general system theory. *Br. J. Philos. Sci.* 1, 134–165. <https://doi.org/10.1093/bjps/I.2.134>
- Ward, J.H., 1963. Hierarchical grouping to optimize an objective function. *J. Am. Stat. Assoc.* 58, 236–244. <https://doi.org/10.1080/01621459.1963.10500845>
- Wassmann, P., Duarte, C.M., Agustí, S., Sejr, M.K., 2011. Footprints of climate change in the Arctic marine ecosystem. *Glob. Chang. Biol.* 17, 1235–1249. <https://doi.org/10.1111/j.1365-2486.2010.02311.x>
- Waycott, M., Duarte, C.M., Carruthers, T.J.B., Orth, R.J., Dennison, W.C., Olyarnik, S., Calladine, A., Fourqurean, J.W., Heck, K.L., Hughes, A.R., Kendrick, G.A., Kenworthy, W.J., Short, F.T., Williams, S.L., 2009. Accelerating loss of seagrasses across the globe threatens coastal ecosystems. *Proc. Natl. Acad. Sci.* 106, 12377–12381. <https://doi.org/10.1073/pnas.0905620106>
- Weise, A.M., Levasseur, M., Saucier, F.J., Senneville, S., Bonneau, E., Roy, S., Sauvé, G., Michaud, S., Fauchot, J., 2002. The link between precipitation, river runoff, and blooms of the toxic dinoflagellate *Alexandrium tamarense* in the St. Lawrence. *Can. J. Fish. Aquat. Sci.* 59, 464–473. <https://doi.org/10.1139/f02-024>
- Weishaar, J.L., Aiken, G.R., Bergamaschi, B.A., Fram, M.S., Fujii, R., Mopper, K., 2003. Evaluation of Specific Ultraviolet Absorbance as an Indicator of the Chemical Composition and Reactivity of Dissolved Organic Carbon. *Environ. Sci. Technol.* 37, 4702–4708. <https://doi.org/10.1021/es030360x>
- Wentzky, V.C., Tittel, J., Jäger, C.G., Bruggeman, J., Rinke, K., 2020. Seasonal succession of functional traits in phytoplankton communities and their interaction with trophic state. *J. Ecol.* 108, 1649–1663. <https://doi.org/10.1111/1365-2745.13395>
- Werdell, P.J., McKinna, L.I.W., Boss, E., Ackleson, S.G., Craig, S.E., Gregg, W.W., Lee, Z., Maritorena, S., Roesler, C.S., Rousseaux, C.S., Stramski, D., Sullivan, J.M., Twardowski, M.S., Tzortziou, M., Zhang, X., 2018. An overview of approaches and challenges for retrieving marine inherent optical properties from ocean color remote

- sensing. *Prog. Oceanogr.* 160, 186–212. <https://doi.org/10.1016/j.pocean.2018.01.001>
- Whitfield, A.K., 2017. The role of seagrass meadows, mangrove forests, salt marshes and reed beds as nursery areas and food sources for fishes in estuaries. *Rev. Fish Biol. Fish.* 27, 75–110. <https://doi.org/10.1007/s11160-016-9454-x>
- Wilson, E.H., Sader, S.A., 2002. Detection of forest harvest type using multiple dates of Landsat TM imagery. *Remote Sens. Environ.* 80, 385–396. [https://doi.org/10.1016/S0034-4257\(01\)00318-2](https://doi.org/10.1016/S0034-4257(01)00318-2)
- Winder, M., Carstensen, J., Galloway, A.W.E., Jakobsen, H.H., Cloern, J.E., 2017. The land-sea interface: A source of high-quality phytoplankton to support secondary production. *Limnol. Oceanogr.* 62, S258–S271. <https://doi.org/10.1002/lno.10650>
- Wulder, M.A., Roy, D.P., Radeloff, V.C., Loveland, T.R., Anderson, M.C., Johnson, D.M., Healey, S., Zhu, Z., Scambos, T.A., Pahlevan, N., Hansen, M., Gorelick, N., Crawford, C.J., Masek, J.G., Hermosilla, T., White, J.C., Belward, A.S., Schaaf, C., Woodcock, C.E., Huntington, J.L., Lymburner, L., Hostert, P., Gao, F., Lyapustin, A., Pekel, J.-F., Strobl, P., Cook, B.D., 2022. Fifty years of Landsat science and impacts. *Remote Sens. Environ.* 280, 113195. <https://doi.org/10.1016/j.rse.2022.113195>
- Xie, H., Aubry, C., Bélanger, S., Song, G., 2012. The dynamics of absorption coefficients of CDOM and particles in the St. Lawrence estuarine system: Biogeochemical and physical implications. *Mar. Chem.* 128–129, 44–56. <https://doi.org/10.1016/j.marchem.2011.10.001>
- Xu, H., 2006. Modification of normalised difference water index (NDWI) to enhance open water features in remotely sensed imagery. *Int. J. Remote Sens.* 27, 3025–3033. <https://doi.org/10.1080/01431160600589179>
- Xu, M., Barnes, B.B., Hu, C., Carlson, P.R., Yarbro, L.A., 2023. Water clarity monitoring in complex coastal environments: Leveraging seagrass light requirement toward more functional satellite ocean color algorithms. *Remote Sens. Environ.* 286, 113418. <https://doi.org/10.1016/j.rse.2022.113418>
- Xu, Y., Feng, L., Zhao, D., Lu, J., 2020. Assessment of Landsat atmospheric correction methods for water color applications using global AERONET-OC data. *Int. J. Appl. Earth Obs. Geoinf.* 93, 102192. <https://doi.org/10.1016/j.jag.2020.102192>
- Yayla, K.M., 2009. Approche empirique de la télédétection de la chlorophylle d'eaux à complexité optique dans l'estuaire et le golfe du Saint-Laurent. PhD Diss. Université de Sherbrooke, Québec, Canada.
- Zapata, M., Rodríguez, F., Garrido, J., 2000. Separation of chlorophylls and carotenoids from marine phytoplankton: a new HPLC method using a reversed phase C8 column and

pyridine-containing mobile phases. *Mar. Ecol. Prog. Ser.* 195, 29–45.
<https://doi.org/10.3354/meps195029>

Zhang, X., Hu, L., He, M.-X., 2009. Scattering by pure seawater at high salinity. *Opt. Express* 17, 5698–5710. <https://doi.org/10.1364/OE.17.012685>

Zhang, Y., Xie, H., 2015. Photomineralization and photomethanification of dissolved organic matter in Saguenay River surface water. *Biogeosciences* 12, 6823–6836.
<https://doi.org/10.5194/bg-12-6823-2015>

Zhu, Z., Woodcock, C.E., 2012. Object-based cloud and cloud shadow detection in Landsat imagery. *Remote Sens. Environ.* 118, 83–94. <https://doi.org/10.1016/j.rse.2011.10.028>

Zoffoli, M.L., Gernez, P., Godet, L., Peters, S., Oiry, S., Barillé, L., 2021. Decadal increase in the ecological status of a North-Atlantic intertidal seagrass meadow observed with multi-mission satellite time-series. *Ecol. Indic.* 130, 108033.
<https://doi.org/10.1016/j.ecolind.2021.108033>

Zoffoli, M.L., Gernez, P., Rosa, P., Le Bris, A., Brando, V.E., Barillé, A.-L., Harin, N., Peters, S., Poser, K., Spaias, L., Peralta, G., Barillé, L., 2020. Sentinel-2 remote sensing of *Zostera noltei*-dominated intertidal seagrass meadows. *Remote Sens. Environ.* 251, 112020. <https://doi.org/10.1016/j.rse.2020.112020>

